Quantifying uncertainty in radar rainfall estimates using an X-band dual polarisation weather radar

David Richard Lloyd Dufton

Submitted in accordance with the requirements for the degree of
Doctor of Philosophy

The University of Leeds
School of Earth and Environment
August 2016

Declaration of Authorship

The candidate confirms that the work submitted is his own, except where work which has formed part of jointly-authored publications has been included. The contribution of the candidate and the other authors to this work has been explicitly indicated below. The candidate confirms that appropriate credit has been given within the thesis where reference has been made to the work of others.

The work in Chapter 5, Section 5.3 has appeared in publication as follows:

Fuzzy logic filtering of radar reflectivity to remove non-meteorological echoes using dual polarization radar moments: Dufton, D. R. L. and Collier, C. G., Atmospheric Measurement Techniques, 8, 3985-4000, 2015

David Dufton was responsible for the development of the method and the data analysis in this paper, along with its writing, submission and response to reviewers. The contribution of the other author was the addition of subject knowledge, guidance and support.

Acknowledgements

Firstly I would like to extend my deepest thanks to my supervisors Chris Collier and Alan Blyth for their guidance and support without which my research would not have been possible. Chris's great breadth of knowledge on radar and its hydrometeorological applications along with his excitement about all things radar has helped steer my research towards its conclusion and provided encouragement along the way. Alan has always been on hand to provide some much needed atmospheric context and his enthusiasm has always been an encouragement to persevere. Thank you both for your encouragement and all the opportunities you have provided me over the last few years.

I would also like to thank everybody involved in the COPE field campaign, particularly Lindsay Bennett who's perseverance and determination in deploying the radar knows no bounds whatever the radar might do. Throughout my research Lindsay has always been around to muse radar and it's myriad complications and her support and guidance has been invaluable over the course of my PhD. Thanks also to the rest of the NCAS radar group, past and present. John and Neely your advice has enriched my research and been an encouragement throughout. James and Dan, thank you for all your technical support over the years, it has definitely made life easier during my research.

Special thanks to my peers over the last few years, Brad, Leighton, Joey, Phil, Jill, Jim, Steve and everyone else. Your help, encouragement, advice and friendship has kept me going over the years and ensured no matter how difficult or frustrating the research was the department has always been a happy place to work.

Finally and most importantly I'd like to thank my family, Chloe and Theo, Mum and Dad. Chloe without your support none of this would have been possible, thank you for always being there no matter what. Theo, thank you for being the perfect distraction over the past 21 months, watching you grow up has been a pleasure, even if you are a cheeky little boy at times. Mum and Dad, thank you for your unconditional love and support, without which life would have been immeasurably harder over the past few years.

Abstract

Weather radars have been used to quantitatively estimate precipitation since their development in the 1940s, yet these estimates are still prone to large uncertainties which dissuade the hydrological community in the UK from adopting these estimates as their primary rainfall data source. Recently dual polarisation radars have become more common, with the national networks in the USA, UK and across Europe being upgraded, and the benefits of dual polarisation radars are beginning to be realised for improving quantitative precipitation estimates (QPE).

The National Centre for Atmospheric Science (NCAS) mobile Doppler X-band dual polarisation weather radar is the first radar of its kind in the UK, and since its acquisition in 2012 has been deployed on several field campaigns in both the UK and abroad. The first of these campaigns was the Convective Precipitation Experiment (COPE) where the radar was deployed in Cornwall (UK) through the summer of 2013. This thesis has used the data acquired during the COPE field campaign to develop a processing chain for the X-band radar which leverages its dual polarisation capabilities.

The processing chain developed includes the removal of spurious echoes including second trip, ground clutter and insects through the use of dual polarisation texture fields, logical decision thresholds and fuzzy logic classification. The radar data is then corrected for the effects of attenuation and partial beam blockage (PBB) by using the differential phase shift (Φ_{DP}) to constrain the total path integrated attenuation and calibrate the radar azimuthally. A new smoothing technique has been developed to account for backscatter differential phase in the smoothing of Φ_{DP} which incorporates a long and a short averaging window in conjunction with weighting smoothing using the copolar correlation coefficient (ρ_{hv}). During the correction process it is shown that the calculation of PBB is insensitive to the variation in the ratio between specific attenuation and specific differential phase shift (α) provided a consistent value is used. It is also shown that the uncertainty in attenuation correction is lower when using a constrained correction such as the ZPHI approach rather than a direct linear correction using differential phase shift and is the preferred method of correction where possible.

Finally the quality controlled, corrected radar moments are used to develop a rainfall estimation for the COPE field campaign. Results show that the quality control and correction process increases the agreement between radar rainfall estimates and rain gauges when using horizontal reflectivity from an R^2 of -0.01 to 0.34, with a reduction in the mean absolute percentage difference (MAPD) from 86% to 31%. Using dual polarisation moments to directly estimate rainfall shows that rainfall estimates based on the theoretical conversion of specific attenuation to reflectivity produce the closest agreement to rain gauges for the field campaign with a MAPD of 24%. Finally it is demonstrated that merging multiple dual polarisation rainfall estimates together improves the performance of the rainfall estimates in high intensity rainfall events while maintaining the overall accuracy of the rainfall estimates when compared to rain gauges.

Contents

List of Figures

List of Tables

Symbols

A	specific attenuation
C	radar calibration constant
D	drop diameter
G	radar antenna gain
K_p / K_w	dielectric factor of a particle (p) or water (w)
K_{DP}	specific differential phase
N_i	drop number concentration
P_t	transmitted power
$\bar{P}_r$	mean received power
R	instantaneous rainfall intensity
V_t	particle terminal fall velocity
Z_e	equivalent reflectivity factor
Z_m	measured reflectivity factor
Z_{DR}	differential reflectivity

a	coefficient of standard rainfall rate equations
b	exponent of standard rainfall rate equations
c	speed of light in a vacuum
$_{h,v}$	subscripts denoting horizontal and vertical polarisation
r	range of target
r_{max}	maximum unambiguous range of the radar
t	observation at time, t

α	slope of linear relationship between specific attenuation and specific differential phase

β	slope of linear relationship between specific differential attenuation and specific differential phase
δ_{co}	backscatter differential phase between co-polar signals
$\delta\Phi$	median azimuthal phase difference
ϵ_p / ϵ_w	complex index of refraction of the observed particle (p) or water (w)
λ	wavelength
ρ_{co}, ρ_{hv}	co-polar correlation coefficient
Ψ_{DP}	differential phase between co-polar signals
ϕ_{DP}	forward propagation differential phase shift between co-polar signals
$\sigma(...)$	texture of variable ...
θ_1	3 dB beam width in the vertical plane
ϕ_1	3 dB beam width in the horizontal plane
τ	transmitted pulse width

Abbreviations

AP	anomalous propagation
CASA	engineering research centre for Collaborative Adaptive Sensing of the Atmosphere
CC	correlation coefficient, ρ_{co}
COPE	COnvective PrEcipitation experiment
CPU	central processing unit
DOP	degree of polarisation
DSD	drop size distribution
EA	Environment Agency
FIR	finite impulse response
GPU	graphics processing unit
ICE-D	Ice in Clouds Experiment - Dust
IOP	intensive observation period
I/Q	in phase and quadrature
KDEs	kernel density estimates
LDR	linear depolarisation ratio
MAPD	Mean absolute percentage difference
Md	median
MPD	Mean percentage difference
MRR	micro rain radar
NCAS	National Centre for Atmospheric Science
NCP	normalised coherent power
NERC	Natural Environment Research Council
PPI	plan position indicator

PRF	pulse repetition frequency
QPE	quantitative precipitation estimate
QVP	quasi-vertical profile
SEPA	Scottish Environment Protection Agency
SESAR	Single European Sky ATM (Air Traffic Management) Research
SQI	signal quality index
UKMO	UK Met Office

Chapter 1

Introduction

Flooding is a major challenge for many countries around the world, while drought can be equally devastating. Recent flash flooding has caused fatalities in Utah (Sep 2015), Macedonia (Aug 2015) and Morocco (Nov 2014), to name just a few examples, while the economic costs of larger flood events have been substantial, for example the 2007 summer floods in the United Kingdom cost more than £3.2 billion (Morris et al., 2010) and more recent flooding in Europe (2014) led to over €100 million of aid being distributed by the European Commission from the EU solidarity fund. Conversely the western USA, particularly California has experienced an extended period of drought, with over 60% of the region being abnormally dry and at least 20% of the region suffering from severe drought or worse since the spring of 2012 and the UK was experiencing water deficit prior to the wet summer of 2012. Accurate measurements of rainfall allow the effective management of flooding situations, informing flood forecasts and providing context to events, while they also allow the evaluation of drought situations, improving understanding of their hydrological drivers. With the risk of flooding and drought predicted to increase over the coming century, as a result of increased population pressure, changes in land use and climate change (Conway et al., 2015; Veldkamp et al., 2015; Schneider et al., 2013; Kollat et al., 2012; Environment Agency and DEFRA, 2011), action to prevent, mitigate and manage these risks is required to lessen their future impacts. Rainfall measurements are just one aspect of this action, contributing to operational water resources planning and flood risk management, informing hydrological research as a critical input variable and also meteorological research, for assimilation into forecasts, forecast validation and

improved process understanding. The following thesis considers the use of weather radar for rainfall measurement, due to the continued expansion and technological development of weather radar networks across the world. Of particular importance is how the reliability of radar measurements may be improved for hydrological applications, and how the uncertainty of those measurements can be accurately represented.

1.1 Why use weather radar?

Weather radar provide distributed rainfall estimates at high spatial and temporal resolution (1 km^2 and 5 min for the current UKMO composite, for example), allowing rainfall to be estimated in real time across wide areas with a single instrument. As they observe the atmosphere at multiple elevation angles they can provide a more complete three dimensional view of the weather systems observed, allowing regions of interest to be studied in greater detail or short term extrapolations (nowcasts) to be made. The use of nowcasts is particularly relevant during periods of localised convective activity. In particular flash flooding from convective systems is a significant challenge for forecasters and flood risk management professionals (Moore et al., 2006; Collier, 2007; Broxton et al., 2014), and one which weather radar can help with. During convective situations it is common that the forecast location of individual cells is more uncertain than the forecast intensity, with current nowcasting systems using a distributed rainfall input from weather radar as an initial boundary condition to improve their performance, which is then advected to match modelled rainfall over the duration of the nowcast (Bowler et al., 2006; Golding, 2009; Hapuarachchi et al., 2011; Alfieri et al., 2012).

Another benefit of weather radar is the ability to produce distributed rainfall estimates. With the growing availability of distributed hydrological models facilitated by expanding CPU and GPU processing power the need to produce accurate measurements of distributed rainfall as input has never been greater. The traditional hydrological input from rain gauges no longer meets these needs as rain gauge networks with a high enough spatial density for accurate distributed modelling are a rare occurrence and too costly to be implemented on an operational scale (Atencia et al., 2011).

Weather radars also provide the opportunity to measure additional atmospheric variables, in addition to precipitation. Doppler technology allows the measurement of the

radial motion of the atmosphere in relation to the radar location, which can extended to absolute motion vectors provided overlapping radar coverage is available. Another newer technology, particularly in relation to the operational radar networks of Europe, including the network in the UK, is dual polarisation, which allows additional measurements of the shape and size of particles within the atmosphere.

Despite these advantages, and the long held view that weather radar are the next great development in hydro-meteorological observation for flood forecasting, the quantitative precipitation estimates obtained from weather radar are still not viewed as a reliable measurement. These estimates are often ignored in favour of simulated rainfall or interpolated rain gauge data and when they are used they are heavily weighted to conform to rain gauge point measurements obtained at a vastly different temporal and spatial scale (Berne and Krajewski, 2013; Price et al., 2012; Neale, 2012). This approach can be attributed to the many uncertainties which affect quantitative precipitation estimates from radar (QPE) (Villarini and Krajewski, 2010a; Joss and Germann, 2000).

The aforementioned widespread implementation of dual polarisation weather radar systems should change this perception, by improving the data quality and accuracy of radar QPE while better constraining the uncertainty in those measurements.

1.2 Assessing dual polarisation rainfall estimates

The following thesis will assess the magnitude of these improvements using a dual polarisation radar dataset from the COnvective Precipitation Experiment (COPE) field campaign, obtained using a mobile, dual polarisation, Doppler X-band radar. To obtain accurate rainfall estimates the raw reflectivity dataset will be processed and corrected using multiple techniques made possible with dual polarisation observations, before contrasting several methods of dual polarisation rainfall estimation to ascertain the uncertainty within the rainfall estimates. A final rainfall product for the field campaign will then be available which utilises these methods to provide the most accurate rainfall estimate possible. The inclusion of multiple rainfall estimates from the radar in this final rainfall product will reduce its uncertainty through selective merging of the estimates, driven by the uncertainty analysis conducted throughout the thesis.

To achieve the above objectives it is first necessary to introduce rainfall estimation with weather radar, dual polarisation and the benefits of utilising dual polarisation (Chapter 2). Then the datasets used can be described in context (Chapter 3) and evaluated as an initial product (Chapter 4). Following initial analysis, which identifies common radar errors and uncertainties, the data can be quality controlled (Chapter 5) and corrected (Chapter 6) using dual polarisation techniques. Chapter 7 then introduces several methods of rainfall estimation using dual polarisation, comparing their output to rain gauges for the field campaign and describes the combination of these estimates into a final rainfall product for the COPE campaign.

Chapter 2

Introducing weather radar for quantitative precipitation estimation and hydrological applications

The deployment of radar for meteorological observation began soon after its military development (Watson-Watt, 1945; Maynard, 1945). Despite these early beginnings its use for hydrological applications has always been secondary to other measurements of rainfall, especially rain gauges. Since this early inception two notable technological upgrades have occurred. The upgrade to Doppler systems, capable of measuring the radial velocity of detected echoes occurred in the 1980s and 1990s, with many countries across the globe now operating a multi-radar observational Doppler network (Meischner et al., 1997; Collier, 1996, for example). The second major technological improvement, dual polarization, has taken longer to reach operational networks, with networks such as the United Kingdom Met Office (UKMO) radar network and MeteoFrance's radar network currently in the process of upgrade, and the United States WSR-88D network upgrade recently finished in 2013 (Figueras i Ventura et al., 2012; Zhu and Cluckie, 2012).

These technological improvements aim to address many of the major sources of error in single polarisation radar measurements of rainfall, which are often cited as a major reason

for the continuing lack of confidence in radar data within the hydrological community (Villarini and Krajewski, 2010a; Neale, 2012). Another proposed solution to addressing these errors in radar QPE is the statistical modelling of the total combined errors when compared to a reference observation, typically rain gauges (Germann et al., 2009, for example). These error models can then be used to generate ensembles of rainfall fields which encompass the statistical variability of the radar errors.

Here follows an overview of single polarisation weather radar (2.1) and its uncertainties (2.2), dual polarisation radar (2.3) and how the application of dual polarization radar can address some of these uncertainties (2.4) and, finally the combination of radar observations with rain gauge observations which includes the development of observed rainfall ensembles (2.5).

2.1 Rainfall estimation with single polarisation weather radar

Single polarization radars transmit radiation in pulses, polarized along a known plane. These pulses then interact with the atmosphere and the hydrometeors within it, scattering the radiation. The radar then receives incoming radiation from this scattering, thereby observing the atmosphere. As hydrometeors are an incoherent radar target (Marshall and Hitschfeld, 1953) this received power is averaged over a number of pulses to produce the received signal. The number of pulses is determined by the scanning speed of the radar, the azimuthal gate spacing and the pulse repetition frequency. Once calculated the average received power (P_r) can then be converted into the equivalent radar reflectivity factor (Z_e) using the simplified radar range equation (2.1).

$$\bar{P_r} = \frac{C|K_p|^2 Z_e(r_0)}{r_0^2} \tag{2.1}$$

$$K_p = \frac{\epsilon_p^2 - 1}{\epsilon_p^2 + 2} \tag{2.2}$$

$$C = \frac{P_t G^2 \theta_1 \phi_1 \tau c \pi^3}{\lambda^2 1024 \ln(2)} \tag{2.3}$$

In this case C is termed the radar calibration constant and is determined by the radar hardware configuration and pulse characteristics (see symbols section for components of

C) and should remain constant for a given radar, ϵ_p is the complex index of refraction of the observed particles and r_0 is the range of the observed particles. See Collier (1996) or Bringi and Chandrasekar (2001) for full derivations of this formula, including a full treatment of the assumptions required. Equation 2.1 is valid when the observed particles are much smaller than the radar wavelength and Rayleigh scattering occurs, as is usually the case for weather radars. The other most pertinent assumptions are that the observed echo completely fills the radar beam volume and that a single ϵ_p can be used to characterise the observed particles, which is typically taken to be the di-electric constant of water (ϵ_p), both of which can lead to errors in the retrieval of Z_e, which will be covered in the following section (2.2).

The advantage of converting radar received power to the equivalent reflectivity factor is that it can be directly related to the drop size distribution (DSD) of the observed volume, as first shown by Marshall et al. (1947). The relationship can be described as a function of the number of drops (N_i) of a given diameter (D_i) and that diameter raised to the sixth power, integrated over the whole range of diameters within the sample volume (Eq. 2.4).

$$Z_e = \sum_i N_i D_i^6 \tag{2.4}$$

For meteorological observations D can vary from $\approx 50\,\mu$m for cloud droplets to $\approx 8\,$mm for the largest raindrops and hail, leading to large variations in observed Z_e. As a result it is typically expressed in units of decibels of reflectivity (dBZ) using a logarithmic transformation, as opposed to its linear units of $\mathrm{mm}^6\mathrm{m}^{-3}$. The reflectivity of a volume can then be related to rain rate (R) as the rain rate is also a function of the DSD. The relationship between diameter and rain rate (expressed in its common units of mm hr^{-1}) is shown in equation 2.5.

$$R = 0.6\pi \times 10^{-3} \int_0^\infty N(D) D^3 V_t(D) \delta D \tag{2.5}$$

where N_i is again the number of drops of a specified diameter D_i and V_t is the terminal velocity of the drops, which is again a function of diameter. In practice a parametrised DSD is chosen for the climatological situation and then Eq. 2.4 and Eq. 2.5 can be

combined to allow calculation of rain rate using an equation of the form shown in Eq. 2.6.

$$Z = aR^b \tag{2.6}$$

In Eq. 2.6 the coefficient (a) and exponent (b) are dependant on the DSD parametrisation used. Commonly used values are shown in table 2.1, though a wealth of different schemes have been derived for differing geographic locations and atmospheric conditions (for example Battan (1973) lists 60 different options developed across the world). The UK standard is to use a=200 and b=1.6 (Harrison et al., 2012).

Application	a	b	
Drizzle	140	1.5	(Joss et al., 1970)
Stratiform rain	200	1.6	(Marshall et al., 1955)
Convective storm	500	1.5	(Joss et al., 1970)
Met Office C-Band Radar	200	1.6	(Harrison et al., 2012)
WSR-88D Radar	300	1.4	(Fulton et al., 1998)
MeteoSwiss network	316	1.5	(Germann et al., 2006b)

TABLE 2.1: Standard rainfall reflectivity conversion relations for differing atmospheric conditions and locations as presented in the literature

It is also worth noting that across the world three distinct radar frequency bands, commonly referred to as S-band, C-band and X-band, are used for rainfall estimation with weather radar (see Table 2.2 for details). This distinction is important when considering error sources for the radar system, the reasons why one may be chosen and also the potential benefits of dual polarisation to the system. In the United States the NEXRAD system uses high power S-band systems, in Europe C-band systems are more common (UK and Germany for example) and X-band is generally restricted to research systems (NCAS) and more recently urban scale radar coverage (CASA).

Band	Frequency range (GHz)	Wavelength (cm)	Example system (wavelength)
S	2 to 4	7.5 to 15	NEXRAD (10.7 cm)
C	4 to 8	3.75 to 7.5	UKMO (5.4 cm)
X	8 to 12	2.5 to 3.75	NCAS (3.2 cm)

TABLE 2.2: The three most common weather radar frequency bands and their respective frequencies

2.2 Error sources for single polarisation weather radar

The process of estimating rainfall using weather radar has many components which can be subject to error. Firstly there are errors in the process of measuring the received power, then in relating those measurements to the precipitation and finally in translating those precipitation estimates into rainfall accumulations at the ground. Each of these stages has several sources of uncertainty, which are covered in the following section, starting with processes which affect the measurement of the received power.

2.2.1 Radar calibration

The radar calibration constant (C, Eq. 2.3) is a clear source of error in the initial radar equation (Eq. 2.1) as it is a function of several hardware related variables, including the antenna gain, transmitted power, wavelength, the pulse dimensions and system losses. Due to the fluctuations in the radar components due to degradation and temperature fluctuations the true value of C can vary in time, with changes being difficult to detect from the radar data alone. Studies show that C can be calibrated to better than 1 dB (Collier, 1996) but this accuracy deteriorates with time from the calibration. For single polarisation radars detection is possible by comparison with other overlapping radar sites, giving a relative miscalibration between the two, through the use of a range of known reflectors (Atlas (2002) provides a good summary of target techniques) or by comparison to other meteorological observations, such as rain gauge accumulations, disdrometer measurements and aircraft observations of drop sizes. Research by Manz et al. (2000) showed that the use of a target sphere provided the most accurate calibration (0.5 dB) for UK radars, provided that the sphere's position could be accurately known and it be held stationary. Given the difficulty of these conditions, and the fact that a sphere could only be used for offline calibration they recommended an external transponder as the most accurate solution (still offline) or power monitor and test signal generator as the most feasible online calibration solution (quoted accuracy of 1.5 dB). An online solution allows more regular monitoring of the calibration and therefore more consistency in the measurements made, for example Germann et al. (2006b) indicate that weekly relative calibration is undertaken to ensure the stability of the MeteoSwiss radar network, while absolute calibration is not performed. Taking this approach allows for a stable set of

measurements which can then be bias corrected using long term observations to account for the lack of absolute calibration.

While miscalibration can be managed for single polarisation radars it can become a more serious issue when correcting for attenuation, where results can be extremely sensitive to calibration errors due to the cumulative effect of bias in the reflectivity measurements (Nicol and Austin, 2003; Hitschfeld and Bordan, 1954, for example). Attenuation will be explored further in the next section.

2.2.2 Attenuation

A reduction in received power can be caused by attenuation, where the beam power is reduced by hydrometeors between the radar and the target range. This causes the measured power (reflectivity, Z_m) at a given range to no longer be directly comparable to the reflectivity resulting from the observed rainfall DSD (Eq. 2.4, Z_e), but instead being a function of the true reflectivity and the intervening hydrometeors. The effects of attenuation were first detailed by Atlas and Banks (1951) for wavelengths shorter than 7 cm (C-band and X-band, for example) with long wavelength radars being unaffected by all but the most extreme rainfall events. This is a function of the relative size difference between the hydrometeors and the radar wavelength, and it is even possible for attenuation to cause complete extinction of the radar beam, such that observations beyond an attenuating storm cannot be made. Several studies have calculated the expected attenuation due to differing phases of hydrometeors, changing temperature ranges and operating wavelengths (Delrieu et al., 1991; Wexler and Atlas, 1963; Gunn and East, 1954). For example, Delrieu et al. (1991) showed that at X-band attenuation ranged from about 0.1 dB km^{-1} for moderate rainfall intensities (8 mm hr^{-1}) to up to 3 dB km^{-1} for heavy rainfall (100 mm hr^{-1}), with temperature variation only becoming significant at rainfall intensities in excess of 40 mm hr^{-1}. C-band radars occupy a middle ground, with more moderate attenuation for a given rainfall (0.7 dB km^{-1} from a rainfall intensity of 100 mm hr^{-1}) and a reduced temperature dependence at higher rainfall intensities. Clearly attenuation can cause serious changes in measured reflectivity, especially at short wavelengths, which reduces the accuracy of rainfall estimates when heavily precipitating storms are present.

To account for attenuation, many correction schemes have been developed (Nicol and Austin, 2003; Delrieu et al., 1997; Hildebrand, 1978; Hitschfeld and Bordan, 1954, for example), which are based on an attempt to quantify the attenuation and then return the measured reflectivity to a true reflectivity using a variation of the simple formula shown here, where $A(r)$ is the specific attenuation in dB km^{-1}.

$$Z_e(r) = Z_m(r) + 2\int_0^r A(r)\mathrm{d}s \tag{2.7}$$

As Nicol and Austin (2003) explain, single polarisation attenuation corrections largely rely on the corrected reflectivity measurements along a segment to determine the attenuation ($A(r)$) at the end of the segment using an empirical relationship of a similar form to the Z-R relationship (Eq. 2.6), and as such any calibration bias can quickly lead to unstable solutions as the bias accumulates along the radial. As a result attenuation correction relies on a measurable constraint to prevent these divergent solutions, whether these be a power from a 'known' source such as a mountain (Serrar et al., 2000; Delrieu et al., 1999) or the use of external measurements such as rain gauges for a complete bias adjustment (Hildebrand, 1978). Even when these are available, errors persist in correction due to inherent variability in these measures and attenuation remains a significant problem for single polarisation radars.

In addition to attenuation from the atmosphere it is also possible for attenuation to occur due to wetting of the radome (Bechini et al., 2010; Baeck and Smith, 1998). Collier (1996) details the unpublished results of Eccleston and Hill (1980), showing the reduction in observed rainfall to be up to 15 mm h^{-1} due to radome wetting at the Clee Hill radar in the UK. It is possible to reduce these impacts using careful design, such as hydrophobic materials, geometry and size, but as Kurri and Huuskonen (2008) show, all radomes will cause attenuation in wet conditions.

2.2.3 Beam blockage

Another factor influencing the measurement of reflectivity and its comparison to the true reflectivity is the presence of a blockage within the radar beam, such as a hill, trees, buildings and other infrastructure. As the standard radar equation assumes that

the entire beam samples the pulse volume at the given range, a blockage introduces a reduction in received power for observations beyond the blockage and therefore a bias in the measurements. Provided the amount of beam blockage can be calculated, using a method such as that of Gabella and Perona (1998), the bias can be corrected. Calculating the degree of blockage relies on simple geometric optics, but requires accurate measures of surface topography (which is possible), the location and shape of buildings (more difficult), the refractive state of the atmosphere and possibly the vegetative state of the land causing the blockage. Bech et al. (2003) showed that refractivity changes in the atmosphere can change the bias caused by blockage by several dB, and as such static corrections cannot correct for all situations and are prone to errors in anomalous conditions. Many approaches only consider correcting blockage provided the degree of blockage is not too great, for example MeteoSwiss correct beam blocked data if less than 87% of the beam is blocked (Germann et al., 2006b), while the WSR-88D setup in the USA and the UK Met Office correct all data where the beam is 50% blocked or less (Fulton et al., 1998; Harrison et al., 2009). Even in these cases blockage can reduce echoes to below the background noise level, and correction is unable to recover this data leading to under measurement. In these cases and those where total beam blockage occurs, data extrapolation from higher elevation scans or adjacent rays is required (Germann et al., 2006b; Gabella and Perona, 1998).

As data that undergoes beam blockage correction is less reliable than clear sight observations, careful choice of radar site is the best means of ensuring good quality data, the use of a terrain model technique like the one developed by Gabella and Perona (1998) prior to radar placement is therefore advised. Another approach is to only use beam elevations that do not suffer from beam blockage, however these higher elevations are prone to errors caused by sampling higher in the atmosphere, especially at longer ranges.

2.2.4 Non meteorological echoes

Alongside the issue of obtaining accurate reflectivity measurements, it is vital to determine whether those measurements are from hydrometeors or another, non-meteorological, target. Common non-meteorological targets include ground clutter (which includes topography, vegetation and man-made structures), sea clutter (reflections from the sea

surface), biological scatterers (birds and insects), interference (RLAN and other radars) and even clear air echoes (due to humidity changes in the atmosphere).

Identifying, and removing, these spurious echoes is possible using either static techniques for known clutter, signal-level correction of the return pulse (Torres and Zrnić, 1999; Nguyen et al., 2008) or dynamic filtering (Steiner and Smith, 2002). Static maps, usually developed over time with summary statistics, are reasonably successful at removing the effect of ground clutter (Harrison et al., 2014, 2000). However when anomalous propagation (AP) increases the area of the returns, through refraction of the beam closer to the ground surface, or when the ground clutter signals are a result of moving vegetation or wind turbines these static techniques become ineffective. They also are unable to remove echoes from other, non-meteorological sources, particularly biological scatterers.

Dynamic systems that respond to the variation in ground clutter returns due to AP have been developed as a response to these issues. Signal level, spectral filtering of the raw I/Q data received by the radar is one approach to this problem (Doviak and Zrnić, 1984, e.g.), provided the radar has Doppler capability. By processing the data prior to the radar generating a reflectivity measurement from the received power, ground clutter returns, which have a near zero Doppler velocity and a narrow spectral width, can be removed. However this can lead to the removal of weather echoes which also have near zero radial velocity, for example aggressive filtering of the WSR-88D network can lead to up to 20% of meteorological echoes being lost (Serafin and Wilson, 2000). Even with less aggressive filtering reflectivity is still removed along the so-called zero velocity isodop (Hubbert et al., 2009). Doppler filtering schemes also fail to cope with other sources of spurious returns, due to these returns having a velocity component.

There have also been many schemes created which utilise a machine learning approach, such as fuzzy logic, Bayesian inference or a decision tree, which incorporate the reflectivity measurements themselves along with vertical changes in reflectivity, the extent of the reflectivity, the spatial variability of the reflectivity and even Doppler fields if available (Pamment and Conway, 1998; Berenguer et al., 2006; Cho et al., 2006; Steiner and Smith, 2002, for example). In all these cases the identification of other non-meteorological echoes is not considered, due to the difficulty of identification with a single polarisation radar and also the fact that ground clutter / AP returns are the most significant non-meteorological source in terms of returned intensity and frequency of observation.

2.2.5 Parametrising the drop size distribution

As already mentioned, there are a multitude of different possible parametrisations of the drop size distribution available, which determine the values of a and b in the exponential rainfall-reflectivity relationship (Eq. 2.6). The wide range of available values describe differing precipitation processes, from tropical warm rain events which contain larger numbers of smaller drops (Fujiwara, 1967) to intense convective systems where the distribution has a much greater median diameter (Joss et al., 1970). Even within these classically defined precipitation types there is a great variation in the values presented with this variability all inherent within one possible radar scan which leads to uncertainty in the 'best' value to use for a given observation (Atlas et al., 1999; Uijlenhoet et al., 2003). Figure 2.1 shows just a small subset of the available parametrisations and highlights the possible variation in retrieved rainfall depending on the DSD parametrisation chosen, for example just using the four distributions shown a reflectivity measurement of 40 dBZ could equate to a rainfall intensity of between 8 and 20 mm hr^{-1} depending on the type of rainfall being observed. In order to deal with DSD variations, pre-classification of echoes is required to allow the application of an appropriate parametrisation, particularly in the USA where the radar network covers an extensive geographical area with wide variations in atmospheric conditions. For single polarisation radar this is achieved using the intensity of the reflectivity measurements, generally in combination with their three dimensional structure(Rosenfeld et al., 1995; Steiner et al., 1995; Anagnostou, 2004; Qi et al., 2013), with results showing improved rainfall estimation provided the classification can be achieved with a high level of accuracy.

2.2.6 Variations in hydrometeor phase

One of the main limitations of the assumptions is that the particles must be considered to be all of the same phase (water or ice), not a mixture. In practice this leads to K (Eq. 2.2) for water being used as standard and an overestimation of Z_m when solid hydrometeors are observed. To counteract this DSD parametrisations for snow and ice exist, and can be applied provided it is possible to identify solid phase hydrometeors. The presence of both solid and liquid phase precipitation intermixed within a sample volume presents an even greater challenge and single polarisation radars struggle to make accurate

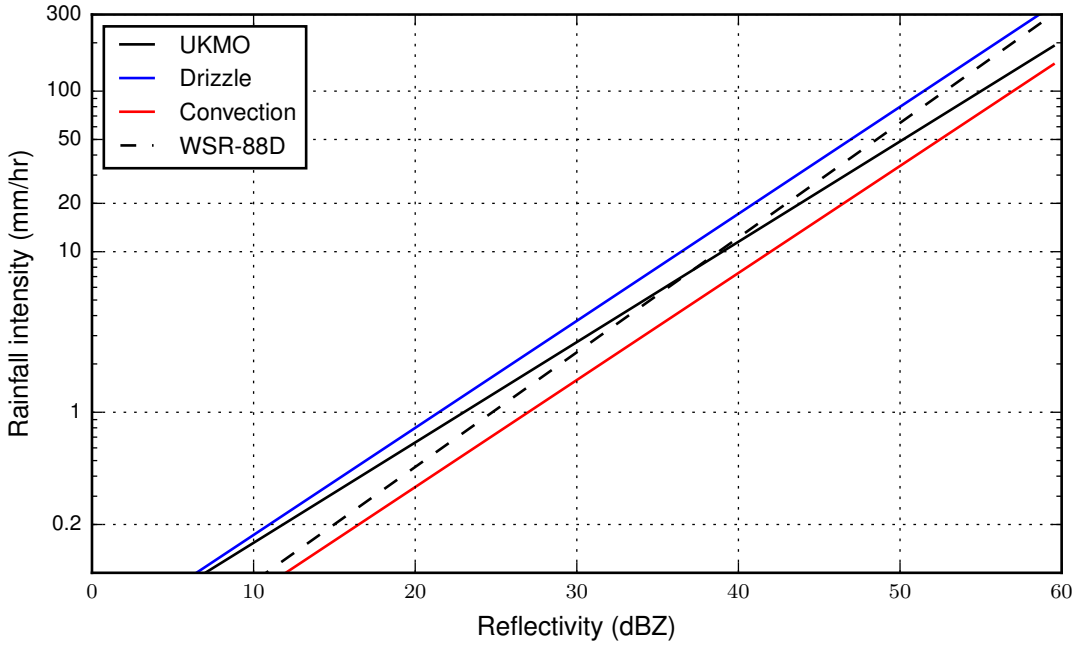

FIGURE 2.1: Variation in retrieved rainfall intensity resulting from the use of different DSD parametrisations. The four shown are taken from Table 2.1.

precipitation estimates in these cases. Another consequence of changes in hydrometeor phase is the impact on attenuation corrections, as mixed phase particles can have a stronger attenuating affect than purely liquid phase particles, with solid cores supporting large liquid drops (Ryzhkov and Zrnić, 1995), while ice crystals have a much smaller attenuating affect than liquid precipitation (Vivekanandan et al., 1994).

The most documented example of hydrometeor phase causing rainfall estimation errors is in the case of the bright band, which is elevated reflectivity due to the radar beam intersecting the melting layer in stratiform conditions (Austin and Bemis, 1950; Hooper and Kippax, 1950; Klaassen, 1988; Huggel et al., 1996; Sánchez-Diezma et al., 2000, for example). The strength of the enhancement is dependent on the elevation angle and the range at which the beam intercepts the melting layer, along with the fall speed of the melting hydrometeors. The regions of enhanced reflectivity can generally be identified using a combination of the radar data and information about the melting layer height (from numerical models or radiosondes for example) and then corrected for using a vertical reflectivity profile to transform elevated reflectivities to their surface equivalent (Smith,

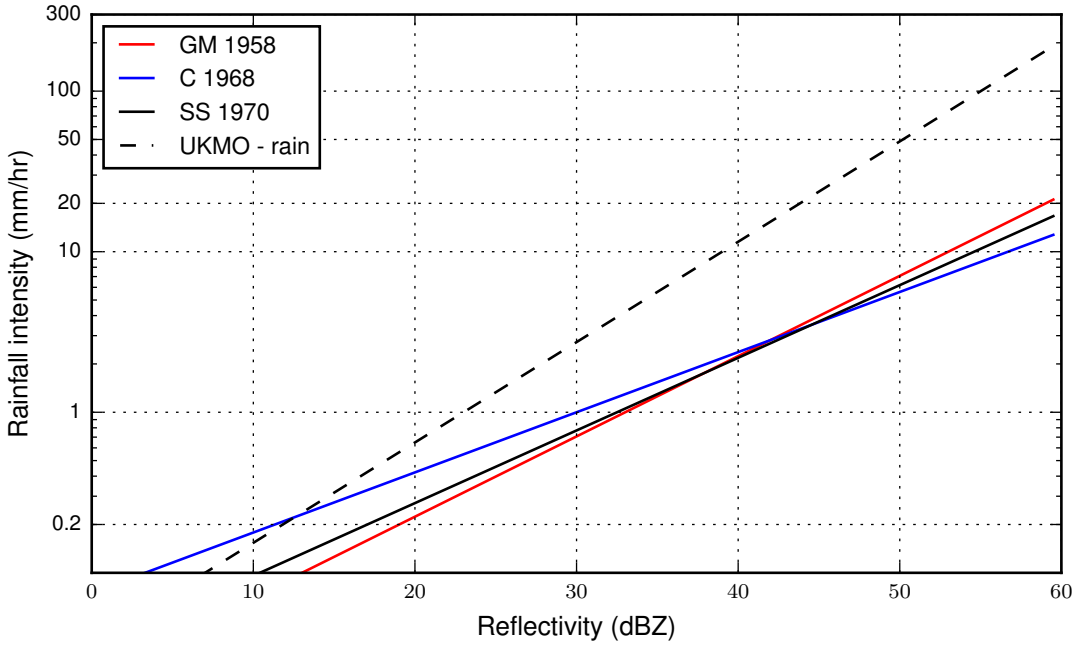

FIGURE 2.2: Variation in retrieved precipitation intensity resulting from the use of different DSD parametrisations for snowfall. The relations shown are from Gunn and Marshall (1958), Carlson (1968) and Sekhon and Srivastava (1970) respectively. The UKMO rainfall parametrisation is shown for comparison.

1986; Kitchen et al., 1994; Hardaker et al., 1995; Smyth and Illingworth, 1998b; Gourley and Calvert, 2003; Rico-Ramirez and Cluckie, 2007).

2.2.7 Rainfall accumulation

An inherent aspect of radar QPE is that the radar observes instantaneous rainfall intensity in specific volumes of the atmosphere, while hydrological applications generally use surface rainfall accumulations in a given time period over a defined area, be it a river catchment or a model grid box (Beven, 2011). Jordan et al. (2000) found that the largest contribution to this uncertainty is the fact that the radar measures at a given height above the ground, with the random variability increasing with height and reducing given the size of the accumulation area. Clearly using radar observations from as close to the ground as possible provides the most representative measurements, but this must be balanced against the increased likelihood of partial beam blockage and ground clutter returns as discussed above. Another uncertainty in converting rainfall intensities

of rainfall to accumulations is the temporal variability of the rainfall over the accumulation interval, and the number of radar observations that fill that sampling volume. For example, Wilson and Brandes (1979) show that the greater the sampling interval the larger the variability in the comparison between radar and rain gauges, while Villarini et al. (2008) show that the variability is largest over the shortest accumulation intervals given a fixed measurement interval. To reduce the uncertainty from a radar perspective it is important to have as short as possible interval between measurements, while schemes have also been developed which interpolate between observations to generate more accurate accumulations (Liu and Krajewski, 1996; Tabary, 2007, for example).

2.3 Dual polarisation weather radar

The first application of dual polarisation to weather radar was by Seliga and Bringi (1976) but it is only in the past decade that dual polarisation radars have been incorporated into national observational networks such as the United States of America's NEXRAD / WSR-88D programme (upgrade completed in summer 2013) and the United Kingdom Met Office's radar network (upgrade ongoing, completion expected in 2018).

As opposed to single polarisation radar, dual polarisation radars transmit and receive along two planes of incidence, typically the horizontal and vertical planes (Fig. 2.3). The addition of a second plane of observation allows comparative radar moments to be studied, which investigate the relative changes between the two planes. These moments include the differential reflectivity, the differential phase shift and the co-polar cross correlation, among others, which are discussed in section 2.3.2. Prior to the discussion of these new moments it is necessary to differentiate between the two possible implementations of dual polarisation available, as they can provide different moments and levels of accuracy.

2.3.1 Simultaneous vs alternating transmission

There are several possible transmission and reception modes for dual polarisation radars determined by the configuration of the radar hardware, particularly the number of receivers and the presence of a waveguide switch. The two main modes of operation are alternating transmission, with dual receivers and simultaneous transmission with dual

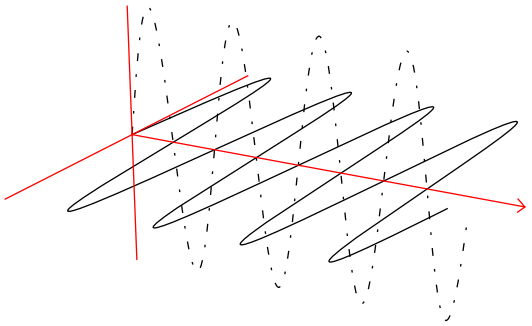

FIGURE 2.3: Two orthogonal polarised planes in the horizontal (solid) and vertical (dashed). Transmitted in the direction of the arrow, with zero phase offset.

receivers (Bringi and Chandrasekar, 2001). In alternating transmission mode the state of the transmitted pulse is switched alternately between the horizontal and vertical state (*hv*), although some systems implement a repeated block pulsing of these states such as *hhv* or *hhvv* (Fig. 2.4). This allows sampling of the cross-polar elements of the scattering matrix, while co-polar elements are only available where that state is transmitted (every other pulse for the simple alternating state). In simultaneous or hybrid transmission mode both planes are transmitted at the same time, with the received orthogonal signals being a combination of the copolar and cross polar return signals from the transmitted wave (Fig. 2.4).

The advantages of alternating transmission mode, or a block pulse style derivative, are that the linear depolarisation ratio (LDR) can be measured, that measurement errors are less sensitive to antenna polarisation errors and that the system isolation requirements are lower for a specific required observational accuracy (Wang and Chandrasekar, 2006). Conversely the advantages of hybrid transmission are direct measurement of the coherency matrix, leading to direct estimation of both the copolar correlation coefficient and the propagation phase (with greater unambiguous range), more accurate variables for

a given scan rate due to twice the number of observations and lower cost radar hardware as a waveguide switch is not required (Doviak et al., 2000).

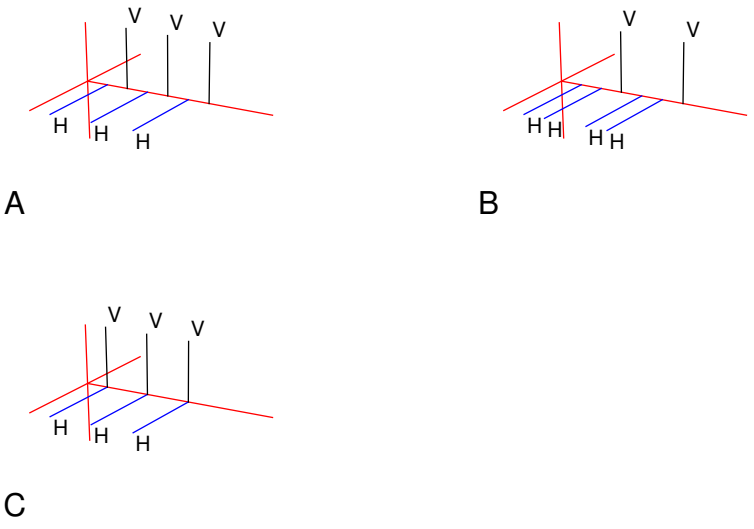

FIGURE 2.4: Schematic pulse diagrams of alternating (A), block pulsed *hhv* (B), and simultaneous (C) transmission.

2.3.2 Dual polarisation moments

As already mentioned, the addition of a second, orthogonal, plane of transmission to weather radars allows the measurement and estimation of several new radar moments based on differences between the two planes. These new moments provide additional information about the echoes being sampled, which are of great use in radar hydrometeorology. These new parameters are the differential reflectivity (Z_{DR}), the differential phase shift (Ψ_{DP}) (which is composed of the forward propagation phase shift (Φ_{DP}) and the backscatter differential phase shift (δ_{co})), the specific differential phase (K_{DP}), the co-polar cross correlation (ρ_{co}) and the linear depolarisation ratio (LDR). The following section describes each of these parameters in turn, along with a description of their physical meaning. The benefits of these new moments are then covered in the following section (2.4)

2.3.2.1 Differential reflectivity

Differential reflectivity (Z_{DR}) is the observed ratio of the horizontally and vertically polarized linear reflectivity measurements. It was first proposed as a method of observing rainfall by Seliga and Bringi (1976), with the aim being to add information to help quantify the rainfall drop size distribution. Due to the oblate spheroidal shape of falling raindrops, they produce a positive reflectivity shift in the horizontal, relative to the vertical, which is proportional to their diameter. Scattering simulations and field measurements show that Z_{DR} ranges from 0.2 dB in very light drizzle to over 4.5 dB for very large rain drops (Seliga and Bringi, 1978; Hall et al., 1984; Balakrishnan and Zrnić, 1990, for example). Scattering simulations by Ryzhkov and Zrnić (2005) quantified this relationship for S, C and X-band wavelengths and show the variation between them, with X-band suffering from minor resonance effects at a diameter of 3.5 mm and C-band suffering from more extreme resonance effects at diameters above 5 mm (Fig. 2.5). These resonance effects are the result of Mie scattering (Matrosov et al., 2002; Meischner et al., 1991), with the reduced resonance at X-band believed to be a consequence of increased absorption dampening the resonance effect (Park et al., 2005; Ryzhkov and Zrnić, 2005).

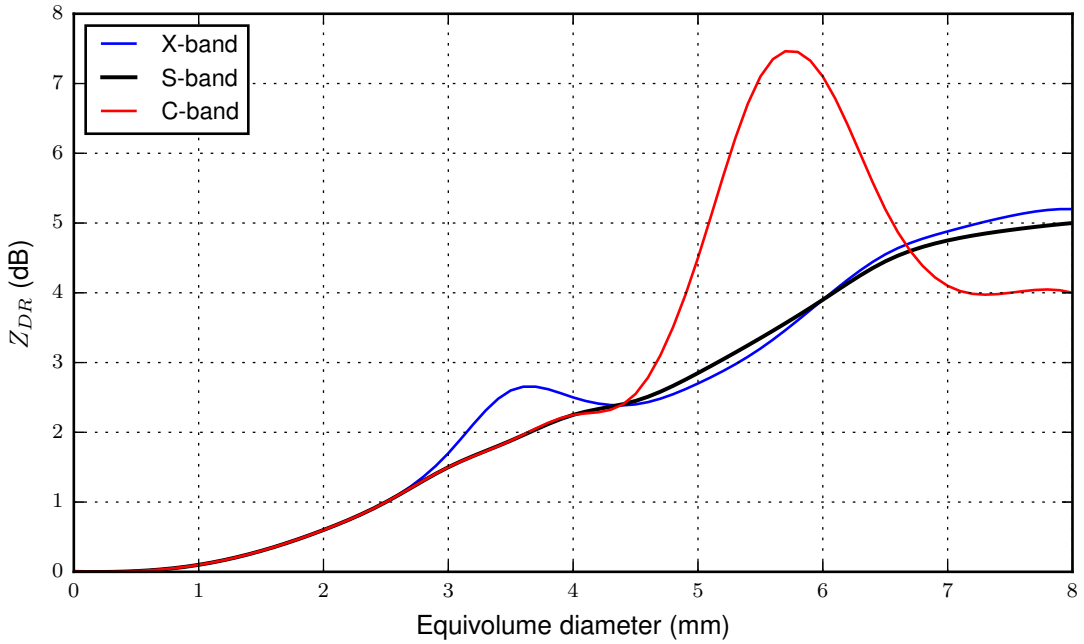

FIGURE 2.5: Theoretical variation of differential reflectivity with increasing equivolume diameter at S, C and X-band. Redrawn from Ryzhkov and Zrnić (2005).

2.3.2.2 Differential phase shift

The total differential phase shift (Ψ_{DP}) is the observed phase difference between the received horizontal and vertical pulses and contains two components, the backscatter differential phase (δ_{co}) and the propagation differential phase Φ_{DP} (Eq. 2.8) (Bringi and Chandrasekar, 2001). As there is often a phase shift on transmission the received phase shift also contains this component, which must be removed to gain the shift resulting from atmospheric interaction.

$$\Psi_{DP} = \Phi_{DP} + \delta_{co} \tag{2.8}$$

The differential propagation phase measures the change in phase between the horizontal and vertical phase of returns along the beam path which varies as a function of the total cross section of scatterers along the path. Therefore it varies as a function of both axis ratio of the drops and number of drops, with measurements in rainfall monotonically increasing along the beam path due to the positive axis ratio of raindrops (Seliga and Bringi, 1978; Jameson, 1985). Due to this dependence on the DSD, phase shift has frequently been proposed as an additional means of estimating rainfall using weather radar (Sachidananda and Zrnic, 1986, for example). These approaches have often been limited to higher rainfall rates as the phase shift is inversely proportional to wavelength for a given rainfall rate, with most early studies using S-band systems (Matrosov et al., 1999). Conversely the phase shift for an X-band system is 3 times greater than at S-band, which increases the sensitivity to lower rainfall rates. As a cumulative quantity the propagation phase is often differentiated with range to calculate the specific differential phase (K_{DP}) for each range gate for the purposes of rainfall estimation (see next section).

The backscatter differential phase forms the second component of the observed phase difference (Eq. 2.8). It is a function of non-Rayleigh scattering and is not cumulative along the rain path but a function of the distribution of scatterers in each range gate. Due to it being a function of non-Rayleigh scattering it is often ignored at S-band, but becomes an increasing component of the measurements at lower wavelengths, particularly X-band when equivolume drop diameters exceed 2 mm (Matrosov et al., 1999). As the backscatter phase has often proven difficult to separate from the total phase difference

measurements its use has been limited, however recent studies including Trömel et al. (2013) and Tyynelä et al. (2014) have begun to explore the potential of using backscatter differential phase, particularly for observing melting particles.

2.3.2.3 Specific differential phase

The specific differential phase (K_{DP}) is simply the range derivative of the forward propagation differential phase Φ_{DP}, typically expressed in units of degrees per kilometre ($^{\circ}$ km^{-1}). It is a calculated, rather than measured, radar moment, being derived from one component of the measured differential phase shift. At shorter wavelengths calculation requires either the filtering of the observed phase shift to remove the backscatter component, or careful selection of the calculation path to ensure the change in backscatter between the start and end of the path is minimal. The simplest method of calculation is a finite difference along a range path, however for rainfall estimation a more accurate method is required (Bringi and Chandrasekar, 2001). These methods include linear regression over varying path lengths (Ryzhkov and Zrnic, 1996), iterative range smoothing (Hubbert and Bringi, 1995), solving linear equations with linear programming (Giangrande et al., 2013) and even calculation using the angular domain with cubic spline estimation of K_{DP} (Wang and Chandrasekar, 2009).

2.3.2.4 Co-polar cross correlation

The co-polar cross correlation coefficient (ρ_{co}) is the correlation between the co-polar return at horizontal polarisation and the co-polar return at vertical polarisation. For alternating transmission mode only one of the co-polar elements can be measured per pulse and the co-polar correlation has to be estimated given the time lag between pulses. For simultaneous transmission the cross-polar components of the received powers are negligible compared to the co-polar components of the powers and therefore the co-polar cross correlation can be taken to be the measured co-polar correlation. However, in the presence of cross-polarizing scatterers, the measured value begins to deviate from its intended physical description as detailed by Galletti and Zrnić (2012). By measuring the correlation between the two pulses the homogeneity of the sample volume can be assessed, for example raindrops exhibit a large degree of spatial homogeneity and therefore have

correlations above approximately 0.97 (Balakrishnan and Zrnić, 1990). Mixed phase returns, particularly the melting layer have lower correlations, typically reported to be around 0.9 (Ryzhkov et al., 2005b; Bringi et al., 1991; Balakrishnan and Zrnić, 1990), although this is somewhat dependant on the radar configuration (particularly the dwell time and the beamwidth), for example Illingworth and Caylor (1989) observed values as low as 0.6 in the bright band with a 0.25 degree beamwidth S-band radar, while Zrnić et al. (2006) showed the variation of correlation with antenna rotation speed, with faster speeds leading to lower expected values. As a result the co-polar cross correlation is a useful parameter for identifying mixed phase returns, and also for identifying regions of non-meteorological echoes (see 2.4.1).

2.3.2.5 Linear depolarisation ratio

The linear depolarisation ratio is the amount of depolarisation which occurs due to cross polarising scatterers. To measure LDR requires the radar to operate in alternating transmission mode, such that a single polarisation is transmitted at any one time, and that both received polarisations are recorded. The LDR is then the amount of signal that is converted from the transmitted orientation (either horizontal or vertical) to the orthogonal direction by the observed hydrometeors. LDR increases with rainfall intensity as heavier rainfall has a more varied DSD, but is greater still for melting snow, hail, and strongly orientated ice crystals which all exhibit more variability in their shape and movement during descent (Bringi et al., 1986; Brandes and Ikeda, 2004; Ryzhkov and Zrnic, 2007). As such LDR is most often used in identification of scatterers, particularly solid phase scatterers.

2.4 Applications to hydrometeorology

There are three main applications of dual polarisation moments which can lead to improvements in rainfall estimates from weather radar. The first is the use of dual polarisation for quality control of the incoming data (2.4.1), filtering out non-meteorological echoes and highlighting areas of degraded signal quality due to attenuation and/or beam blockage. This prevents spurious echoes being converted into rain rate and highlights areas where interpolation or adjustment may be required to improve the data quality. The

second application is to use dual polarisation as a means of data correction (2.4.2), as it is possible to quantify and correct for radar miscalibration, attenuation and beam blockage using a combination of dual polarisation observations. The third area of improvement is through better characterisation of the observed precipitation (2.4.3), through the improved measurement of the DSD, identification of precipitation phase and hydrometeor type (hail vs wet snow for example). This leads to improved rainfall estimation as more appropriate Z-R relationships and other rain rate parametrisations which are a function of multiple dual polarisation moments can be used appropriately.

2.4.1 Quality control

The variation of dual polarisation measurements with target shape, size and orientation provides a distribution of observations which can be used to identify the targets observed (Giuli et al., 1991). One of the main uses of these properties is the identification and removal, or filtering, of non-meteorological or poor quality radar returns. A wide range of techniques exist for this purpose, including simple thresholding, logical decision systems for filtering, including Boolean decision trees, fuzzy logic and Bayesian probability (Lakshmanan et al., 2014; Rico-Ramirez and Cluckie, 2008; Gourley et al., 2007; Da Silveira and Holt, 2001) and more complete logical decision systems which incorporate non-meteorological targets into a wider hydrometeor classification process (Chandrasekar et al., 2013; Dolan and Rutledge, 2009; Park et al., 2009).

The most common elements of these schemes are their incorporation of standard dual polarisation moments, such as ρ_{co} which is used because the majority of meteorological returns having a ρ_{co} greater than 0.85 and Z_{DR} where extremely high or low values are more generally associated with non-meteorological returns. Also incorporated into these schemes are texture fields, particularly the texture of Φ_{DP}, where meteorological conditions are associated with low variation in texture and non-meteorological with high texture.

Another approach to radar quality control using dual polarisation is the production of quality index fields, which the end user can utilise to inform their use of the data. For example Friedrich et al. (2006) combine beam propagation effects, attenuation, cross beam gradients, identification of rainfall and consistency of the dual polarisation parameters

(Z, Z_{DR} and K_{DP}) to calculate a total quality index for each range gate in the radar volume, which can then be used for a weighted combination of overlapping radar scans and general filtering of unsuitable data. A similar approach has been taken in the Baltrad project, where quality indicators are derived during each step of the quality control process and can be combined to produce an overall metric for the quality of the radar data (Collis et al., 2014).

These approaches lead to more accurate rainfall estimates by removing data that would compromise these estimates while also providing quality information to the end user. The range of data available leads to more accurate and dynamic identification of spurious echoes than is possible with single polarisation weather radar.

2.4.2 Data correction

Dual polarisation has also allowed easier implementation of corrections for radar miscalibration, beam blockage and attenuation, through the use of the phase shift parameters (Φ_{DP} and K_{DP}). All of these corrections work as a result of phase shift being independent of received power, therefore errors which alter the received power do not affect phase shift providing a signal can be retrieved (Vivekanandan et al., 1999; Zrnić and Ryzhkov, 1996).

2.4.2.1 Radar miscalibration

Calibration of radar using the self consistency of dual polarisation variables has been proposed by Gourley et al. (2009) and Vivekanandan et al. (2003) for example. These techniques rely on the principle that reflectivity and differential reflectivity and also differential phase shift are a function of the DSD, and therefore phase measurements can be estimated using power measurements. These can then be compared to measured phase shifts (Scarchilli et al., 1996). In the work of Vivekanandan et al. (2003) K_{DP} is estimated using Eq. 2.9 and then integrated to calculate a total path phase shift which can be compared to the actual phase shift, the bias between which is a result of miscalibration of reflectivity. Gourley et al. (2009) apply the same approach, but using a variation of Eq. 2.9 and show calibration accuracy of 0.6 dB when using a C-band radar.

$$K_{DP} = 2.79 \times 10^{-5} Z^{1.0086} Z_{DR}^{-0.9543} \tag{2.9}$$

Another approach, proposed by Ryzhkov et al. (2005a), is to directly compared reflectivity and differential reflectivity to specific differential phase, using area-time integrals rather than path integrals. This approach was more suited to the S-band radar used as it allows lower values of K_{DP} to be used than the path integral approach, and it again showed calibration was possible to within 1 dB.

The main advantage of these techniques is their applicability during normal operating conditions, as they lack the requirement of an external calibration device, and testing procedure, allowing the calibration to be performed regularly without compromising the operational usage or performance of the radar. Therefore ongoing monitoring of the radar calibration is possible without additional costs, which allows easier updating of the calibration, where required.

2.4.2.2 Partial beam blockage

An extension of these approaches is the use of dual polarisation consistency in partial beam blockage correction. In theory, once a radar is well calibrated, any azimuthal differences in self consistency are a result of partial beam blockage and can therefore be used to correct the reflectivity fields accordingly, while it is also possible to apply a simplified approach, where differential reflectivity is not considered (Zhang et al., 2013; Lang et al., 2009). This simplification negates the required correction of differential reflectivity for partial beam blockage, an issue first noted in the literature by Giangrande and Ryzhkov (2005), although correction is still advisable for other uses of differential reflectivity. These approaches all show calibration is possible even in severely blocked sectors (over 90% in the case of Lang et al. (2009)) provided extensive dual polarisation data is available. Another approach recently employed is the use of specific attenuation to quantify partial beam blockage (Diederich et al., 2015a; Ryzhkov et al., 2014), which also allows accurate calibration provided sufficient data is available, with Diederich et al. (2015a) calculating that 19 days of rainfall data may be required to provide a stable correction to within 1 dB.

The main advantage of these methods is their ability to account for buildings, vegetation and subtle topographic effects not captured by the traditional digital terrain model approach, and also their independence, as they do not require detailed elevation models which may not be available in some locations. Another advantage is the ability to recalculate corrections seasonally, which can respond to changes in the local vegetation and new or removed structures. The main disadvantage of these approaches is the amount of data required for stable results, which precludes their use during the initial stages of a deployment.

2.4.2.3 Attenuation

Another application of dual polarisation is the correction of the hydrometeor attenuation particularly prevalent at shorter wavelengths. As discussed in section 2.2.2 attenuation results in a decreasing signal as path integrated rainfall increases, with correction routines relying on estimating the attenuation along the path using empirical relationships or returns from a fixed source. Dual polarisation radars can improve on these corrections as they allow better constraint of the path total attenuation through the use of differential reflectivity (Smyth and Illingworth, 1998a) or differential phase measurements (Schneider et al., 2013; Jameson, 1992, for example). Again these dual polarisation techniques utilise the consistency of dual polarisation measurements, for example Smyth and Illingworth (1998a) constrain attenuation using light drizzle beyond the attenuating rainfall, which should produce an expected differential reflectivity value of between 0 to 0.2 dB. By attributing under measuring in this region to differential attenuation, reflectivity and differential reflectivity can then be corrected, distributing the total attenuation along the path using specific differential phase. They report accuracy of corrections to within 1 dBZ, however the scheme is limited by identifying and observing the correct precipitation beyond the attenuating region, which is not always possible.

Other techniques choose to use differential phase shift to calculate path integrated attenuation, and then distribute the attenuation using reflectivity measurements. The path integrated attenuation is calculated using DSD coefficients derived from disdrometer measurements or scattering simulations. The application of this method varies through the choice of integral path, coefficients and final application, for example Testud et al. (2000) use segments of the radial as the integration path and use attenuation estimation as a

precursor to rainfall estimation using an estimated normalised intercept parameter of the DSD, while Ryzhkov et al. (2014) use the whole radial below the melting layer as the integration path and derive rainfall directly from the specific attenuation calculated during the process. It is also worth noting that these methodologies are sensitive to the presence of hail, where the relationship between phase shift and attenuation is much stronger than in rainfall, the so called “hot-spot" effect, which requires these regions to be treated separately for best results (Ryzhkov et al., 2014, 2013, 2012).

Subject to the accurate estimation of the relationship between specific phase shift and attenuation (the parameter α), the correct treatment of “hot spots" and attenuation not reducing the signal to noise levels, dual polarisation techniques can successfully correct for attenuation. For example, Gu et al. (2011) used simultaneously collected S-band and C-band data to validate successful correction of the C-band data using a variation of the Testud et al. (2000) technique. While most studies use attenuation correction as an intermediary to rainfall estimation, with their results showing the positive impact of attenuation correction, some recent studies have begun to directly estimate rainfall from specific attenuation, which is also showing promising results, particularly when multi radar compositing is required (Diederich et al., 2015b; Ryzhkov et al., 2014; Schneider et al., 2013; Zhu and Cluckie, 2012, for example).

2.4.3 Improved rainfall characterisation

Beyond the correction of data, dual polarisation observations provide the ability to identify hydrometeors, allowing specific approaches for different particles during rainfall estimation. Another advantage of dual polarisation is the ability to use combinations of parameters to estimate rainfall, such as combining reflectivity and differential reflectivity to better estimate the DSD or using specific differential phase as a rainfall estimator.

Hydrometeor classification is an extension of the quality control methods discussed in section 2.4.1, where the dual polarisation observations are combined with external data, such as temperature to classify the observed hydrometeor population. There are numerous classification schemes available, which use various machine learning techniques including fuzzy logic, unsupervised clustering and Bayesian statistics to partition the observed volume into identifiable hydrometeor classes, including heavy rainfall, drizzle,

hail, graupel, etc. (Grazioli et al., 2015; Al-Sakka et al., 2013; Dolan and Rutledge, 2009; Marzano et al., 2008, to name but a few). As discussed in section 2.2.6, changing hydrometeor phase produces very different precipitation estimates from the same reflectivity measurements, particularly for hail and snow, and therefore identification of these hydrometeors can lead to improvements in rainfall estimation (Dixon et al., 2015; Lim et al., 2013; Schneider et al., 2013).

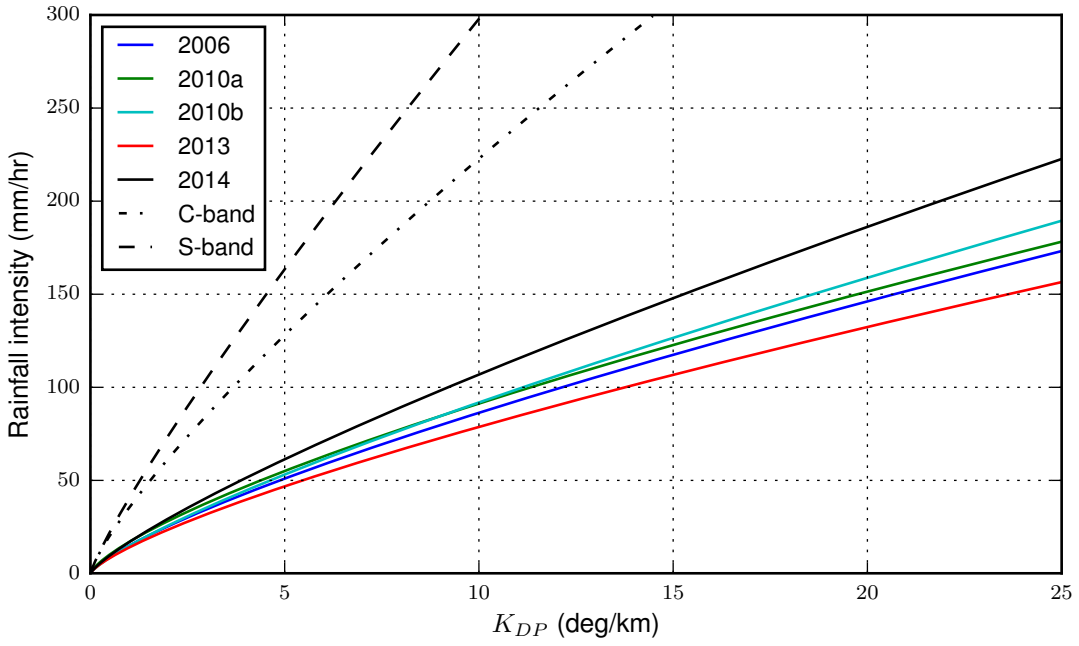

FIGURE 2.6: Parametrised rainfall estimation using specific differential. Variation with frequency band shows increasing sensitivity with decreasing wavelength and variation of parametrisations within X-band is also shown, showing increasing variation at extreme rainfall intensities (>100 mm/hr). These parametrisations are from the following sources: S-band (Sachidananda and Zrnic, 1986), C-band (Wang et al., 2014) and X-band (Ryzhkov et al., 2014; Matrosov et al., 2013; Matrosov, 2010; Matrosov et al., 2006)

To best utilise the ability to identify hydrometeors, specific precipitation algorithms are required, for example Cifelli et al. (2011) use 6 different algorithms to quantify precipitation which use reflectivity, differential reflectivity and specific differential phase as inputs, while Dixon et al. (2015) use 4 different algorithms. In both cases an algorithm based on specific differential phase is used. K_{DP} is an attractive proposition for rainfall estimation because it is proportional to D^3 making it less sensitive to changes in the DSD than reflectivity and Z_{DR} (which are proportional to D^6). K_{DP} is related to rain rate using

equations of the same form as Eq. 2.6, however unlike these reflectivity relationships the parametrisations are wavelength specific due to the scaling of K_{DP} with wavelength. Figure 2.6 illustrates a sample of these relationships for different wavelengths, highlighting the sensitivity differences between the frequency bands. Research by Matrosov and colleagues (2013; 2010; 2006) and also Ryzhkov et al. (2014) suggest the values used for a and b in the parametrisations at X-band can vary substantially, with a specific phase shift of 10 degrees per kilometre being equivalent to a rainfall intensity between 80 and 110 mm hr^{-1} (Fig. 2.6).

Multi algorithm QPE is a clear advantage of dual polarisation radar, particularly when mixed phase hydrometeors are likely to be present. These advantages are likely to be greater at shorter wavelengths where the greater sensitivity of rainfall estimates which use specific differential phase allows for greater diversity of measurements in complex mixed phase environments, particularly when hail is present.

2.5 Rainfall estimation using both radar and rain gauges

Another complementary approach to rainfall estimation with radar is the combination of radar QPE with external rainfall measurements, mainly from rain gauges. The approaches taken include using rain gauges to adjust radar data at a given temporal scale (Cole and Moore, 2008; Joss and Lee, 1995; Collier, 1986, for example), the merging of the data sources together using geospatial techniques such as Kriging (Jewell and Gaussiat, 2015; Goudenhoofdt and Delobbe, 2009, for example) and recent developments in the generation of stochastic ensembles which represent the combined error structure of the two data sources (Wu et al., 2015; Germann et al., 2009; Llort et al., 2008, for example). Each of these methods utilises rain gauge measurements of rainfall as do many validations of radar QPE, and it is important to recognise that rain gauges have their own sources of error and operate at a different spatial and temporal scale to weather radars.

2.5.1 Rain gauge measurements of rainfall

Rain gauges measure the amount of rainfall falling in a small area (typically in the order of 200 cm^2) and vary in complexity from manually read devices to weighing principle gauges

with complex filtering electronics. Many studies have been undertaken to determine the accuracy of these gauges with common sources of error being evaporation, wetting loss, wind under catch, splash and false readings during high intensity rainfall (Beven, 2011; Lanza and Vuerich, 2009; Sieck et al., 2007; Sevruk, 1982). While many of these errors have corrections or mitigation techniques rain gauge measurements of rainfall are still subject to a degree of uncertainty which is highly dependant on the type of gauge used and its location. (Sevruk et al., 2009; Duchon and Essenberg, 2001; Humphrey et al., 1997).

Another aspect of uncertainty when comparing or merging rain gauges and radar estimates of rainfall is the resolution differences between the two observations. Rain gauges are an accumulated point measurement while radar is an instantaneous measurement over a wider area. Studies have shown that the effect of these differences on comparisons are most apparent when comparing data on short time scales in small areas and that both spatial and temporal integration of the data reduces the random errors in the comparison (Villarini and Krajewski, 2008; Ciach, 2003; Habib et al., 2001).

Despite these errors rain gauges are routinely used as the primary measurement of rainfall both for validation of other datasets (radar QPE, satellite QPE, numerical weather prediction) and for hydrological modelling. The next section covers there usage in conjunction with radar QPE.

2.5.2 Combination with radar

The simplest application of rain gauges in relation to radar is for validation of new rainfall estimation methods (Diederich et al., 2015b; Jiang et al., 2012; Biggs and Atkinson, 2011, for example) however they have also been used to adjust radar measurements to account for differences between radar and rain gauges accumulations. Radar rainfall estimates are often adjusted to remove any bias between them and rain gauges over a given time period (Collier, 1996, 1986). For example the UKMO adjust radar rainfall estimates such that 24 hour accumulations are unbiased in relation to 24 hour rain gauge accumulations (Harrison et al., 2000; Golding, 1998).

More recent adjustment techniques are actually spatial merging of the two data sources, typically using a variant of Kriging (Jewell and Gaussiat, 2015; Goudenhoofdt and Delobbe, 2009, for example). These techniques account more for the spatial variation of the biases between gauge and radar while maintaining the spatial resolution of the radar data. A new variation of the Kriging with external drift technique has just become operational in the UKMO radar system based on the work of Jewell and Gaussiat (2015) (Katie Norman, personal communication, July 2016).

Stochastic rainfall ensembles derived from radar are another relatively new addition to hydro–meteorology (Ciach et al., 2007; Germann et al., 2006a). The main advantage of these statistical ensembles are their computational and experimental ease of implementation, as all the radar's error sources are lumped into one residual error derived through comparison with the rain gauges. One limitation is that the residual error is also influenced by the errors in ground observations, another being that the method does not directly identify the cause of the errors be they beam blockage, attenuation or parametrisation errors. Each of the ensemble techniques contains a stochastic perturbation which is modulated by residual error distributions obtained by comparison to ground observations (Villarini and Krajewski, 2010b; Germann et al., 2009, for example). This perturbation can then be used to generate multiple realisations of the rainfall, the distribution of which has the same statistical structure as the radar gauge comparisons. One emerging use of these ensembles is the quantification of overall uncertainty in the hydrological modelling process, allowing comparison with other sources of uncertainty including other inputs, model structure and seasonal parametrisations (Liechti et al., 2013; Quintero et al., 2012; Schröter et al., 2011; Zappa et al., 2011).

Each of these merging and ensemble techniques will provide more accurate rainfall estimates if the radar QPEs used within them is the best possible estimate available, and dual polarisation provides the ability to improve these estimates as discussed earlier in this Chapter. The primary focus of the following research is to ensure this accuracy for rainfall estimates from the NCAS mobile radar, prior to their application in any future stochastic studies of hydrological modelling of river flow.

Chapter 3

Instrumentation and data acquisition

The data used in this study comes from the National Centre for Atmospheric Science's dual polarisation Doppler mobile X-band radar, primarily obtained during the Convective Precipitation (COPE) field experiment in the summer of 2013 (3.2). This data is supported by additional measurements from the field campaign (3.2.2) and also from the United Kingdom's operational monitoring network (3.4). Additional data has been analysed obtained during testing deployments of the radar at the Burn field site (Yorkshire, UK) and also during the ICE-D (Cape Verde) and SESAR (Braunschweig, Germany) projects (3.3).

3.1 The NCAS dual polarisation Doppler mobile X-band radar

The primary data source for this study is a dual polarisation Doppler mobile X-band radar operated by NCAS. The radar is a Meteor 50DX manufactured by Selex ES GmbH, with a custom fitted 2.4 m antenna which precludes the use of a radome (Fig. 3.1). The radar operates at a frequency of 9.375 GHz (a wavelength of 3.2 cm) at a peak transmission power of 83 kW allowing operational ranges in excess of 150 km. The addition of a larger antenna reduces the half power beam width to 0.98 degrees and the radar is capable of

scanning from -1 to 90 degrees in elevation (unlike many operational radars) at a speed of up to 36 $^{\circ}s^{-1}$. The radar operates in hybrid transmission mode, simultaneously transmitting in horizontal and vertical polarisations, and can also transmit in single polarisation (H or V) while still receiving in both channels. Many of the specific scan parameters, including the azimuth and range gate spacing, the pulse repetition frequency and the antenna rotation speed are fully customisable depending on the research requirements and as such are specific to each deployment. The following section (3.2) covers the specifics of the radar's deployment during COPE, along with a more general introduction to the field campaign.

FIGURE 3.1: The modified Meteor 50DX operated by NCAS deployed at the Burn testing site, 30-01-2013. Notice the absence of a radome due to the oversized parabolic antenna fitted to the radar.

3.2 The COPE field campaign

The COnvective PrEcipitation (COPE) experiment is a NERC funded project to improve forecasts of flash flooding. The field campaign for the project took place in Cornwall, south west UK, between June and August 2013 (Blyth et al., 2015; Leon et al., 2016). During this period the mobile radar was operated from Davidstow airfield on a case by case basis. Figure 3.2 shows the location of Davidstow airfield, along with the maximum, 150 km, range observed by the radar during the project.

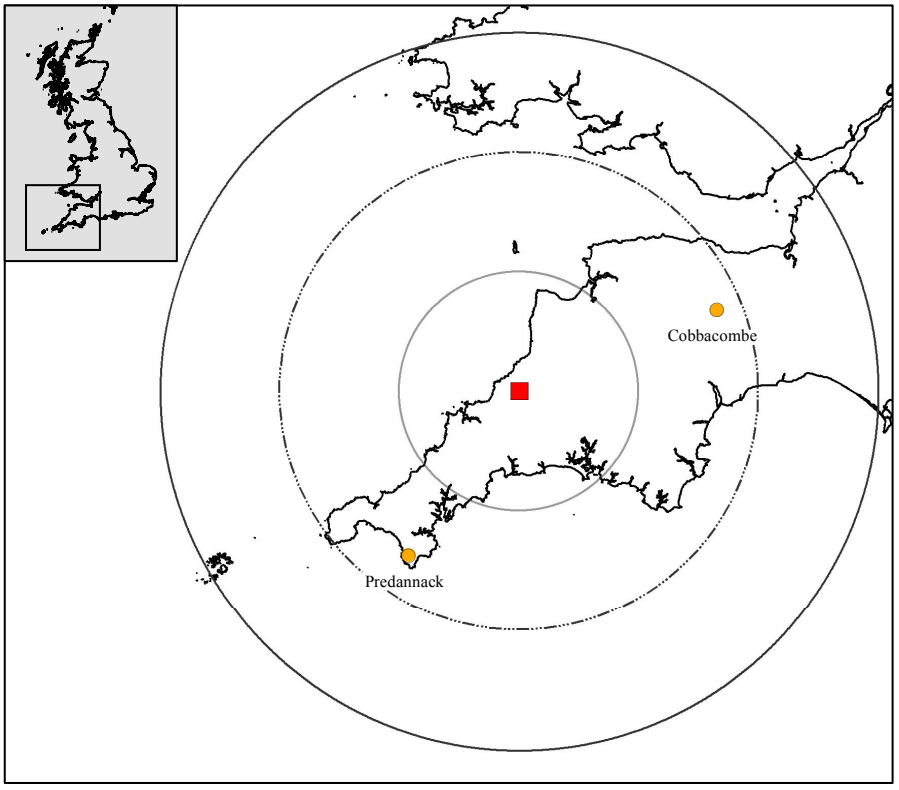

FIGURE 3.2: Location of Davidstow airfield (red square), range rings are at 50 km intervals out to 150 km range, the maximum range observed during COPE. Orange circles indicate the location of two C-band UKMO radars, see section 3.4 for more details.

During the field campaign the radar operated in 5 primary scanning patterns, all of which were azimuth scanning volumes as opposed to the range height indicators (RHIs) often used during research field campaigns. Four of these volumes were a variation of the most often used scan strategy, COPE10, which accounts for 1110 of the 1451 netcdf files available from the project. COPE10 is a general purpose volume scan pattern, containing plane position azimuth sweeps at 10 elevations spaced at one degree intervals from 0.5 degrees up to 9.5 degrees (Fig. 3.3). The antenna rotation speed was 20 degrees per second, allowing a full volume scan to be completed in under 5 minutes. Actual volume scan spacing during the campaign ranged from 4 minutes to 6 minutes, which will require consideration in the analysis when computing rainfall accumulations and evaluating the temporal evolution of convection. The pulse width for COPE10 was one microsecond, matched to a gate spacing of 150m with a dual pulse repetition frequency (PRF) set to 1000/800 Hz (a 5/4 ratio). Data was sampled using one degree angle steps.

These parameters combined to give 44 samples per range gate, an unambiguous range of 149 km and a unambiguous Doppler velocity range of 31.89 metres per second. The three additional volume scan patterns based on COPE10 were COPE20, COPE30 and COPE40, these varied only in the spacing of the 10 elevations contained within the volume, which increased from one degree for COPE10 to two, three and four degrees respectively. As can be seen in Figure 3.3, the default scan strategy could not observe the tops of deep convective clouds when they were close to the radar, for example a cloud top height of only 5 km was only visible if the cloud was at least 30 km from the radar. These additional strategies were used to increase the maximum height observable close to the radar, when convection was occurring in this region. This increased height was at the expense of lower vertical resolution of measurements due to the increased sweep spacing. All of these scan patterns contained a lowest scan of 0.5 degrees elevation, which provides the close to ground observations most applicable for rainfall estimation.

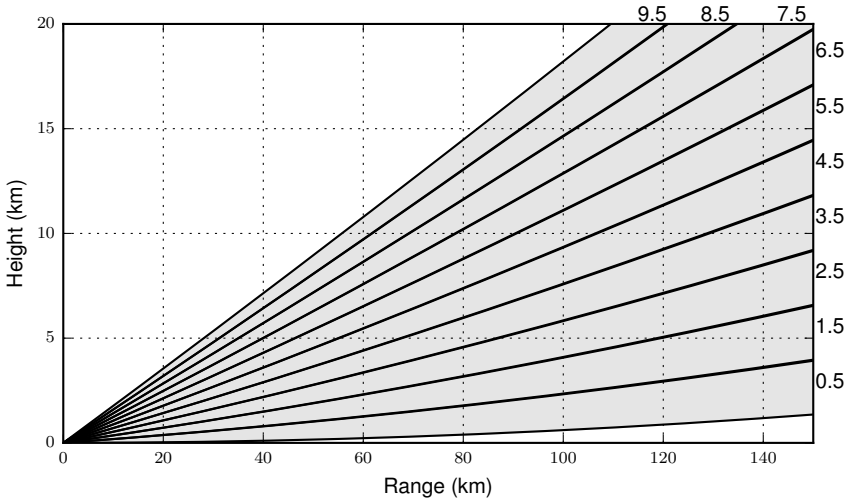

FIGURE 3.3: Scan volume coverage for the COPE10 scan strategy. Height is measured with the radar as reference, during COPE the radar was sited at 298.9 m above mean sea level. The sweeps are labelled with their elevation angle running around the right and top edge of the plot. The radar scanned at 20 ms^{-1} during the campaign.

The other scan strategy used during COPE was ClearAir (CA), a volume scan containing 5 elevation sweeps, at one degree spacing from 0.5 to 4.5 degrees. The antenna scan speed was reduced to five degrees per second and the PRF mode was changed to single frequency at 1000 Hz. Data was collected to a maximum range of 100 km. This reduced the unambiguous Doppler velocity to 7.9 metres per second but increased the number of

samples per range gate to 198. The scan was operated during periods of no precipitation, with the purpose being to increase the sensitivity of measurements to allow more clear air echoes to be observed (typically insects, but also associated with humidity gradients). This allows zones of convergence to be detected prior to convective initiation.

Between 20 June 2013 and 17 August 2013 the radar operated on 23 days, of which 14 were IOPs for the field campaign. Prior to the 4 July, the radar operated on 5 testing days, while there were 3 days of operation during the IOP period which were insignificant in regards to convective precipitation and are not considered to be IOPs. A summary of operations is shown in Table 3.1, while full details of all the scans are available in Appendix A.

TABLE 3.1: Operating periods for the X-band radar during COPE. Times represent the start and end point for each day in UTC but do not guarantee continuous running. Scan strategies are listed by their number with the prefix COPE removed. Strategies X1-X4 represent scans that are not described in the text, occur infrequently but are described fully in Appendix A

Date	Scan period	Number of scans	Scan strategy
20/06/2013	09:51 to 17:38	70	Testing only
27/06/2013	14:57 to 15:17	6	
01/07/2013	13:42 to 15:33	16	
02/07/2013	10:01 to 15:42	84	
03/07/2013	08:57 to 12:25	47	
04/07/2013	09:47 to 16:06	73	
05/07/2013	09:00 to 16:08	55	CA
16/07/2013	10:37 to 15:51	46	CA
17/07/2013	10:10 to 16:16	48	CA
18/07/2013	08:48 to 15:23	78	CA, 10, 20, 30, 40, X1, X2
23/07/2013	09:13 to 16:18	33	10
25/07/2013	08:26 to 14:47	88	10
27/07/2013	11:16 to 15:56	60	10
28/07/2013	09:13 to 15:53	82	10
29/07/2013	10:50 to 16:29	75	10
31/07/2013	08:40 to 12:03	50	10
02/08/2013	09:55 to 18:14	101	10, 20, 30
03/08/2013	09:25 to 15:40	71	10, 20, X3, X4
05/08/2013	10:51 to 15:25	51	10, 20
06/08/2013	08:20 to 15:01	77	CA, 10
14/08/2013	10:31 to 15:06	56	10
15/08/2013	09:01 to 14:56	72	10
17/08/2013	07:31 to 16:23	112	10, 20

3.2.1 Data fields obtained during COPE

During the COPE field campaign the radar stored the following radar moments, 19 fields in total. Of these 19, 17 are included in the processed CF-radial files provided after quality control, with reflectivity and filtered reflectivity from vertical polarisation omitted. Quality control also corrects for drift in the transmitted frequency, along with the application of a fixed value differential reflectivity calibration and reflectivity calibration based on the self consistency of dual polarisation returns, which will be discussed more in section 4.1.

1. Reflectivity from both horizontal and vertical polarisations
2. Reflectivity from both polarisations filtered using a Doppler FIR filter
3. Differential reflectivity using Doppler filtered fields
4. Co-polar cross correlation coefficient
5. Degree of polarisation
6. Differential phase shift
7. Differential phase shift filtered using Fourier transform
8. Specific differential phase (derived by signal processor)
9. Specific differential phase (derived by Rainbow© from filtered differential phase shift)
10. Doppler velocities using both horizontal and vertical polarisations
11. Doppler velocities using filtered horizontal and vertical returns
12. Signal quality index from both polarisations
13. Spectral width from both horizontal and vertical polarisations

3.2.2 Additional COPE instrumentation

A number of other meteorological instruments were deployed during the field campaign at a site within 1 km of the radar deployment site at Burn airfield and also throughout Cornwall. The Davidstow field site contained a vertically pointing micro rain radar, a scanning Lidar, a wind profiler and a tower mounted weather station along with a suite of aerosol measuring instruments. Beyond the field site, radiosondes were launched from the radar location throughout the project and automated weather stations were installed by the UKMO in locations around Cornwall for the duration of the project. Measurements from these instruments have been used to add context to the research and to complement the observations from the mobile radar where possible.

Table 3.2: Summary of other instruments deployed during COPE.

Instrument	Operating period	Summary
Micro rain radar	24/06 to 21/08/2013	24 GHz vertically pointing radar with 1.5° beam width. Sampling 31 levels from 35 m up to 1085 m.
Halo Lidar	20/06 to 21/08/2013	1.55 μm scanning Lidar providing aerosol backscatter coefficient and radial velocity. Scanned two fixed azimuth RHI profiles and vertically during the campaign.
Wind profiler	27/06 to 31/08/2013	Boundary layer UHF (1290 MHz) Doppler radar recording boundary layer wind speed and direction, along with SNR and spectral width at continuous 15 minute intervals.
Davis AWS	20/06 to 20/08/2013	Automated weather station measuring temperature, humidity, pressure, wind speed and direction, rainfall and humidity at continuous 5 minute intervals.
Radiosondes	18/07 to 14/08/2013	Event specific soundings measuring height, temperature, pressure and humidity. Launched from radar deployment location.

3.3 Additional radar deployments

During the course of this research the NCAS radar has also been deployed in other field locations, for both testing at the Burn Airfield site (3.3.1) and for research deployments in Cape Verde, Germany and Scotland (Appendix B). Data from these deployments has been used to guide the techniques applied to the COPE data throughout the rest of this thesis and will be invaluable for future investigations of these techniques. The following section provides a brief summary of the Burn field site while summaries of the other deployments can be found in Appendix B.

3.3.1 Burn airfield

The mobile radar has been deployed at Burn airfield, North Yorkshire (Fig. 3.4) for testing, on several occasions since its acquisition in 2012. The airfield site is prone to blockage at low elevations, mainly as a result of trees and the extensive power infrastructure present in this location (two coal fired power stations and their associated power lines). The site does however offer extensive coverage of Yorkshire and also provides higher level observations over the western side of the Pennines. Data from a deployment on 6 October 2014 has been used during this study, particularly for the testing of clutter identification and correction routines discussed in later chapters. During this deployment the COPE10 and COPE20 scan strategies were reused. Data was collected for the traverse of a frontal system across the UK from west to east, with the radar operating between 09:46 UTC and 13:06 UTC and collecting 43 volume scans. All the fields collected during COPE were also recorded here, but unlike the COPE data, they have not been calibrated by the instrument scientist.

3.4 UK operational monitoring networks

The UK Met Office (UKMO), Environment Agency (EA), Natural Resources Wales, Scottish Environment Protection Agency (SEPA) and the Rivers Agency Northern Ireland between them operate and collate a network of meteorological and hydrological monitoring stations across the UK providing the observational basis for the UK flood warning

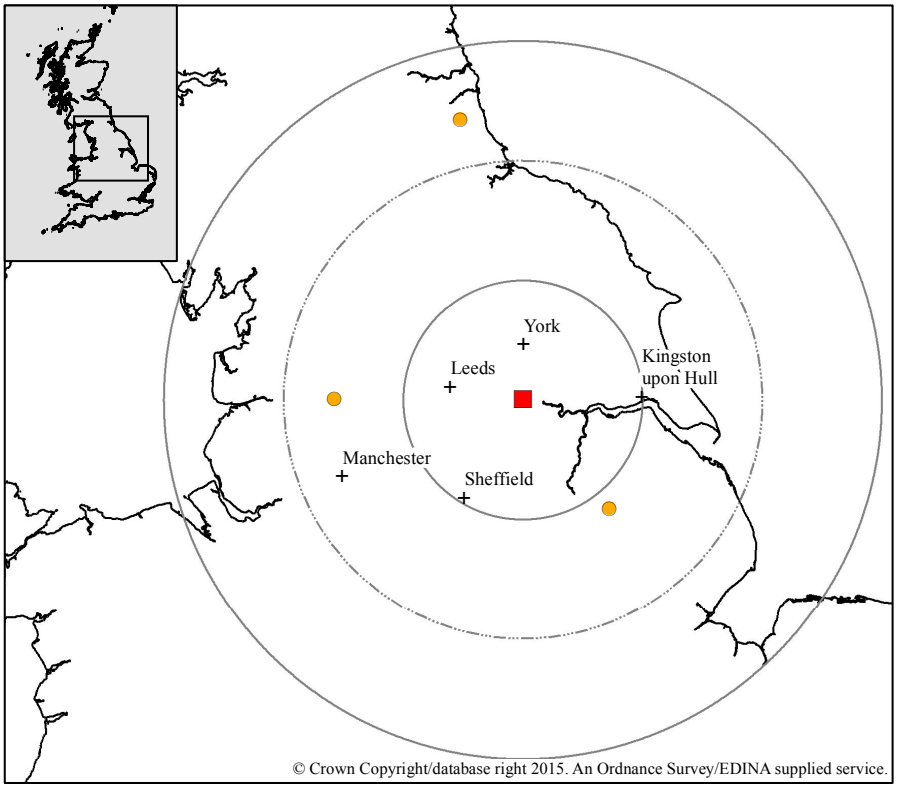

FIGURE 3.4: Location of Burn airfield (red square), range rings are at 50 km intervals out to 150 km range. Orange circles indicate the location of three closest C-band UKMO radars, see section 3.4 for more details. Within range of the radar are several major UK cities which have experienced flooding, these are labelled on the map with a cross marking their location. Other smaller towns and cities prone to flooding are also within range of the deployment site.

systems. These monitoring systems include a network of C-band weather radars, rain gauges, river level, river flow and reservoir level stations. For the purposes of this research data from the C-band radar network and rain gauges and river telemetry from within the EA's network have been used, details of which are covered below.

3.4.1 C-band radar network

The UKMO operate a network of 15 C-band radars across the UK (Fig. 3.5). This network is currently being upgraded to dual polarisation with 9 of the radars now upgraded. Though many of the dual polarisation radar have been operational for a few years the composite radar rainfall product (Nimrod) produced by the UKMO does not yet incorporate dual polarisation corrections and enhancements. The Nimrod product is the final

result of a single polarisation processing chain implemented on the polar raw radar reflectivities obtained from the network. The processing chain includes the removal of noise, ground clutter and occlusions, attenuation correction, bias correction using surface rain gauge adjustment, conversion to a Cartesian grid with 1 km resolution and compositing of data with the lowest uncertainty available (Harrison et al., 2009; Golding, 1998). The Nimrod product is supplied to researchers via the British Atmospheric Date Centre (BADC) as a gridded instantaneous rain rate in millimetres per hour for the whole of the UK at five minute intervals, with a 1 km grid resolution. Dual polarisation polar data from individual radars is also available from the BADC, however it is worth noting that during the COPE campaign the Predannack radar was non-operational due to it being upgraded to dual polarisation and the Cobbacombe radar had not yet been upgraded to dual polarisation. As a result the nimrod composite is the only available network radar data for the period of the field campaign.

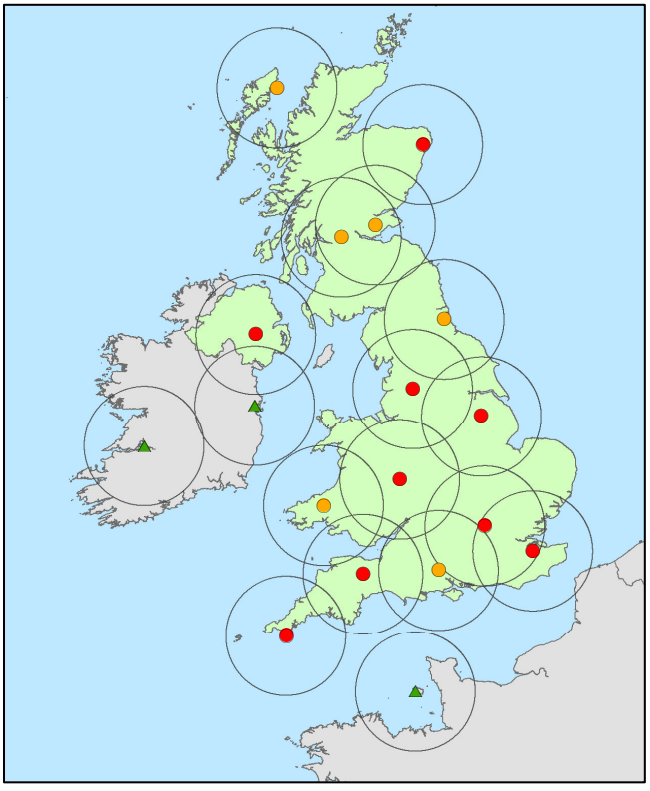

FIGURE 3.5: Location of the UKMO C-band weather radars, shown with the coloured circles. Red circles denote those radars already upgraded to dual polarisation. Orange circles are awaiting upgrade. The green triangles denote radars which are not operated by the UKMO but contribute to the nimrod composite. Range rings are drawn at 100 km.

3.4.2 Tipping bucket rain gauges

The EA in England collates and records data from a telemetered network of rain gauges, operated by itself, water authorities and the UKMO. These rain gauges are tipping bucket gauges, with a bucket size of 0.2 mm recording data at 15 minute intervals. These gauges are collocated with a daily check gauge to provide a measure of quality control. For the purposes of this research, data from the 20 rain gauges within 50 km of the Davidstow deployment site (Fig. 3.6) were obtained from the EA. These gauges cover the Cornish peninsula in this area, providing distributed point observations to compare with the radar data.

FIGURE 3.6: Location of the rain gauges telemetered by the Environment Agency (grey triangles). Davidstow radar site is shown with red square and 50 km range ring is shown for scale.

Chapter 4

Evaluation of the COPE dataset

The primary dataset for this study is that collected during the COPE field campaign, particularly the data collected with the X-band radar. The following chapter provides an overview of the data collected, highlighting data quality issues, reviewing the spatial distribution and occurrence of radar echoes and comparing the derived rainfall rates with those obtained from rain gauges and the network weather radar. As discussed in 3.2.1 the data has been pre-processed to calibrate reflectivity and differential reflectivity, with particular attention paid to frequency drift during the field campaign (4.1).

4.1 Pre-processing

Data from the X-band radar has been calibrated using the dual polarisation consistency principles by the radar instrument scientist (Bennett, personal communication, February 2015). Firstly differential reflectivity has been corrected using measurements of very light drizzle, where drops are expected to be spherical and differential reflectivity should be in the region of 0 to 0.2 dB. Secondly the self-consistency technique of Gourley et al. (2009) has been used to correct the miss-calibration of horizontal reflectivity. Finally both reflectivity and differential reflectivity were corrected for drifts in the radars intermediate frequency, which varied from 55 to 69 MHz during the field campaign due to a hardware fault causing increased warm up durations on startup (Fig. 4.1). A linearly interpolated correction has been applied to both fields to correct for the combination of frequency drift and miss-calibration. The correction varies between -3 to -4.3 dBZ for reflectivity

and -0.5 to -2 dB for differential reflectivity. These corrections are applied during the conversion of raw radar files to the cf radial standard for radar data storage. Analysis shows that for later radar deployments frequency drift occurs over a much smaller range, for example during ICE-D (Section B.1) frequency varied between 58 and 62 MHz.

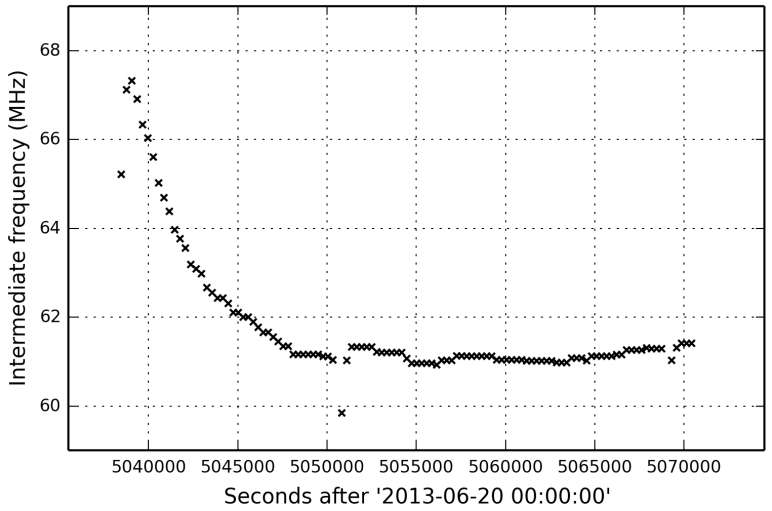

FIGURE 4.1: Intermediate frequency drift on the 17th August 2013, typical of the standard drift seen during the field campaign on radar start up. Time axis displays number of seconds since the beginning of the field campaign, with frequency stabilising after approximately 2.7 hours.

4.2 Mobile radar location

During the field campaign the mobile radar required off-site storage and redeployment every day, which led to a variation in radar position between days. For the majority of the campaign the position of the radar varied over a distance of approximately 5 metres, however on the 27-06-2013 and 05-08-2013 the radar was sited approximately 60 metres to the north east (Fig 4.2). Although this was only a relatively small shift in position, it had significant implications for the location of beam blockages caused by obstructions close to the radar and has required consideration in further analysis. The published cf radial files will require modification as they were set with a fixed position for the entire campaign, which is not representative for the two dates mentioned.

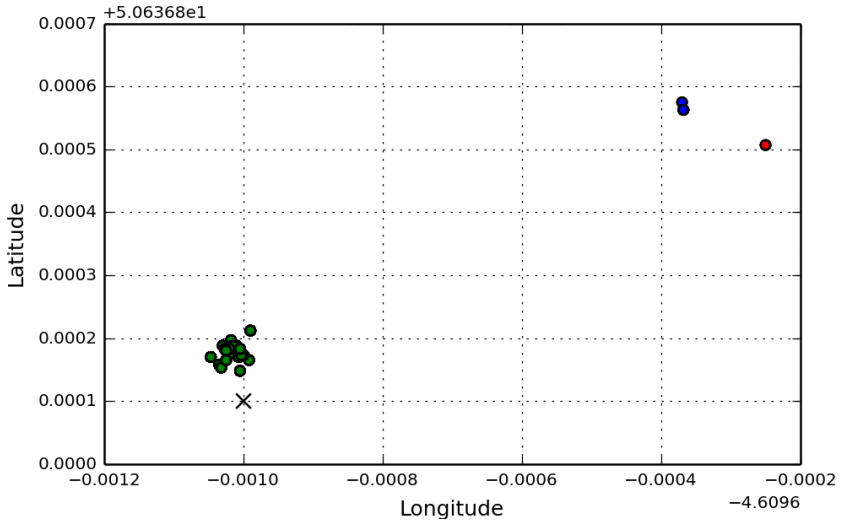

FIGURE 4.2: Variation of radar's position during the COPE field campaign. Green circles show the actual radar position for the majority of the campaign, while red circles show position on 27-06-2013 and blue circles show position on 05-08-2013. The black cross shows the fixed position coded into the cf radial files available on the BADC.

4.3 Reflectivity analysis

Initial inspection of the raw reflectivity fields easily identified common radar errors occurring in the data, namely beam blocking, ground clutter returns, non-meteorological echoes, radio interference, attenuation and second trip echoes. Examples of these features are shown later in the work when discussing their identification and/or correction using dual polarisation. Initial analysis focused on the bulk characteristics of the polar reflectivity fields, including the frequency and magnitude of echo occurrence. As Harrison et al. (2014) discuss, the computation of bulk statistics allows radar errors, including ground clutter and beam blockage, to be easily identified, and can be used to assess the quality of the correction routines applied. Therefore establishing a set of benchmarks from the raw data has allowed the later corrections to be assessed. As the statistical methods focused on polar data (rather than regridded cartesian data), a subset of the whole dataset has been used, which omitted those scans which are not directly comparable. This included the omission of the two dates mentioned above, where the radar position was altered significantly, and also those scans which do not have 1000 range gates at a spacing of 150 m and a one degree azimuth angle step. Using a common data array allowed bulk statistics to be computed without introducing uncertainties through interpolation or re-gridding.

4.3.1 Echo occurrence percentage

The first statistical measure considered is the echo occurrence percentage for each range gate, which is simply the count of all reflectivity observations exceeding a threshold value divided by the total number of scans in the dataset. As precipitation occurs in variable locations, and is not persistent over long time periods, the echo occurrence percentage can indicate locations which are prone to persistent non-meteorological echoes, such as ground clutter. Azimuthal gradients in the echo percentage also indicate where beam blockage may be causing a reduction in sensitivity for the radar. Data from the lowest four elevations is shown in Figure 4.3, where both these signals are visible.

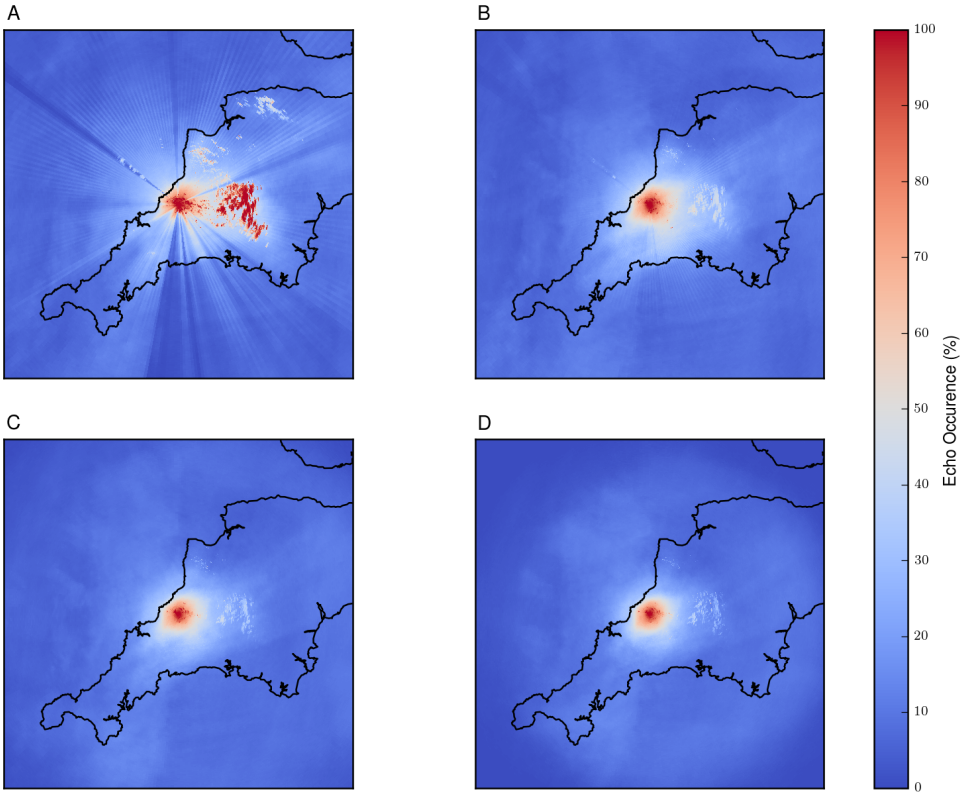

FIGURE 4.3: Percentage of radar scans containing a non zero reflectivity observation during the COPE field campaign when using raw reflectivity data. A shows the percentage for 0.5° elevation scans (1075 scans during the campaign), B shows 1.5° elevation (1041 scans), C shows 2.5° elevation (1075 scans) and D shows 3.5° elevation (1041 scans). Images cover 200 km x 200 km centred on the mobile radar.

The echo occurrence percentages in excess of 90% to the east of the radar at 0.5° indicate the presence of persistent signals from Dartmoor (an area of elevated topography, shown

in Figure 4.4), this is supported by the reduced occurrence of the these echoes with increasing elevation.

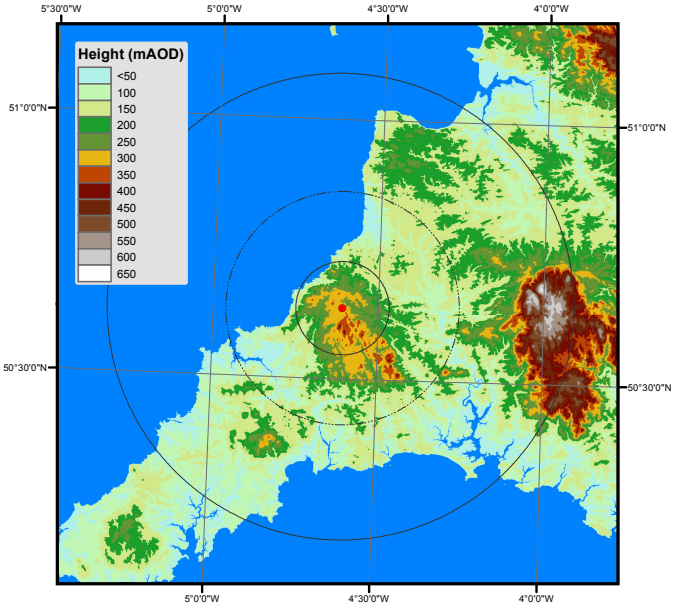

FIGURE 4.4: Surface elevation of Cornwall in region surrounding Davidstow radar site.

Similarly beam blockages are indicated by the reduction in echo occurrence at fixed azimuths in the lowest elevation scan, which do not occur at higher elevations. The beam blockages visible are caused by a mixture of topography and man-made structures (unfortunately including the radar command centre for the project at 68 degrees azimuth). These blockages are better represented when azimuthally averaging the echo occurrence (Figure 4.5). Given normal atmospheric conditions with no beam blockage you would expect the number of echoes to decrease with increasing elevation angle, as the radar beam begins to overshoot low level precipitation (particularly at far range). This is observable in the zero to fifty degree azimuth range, however there are clear azimuth ranges at 0.5° elevation where the echo occurrence decreases compared to the surrounding angles and higher elevations, indicating areas of beam blockage. For example the blockage at 305° is caused by the old airfield control tower, while the less pronounced blockage signal between 210° and 230° is caused by Davidstow Woods. Comparison between the 1.5° and 2.5° elevations indicates that the 1.5° scan clears almost all of the blockages, with some

blockage from the control tower at 305° and from the high topography between 170 and 190 degrees. The degree of blockage is quantified and corrected for in Chapter 6.

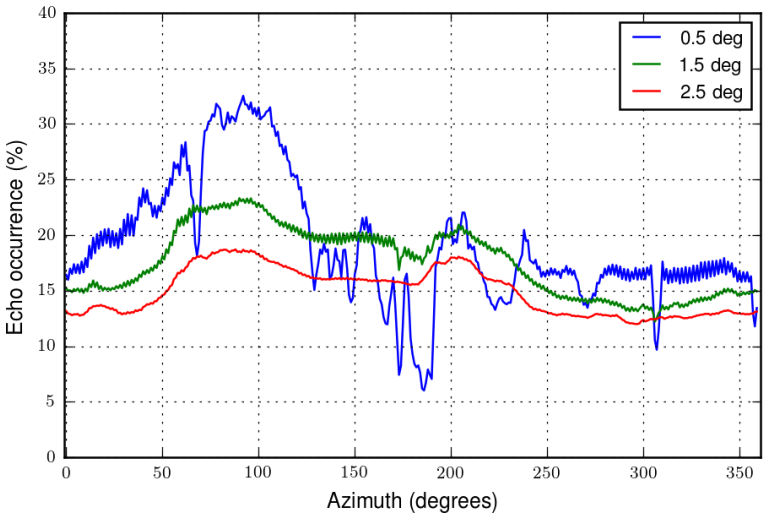

FIGURE 4.5: Azimuthal average echo occurrence percentages for the lowest three elevation angles used during the campaign. These are 0.5° (blue line), 1.5° (green line) and 2.5° (red line). Echo occurrences are as per the data periods in Figure 4.3 with 1075 scans used for the 0.5° and 2.5° elevations and 1041 scans used for the 1.5° elevation.

The azimuthal averaging of echo occurrence also highlights an oscillating signature within the lower elevations, which is more extreme at 0.5° . The signal indicates the likely presence of second trip echoes within the dataset, which are made apparent by the staggered PRF transmission mode operated during the campaign, where the maximum unambiguous range varies between high and low PRF pulses (150 km and 187.5 km at 1000 Hz and 800 Hz respectively). Echoes beyond the unambiguous range can be observed as closer echoes during the next pulse, leading to superposition of signals. The staggered PRF causes this superposition to fluctuate position as the unambiguous range changes, creating different echo distributions dependant on the PRF being transmitted. The phenomena occurs more frequently at lower elevations because higher elevation sweeps overshoot most precipitation at longer ranges. As these echoes are clearly visible using the echo occurrence statistic, they have been identified in individual scans and have been removed, where possible, during the quality control process (Chapter 5).

Another feature visible using the echo occurrence measure is the central bullseye of high values which is present at all four elevations. This is caused by clear air echoes, most

likely insects, which are detected at close range, where the radar sensitivity is highest. This is confirmed by Figure 4.6, which shows the echo occurrence when reflectivity is greater than a threshold of -1.4 dBZ (which equates to the 0.03 mm/hr threhsold used by Harrison et al. (2014) if the UKMO standard Z-R relation is used). After thresholding the bullseye is no longer visible due to clear air echoes typically being low intensity and therefore under the threshold. Again these echoes have been identified as either precipitation or clear air clutter during the quality control process, and removed where necessary (Chapter 5).

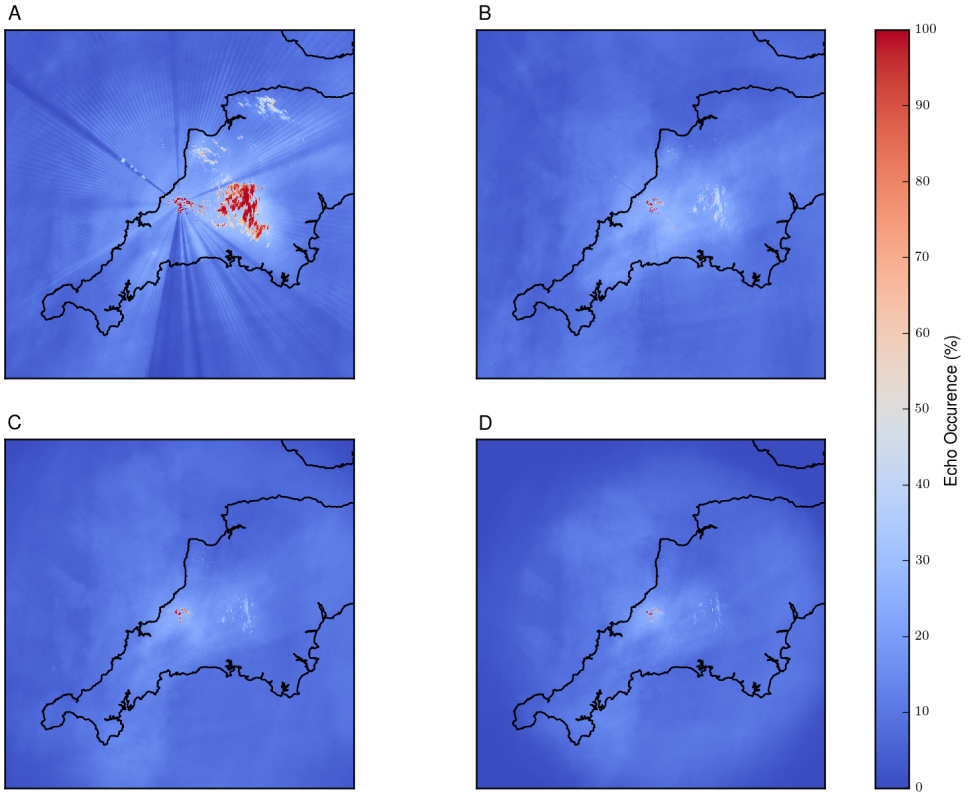

FIGURE 4.6: Percentage of radar scans containing a reflectivity observation greater than -1.4 dBZ during the COPE field campaign. Panels are as in Fig. 4.3. Panels cover 200 km x 200 km centred on the mobile radar.

4.3.2 Conditional average reflectivity

A second long duration statistical measure that is also used to analyse radar data quality is the conditional average reflectivity or conditional average rainfall. In this case the

average reflectivity has been calculated for all echoes exceeding a threshold of 0 dBZ (which is equivalent to 0.0365 mm/hr if using the Marshall-Palmer relation) using the same data subset as for the echo occurrence calculations. Figure 4.7 shows the results from the four lowest elevations used in the COPE campaign, further highlighting the data quality issues shown by echo occurrence percentages.

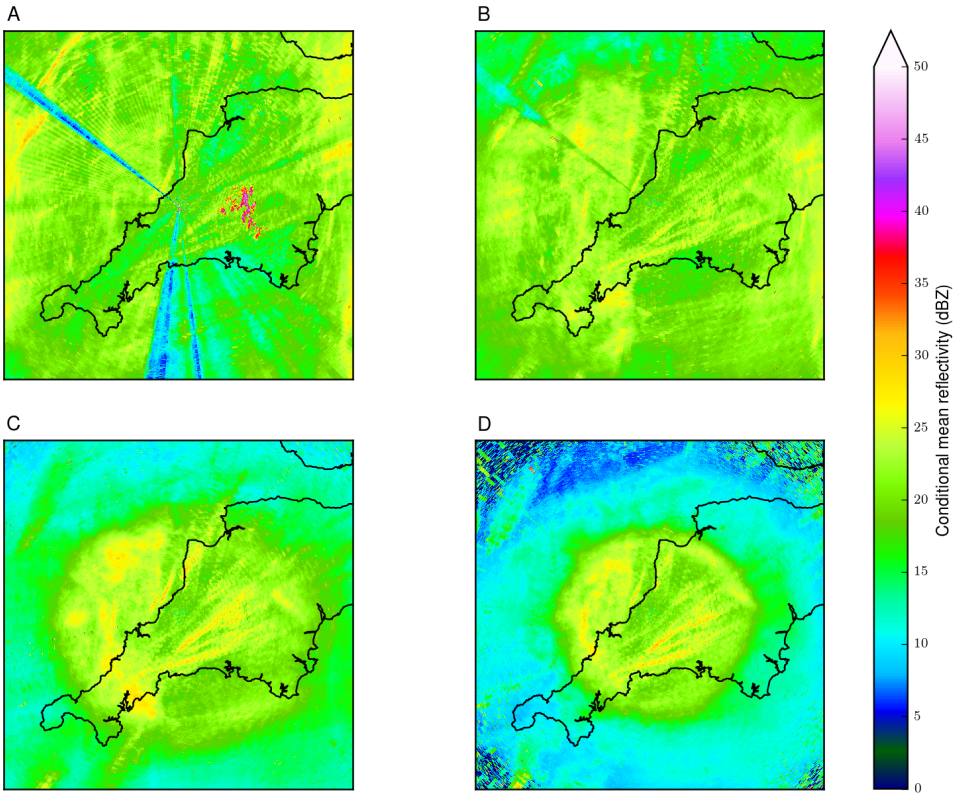

FIGURE 4.7: Average reflectivity observed at each elevation conditional on the observation exceeding a threshold of 0 dBZ. Panels are as in Fig. 4.3. Images cover 200 km x 200 km centred on the mobile radar.

Panel A in Figure 4.7 clearly shows the effect of beam blockage due to the airfield control tower, where the average reflectivity observation is approximately 15 dBZ lower than the surrounding areas, and also the high topography to the south of the radar, which suffers a similar magnitude of change. The results show that the other areas of beam blockage identified using echo occurrence percentages are less severe, but will still need correction. Also clearly visible in panel A is the elevated mean reflectivity to the east of the radar, which confirms that the echo occurrence percentages of over 90% in this area are a result of strong ground clutter returns. Both these signals are not present in panels C and D,

with only the extreme beam blockage resulting from the airfield control tower affecting scans at 1.5° elevation (panel B).

4.4 Radar filtered reflectivity

A potential option to alleviate the issue of ground clutter is to use the radar's filtered reflectivity field, which uses discrete Fourier transform notch filter in the IQ data to remove reflectivity signals centred on zero velocity. However this filtered field has two noticeable flaws, the first of which being that the filter tends to reduce but not remove ground clutter reflectivity signals when there is no rainfall due to the velocity notch being smaller than the velocity range of the ground clutter signals (Figure 4.8).

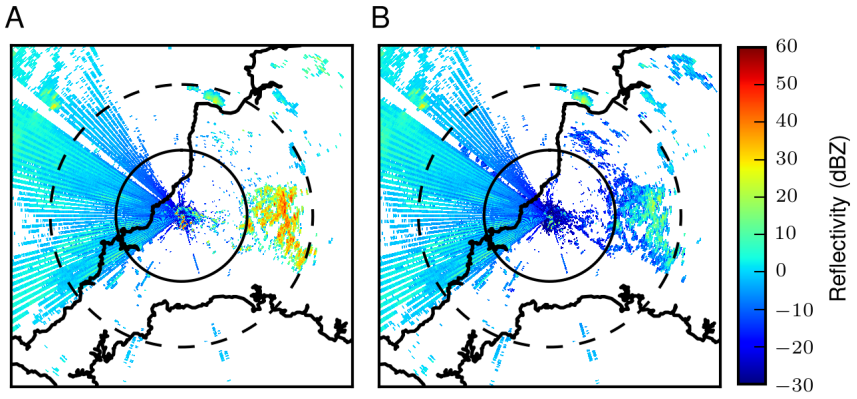

FIGURE 4.8: Reflectivity PPIs at 0.5° elevation from the 2013-08-17 07:56:03 UTC volume scan. Panel A shows the raw reflectivity field (dBuZ) measured by the radar and Panel B shows the filtered reflectivity field from the signal processor. The panels are 130 km boxes centred on the radar, with range rings at 25 km (solid line) and 50 km (dashed line).

Figure 4.8 shows two reflectivity PPIs (0.5° elevation) from the 07:56 UTC volume scan on 17 August 2013, with Panel A showing the raw reflectivity field and Panel B the radar filtered reflectivity field. Rainfall at this time is sparse (based on rain gauges and higher elevation data), with the majority of the echoes observed being spurious. Most noticeable are the second trip echoes to the west and the ground clutter echoes from Dartmoor to the east. The presence of the ground clutter echoes in Panel B but at a lower intensity

(10 to 20 dBZ as opposed to 30 to 50 dBZ) indicates that the filter notch is too narrow to completely eliminate the ground clutter signal. The filter has also boosted the signal in some regions, most noticeably for Exmoor in the north east at 70 km range. Changes to the ground clutter signals are likely to be noticed in long term statistical overviews of the data, and the echo occurrence percentages for these two fields are compared in Figure 4.9.

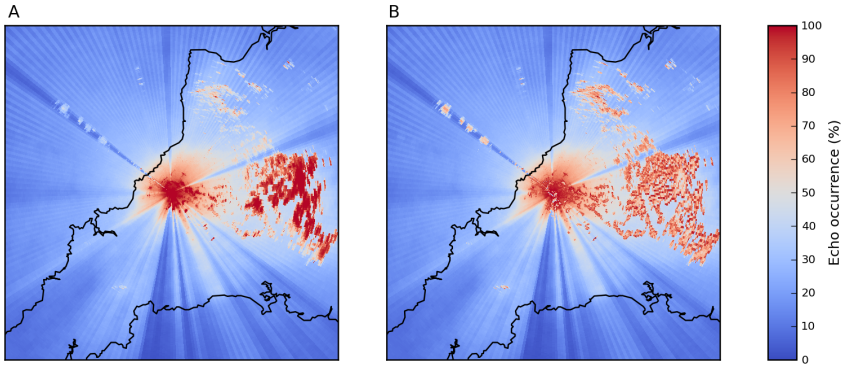

FIGURE 4.9: Percentage of radar scans containing a reflectivity observation greater than -30 dBZ during the COPE field campaign. Panel A shows the occurrence percentage for raw reflectivity at 0.5° elevation and Panel B shows the percentage for radar filtered reflectivity at 0.5° elevation. Panels are 100 km boxes centred on the mobile radar.

As previously shown in Figure 4.3 the echo occurrence percentages in regions of ground clutter are very high, typically greater than 90% for COPE. The radar's internal clutter filtering reduces the occurrence of echoes over Dartmoor to nearer 50% in places, though some regions still have over 90% echo occurrence, highlighting that the filter often reduces these echoes without removing them. There is also an increase in echo occurrence percentage to the north east of the radar and strangely within the beam blocked sector to the north west. Another feature of the radar filter which can't be observed in long term statistics but is noticeable in individual PPIs is the reduction in intensity of echoes along the naturally occurring zero velocity isodop, where the wind is travelling tangentially to the radar beam and therefore has zero radial velocity. This can be seen in Figure 4.10 which shows reflectivity data from the Burn test site (10:30 UTC 2014-10-06) again at 0.5° elevation. On each panel the 3 ms^{-1} radial wind speed both towards and away from the radar is shown, with a decrease in reflectivity observed within the low velocity region between these contours in the filtered data. The magnitude of this change is up to 8 dBZ

which could be significant for rainfall estimation, although this will be a transient effect dependant on wind speed and direction.

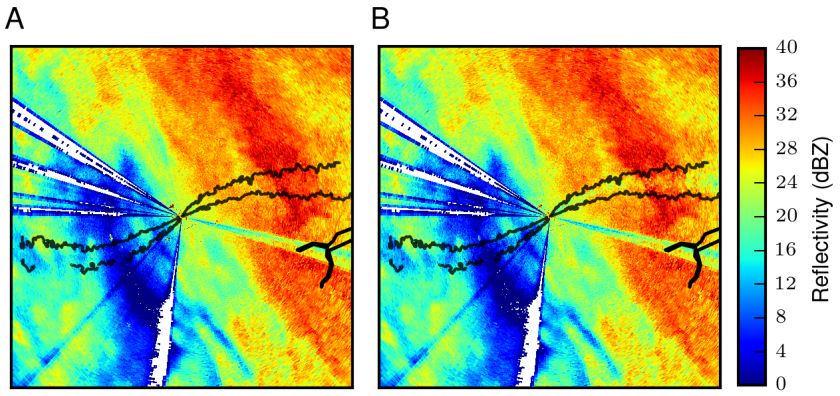

FIGURE 4.10: Reflectivity PPIs at 0.5° elevation from the 2014-10-06 10:30:40 UTC volume scan. Panel A shows the raw reflectivity field (dBuZ) measured by the radar and Panel B shows the filtered reflectivity field from the signal processor. The thin solid black lines on each panel are the $3\,\mathrm{ms}^{-1}$ and $-3\,\mathrm{ms}^{-1}$ radial velocity contours with the region between them being the low velocity zone including the zero velocity isodop. The panels are 60 km boxes centred on the radar, with the Humber estuary marked as coastline on the eastern edge of each panel.

The presence of these errors within the filtered reflectivity data suggests an alternative approach to filtering radar echoes is required for accurate rainfall estimates in this region, and the following Chapter covers the development and implementation of both threshold filtering of second trip echoes and fuzzy logic filtering of non-meteorological echoes to provide an alternative filtered reflectivity field for analysis.

Chapter 5

Dual polarisation radar data quality control

Given the indiscriminate radiation pattern of radar it is no surprise that they detect echoes from a range of source objects, including those which are not of meteorological origin (see section 2.2.4). To provide accurate rainfall estimates these echoes must be removed from the dataset where possible, while those echoes which are a mix of meteorological and non meteorological returns should be treated with caution.

Though a variety of quality control methods have previously been implemented on both single and dual polarisation radar, either by processing the raw I/Q data (Torres and Zrnić, 1999) or by classifying echoes with the radar moments using machine learning (Chandrasekar et al. (2013), also see sections 2.2.4 and 2.4.1) there is no clearly applied approach in the literature, with each organisation tending to produce a bespoke solution (or several) which fits their requirements. The following chapter outlines an approach for identifying and removing these erroneous echoes developed using the COPE data, befitting the needs of the mobile X-band radar operated by NCAS. The data processing and visualisation in Chapter 4 shows the clear need for the application of quality control, with both ground clutter and insect contamination occurring in the data along with single point interference from other radiation sources and second trip echoes from beyond the maximum unambiguous range of the radar. Given the varied end user applications of the data (cloud microphysics studies, model comparison, hydrological modelling) an approach

has been developed which is adaptable to the end user, with the implementation here focusing on the need for accurate rainfall estimation for hydrological modelling.

5.1 Dual polarisation rainfall signature

To identify spurious radar echoes is it first necessary to determine how a true rainfall echo appears using dual polarisation radar moments. Previous studies have shown that rainfall should have a correlation coefficient of generally greater than 0.97 (Balakrishnan and Zrnić, 1990; Zrnić and Ryzhkov, 1999), differential reflectivity in the range 0 dB to 5 dB (see 2.3.2) with the majority of rainfall at the lower end of that range and positive differential phase shift ranging from 0° km^{-1} in light drizzle to over 15° km^{-1} in very heavy rainfall at X-band (also see 2.3.2). To determine how the mobile X-band radar performs in relation to these usual expected values several rainfall events from the COPE dataset were identified, using rain gauges and the UKMO radar composite to "ground truth" the identification. The rainfall event on 5 August was then analysed to extract the dual polarisation moments from range gates which contained rainfall. This process was aided by the raw statistics discussed in Chapter 4 to avoid regions of potential ground clutter contamination. By collating data collected over an hour, the distribution of radar moments for those range gates identified as rain can be constructed using histograms. Figure 5.1 shows the constructed histogram for horizontal radar reflectivity, as you would also obtain from a single polarisation radar, showing the rainfall event to be mainly of moderate intensity, with some echoes representing heavier rainfall if considering reflectivity alone.

Histograms of differential reflectivity, specific differential phase shift, correlation coefficient and normalised coherent power for the same rainfall event are shown in Figure 5.2. The differential reflectivity histogram indicates a range expected for smaller median rain drop diameters, with the majority of the observations being between 0 dB and 1 dB. The presence of negative values indicates a small degree of measurement noise influencing the observations and also shows the effect of differential attenuation reducing the observed differential reflectivity. With the exception of the negative observations, the observations lie within those expected based on previous research, with the absence of very high values

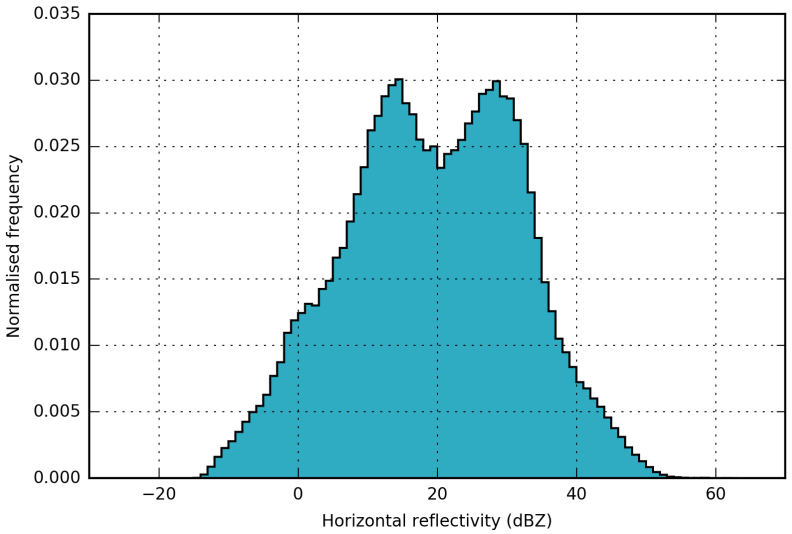

FIGURE 5.1: Histogram of raw horizontal radar reflectivity during rainfall event on the 5 August 2013, from 12:08:04 UTC to 13:03:04 UTC. N=367213.

indicating that the high reflectivity values are likely a result of an increased concentration of moderately sized drops, rather than fewer large rain drops.

The observed correlation coefficients are as expected from the literature, with over three quarters of the observations exceeding a correlation of 0.97, over 90% of the observations exceeding 0.9 and only 3% of the observations being below 0.8. However these lower values present indicate the correlation coefficient in rainfall can be affected by measurement errors, resulting from low signal to noise ratios and non-uniform beam filling.

The specific differential phase observed during the rainfall event largely matches expectations, however 29% of the observations are between 0 $^{\circ}\mathrm{km}^{-1}$ and -0.5 $^{\circ}\mathrm{km}^{-1}$ indicating the internal processing of K_{DP} is generating negative values in light rain where the total differential phase shift is low, which is a known difficulty for K_{DP} calculation and a reason for the use of hybrid rainfall algorithms which use reflectivity for light rainfall and K_{DP} for heavier rainfall. Alternative options for processing K_{DP} have been explored in Chapter 6.

The final radar moment shown in Figure 5.2 is the normalised coherent power (NCP) also known as the signal quality index (SQI), which is available to both single and dual polarisation radars. The normalised coherent power is given by the magnitude of the

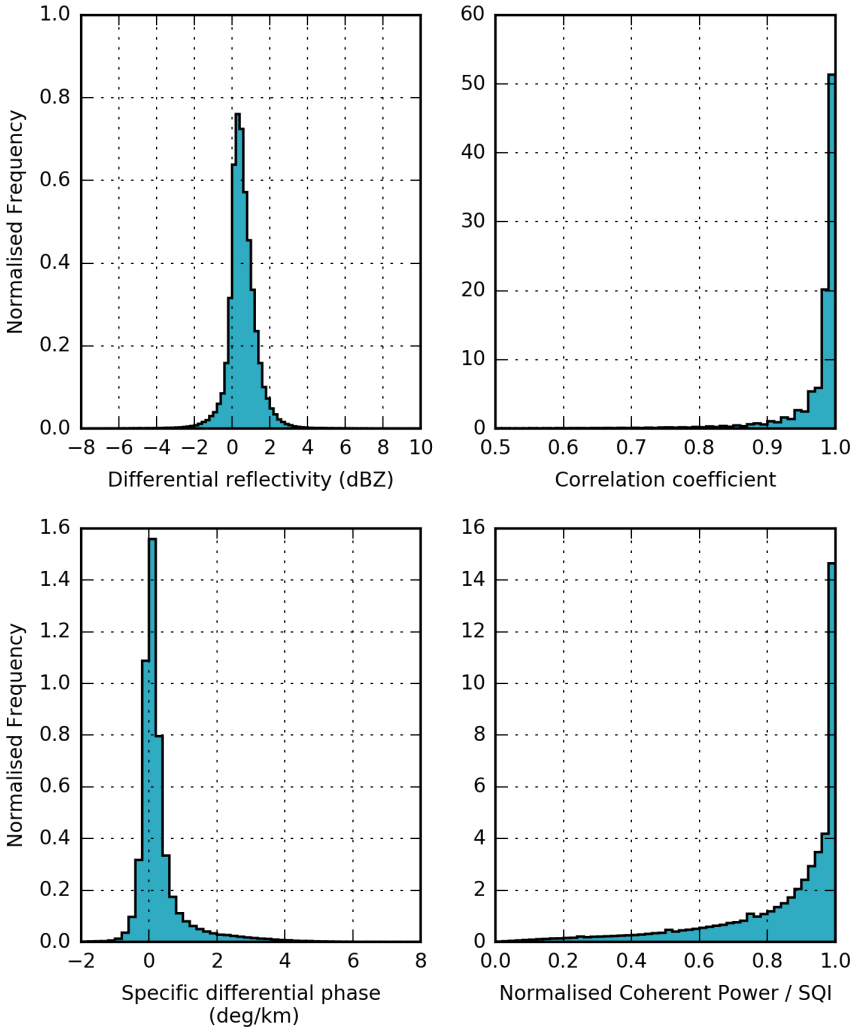

FIGURE 5.2: Histograms of the dual polarisation radar moments, differential reflectivity, correlation coefficient and specific differential phase along with normalised coherent power during a rainfall event on the 5 August 2013, from 12:08:04 UTC to 13:03:04 UTC. The data was pre-classified to sample only range gates highly likely to be rainfall of variable intensity.

covariance at t_1, divided by the power at t_0, and indicates how predictable the signal is from one pulse to the next (Bell et al., 2013; Dixon and Hubbert, 2012). The observations indicate a high degree of coherence in rainfall, with 71% of the observations exceeding 0.8, and 96% of the observations exceeding 0.3, with lower values being attributable to increased turbulence, indicated by increased spectral width as noted by Dixon and Hubbert (2012).

It is worth noting that Doppler velocity, spectral width and degree of polarisation (DOP)

are also observed by the NCAS radar, however these results have not been presented. In the case of Doppler velocity, it can be expected to be of any value within the Nyquist velocity range for a moving rainfall system, depending on its true atmospheric velocity and the position of the radar relative to the system, while DOP mirrors correlation coefficient almost exactly and adds no additional value to characterising rainfall observations in this case.

The observations presented in Figures 5.1 and 5.2 show that the expected dual polarisation rainfall signature is replicated in the NCAS radar observations from COPE, and provide a point of reference for comparisons with dual polarisation observations that are not of meteorological origin.

5.2 Second trip echoes

A clear feature of the analysis in Chapter 4, particularly evident in Figure 4.5, is the presence of second trip echoes, which vary by azimuth due to the staggered PRF operated by the radar. Second trip echoes occur when a target reflects a signal back to the radar after the time the radar was expecting that pulse to generate a return (Figure 5.3). In the example shown a signal from pulse 1, the blue pulse, returns to the radar during the listening period for pulse 2 (in the yellow box). This superimposes the signal from pulse 1 onto the returns from the second pulse and generates a second trip echo within the radars unambiguous range. The maximum unambiguous range for a radar (r_{max}) is a function of the pulse repetition frequency used by the radar and is given by equation 5.1. A second trip echo will be visible at a distance equal to the actual range of the cloud minus the maximum unambiguous range. For the COPE scans this equates to a variable maximum range of either 187.5 km or 150 km when the staggered PRF settings of 800 Hz and 1000 Hz were used (the majority of the scans). This variation allows second trip echoes to be identified more effectively than when a single PRF is implemented, as the second trip echo location varies depending on the PRF of the given azimuth. For example, for the two PRFs given an echo at 200 km range would produce a second trip echo at either 50 km or 12.5 km depending on the PRF staggering used.

$$r_{max} = \frac{c}{2.PRF} \tag{5.1}$$

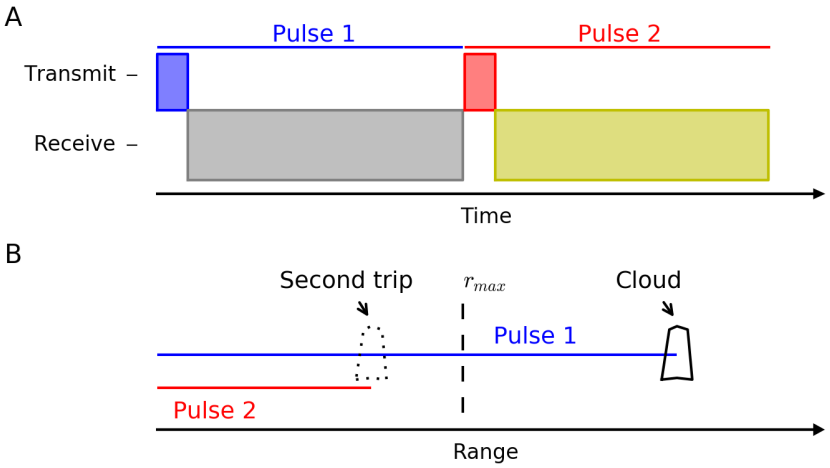

FIGURE 5.3: Schematic representation of second trip echoes, A shows a simplified sketch of the radar procedure for 2 pulses, while B relates this to the maximum unambiguous range of the radar (r_max), showing pulse 1 travelling beyond this range and returning the signal from the cloud during the receive period of pulse 2, creating a second trip echo as though pulse 2 was observing the cloud at a closer distance to the radar.

5.2.1 Identifying second trip echoes

To develop a filtering method individual examples of second trip echoes were identified in the COPE data, such as the one shown in Figure 5.4 from 17 August, where widespread rainfall approached from the west, extending from the southern Irish coast to the English Channel as seen in the wider rainfall composite produced by the UKMO (Fig. 5.5). The example shows an alternating reflectivity signal between radials to the west and north west of the radar, as a result of the staggered PRF used and the presence of second trip echoes. Embedded within that region is a first trip rainfall echo, which is visible in both of the lowest elevations and in the UKMO composite.

Although the second trip echoes are clearly identifiable visibly it is beneficial to identify and remove the second trip echoes automatically during processing of the radar data. Dual polarisation was a potential solution to this filtering, provided the second trip echoes had a dual polarisation signature that was distinct from the rainfall signature presented in the preceding section. Figure 5.6 shows six of the available moments for the second trip echo example shown previously in Figure 5.4. On visual inspection the second trip echoes observed have a differential reflectivity comparable to rainfall (panel A), with the first trip echo not being distinct from the second trip echo. There is evidence of

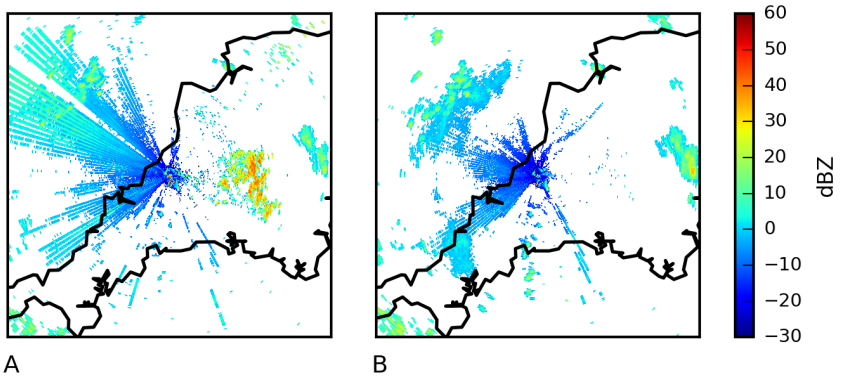

FIGURE 5.4: Example of second trip echoes identified in the COPE data, 2013-08-17 08:16 UTC. A shows the 0.5° elevation scan and B shows the 1.5° scan, showing the discontinuity of echoes with increasing elevation. Both panels are 150 km squares centred on the radar.

differential attenuation impacting the second trip echoes to the west of the radar, which is supported by the high differential phase shift values observed there (panel D), but again the differential phase shift values generally are not unusual for a rainfall event. The correlation coefficient (panel E) for the second trip echoes (≈0.95) is slightly lower than for the first trip (>0.97), which could be useful for filtering. This decrease is expected due to non uniform beam filling, which is more likely at the true range of the second trip echoes than close to the radar where the first trip echoes occur. However non uniform beam filling and therefore decreased CC is possible within the range of the radar (150 km) which may lead to difficulties with a filter based on CC. The specific differential phase shown in panel F is again within the bounds expected for a rainfall echo, with the only distinguishing feature being a strong negative K_{DP} along the radial boundary of the first trip echo, caused by the superposition of elevated phase shifts closer to the radar than the first trip echo which then decrease where the first trip echo occurs. The panel also shows that the radar's internal filtering is removing some but not all of the second trip echoes prior to K_{DP} calculation. The internal filter thresholds the data, removing segments which contain bad data, with the thresholds being a signal to noise ratio below 3, a CC below 0.8 and a standard deviation of phase shift below 12. Clearly a different filter will be required to adequately remove second trip echoes from the data. Finally panel B suggests the NCP/SQI may be a useful parameter for filtering second trip echoes, with the first trip echo to the north west having values expected for rainfall of 0.9 and

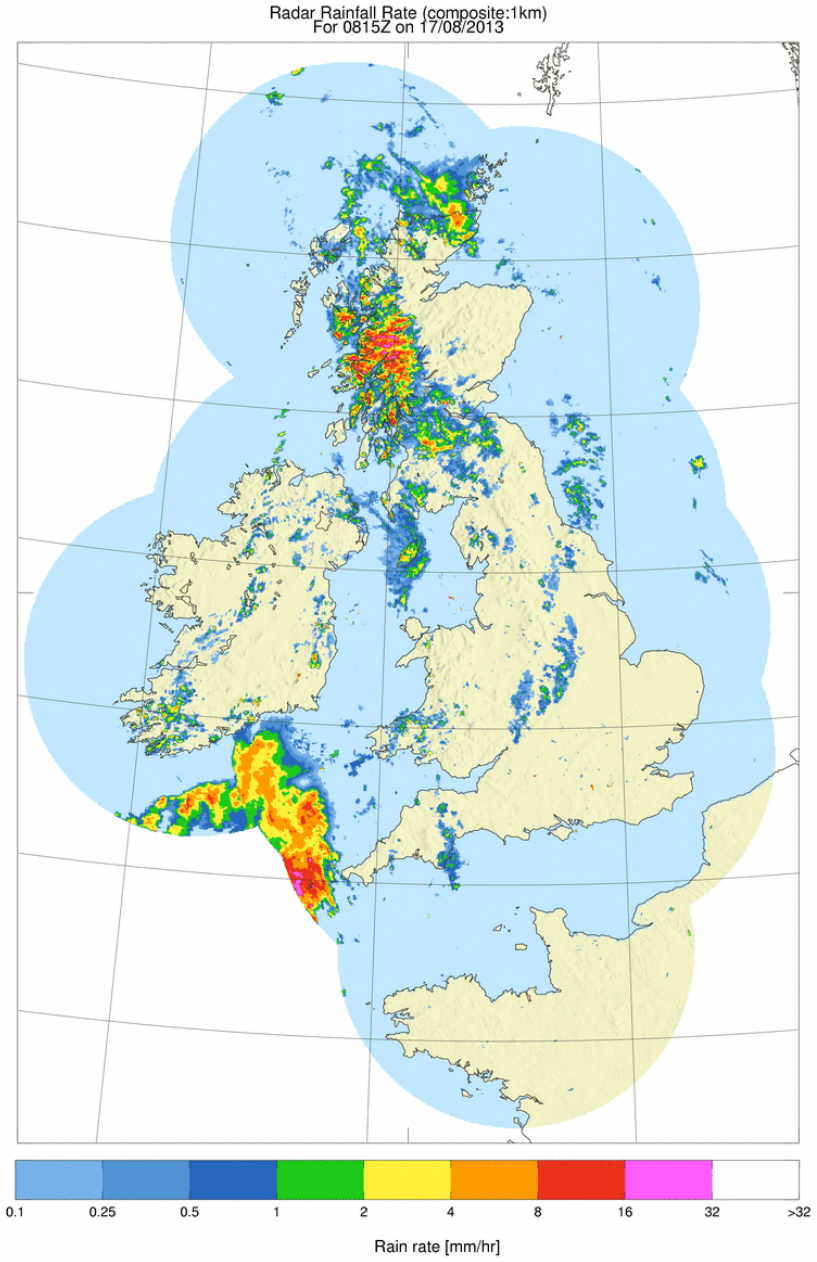

FIGURE 5.5: UK Nimrod radar composite provided by the UK Met Office for the COPE field campaign, 2013-08-17 08:15 UTC.

above, while the second trip echoes in that region blend into the background noise data and have a SQI of 0.4 and below.

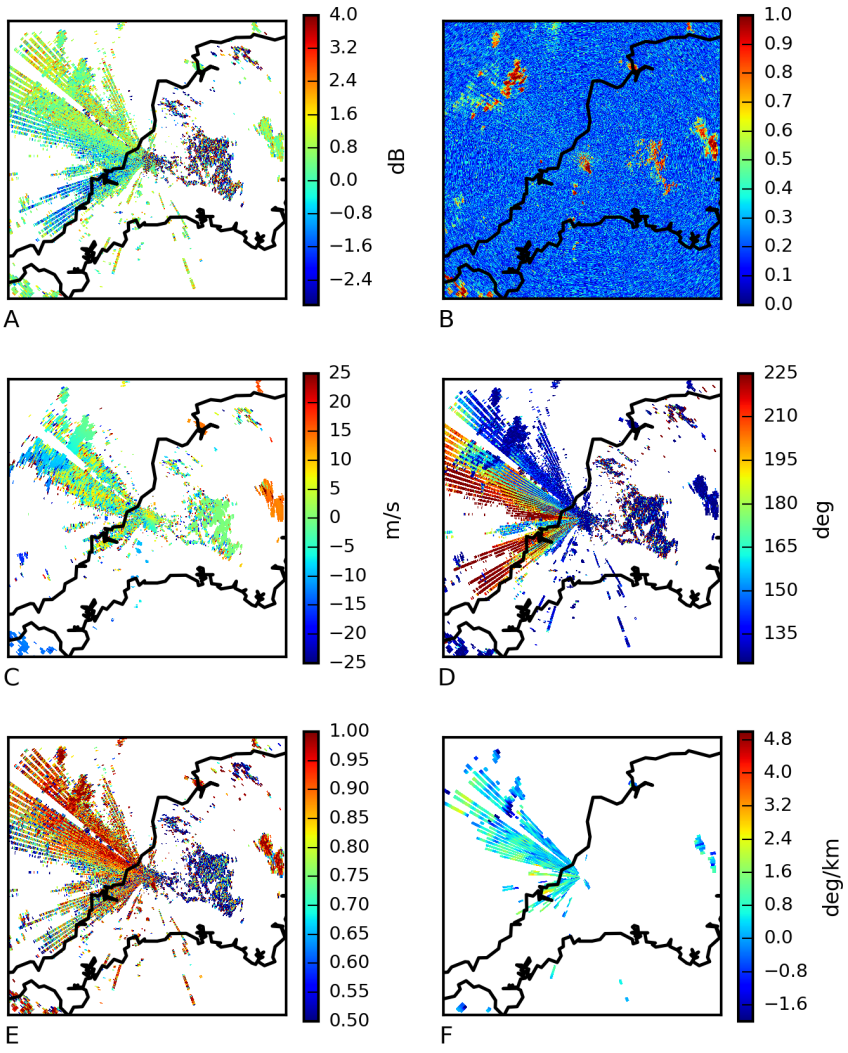

FIGURE 5.6: Multiple radar moments for the example shown in Figure 5.4. A shows the ZDR, B the signal quality index (SQI), C the Doppler velocity, D the differential phase shift, E the correlation coefficient and F the specific differential phase. Again these are 150 km squares centred on the radar.

Extending the analysis to multiple radar scans using moment histograms supports these initial findings, with the histograms in Figure 5.7 indicating an overlap of both K_{DP} and ZDR between rain and second trip echoes, with CC having a broader distribution of moderately high values for second trip echoes (>0.8) than rainfall echoes, which are strongly distributed towards high values (>0.95). However, as 20% of the second trip echo observations have a CC greater than 0.98 there is still significant overlap between

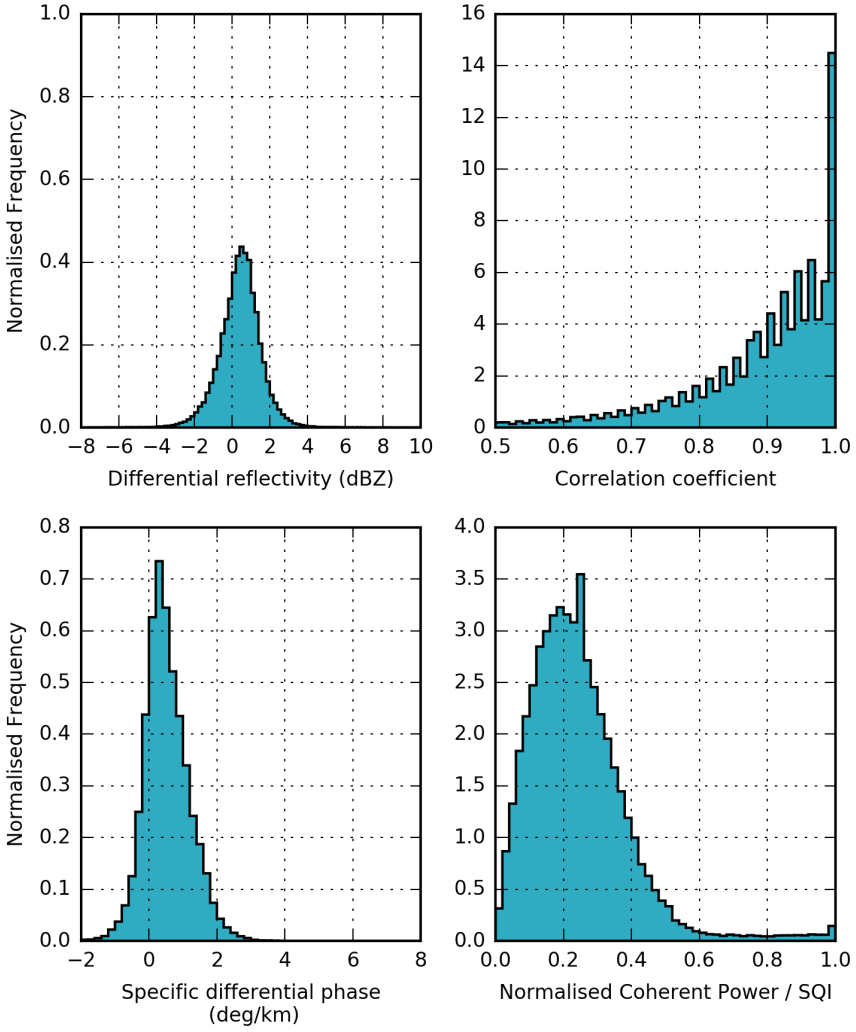

FIGURE 5.7: Histograms of the dual polarisation radar moments, differential reflectivity, correlation coefficient and specific differential phase along with normalised coherent power during a rainfall event on the 17 August 2013, from 07:56:03 UTC to 08:56:03 UTC. The data was pre-classified to sample only range gates highly likely to be caused by second trip echoes returning from rainfall beyond the maximum unambiguous range of the radar.

the two distributions. In contrast the SQI observations have a very different distribution for second trip echoes than for first trip rainfall echoes, with over 70% of the observations below 0.3 and over 95% below 0.5, compared to the rainfall echoes where 71% of the observations were greater than 0.8 and 91% were greater than 0.5. Dixon and Hubbert (2012) suggested that SQI could be used to filter noise from radar observations, with these results indicating it can also be used to filter second trip echoes. Following the suggestion in that paper, the possibility of using SQI averaged over a window of range gates has been explored. Figure 5.8 shows the variation in SQI when it is taken from an individual range gate compared to taking the mean of the field over a three by three gate window and a five by five gate window, for both rainfall and second trip echoes.

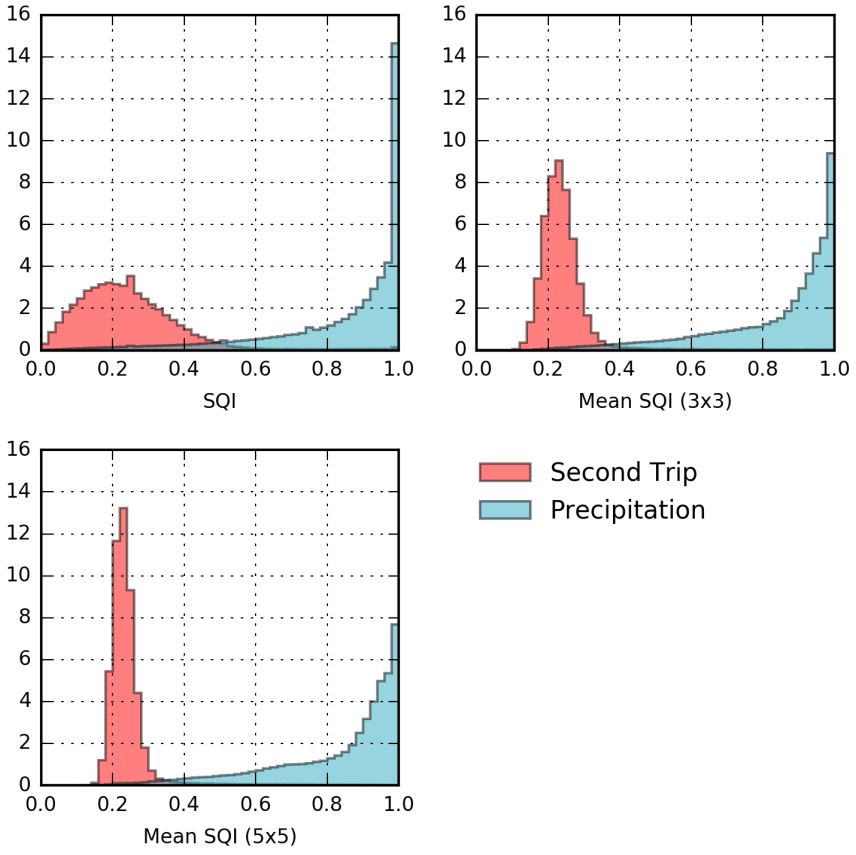

FIGURE 5.8: Histograms of raw SQI and SQI averaged over a 3x3 and 5x5 gate moving window centred on the observation range gate. The observations are from the same events shown in Figure 5.1 for precipitation and Figure 5.7 for second trip echoes.

Figure 5.8 shows that as the size of the averaging window increases the distribution of SQI values observed during second trip echoes narrows, while the rainfall distribution varies

only slightly. For second trip echoes the interquartile range is 0.17 when using the raw data, while this decreases to 0.04 when using a 5 gate averaging window, similarly 90% of the data in the later case is within a range of 0.12, while this increases to 0.42 for the raw data. In contrast the 90 percentile range of the rainfall observations only decreases from 0.63 to 0.56, and interquartile range doesn't vary by more than 0.003 across the three averaging domains. The narrowing of the distribution of second trip echo observations when using an averaging window reduces the overlap between the two distributions, suggesting a better ability to discriminate between the two signals when using averaging windows. Another potentially viable discriminator between the two signals is to generate azimuthal difference fields which take advantage of the dual PRF of the radar producing the alternating signals already seen in the data.

To take advantage of these signals a difference function was developed to calculate the median difference between a radial and its adjacent radials, along a moving five range gate window which is shown in equations 5.2 and 5.2.

$$x_{i,j} = Md\,\mathrm{P} \tag{5.2}$$

Where P is the following set and i varies in azimuth and j varies in range:

$$\mathrm{P} = \{|x_{i-1,r} - x_{i,r}|, |x_{i+1,r} - x_{i,r}| : x_{j-2} \leqslant r \leqslant x_{j+2}\} \tag{5.3}$$

Using equation 5.2 the radial differences of the radar moments were computed for the rainfall and second trip echoes identified previously, with only reflectivity and phase shift showing a noticeable signal difference between the two echo types. Histograms for these two moments are shown in Figure 5.9.

Figure 5.9 shows a stronger signal difference between rainfall and second trip rainfall echoes when using median phase shift compared to median reflectivity, with only 14% overlap compared to 56% overlap. Given the two distributions are largely distinct there is potential for using median azimuthal phase shift difference for identifying and removing second trip echoes.

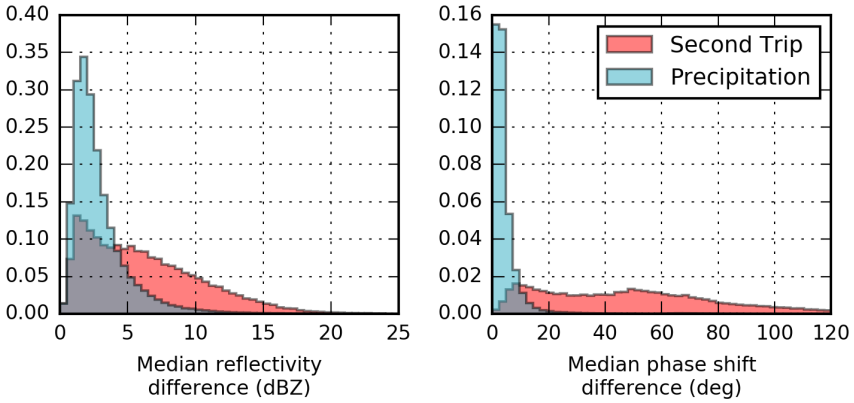

FIGURE 5.9: Histograms of median azimuthal difference in raw reflectivity and phase shift over a 5 gate window centred on the observation range gate. The observations are from the same events shown in Figure 5.1 for precipitation and Figure 5.7 for second trip echoes.

5.2.2 Removing second trip echoes

The identification of second trip echoes within the COPE dataset has shown that they have distinct signatures when observed using normalised coherent power, especially when averaged over a moving window, and median azimuthal phase shift difference. These signatures have been used to remove second trip echoes during processing, removing the effects previously seen in Figure 4.3 and Figure 4.5, using a logical decision process. Potential options for the logical decision process were based on those used previously in radar filtering and included threshold filtering, a decision tree and fuzzy logic (Chandrasekar et al., 2013). As the filter only has to identify and remove one signal, based on at most two radar moments a simple threshold approach was taken, akin to a very basic decision tree. The distribution of both mean SQI and azimuthal phase shift change were re-examined in a two dimensional distribution space (Figure 5.10) to determine the relationship between echo type, mean SQI and phase difference. Two possible filtering approaches were developed based on these distributions. Option 1 is a simple threshold filter, based only on the mean SQI in the 25 gate moving window, with any observations with a mean SQI below 0.3 being removed as a second trip echo. Option 2 applies a mean SQI threshold which varies as a function of the median azimuthal phase difference, as shown in equation 5.4, where $\delta\Phi$ is the median azimuthal phase difference and $\mathrm{SQI}_{\mathrm{thr}}$ is the variable threshold.

$$\mathrm{SQI}_{\mathrm{thr}}(\delta\Phi)\begin{cases}0.2+0.02\delta\Phi, & \text{if } 0 \leqslant \delta\Phi \leqslant 10\\ 0.4, & \text{if } \delta\Phi > 10\\ 0.3, & \text{where } \delta\Phi \text{ is missing}\end{cases} \tag{5.4}$$

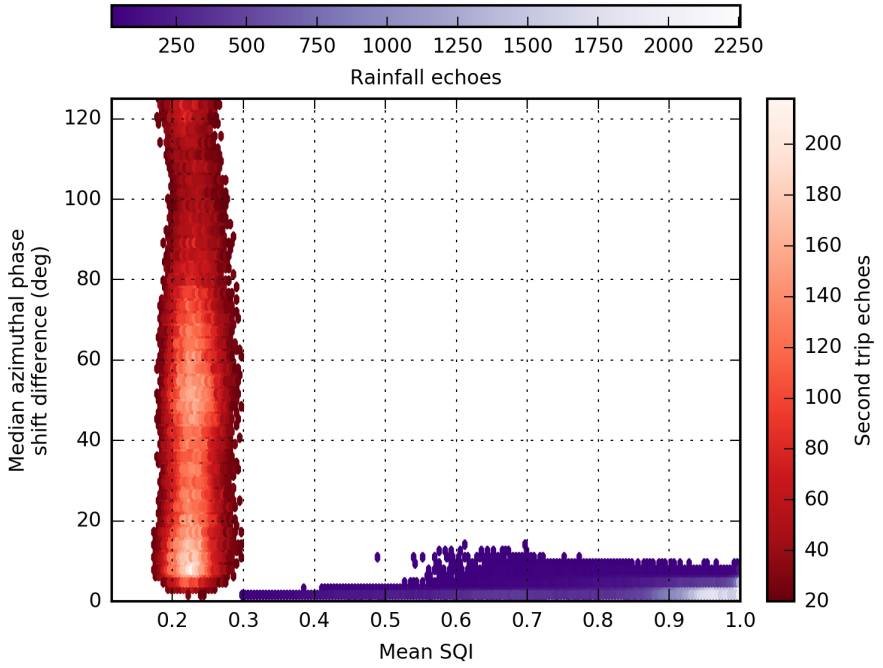

FIGURE 5.10: Two moment heat maps, indicating the number of observations identified that fall within the given hexagonal bins. Identified rainfall echoes are indicated with the purple colour scaling, while second trip echoes are shown with the red colour scale. A hexagonal bin is only coloured if it contains at least 20 observations, which is less than 0.01% of the total observations in each category. The observations are from the same events shown in Figure 5.1 for precipitation and Figure 5.7 for second trip echoes.

To assess the merits of each filtering approach the 111 volume scans taken on the 17 Aug 2013 were processed using both filters. The 17 August was chosen as it has a significant number of second trip echoes, located across a range of azimuths at varying intensities. Figure 5.11 shows the impact of applying the filter to the number of echoes observed as a percentage of the total number of scans at 0.5° elevation. The raw data shows the alternating pattern also seen in Figure 4.5, where the second trip echoes are visible in every other radial due to the staggered PRF. Application of the simple threshold filter removes this affect, suggesting it is successfully removing second trip echoes and the variable filter also successfully removes the affect. The difference between the two

filtering options is that the variable filter is more aggressive, removing more echoes as second trip signals in comparison to the simpler option, removing 1-2% more echoes on average. Analysis of the data using animated comparisons suggests this aggressive filtering is robust and indicated much better performance of the variable filter compared to the simple filter in turbulent conditions.

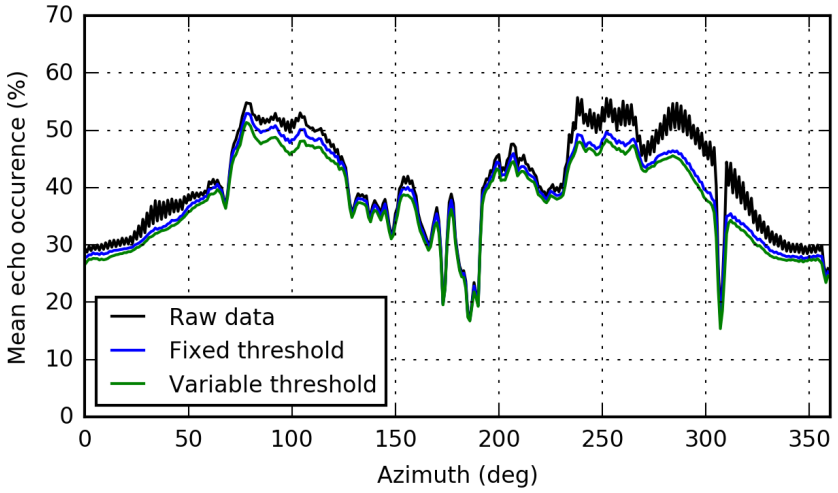

FIGURE 5.11: Azimuthal variation of mean echo occurrence within a radial on the 17 August 2013. Solid black line shows the echo occurrence for the raw reflectivity data, the blue line shows the impact of using a single value threshold filter of 0.3 and the green line indicates the echo occurrence for the variable filter shown in equation 5.4.

Figure 5.12 shows an example of the two filtering options, compared to the raw data, from a single elevation scan (2013-08-17 09:48 UTC, 0.5° elevation). In this example both filters are successfully removing the second trip echoes occurring to the north east of the radar, with the variable filter being more aggressive in its filtering of the interlaced first and second trip echoes at about 30 km range. The variable filter also removes some of the ground clutter signals resulting from Dartmoor due east of the radar, which is a primary reason for the differences in echo occurrence percentages between the two filters seen between 75° and 120° in Figure 5.11. The main difference between the two filtering options occurs to the north west of the radar, at around 40 km range, where the simple filter is removing a large region of reflectivity which shows no visible indication it is a second trip echo (using reflectivity and the other available radar moments). The variable filter does not remove this region as it has a low $\delta\Phi$, which results in a lower $\mathrm{SQI}_{\mathrm{thr}}$ being applied in this region. Further investigation reveals this area to have unusually low SQI values for

first trip echoes, which are coincident with a zone of convergence indicated in the Doppler wind field and in the Doppler spectral width. These observations are consistent with the presence of a warm front indicated on UKMO analysis charts which passes through this area at this time. This signature and the associated removal of first trip echoes by the simple filter can be seen in the preceding and following volume scans. Dixon and Hubbert (2012) indicate this potential issue with SQI in turbulent areas, only suggesting that elevated spectral width may help in moderating the threshold used, although this is also susceptible to increase in areas of noise and second trip echoes, indicating the two moments are not mutually exclusive. It is noticeable that the introduction of $\delta\Phi$ to the filter (Fig. 5.12, panel C) greatly reduces this erroneous filtering, and strongly supports the use of the two moment variable filter for the removal of second trip echoes.

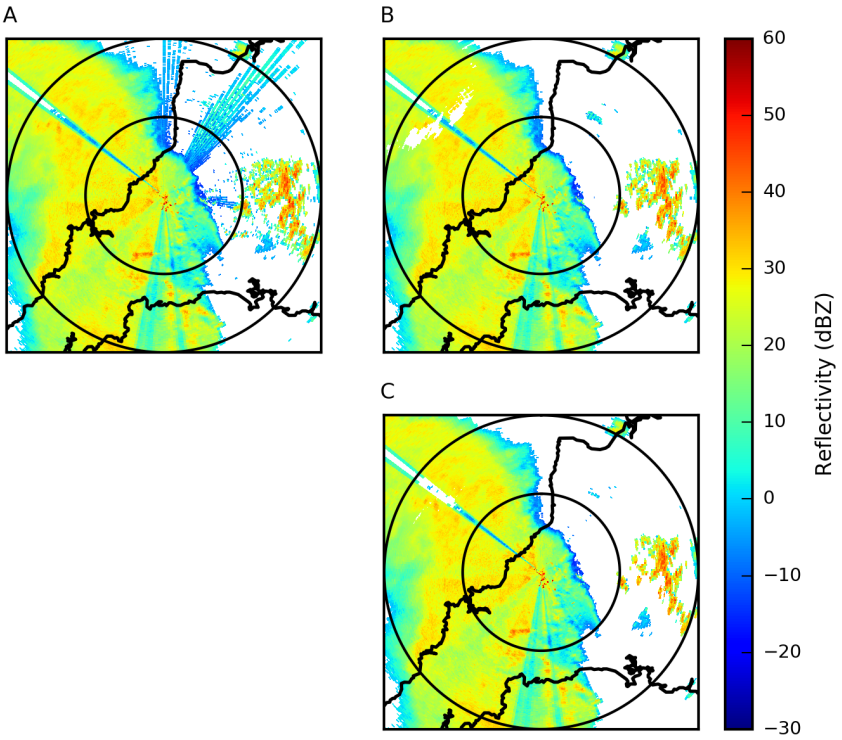

FIGURE 5.12: Error in simple second trip filter due to turbulent mixing as a result of frontal convergence. Data shown is the 0.5° elevation angle reflectivity data from 2013-08-17 09:48 UTC in raw form (A), after the application of the simple filter (B) and after application of the variable filter (C). Range rings shown at 25 km and 50 km from the radar.

5.2.3 Second trip echoes - concluding remarks

Section 5.2 has shown that second trip echoes can be identified and filtered using the radar moments available from the mobile X-band radar as operated during COPE. The most effective filtering was achieved using a combination of space averaged normalised coherent power (SQI) and the median azimuthal difference in phase shift ($\delta\Phi$) due to a staggered PRF, which were combined to produce a variable SQI threshold using equation 5.4, derived from empirical analysis of the distribution of both second trip and rainfall echoes. This variable threshold filter has been applied to the entire COPE dataset and the filtered reflectivity obtained using this filter will be used in all further processing steps. The impact of the filter on echo occurrence percentages is shown in Figure 5.13. The filtering process successfully removes the staggered echo occurrences most visible to the north west and north east in the raw data shown in panel A, while also partially filtering the ground clutter echoes to the north east and east of the radar, which is an unexpected benefit of the filtering process. However the filtering does not sufficiently remove these non meteorological echoes, and a dedicated approach to filtering these echoes is required to provide a more accurate rainfall product from the data. The following section describes the filter used to remove these non meteorological echoes as the final stage of the initial radar quality control process.

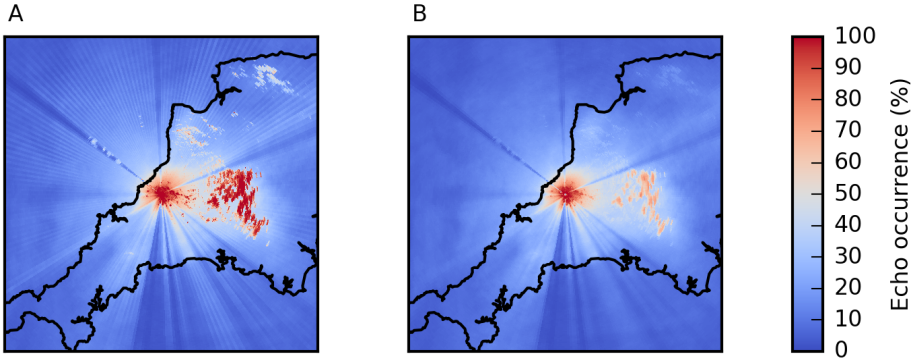

FIGURE 5.13: Echo occurrence percentages at 0.5° elevation angle for the 1075 COPE files which meet the standard scan parameters and contain all dual polarisation variables. A shows the percentage for raw reflectivity data, while B shows the percentage after removal of second trip echoes with the variable filter.

5.3 Identifying non meteorological returns using fuzzy logic

The ability of polarimetric radars to provide distinctive signatures for differing echo types, as already demonstrated for rainfall and second trip rainfall echoes in sections 5.1 and 5.2.1 respectively, has led to the widespread development of dynamic filtering and identification algorithms based on machine learning / artificial intelligence techniques. These include the use of decision trees, neural networks, Bayesian classification and fuzzy logic classification (Berenguer et al., 2006; Lakshmanan et al., 2007; Chandrasekar et al., 2013). The following section describes the implementation of a fuzzy logic identification scheme, which is highly adaptable, and has been implemented in this case to focus on identifying echoes at low elevation angles for the purpose of accurate rainfall estimation, particularly the need to remove the non meteorological echoes already identified in the data (Chapter 4).

5.3.1 Fuzzy logic and weather radars

Fuzzy logic schemes are a popular tool for the classification of weather radar echoes, be that the filtering of spurious echoes (Gourley et al., 2007; Rico-Ramirez and Cluckie, 2008, for example) or for the identification of different hydrometeors (Dolan and Rutledge, 2009; Park et al., 2009). These schemes all rely on the basic principles of fuzzy logic (Zadeh, 1983), but take different approaches to the variables, classifications and post processing used.

Gourley et al. (2007), for example, limit the fuzzy classifier to three fields (texture of specific differential phase ($\sigma(\Phi_{\mathrm{DP}})$), texture of differential reflectivity ($\sigma(Z_{\mathrm{DR}})$) and cross-correlation coefficient (ρ_{HV})), using probability density functions to define their sets. They then apply post-fuzzy reclassification based on an additional 3 fields (velocity, reflectivity and Φ_{DP}). Their scheme successfully identifies non-precipitating echoes in a range of cases. In contrast, Dolan and Rutledge (2009) use five fields, including temperature, to define their one dimensional beta functions for hydrometeor classification. In this way, fuzzy logic presents a highly adaptable framework, the advantage of which is the ability to use the increasing number of moments available from dual polarisation weather radars to produce dynamic filters. These schemes are highly adaptable and can be trained with a limited volume of both empirical and simulated data, which allows rapid

implementation in the field or application to limited datasets. The non-meteorological echo classification filter developed for the NCAS radar is based on fuzzy logic as a result of these characteristics, allowing continuing development and improvements as new field campaigns provide different requirements for the filter.

The scheme uses novel radial texture parameters of reflectivity, differential reflectivity and correlation coefficient, which are corrected for range effects, in combination with standard dual polarisation moments and beam height to identify and remove spurious echoes. The scheme has been developed and then tested using data from COPE, with some additional verification achieved using data from the Burn testing site. The filter uses empirically derived membership functions of variable form, based on human classification of the radar data using ground observations and previous studies' dual polarisation signatures. These functions were derived using a similar approach to the method used in Section 5.1 for identifying dual polarisation signatures of rainfall. Although the filter results presented here are for reprocessed data, the scheme was designed to compute classifications in near real time, allowing filtering of echoes during future radar deployments. The code has also been developed to allow the addition of more echo classes in the future, allowing additional hydrometeor types to be added to the identification process in the future.

The following sections will describe the fuzzy filtering methodology in detail, including the polarimetric signatures of ground clutter and insects, the development of linear texture fields, the derivation of the empirical membership functions used, the combination of these functions using fuzzy logic, additional post filtering radar processing and finally present examples of the fuzzy filter applied to test cases from both COPE and a testing deployment at Burn airfield.

5.3.2 The expected dual polarisation signature of non-meteorological echoes

The commonly available dual polarisation parameters have been widely studied in relation to non meteorological echoes, for example Mueller and Larkin made the first dual polarisation observations of insects in 1985, using the S-band CHILL radar, with numerous studies following that (Zrnić and Ryzhkov, 1998; Chilson et al., 2012, for example),

while Zrnić and Ryzhkov (1998, 1999) have made several notable dual polarisation observations of ground clutter, which have been supported by the results from additional filtering studies. The following sections summarise these results, to inform identification of these non meteorological echoes.

5.3.2.1 Ground clutter

Ground clutter returns have no obvious Z_{DR} signature, being broadly distributed through a range of values, with an average value of 0 dB (reported in Zrnić and Ryzhkov, 1999; Zrnić et al., 2006, for example). They are also known to have widely distributed correlation coefficients ranging from very low to moderately high values (0.2-0.95). Filtering studies typically take advantage of known locations of ground clutter, or the widely varying texture of the dual polarisation fields, rather than the absolute values observed (Gourley et al., 2007; Rico-Ramirez and Cluckie, 2008; Hubbert et al., 2009).

5.3.2.2 Insects

Single polarisation observations have successfully attributed some clear air radar echoes to both insect and bird targets, with insects having relatively low reflectivity values (Plank, 1956; Harper, 1958). The dual polarisation attributes of these returns were first observed using the S-band CHILL radar by Mueller and Larkin (1985). These observations show Z_{DR} to be a function of insect orientation, ranging from 0.5 dB if the insects are aligned radially (head-on/tail-on) to the radar, increasing to 5 dB when viewed azimuthally (broadside) to the radar. More recent studies have confirmed these results with a range of radar systems, with the typical reported insect Z_{DR} range being 2 dB to 9 dB depending on orientation (Zrnić and Ryzhkov, 1998; Chilson et al., 2012). However Melnikov et al. (2015) indicate that this variation may in fact be a result of depolarisation associated with simultaneous transmit and receive radars. Correlation coefficients are also known to be asymmetric for insects, and range from very low values (0.2) to moderately high (around 0.8). There is no distinct differential phase shift associated with insects, due to their low number concentrations, although they again show azimuthal variation of total phase shift as a result of potential depolarisation effects. In comparison to rainfall the

combination of lower correlation coefficients with higher Z_{DR} and low reflectivity allows a probable distinction to be made, allowing for filtering of these returns.

5.3.2.3 Noise and clear air returns

Radars often observe echoes from clear air, which can not be attributed to precipitation or biotic scatterers. These clear air echoes are attributed to changes in the refractive index of the atmosphere (Wilson et al., 1994; Lane, 1969), and are most often observed close to the radar where the absolute received power is greater. In addition to these echoes, the atmosphere typically has a background radiation signature which can sometimes be visible, depending on the noise filtering active on the radar instrument. These echoes are typically of very low reflectivity (>0 dBZ), especially at X-band. Though there are few observational studies of non biological clear air echoes and background noise with dual polarisation radar, Dixon and Hubbert (2012) showed that noise can be identified as it has a high radial texture of phase shift (in their case a standard deviation greater than 45°) and also a low normalised coherent power (below 0.15).

5.3.3 Identifying polarimetric signatures empirically

Fuzzy logic requires membership functions to be defined for each echo type to be classified. These membership functions define the radar signature of the echoes, with each radar parameter requiring its own separate function. The parameters used for classification in the following scheme are shown in Table 5.1. As previously mentioned texture fields have been computed to improve the classification scheme, in addition to the use of standard radar moments. It is first necessary to introduce these texture fields, and their calculation before showing the empirical radar signatures developed which use both standard radar moments and these new texture parameters. These empirical signatures were derived using examples of typical spurious echoes, identified using inspection, and manual classification, of the polar data, cross-checked with field observations and the expected radar signatures outlined above.

Parameter	Shorthand	Units
Uncorrected horizontal radar reflectivity	dBuZ	dBZ
Texture of horizontal radar reflectivity	$\sigma(Z)$	dBZ
Differential radar reflectivity between h&v	Z_{DR}	dB
Texture of differential radar reflectivity	$\sigma(Z_{DR})$	dB
Cross polar correlation coefficient	ρ_{HV}	–
Texture of cross polar correlation coefficient	$\sigma(\rho_{HV})$	–
Texture of differential phase shift between h&v	$\sigma(\Psi_{DP})$	∘
Height of radar beam centre above sea level	H	metres

TABLE 5.1: Radar parameters used in the classification scheme, as seen in Dufton and Collier (2015).

5.3.3.1 Radial texture parameters

Texture parameters are frequently used in fuzzy logic classification schemes, particularly for the removal of spurious echoes. The majority of texture fields derived use a 3×3 (range gates by azimuth sector) or larger moving window (Chandrasekar et al., 2013), and compute either the standard deviation or root mean square difference within this window to obtain texture. Texture parameters for the present classification are defined using a radial window of 7 range gates length by 1 azimuth step width producing a one degree by one kilometre moving window. The standard deviation for this window then defines the texture for the central point (Eq. 5.5). A similar window has been shown to be successful by Cho et al. (2006), who used the parameter for 1 km classifications. This method of calculating texture parameters was chosen to retain the finer resolution of the radar observations, allowing further processing at maximum polar resolution. The linear method is also computationally faster than a moving window which includes multiple azimuths and as such is advantageous for real time processing applications. Simple side by side comparisons show that a linear window gives comparable texture fields to using a multi azimuth moving window, while more detailed analysis shows that the differences between the fields are insignificant when computing membership functions. Figure 5.14 shows ground clutter histograms of two texture fields, computed using a radial window (1×7) and a multi azimuth window (3×3), with the histograms overlapping by 87% and 92% for correlation coefficient and phase shift respectively.

$$\sigma(x_r) = \sqrt{\frac{1}{N-1}\sum_{i=-(N-1)/2}^{(N-1)/2}(x_{r+i} - \overline{x})^2} \tag{5.5}$$

As many other radar error sources operate along the radials of the collected data (partial beam blockage for example), the use of this radial window also prevents these effects influencing the surrounding data.

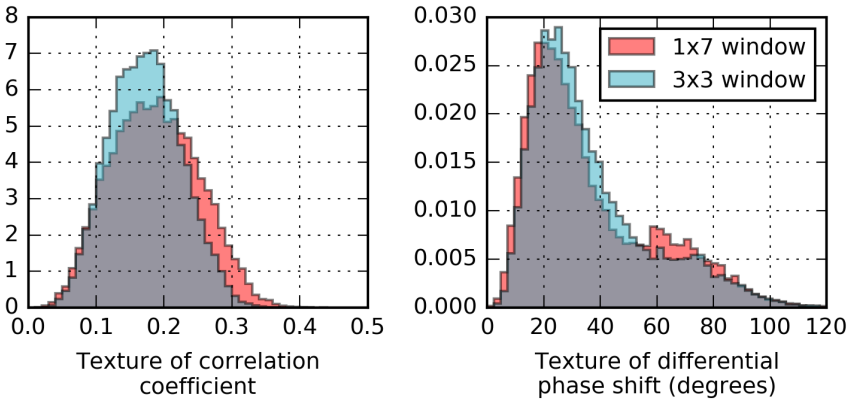

FIGURE 5.14: Texture histograms for correlation coefficient (left) and differential phase shift (right) taken from 13 radar scans from the 17 August 2013, from 10:06:04 UTC to 11:23:05 UTC. The radial windows are shown in red, while the square windows are shown in blue, the overlapping section of these methods is shown in grey. Histograms were computed for ground clutter echoes identified using a ground clutter mask. Details of the mask can be found in section 5.3.3.3.

As previously noted by Gourley et al. (2007), texture parameters exhibit a range dependent structure as a result of increasing sample volume due to beam spreading. To allow the universal application of derived membership functions it is necessary to correct for this range dependent behaviour. The linear textures used for this classification are shown to exhibit the same range dependent variation, and correction has been achieved by inverting a third order polynomial fitted to the range average texture over a period of 12 scans from the 17 August 2013. This date was chosen as radiosonde soundings place the zero degree isotherm at 4 km elevation, reducing the chances of mixed phase echoes biasing the range averaged texture of the lowest elevation scan. The polynomial is then used as a multiplicative correction factor beyond a fixed range of 25 km for $\sigma(Z_{\mathrm{DR}})$ and

$\sigma(\Psi_{DP})$ and 45 km for $\sigma(\rho_{HV})$. Figure 5.15 shows an example of range corrected texture of differential reflectivity, including the correction polynomial. The corrected signal clearly shows the variability within the texture field, while the range dependent increase in texture has been removed when compared to the original signal, making comparisons between echoes at differing ranges possible.

5.3.3.2 The texture field signatures of rainfall

To fully utilise the radial texture fields in a classification scheme it was necessary to create their signatures for rainfall to compare with those from non meteorological echoes. These new signatures were added to the dual polarisation rainfall signatures already characterised in section 5.1 to create a complete picture of the expected dual polarisation rainfall signature for the NCAS X-band radar. Using the same rainfall echoes as those identified in section 5.1 histograms and normalised kernel density estimates were constructed for the textures of horizontal reflectivity, differential reflectivity, correlation coefficient and differential phase shift and are shown in Figure 5.16. The skewed, peaked distributions shown indicate rainfall echoes typically have low texture values indicative of low variability within the rainfall field, which is a valuable signature when compared to the distributions found for non meteorological echoes as described in the following sections and shown in Figure 5.17.

5.3.3.3 Empirical ground clutter signature

Normal propagation condition ground clutter is the easiest spurious echo to identify, especially once a reference period of radar data is available, like the results presented in Chapter 4. Statistical analysis of multiple radar scans easily identifies range gates affected by ground clutter. In this case a mask was created to extract clutter signals, defining clutter stringently using two measures. The first measure is the echo occurrence percentage across the campaign, taken to be greater than 95% for clutter, the second being the total reflectivity summation during the campaign, where values exceeding the mean total plus three standard deviations were taken to be clutter (a summation threshold of 9516 dBZ). This method identified 1408 range gates which are highly likely to contain

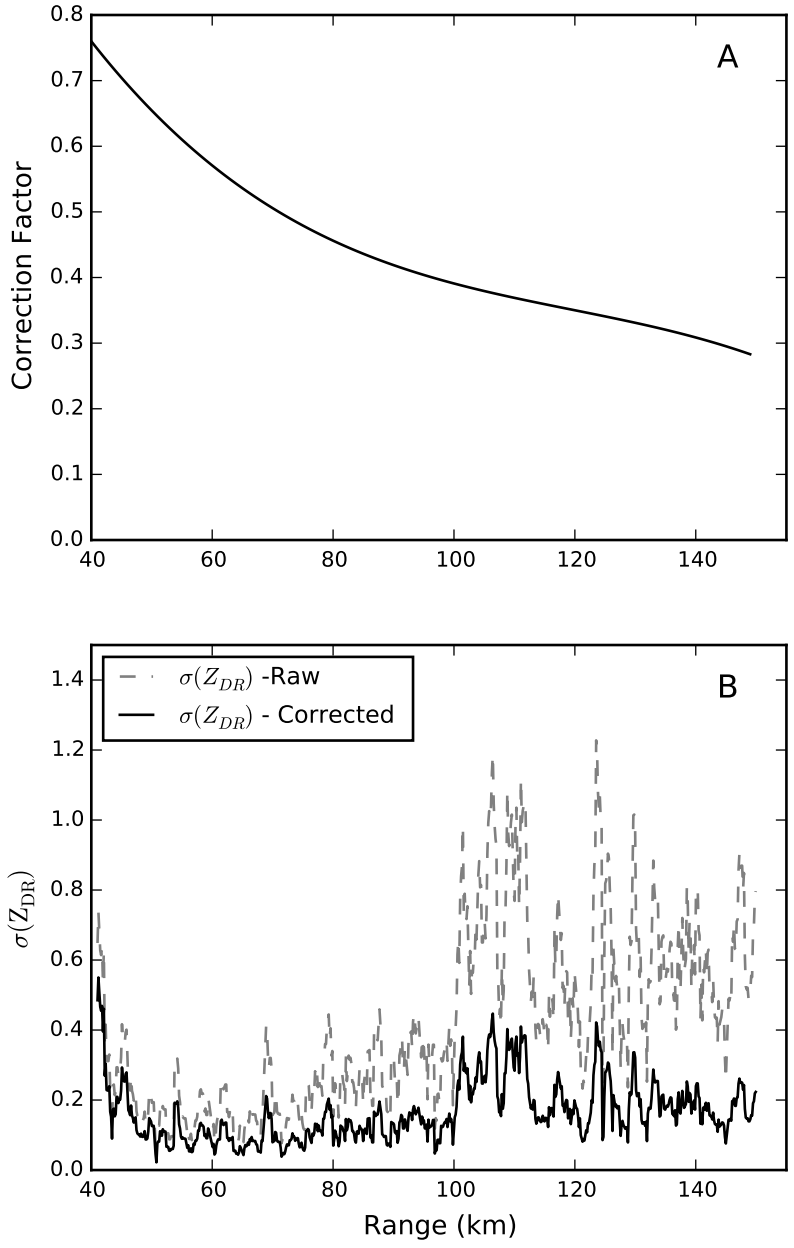

FIGURE 5.15: A. Multiplicative correction factor used to correct differential reflectivity texture. B. Range variance of $\sigma(Z_{DR})$ along the 281° azimuth for the 09:11:04 2013-08-17 volume scan at 0.5° elevation, Davidstow deployment site. Dashed line is before correction and solid line is corrected texture as used in the fuzzy logic classifier. Figure is redrawn from Dufton and Collier (2015).

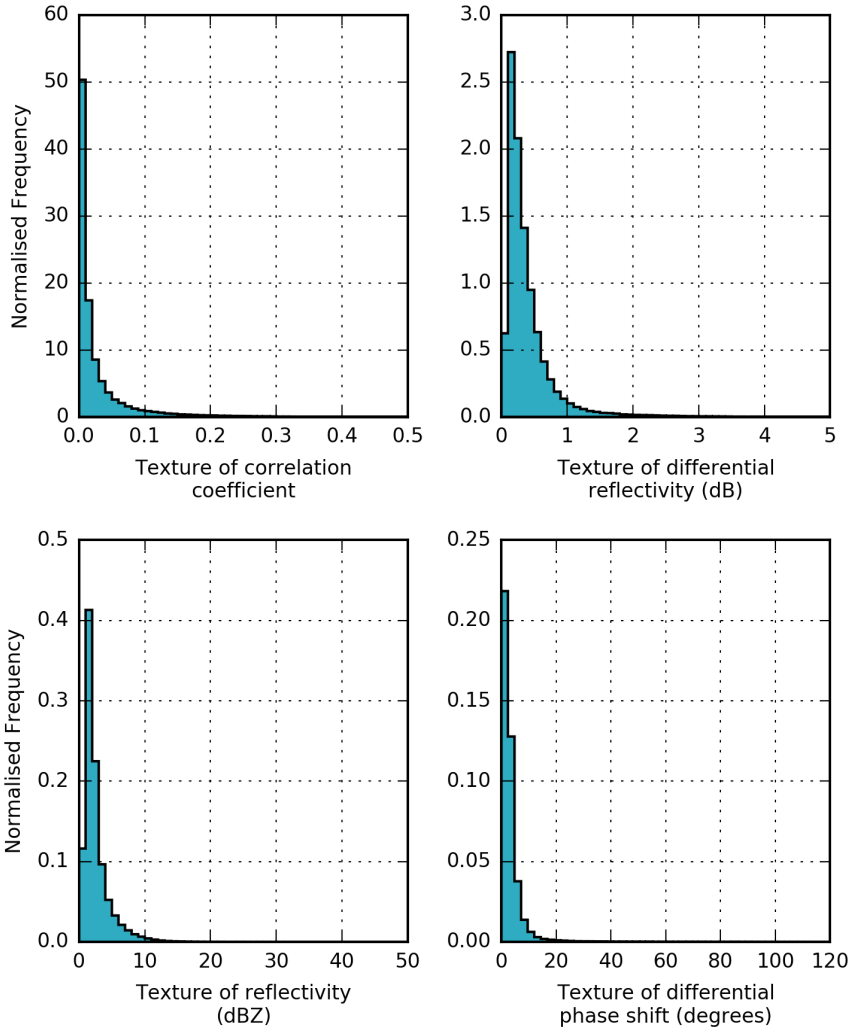

FIGURE 5.16: Histograms of calculated texture of correlation coefficient, differential reflectivity, horizontal reflectivity and differential phase shift for rainfall echoes. The observations are from the same echoes used in Figure 5.1 for conventional radar moments.

ground clutter, which were then cross checked against topographic mapping. This statistical mask was then applied to 26 radar scans from the 18th July 2013 (dry day, 13 scans) and 17th August 2013 (stratiform rainfall, 13 scans) to produce histograms and normalised kernel density estimates (KDEs) for the classification parameters, a selection of which are shown in Figure 5.17. Greatest discrimination between ground clutter and precipitation was found in the texture fields, particularly $\sigma(\rho_{HV})$. It is worth noting that ρ_{HV} values extend across a wide range and overlap with precipitation, although not as much as in previous studies such as Zrnić et al. (2006). This difference is down to the shorter wavelength and faster antenna speed used during the COPE campaign, which

reduces the expected cross correlation of ground clutter returns.

5.3.3.4 Empirical insect signature

The presence of biological scatters within weather radar echoes is difficult to independently verify, yet research has indicated a typical echo signature can be observed (see section 5.3.2.2). To recap, insect echoes typically have low reflectivity (0-15dBZ), high Z_{DR} (>3dB) and low ρ_{HV} (0.3-0.6). Manual classification indicates a potential large concentration of insect returns on the 18th July 2013 which was a warm day with morning temperatures in excess of 24°C, a moderate onshore breeze and rainfall restricted to isolated locations in the afternoon. Using 13 scans insect signature histograms and unit normalised KDEs were again constructed (Figure 5.17, dash-dot lines). The Z_{DR} observations show a bimodal distribution above 4dB, which could be attributed to the two preferred orientations of insect flight. The ρ_{HV} signature from these observations lies between 0.7 and 1, higher than previously shown by most other studies. This may be indicative of a highly uniform insect population, which exhibits little variation given the short dwell time of the radar scan strategy. A similarly high region of ρ_{HV} was detected by Bachmann and Zrnić (2007) when distinguishing between insect and bird echoes. The observed texture parameters lie between those of precipitation and ground clutter, with the exception of reflectivity texture which has a peaked signature of less than 3dBZ.

5.3.3.5 Empirical noise signature

The X-band radar used in this study uses a passive scan to set a zero level for environmental noise, repeated at regular intervals. At times environmental conditions change such that the noise level increases in this intermittent period causing an abundance of low reflectivity echoes within the radar observations. The introduction of the second trip echo filter described in section 5.2 has removed the majority of this low level echo breakthrough as the noise echoes have a low normalised coherent power, similar to second trip echoes. Even so, it was straightforward to identify these echoes when they occurred in the raw reflectivity and generate a classification set for them, to allow for the filtering of any noise echoes that did pass through the second trip filter. Histograms for noise have been omitted from Figure 5.17 for clarity but those computed showed noise echoes have

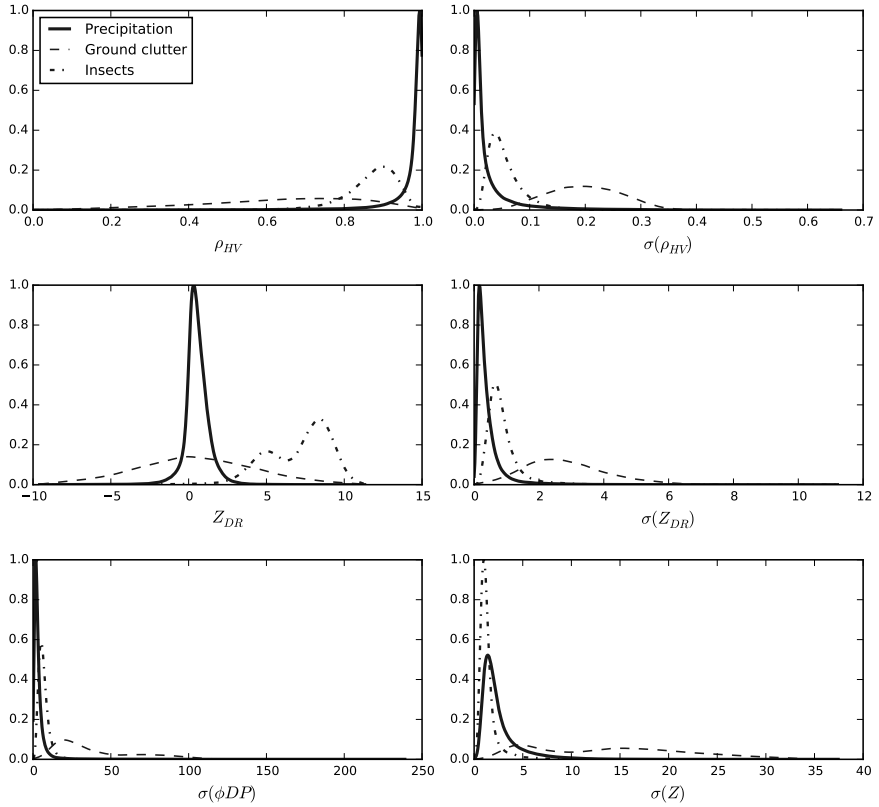

FIGURE 5.17: Normalised kernel density estimates for a sample of the dual-polarisation and texture parameters used in this study. Classes are precipitation (solid line), ground clutter (dashed line) and insects (dash-dot line). Derived from expert analysis of radar data from the COPE campaign. Figure is redrawn from Dufton and Collier (2015).

very low texture of reflectivity (<1 dBZ) and low cross correlation coefficient (<0.7), yet a very high texture of differential phase shift (>30°).

5.3.4 Fuzzy logic membership filtering

Having defined the parameter ranges of the desired filtering classes, a filtering scheme has been implemented which uses fuzzy logic to combine the available parameters, allowing classification of the radar echoes. Firstly the empirical signatures identified above were simplified into membership functions for each class and parameter, using a variable vertex method. These membership functions were then applied to the available radar moments to generate individual parameter scores, which are combined to calculate a single fractional membership score for each echo class. Defuzzification of the fractional totals is achieved by selecting the class with the maximum fractional score provided a certainty

threshold has been crossed. Once identified, meteorological echoes are then retained by the filter and despeckled to remove isolated range gates that passed through the filter. This filter has been applied to the COPE field dataset and testing data from Burn airfield, examples from which are shown in section 5.3.5. The process can be run in near real time, taking less than 30 s per radar volume (10 elevation scans), making it suitable for real-time application in future field deployments.

5.3.4.1 Variable vertex membership functions

Typical fuzzy logic membership functions are often triangular and trapezoid in shape or defined by a centrally peaked decaying function. In the present work a variable vertex membership scheme has been implemented, which allowed variation of the membership functions' form for different parameters and classes. Between vertices linear interpolation was used to define the membership function. The minimum number of vertices required for the function to operate is 2, defining the parameters' limits (x_0 and x_n) and the membership score at those limits (y_0 and y_n). Outside of these limits the membership score is always zero. An example of this approach is shown in Fig. 5.18. The approach allows greater flexibility in the membership functions than the use of a fixed shape for membership functions, and incorporates parameter weighting in the individual scores themselves.

Each of the empirical radar signatures derived in the previous section were then simplified to a multiple vertex function, which approximated the shape of the distribution around its peak. During the analysis it was found that using equally weighted membership functions (maximum score of 1) was no less effective than using variable weighting optimised with a genetic algorithm. Ultimately the most parsimonious set of variables was chosen for each class. This was tested using a validation set of problem cases, where identification was deemed to be challenging, including rainfall signals mixed with wind farm ground clutter and convection embedded within probable insect returns.

For each of the four echo classes (precipitation, ground clutter, insects and noise) a limiting set of observations was identified, for example in the case of noise it was simply that the reflectivity would be below 5 dBZ and in the case of ground clutter it was a combination of reflectivity being greater than 10 dBZ and the altitude of the radar

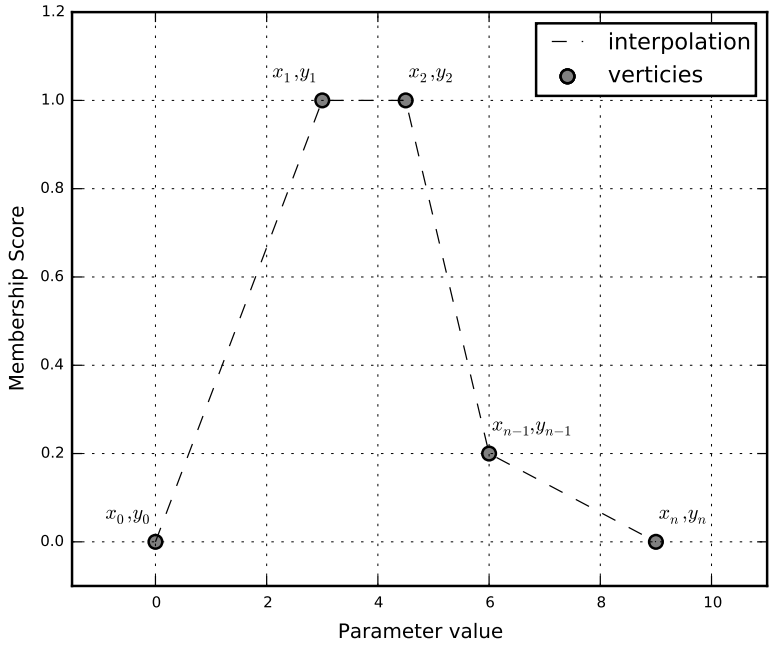

FIGURE 5.18: Example of the multiple vertex membership function approach, with vertices in the range 0 to n. Grey points represent vertices defining the membership function, with the dashed line indicating the interpolation between those points. Figure is redrawn from Dufton and Collier (2015).

return being below 2000 m. This allowed these limits to be incorporated into the fuzzy combination process as described in the next section, removing the need for a secondary re-classification stage as found in some fuzzy logic radar filters (Gourley et al., 2007, for example).

All the membership vertices derived for the fuzzy classifier are shown in tables 5.2–5.5, with the limiting parameters being shown at the end of each table.

TABLE 5.2: Precipitation membership functions, reproduced from Dufton and Collier (2015).

Parameter	Parameter vertices	Membership vertices
$\sigma(\mathrm{Z_{DR}})$	0, 1, 5	1, 0.1, 0
ρ_{HV}	0.9, 0.94, 0.98, 1.0	0, 0.4, 1, 1
$\sigma(\rho_{HV})$	0, 0.05, 0.1	1, 0.1, 0
$\sigma(\Psi DP)$	0, 6, 20	1, 0.2, 0
dBuZ	-11,-10, 100, 101	0, 1, 1, 0

Table 5.3: Ground clutter membership functions, reproduced from Dufton and Collier (2015).

Parameter	Parameter vertices	Membership vertices
$\sigma(Z)$	0, 5, 15, 40, 50	0, 0.6, 1, 1, 0
$\sigma(\mathrm{Z_{DR}})$	0, 1, 3, 10	0, 0.1, 1, 1
ρ_{HV}	0, 0.4, 0.7, 1	0, 1, 1, 0
$\sigma(\rho_{HV})$	0.05, 0.2, 0.4	0, 1, 0
$\sigma(\Psi DP)$	0, 20, 50, 100, 120	0, 1, 0.8, 0.8, 1
dBuZ	-50, 10, 20, 200	0, 0, 1, 1
H	0, 1000, 2000	1, 1, 0

Table 5.4: Noise membership functions, reproduced from Dufton and Collier (2015).

Parameter	Parameter vertices	Membership vertices
$\sigma(Z)$	0, 0.5, 1, 2	1, 0.8, 0.1, 0
ρ_{HV}	0, 0.6, 0.7, 1	1, 0.75, 0, 0
$\sigma(\Psi DP)$	0, 15, 30, 100	0, 0.1, 1, 1
dBuZ	-30, 5, 10, 200	1, 1, 0, 0

Table 5.5: Insect membership functions, reproduced from Dufton and Collier (2015).

Parameter	Parameter vertices	Membership vertices
$\sigma(Z)$	0, 1, 2, 5	0.4, 1, 0.2, 0
$\sigma(\mathrm{Z_{DR}})$	0, 1, 2	0, 1, 0
ρ_{HV}	0.6, 0.8, 0.89, 1	0, 0.5, 1, 0
$\sigma(\rho_{HV})$	0, 0.05, 0.1	0, 1, 0
$\sigma(\Psi DP)$	0, 8, 20	0, 1, 0
dBuZ	-11,-10, 20, 21	0, 1, 1, 0
$\mathrm{Z_{DR}}$	0, 2, 4, 20	0, 0, 1, 1

5.3.4.2 Combination and defuzzification

To calculate an overall membership score for each echo it was necessary to define a method of combining the individual membership functions specified above. The method used was a combination of additive and multiplicative elements to allow the limit control discussed above, leading to the total fuzzy membership score for each class ($F(x)$) being calculated using Eq. 5.6.

$$F(x) = F(x)_K \times F(x)_J \tag{5.6}$$

where

$$F(x)_J = \sum_{j \in J} M(x)_j \tag{5.7}$$

and

$$F(x)_K = \prod_{k \in K} M(x)_k \tag{5.8}$$

The process requires individual membership scores ($M(x)$) for each parameter to be calculated using the defined variable vertex membership functions. Those parameters which form the additive group (J) then have their totals summed to calculate the additive total ($F(x)_J$). Those parameters in the multiplicative threshold switch set (K) conversely have their totals multiplied together to calculate their total ($F(x)_K$). These two totals are then multiplied together to calculate the final class score ($F(x)$). The multiplicative threshold parameters are used to suppress certain classifications based on observational constraints, as discussed in the preceding section. The total score($F(x)$) is then converted to a fraction of the maximum possible score obtainable for that class. Classification is assigned to the class with the highest fractional score, provided the fractional score exceeds a predetermined certainty threshold. Using the complex validation cases mentioned

above this threshold was set to 0.25, using a critical success index to find the optimal balance between false alarms and probability of detecting echoes. Threshold exceedance prevents uncertain range gates from being classified based on very low total class scores, instead marking these cells as unknown echo type. Once echo classification is complete, the new classification field is used for filtering of the radar data. In the examples presented in section 5.3.5, the filter has been set to pass through only echoes identified as precipitation, though the inverse is also possible depending on the final application of the data.

5.3.4.3 De-speckling using connected component analysis

To further process the resulting rainfall field a de-speckling procedure has been introduced to remove isolated range gates which pass through the filter. The de-speckling applies connected component analysis (with 8 connectivity) (Dillencourt et al., 1992), to determine the independently connected areas of rainfall within the radar scan. Once identified those regions smaller than 5 range gates in size are removed. This approach removes regions that are unlikely to be precipitating rain cells due to their small size (no more than 1.6 km^2 at the extreme limit of the radar and no more than 0.7 km^2 within 50 km of the radar). This is similar to the nearest neighbour count approach used in other classification schemes, but has the advantages of retaining connectivity on the edge of large cells and of not reclassifying range gates surrounded by a different classification, which can be a reasonable outcome in the case of point target clutter for example. The de-speckling only applies to the classified fields, and not to the classification itself, which is retained for future analysis. This process is the final stage in the quality control procedure developed for the NCAS radar as deployed during the COPE field campaign. The following section presents examples of the quality control process in action for individual radar scans, along with an overview of its impact on the campaign data as a whole using the statistics first shown in Chapter 4.

5.3.5 Examples of the application of the fuzzy classifier

The fuzzy classifier has been applied retrospectively as a rainfall filter to all the data collected during the COPE field campaign, and has also been applied to subsequent

deployments of the radar at the Burn field site. The following examples show its benefits for both qualitative and quantitative analysis of the radar data, using individual case studies from COPE and Burn and also longer term, cumulative analysis of the COPE dataset. These examples show the filters impact in different situations and draw attention to both its benefits and limitations, which are summarised in the concluding remarks of this chapter.

5.3.5.1 Example 1: Convection embedded within biological scatterers

The first example presented here is from the 18 July 2013. With daytime temperatures in excess of 20° C driving an onshore sea breeze, convective showers eventually developed during the afternoon, breaking through a stable boundary layer. Rain gauges observed only two isolated events during the day, with accumulations of 0.2 mm recorded at two gauges.

Panel A in Figure 5.19 shows a snapshot of these isolated convective showers, two to the north east and one to the south of the radar, embedded within a strong clear air signal prevalent across the radar sweep. The application of the fuzzy classifier identifies the three convective showers, using the parameters shown in Fig. 5.20, while also identifying ground clutter signals from Dartmoor to the east and local topography around the radar.

By passing through only the precipitation echoes identified by the fuzzy classifier a much clearer picture of the convective showers is available, as shown in Fig. 5.19c. From Fig. 5.20 it is clear that the cells are identifiable in all of the parameters shown, with the textures of Ψ_{DP} and ρ_{HV} being particularly indicative. These convective cells extended up to ten kilometres in altitude, with reflectivity in excess of 50 dBZ and differential reflectivity over 6 dB in the cores, indicating very large rain drops in places. It should be noted that the fringes of these cells are generally unclassified by the filter due to the certainty threshold, which is due to a combination of elevated linear textures at the margins of strong convective cells and also low reflectivity. Although identifiable by eye, the non classification of these range gates is negligible for radar QPE, as the reflectivity values removed relate to inconsequential, near-zero, rainfall intensities.

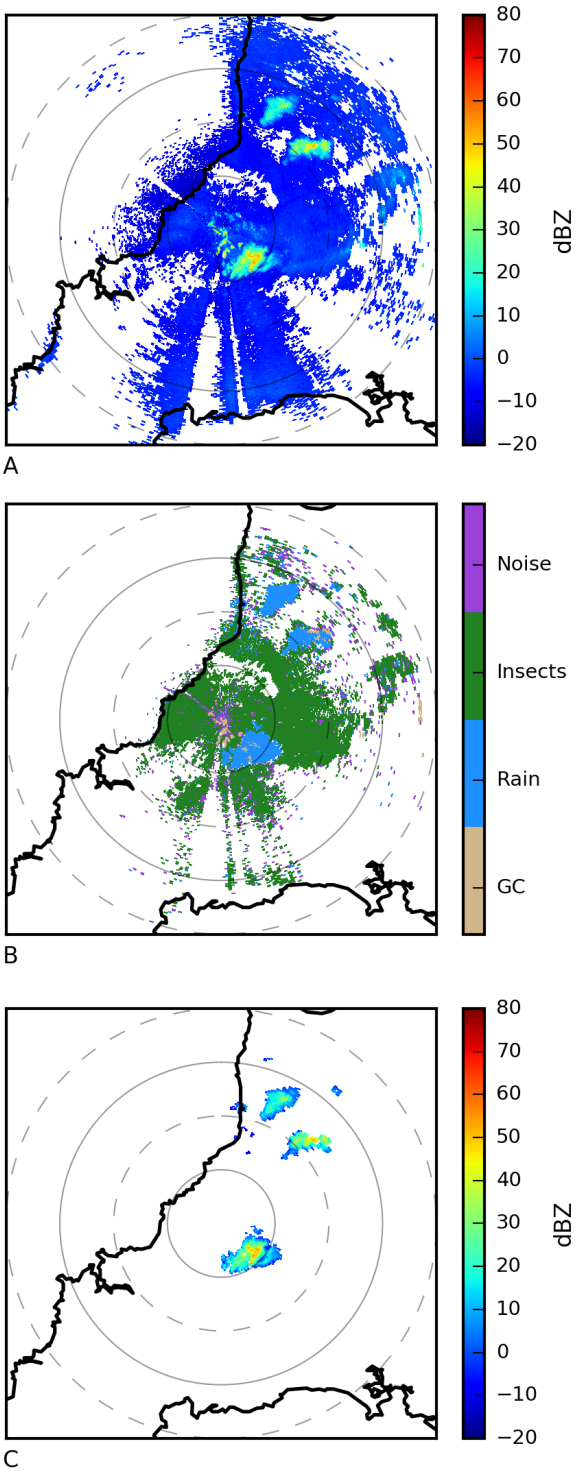

FIGURE 5.19: Application of fuzzy logic classifier to 0.5° elevation scan, 18 July 2013, 14:15 UTC. **A** shows the horizontal reflectivity following second trip filtering, **B** the results of applying the fuzzy classifier and **C** the filtered reflectivity from those echoes identified as rainfall. Range rings are at 10 km intervals.

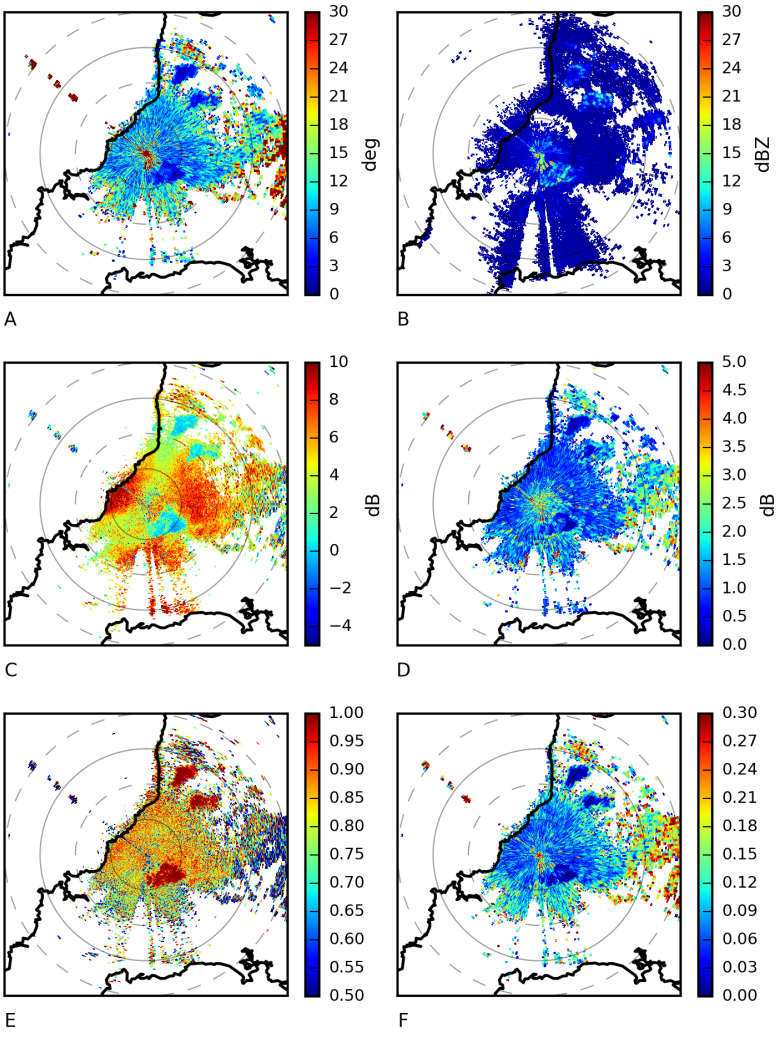

FIGURE 5.20: Radar parameters used for the classification of Fig. 5.19. **A** shows $\sigma(\Psi_{\mathrm{DP}})$, **B** $\sigma(Z)$, **C** Z_{DR}, **D** $\sigma(Z_{\mathrm{DR}})$, **E** ρ_{HV} and **F** $\sigma(\rho_{\mathrm{HV}})$.

5.3.5.2 Example 2: Frontal rainfall traversing the radar

A second example is the traversal of light rainfall across the radar, and more importantly, local ground clutter targets. In this situation the rainfall dampens the signal from the ground clutter, but there is still an elevated reflectivity signal due to its presence. On the 17 August 2013 a frontal system moved across the Cornish peninsula during the day, with widespread light rainfall (6–13 mm in 12 h) recorded across the region by the rain gauge network. Figure 5.21 shows the filter removing ground clutter within 10 km of the radar. The clutter signals removed are easily identifiable with local knowledge and

include the high topography of Rough Tor and Brown Willy to the south of the radar at approximately 5 km range, Davidstow Woods to the south west of the radar within 2.5 km and the wind turbines located due east of the radar at 5 to 8 km range. During this period rainfall is falling over these targets, creating a mixed signal echo which are often the most difficult to process. In this case there is evidence of some clutter signals passing through the filter on the fringes of the stronger returns and where the contrast between clutter and rainfall reflectivity is minimal. These occurrences are preferable to the wholesale removal of all echoes above known ground clutter, which could be achieved with a static filtering approach however this example does highlight a limitation of this approach, in that the removed signal is not replaced, thereby removing the rainfall component of the mixed signal echo. This limitation is also highlighted in the quantitative analysis shown in section 5.3.5.3.

5.3.5.3 Cumulative analysis of the COPE dataset

To fully analyse the impact of the fuzzy logic filtering, summary measures as already used in Chapter 4 and section 5.2.3 have been calculated. These demonstrate the effectiveness of the fuzzy filter in removing many of the spurious echo signatures seen in the previous sections. Firstly the echo occurrence percentage has been calculated for the lowest elevation angle (0.5°) of the 1075 volume scans collected during the field campaign, as shown in Figure 5.22. The echo occurrence result shows the removal of nearly all echoes over Dartmoor to the east of the radar, with echo occurrence decreasing from over 90% to less than 5%, indicating the ground clutter removal is effectively removing these echoes. The filters also reduce the echo percentage close to the radar from over 90% to between 20-40%. These echoes were earlier (Chapter 4) shown to be a result of numerous low reflectivity echoes, which have been filtered out through a combination of the noise and insect classes. Two other regions of known ground clutter to the north east of the radar are shown to be removed by these results, with their echo occurrences decreasing from greater than 40% to between 20% and 40% in line with their surroundings. These echoes demonstrate the capability of the filter to retain rainfall in these locations when the mixed echo becomes dominated by the rainfall signal as opposed to the underlying ground clutter signal. The mean azimuthal echo occurrence following both stages of filtering shows a lot less variation than for the raw results and those that have undergone

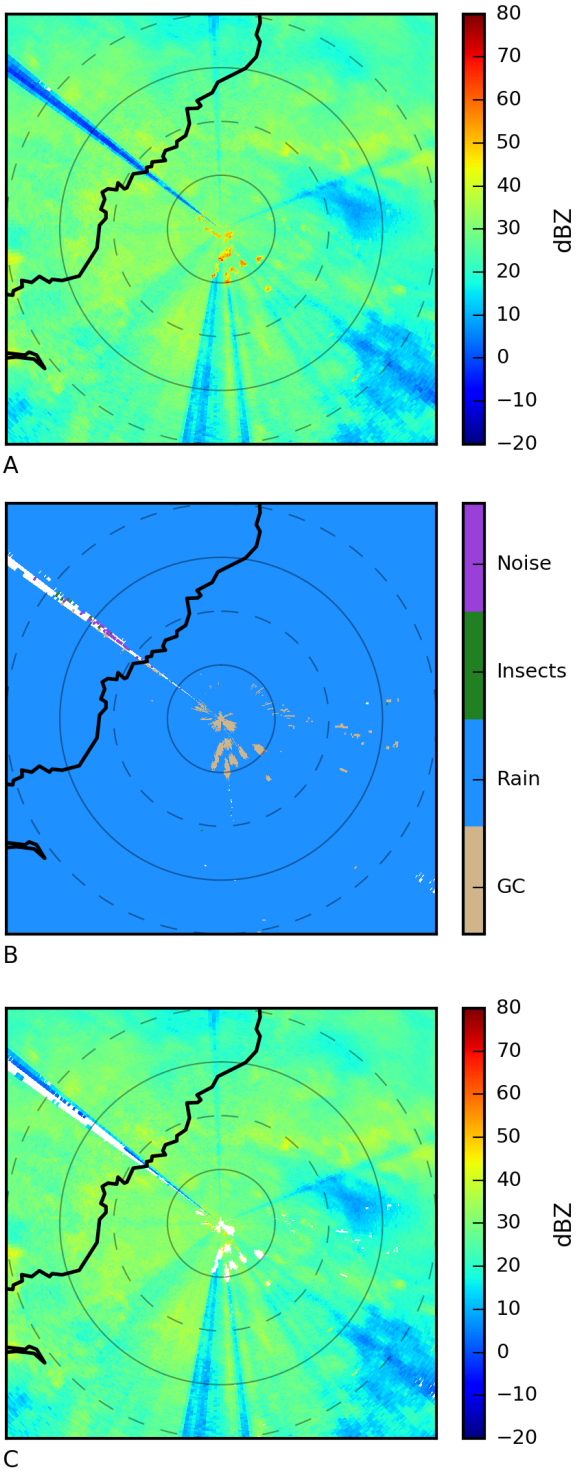

FIGURE 5.21: Application of fuzzy logic classifier to 0.5° elevation scan, 17 August 2013, 11:57 UTC. **A**–**C** as for Fig. 5.19. Range rings are at 5 km intervals.

only second trip echo filtering (Figure 5.23). These results indicate the removal of the ground clutter echoes that predominate to the east of the radar between 70° and 100° , while showing the widespread removal of 2-3% of the echoes elsewhere. This reduction is a result of the removal of the low power echoes highlighted above, along with individual erroneous echoes occurring elsewhere in the radar scan. The inclusion of the reflectivity occurrence after stage one of the filtering process indicates the consistency of the result shown in Figure 5.13 where only one day of the field campaign was analysed as opposed to the entire available dataset.

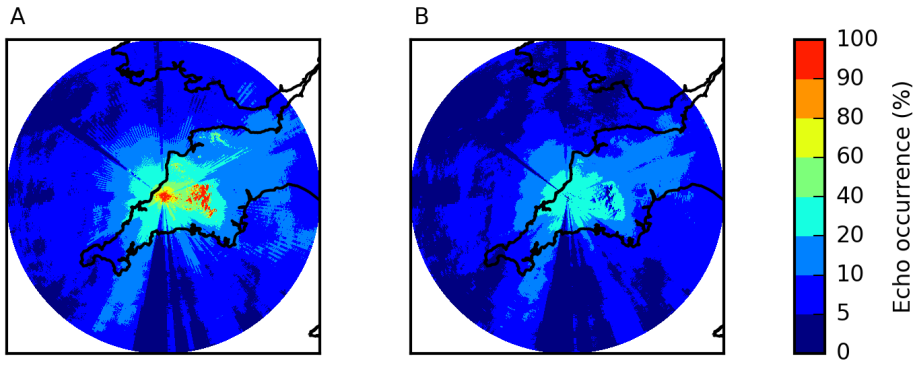

FIGURE 5.22: Change in echo occurrence percentage for the COPE field campaign through application of quality control process. Panel A shows the percentage number of 0.5° radar scans that contain a raw reflectivity echo and B shows the percentage number of 0.5° radar scans that contain a reflectivity echo after the filtering process. The panels both show a 300 km box centred on the radar location. Total number of scans included is 1075.

Analysis of rainfall totals produced using the UKMO Z-R relation (Chapter 2) and a simple backwards projection accumulation show significant reductions over ground clutter targets as expected. Comparison with rain gauges found only one site where the radar accumulation changes significantly as a result of quality control filtering. Radar accumulation for the St Clether rain gauge decreases from 155 mm to 6.8 mm while the rain gauge itself measured 18.8 mm during the same time period. This rain gauge is located within the St Clether wind farm, and as a result the radar totals have changed from significant overestimation due to clutter to underestimation due to the removal of rainfall when mixed with a strong clutter signature. The other 19 rain gauges across the peninsula show only small changes as a result of the process with 13 decreasing by less than 2% and the remaining six decreasing by no more than 13%.

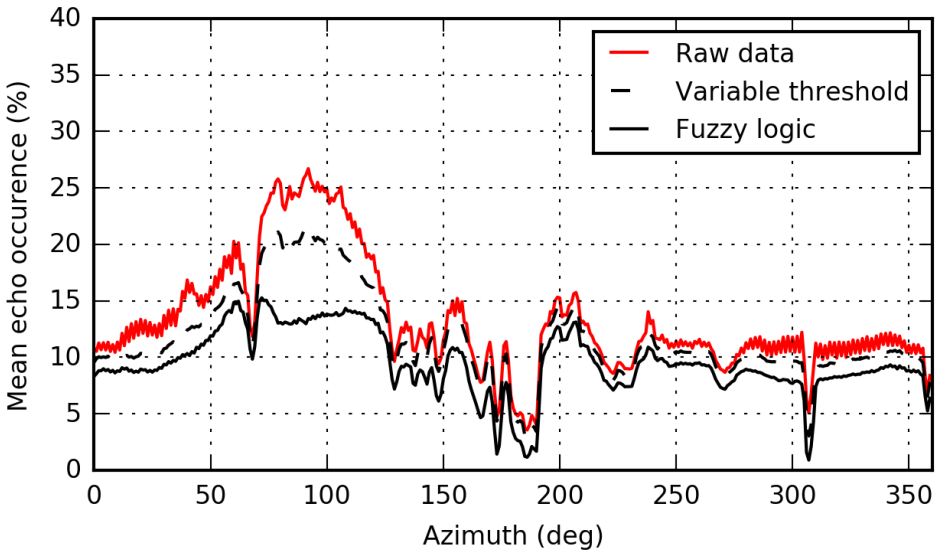

FIGURE 5.23: Azimuthal variation of echo percentage during the quality control process. Results shown are for raw reflectivity (red line), reflectivity after stage one of the process (dashed black line) and reflectivity classified as rainfall (solid black line). These results are from the whole of the COPE field campaign.

5.3.5.4 Example 3: The Burn field site

This final example is taken from the Burn airfield site. On the 6th October 2014 the radar was deployed to observe the passage of a low pressure system across the UK. The system brought persistent rainfall and strong winds. The Burn site suffers from severe ground clutter at low elevations, as shown by the 0.5° scans shown in Panel A of Figure 5.24. Panel C of Figure 5.24 shows the success of the fuzzy filter in removing these spurious echoes, even those caused by small features such as power lines and individual clusters of power station cooling towers which are numerous across this area. The filter applied is based on the membership functions derived from observations during COPE, with no adjustments made due to the change in field site. The success of the filter in this instance indicates that the filtering methodology is dependent on the scan parameters used (such as pulse width and range spacing) rather than the location in which the radar is deployed, at least within a similar climatic region. During future longer term field deployments it would be advantageous to monitor the performance of the filter and re-calibrate the membership functions if required due to specific nuances of the site or the season of deployment.

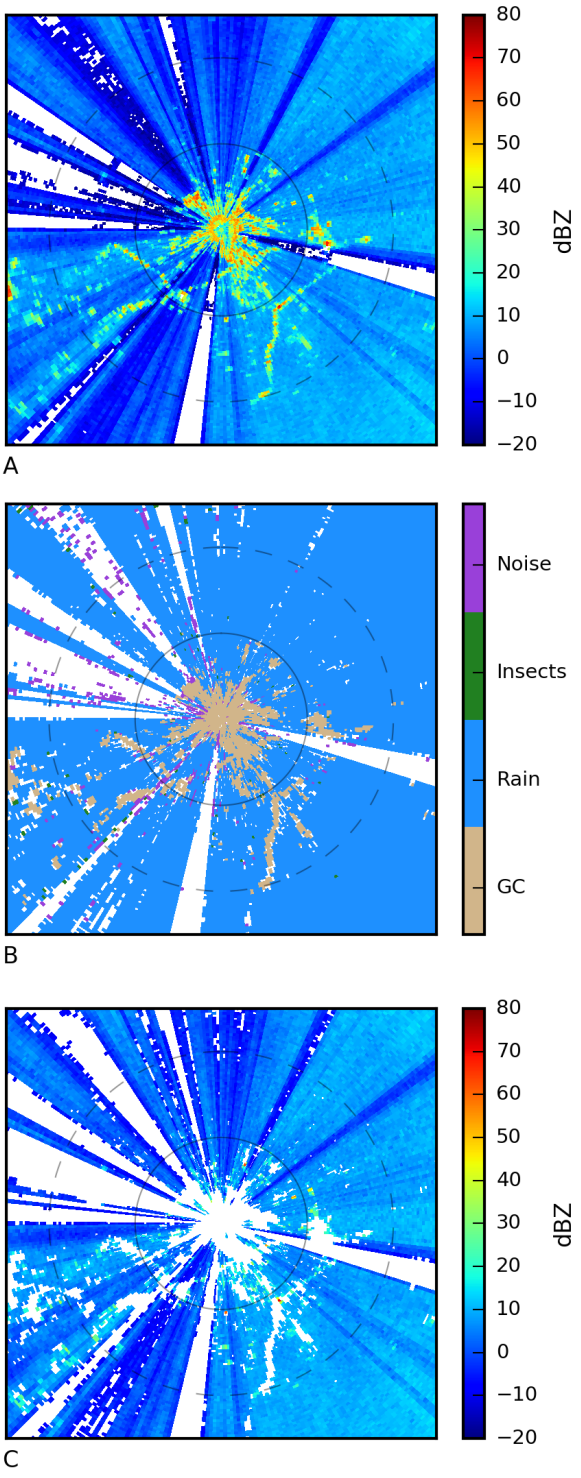

FIGURE 5.24: Application of fuzzy logic classifier to 0.5° elevation scan from Burn airfield, 06 October 2014, 12:06 UTC. **A**–**C** as for Fig. 5.19. Range rings are at 5 km intervals.

5.4 Conclusion

The identification and removal of spurious echoes from radar data has clear benefits for both visualising weather systems and quantitative analysis of those systems, including further post-processing of data to correct for other error sources. The two stage methodology outlined here uses both primary dual polarisation moments and secondary texture fields, along with beam height to remove second trip echoes with a decision tree and then identify and remove non meteorological echoes using a fuzzy logic classifier. The main advantages of this approach are:

- Second trip echoes are easily removed, before they become confused with first trip rainfall echoes
- Non meteorological echoes are dynamically classified in near real time, allowing for changes in atmospheric conditions
- The fuzzy classifier only requires a limited sample of training data to produce successful results, as shown here by the use of no more than 26 scans per echo type.
- The multi-vertex membership functions used are highly adaptable, allowing differing distributions to be specified for the range of parameters used in the scheme, while also allowing easy addition of future variables and echo types.

This approach successfully identifies, and therefore filters, the majority of echoes as shown by the three examples and longer term statistics presented here. The variety of examples highlights the adaptability of the approach, and from these examples the following conclusions become evident:

- Static ground clutter is identified successfully, both in the near field region and at longer ranges (Dartmoor, for example). This is most evident in the long term statistics derived from the COPE field campaign.
- Insect classification is strongly influenced by the dual-polarimetry moments available, particularly Z_{DR}, ρ_{HV} and $\sigma(\rho_{HV})$ as the insect signatures differ from those of rain and ground echoes. The other texture parameters provide less value here, but are vital for distinguishing between rain, ground echoes and background noise.

- The fringes of convective cells are often misclassified as noise, insects or left unclassified due to the threshold filter. As these echoes are typically below 10 dBZ the impact on precipitation estimates is minimal, but the effect should be noted for process studies of cell evolution and extent.
- Deployment at a second field site (Burn) shows that the method is transferable, without recalibration of the membership functions, provided the scan parameters are similar and the local climate does not vary greatly.
- The Burn site also indicates the classifier is able to identify small scale clutter features such as the evident power lines seen within 5 km of the radar.

The methodology presented here is applicable to not only X-band but also C- and S-band dual polarisation radars, with the only requirement being training data with which to develop the membership functions. The use of fuzzy logic provides the dynamic filtering necessary to deal with transient spurious echoes such as anomalous propagation ground clutter and biological scatterers, while other non meteorological echoes should be equally detectable given sufficient training data (such as chaff). The methodology also allows for expansion to include a more complete hydrometeor classification, including potential identification of the melting layer, snow and hail. The texture fields presented here will be of great value in such a classification, alongside the standard radar moments available.

While the results show the clear benefit of the implemented quality control process they also highlight some of the errors that remain to be corrected. These are largely beam propagation effects including beam blockage and attenuation. The following chapter will address these errors, using dual polarisation radar moments to correct the filtered reflectivity data to derive more accurate rainfall estimates.

Chapter 6

Data correction using dual polarisation

As discussed in section 4.3 the radar data acquired during the COPE field campaign requires correction for radar miss-calibration, partial beam blockage and attenuation. Radar miss-calibration has already been corrected for by L. Bennett using the self-consistency approach proposed by Gourley et al. (2009) but correction for beam blockage and attenuation is still required to obtain the most accurate reflectivity measurements possible (Bennett, personal communication, February 2015). The following chapter covers dual polarisation correction of both of these propagation affects using the additional information provided by dual polarisation moments. Differential phase shift is the key dual polarisation moment for correcting for attenuation and beam blockage due to it being proportional to atmospheric attenuation and immune to the effects of beam blockage (Zrnić and Ryzhkov, 1999; Kumjian, 2013). This chapter first focuses on differential phase shift and smoothing the data to remove measurement noise before applying correction algorithms for both attenuation and partial beam blockage.

6.1 Differential phase shift

The differential phase shift (Ψ_{DP}), as measured by the radar is a combination of the atmospheric forward propagation phase shift (Φ_{DP}), the backscatter differential phase shift (δ_{co}) and the radar system offset (Ψ_{sys}) as shown in equation 6.1 and measures the

change in phase between the horizontal and vertical signal along the radar path. As the radar is measuring the phase of the signals, not their power, the measurements are viewed to be immune to the power reducing effects of both attenuation and beam blockage. As both the differential phase shift and attenuation are a function of the number, orientation and shape of the scatterers through which the beam propagates the phase shift can be used to estimate attenuation (see 2.3.2.2 and 2.4.2.3 for more details).

$$\Psi_{DP} = \Phi_{DP} + \delta_{co} - \Psi_{sys} \tag{6.1}$$

During the COPE campaign two variables were stored by the radar, the raw measurement of differential phase shift and a smoothed field generated by the radar software to remove measurement noise and the system offset. To generate the smoothed signal the radar software calculates continuous paths of "good" echoes using a data mask consisting of a cross correlation threshold, a standard deviation of phase shift threshold and a signal to noise ratio threshold, and then iteratively smooths these paths using an FIR filter. Iterative smoothing is applied to remove the backscatter signature as first discussed by Hubbert and Bringi (1995). The system offset is removed through an averaging of the first range gates of each radial, and then taking 15° sector averages to reduce fluctuations in the final interpolated estimation (Gematronik Weather Radar Systems, 2012). A single ray example of each field is shown in figure 6.1, which shows the removal of the system offset of approximately 131° , the smoothing of measurement noise throughout the range of the radial and the removal of suspect data at the end of the signal.

However the simplicity of the smoothing method's "good" data identification has been found to produce erroneous results when processing radials containing second trip echoes and these errors cannot be masked out using the identification methods developed in Chapter 5 as they propagate into regions containing first trip echoes. To account for these errors manual smoothing of the data is required prior to the implementation of corrections based on differential phase shift.

The generation of a new smoothed phase shift field for the COPE data has been achieved using a moving window average filter, weighted by the observed correlation coefficient and then iterated to remove backscatter differential phase. The process is achieved as follows:

1. Mask the raw phase shift measurements (Ψ_{DP}) to those with a valid reflectivity after second trip filtering, a ρ_{hv} of greater than 0.7 and a standard deviation of Ψ_{DP} of less than 20.

2. Calculate a moving window average (Eq. 6.2) along each radial containing 28 range gates. The weights, w_i, are the correlation coefficient values of each valid phase shift measurement within the window.

$$\overline{x} = \frac{\sum_i^n x_i w_i}{\sum_i^n w_i} \tag{6.2}$$

3. Compare the moving window average to the original phase shift measurements and replace the phase shift measurements with the average where there is a difference greater than 5° .

4. Repeat steps 2 and 3 a further 9 times for a total of 10 iterations, as per Hubbert and Bringi (1995).

5. Calculate an estimate of the backscatter differential phase for the radial by subtracting the average profile from the original data, with all values greater than 0.5° being taken to be δ_{co}.

6. Calculate the forward phase shift (Φ_{DP}) by subtracting the estimated backscatter differential phase.

7. Repeat steps 2, 3 and 4 using the forward phase shift rather than the raw measurements with a reduced window length of 14 range gates to generate a final smoothed estimate of the forward phase shift.

An iterated moving window weighted average smoother has been used in this instance, as opposed to the newer linear programming technique of Giangrande et al. (2013) or the Kalman filtering technique of Schneebeli and Berne (2012) due to several observations of negative forward propagation phase shift within the data, either as a result of beam shielding, non uniform beam filling or vertically aligned ice crystals. These newer techniques are predicated on the monotonic increase of Φ_{DP} with range and therefore produce erroneous results in the presence of negative phase shift.

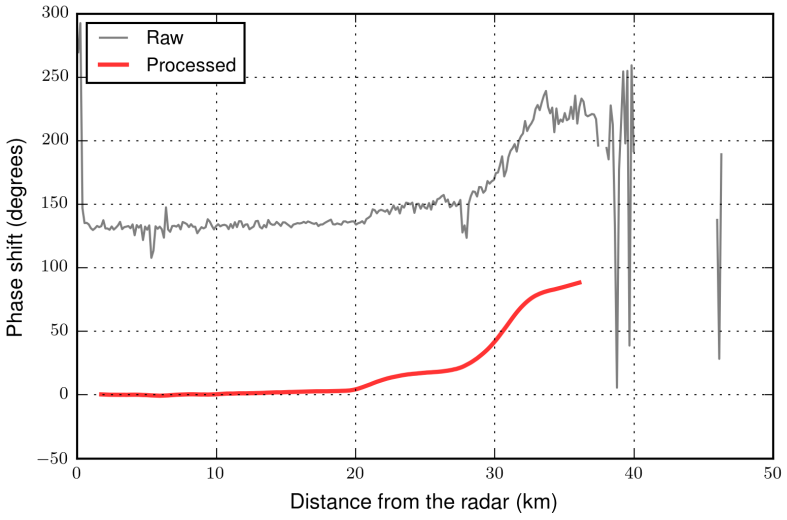

FIGURE 6.1: Measured differential phase shift (solid grey line) and radar processed atmospheric phase shift (thick red line). Example taken from 0.5° elevation scan, 2013-08-02 17:51 UTC, at an azimuth of 87° .

An example of the smoothed phase shift is shown in figure 6.2, which also shows the erroneous radar processed phase shift as a result of the second trip echo signature shown in the first 40 km of the profile. The major point of error in this example being the incorrectly calculated system offset, while there is also an error due to rebound from the second trip echoes which have higher phase shift than the first trip echoes observed at far range. As the iterative smoothing technique only processes the first trip echoes it more closely replicates the underlying signal in the data making it suitable for application in the corrections detailed in the remainder of this chapter.

6.2 Attenuation correction using dual polarisation

One of the primary benefits of dual polarisation radar is its ability to correct for atmospheric attenuation (Section 2.4.2.3). During the process of attenuation correction there are several elements that lead to uncertainty in the correction, including the choice of method and the characterisation of the atmosphere. The following section explores both the simplest method of attenuation correction (linear correction) and the most commonly implemented method (ZPHI) to assess the uncertainty within these methods.

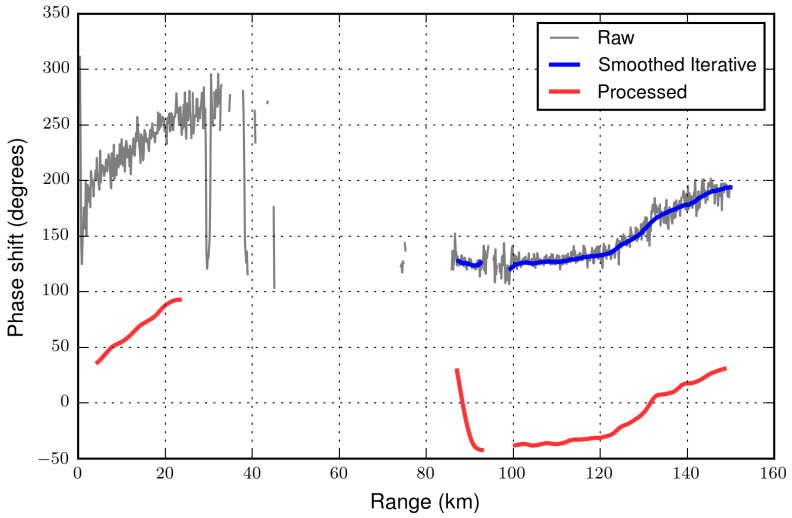

FIGURE 6.2: Measured differential phase shift (solid grey line) and radar processed atmospheric phase shift (thick red line), compared to new weighted average smoothing (solid blue line). Example taken from 1.5° elevation scan, 2013-08-17 08:16 UTC, at an azimuth of 339° .

6.2.1 Linear correction

The linear correction methodology for attenuation and differential attenuation is derived from the proportionality of attenuation (both A_h and A_{DP}) to differential phase shift (K_{DP}), as shown in Equation 6.3 (Bringi and Chandrasekar, 2001). The parameter α is a function of the radar frequency, temperature and the atmospheric conditions and has been shown to vary in time and space particularly at C-band and X-band frequencies (Tabary et al., 2009; Park et al., 2005).

$$A_h = \alpha K_{DP}(r) \tag{6.3}$$

As the attenuation at any point along a radial is a function of all preceding attenuation, a correction for attenuation can be achieved using a range integral (Equation 6.4), where Z_c is the corrected reflectivity and Z_m is the measured reflectivity. By then substituting the specific differential phase into Equation 6.4 using the relationship shown in Equation 6.3 (Equation 6.5) and expanding the integral of specific differential phase shift along a path to simply the change in path forward differential phase shift (Φ_{DP}) along the path a simple correction for attenuation can be obtained (Equation 6.6).

$$10\log_{10}[Z_c(r)] = 10\log_{10}[Z_m(r)] + 2\int_0^r A_h(s)ds \tag{6.4}$$

$$10\log_{10}[Z_c(r)] = 10\log_{10}[Z_m(r)] + 2\alpha\int_0^r K_{DP}(s)ds \tag{6.5}$$

$$10\log_{10}[Z_c(r)] = 10\log_{10}[Z_m(r)] + \alpha[\Phi_{DP}(r) - \Phi_{DP}(0)] \tag{6.6}$$

Equation 6.6 can therefore be applied to correct for attenuation, using the smoothed profiles of forward phase shift calculated in the previous section, provided a value for α can be defined. Park et al. (2005) show that α varies between 0.139 and 0.335 dB/deg at X-band with a mean value of 0.254 dB/deg in their scattering simulations, while A. Ryzhkov (personal communication, April 2015) expects α to vary between 0.17 and 0.35 dB/deg with an expected value of 0.27 dB/deg. Similarly differential reflectivity can be corrected in the same way by exchanging the proportionality constant α with the proportionality constant between differential attenuation and specific differential phase (β). Again β can take a range of values, typically in the range 0.03 to 0.06 dB/deg as noted by A. Ryzhkov (personal communication, April 2015). Due to the inherent variability of these parameters, and the simplification in Equation 6.3 (omitting the exponent of K_{DP} to provide linearity), the correction obtained from this approach is only approximate, but is significantly more stable than the methods of attenuation correction typically applied to single polarisation radar data (see Section 2.2.2).

The linear method has been implemented for both a stratiform and convective rainfall event during the COPE campaign to identify the uncertainty introduced by the method. For the stratiform case with widespread rainfall the uncertainty increases with distance from the radar as the phase shift slowly increases with range, with every 5 degrees of phase shift introducing an uncertainty of 1 dBZ for corrected reflectivity and 0.15 dB for differential reflectivity if taking the widest range of values possible for α and β.

Figure 6.3. demonstrates the range of uncertainty introduced through attenuation correction for both horizontal reflectivity and differential reflectivity during a stratifrom rainfall event with low differential phase shift ($<20°$). The phase shift profile used to correct the reflectivity measurements is shown in the bottom panel, and shows periods of decreasing

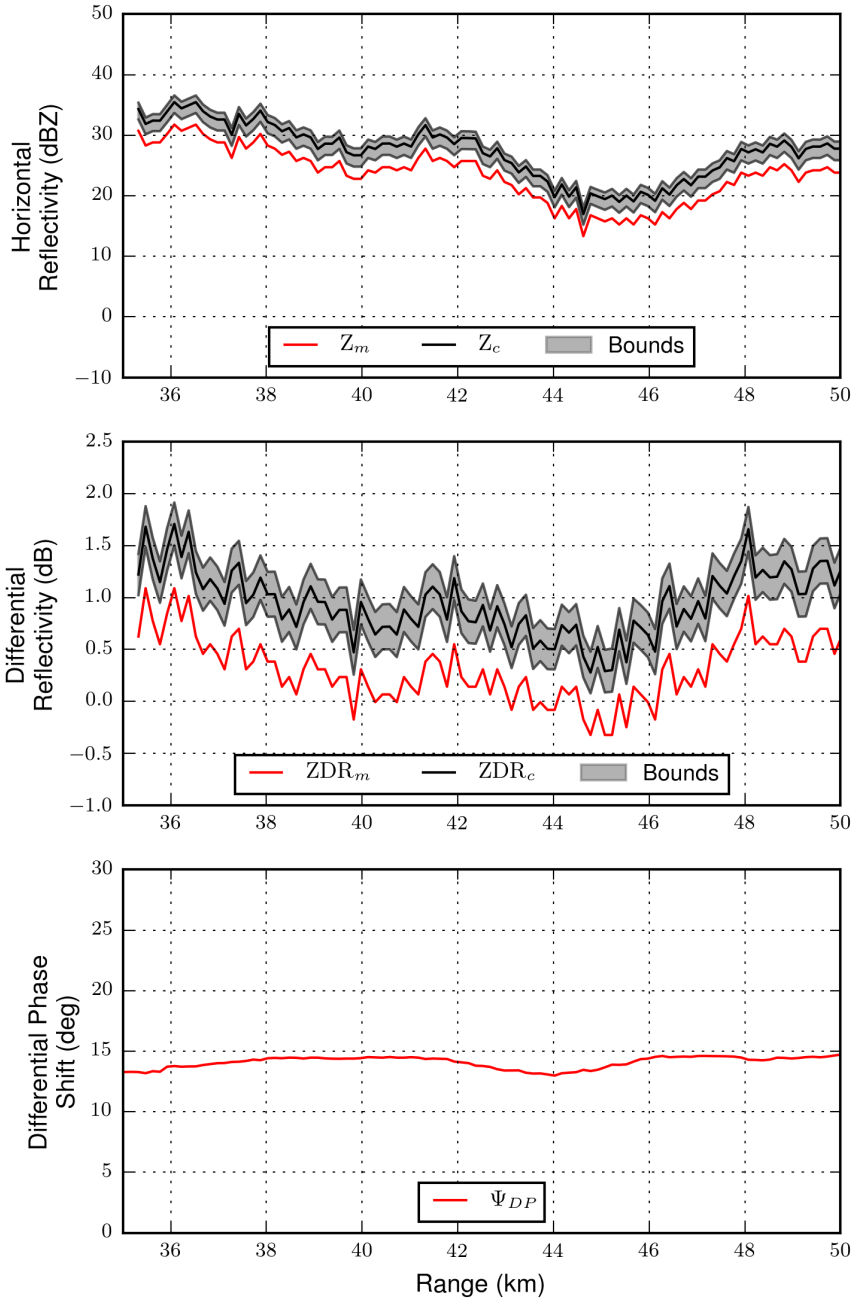

FIGURE 6.3: Linear correction of horizontal reflectivity and differential reflectivity using a linear transformation of Ψ_{DP}. Data shown is taken from the 2013-08-17 12:16UTC radar volume at an azimuth of 72° and elevation of 0.5° . Measured radar variables are shown by solid red lines, with the top panel showing horizontal reflectivity corrected with an α of 0.27 dB/deg (solid black line) and bounded with α of 0.14 and 0.35 dB/deg, the middle panel showing differential reflectivity corrected with a β of 0.045 dB/deg and bounded with β of 0.03 to 0.06 dB/deg.

phase shift which are a result of noise smoothing rather than a true atmospheric signal. During convective events the smoothing no longer exhibits these fluctuations as the atmospheric phase shift dominates the noise. Figure 6.4 shows a single radial from 2 August 2013 with almost 100° of atmospheric forward phase shift as a result of an evolving convective line system. Both the measured profile of horizontal reflectivity and differential reflectivity show significant attenuation, with differential reflectivity of -6 dB in rainfall being over 6 dB less than the expected value in rainfall. Smyth and Illingworth (1998a) previously used the positive differential reflectivity signal in the rainfall region beyond an attenuating cell to constrain the value of β within the cell, which would indicate that even the expected value of 0.045 dB/deg is too low for the atmospheric conditions shown in Figure 6.4 as the corrected value (solid black line) descends to below 0 dB in this region. The potential for under correction of differential reflectivity is significant in these convective events where high differential phase shift is observed. This uncertainty should be considered when using differential reflectivity for rainfall estimation, as has been covered in Chapter 7.

The following section presents the ZPHI methodology which distributes attenuation with the measured reflectivity constrained by the total phase shift along a radial. The advantages of this methodology are the removal of errors resulting from smoothing fluctuations in the phase shift or the presence of backscatter differential phase and also that the ZPHI algorithms return the specific attenuation for each range gate, which can be utilised for rainfall estimation and radar correction.

6.2.2 Correction using the simplified ZPHI method

6.2.2.1 Introduction to ZPHI

The ZPHI methodology is a rain profiling technique which is an extension of the single polarisation methodology first proposed by Hitschfeld and Bordan (1954) and relies on the relationship between reflectivity and attenuation (Equation 6.7) alongside the previously mentioned linear relationship between attenuation and specific differential phase shift (Equation 6.3).

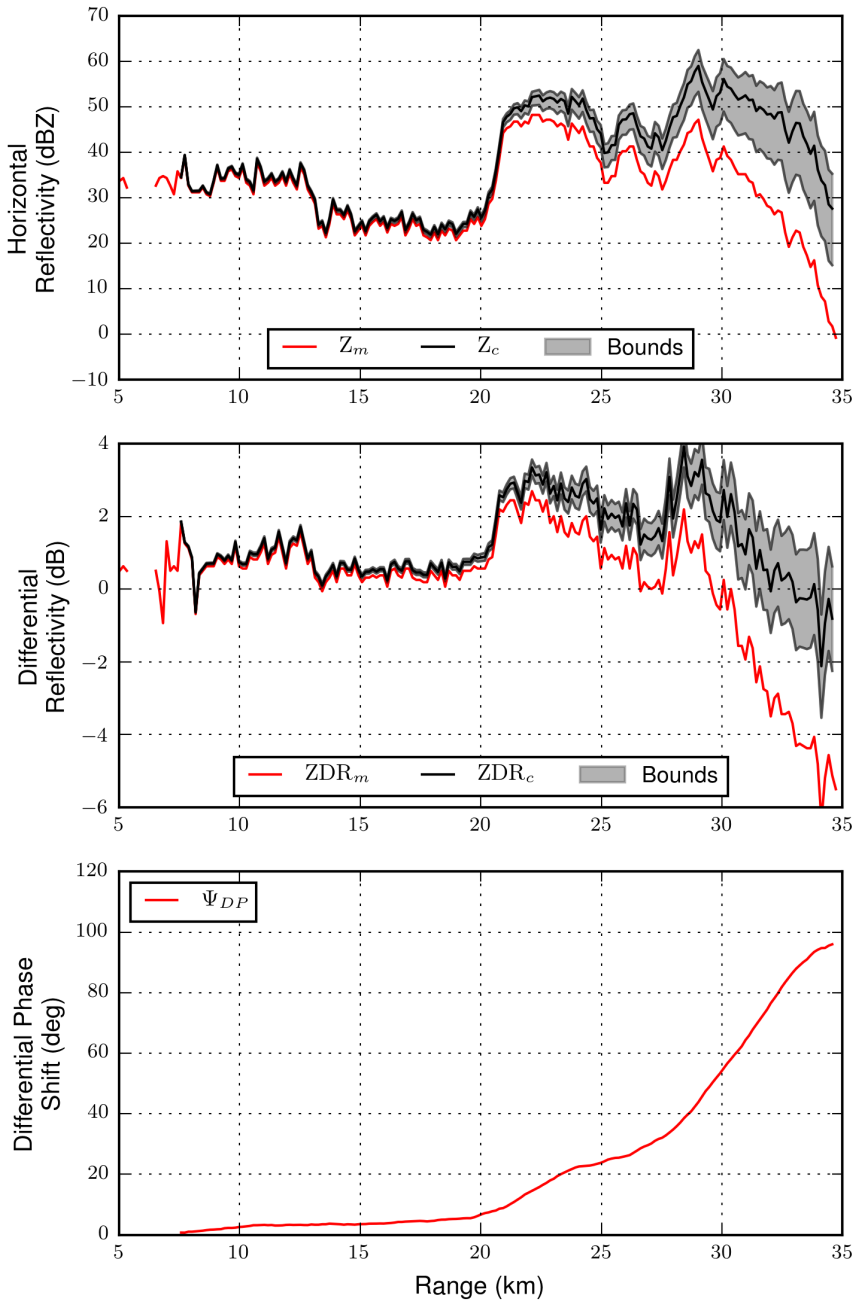

FIGURE 6.4: Linear correction of horizontal reflectivity and differential reflectivity using a linear transformation of Ψ_{DP}. Data shown is taken from the 2013-08-02 17:51UTC radar volume at an azimuth of 86° and elevation of 0.5° . Measured radar variables are shown by solid red lines, with the top panel showing horizontal reflectivity corrected with an α of 0.27 dB/deg (solid black line) and bounded with α of 0.14 and 0.35 dB/deg, the middle panel showing differential reflectivity corrected with a β of 0.045 dB/deg and bounded with β of 0.03 to 0.06 dB/deg.

$$A_h(r) = a[Z_h(r)]^b \tag{6.7}$$

The technique as applied to ground based weather radars was proposed by Testud et al. (2000) as the first component of a two stage rainfall estimation process and has been utilised extensively for attenuation estimation since then (Diederich et al., 2015a; Wang et al., 2014; Lim et al., 2013; Park et al., 2005, for example). Specific attenuation is calculated using the following formula (Equation 6.8).

$$A_h(r_1) = \frac{[Z_h(r_1)]^b}{I(r_0, r_2) + C(b, PIA)I(r_1, r_2)} C(b, PIA) \tag{6.8}$$

Where the components of Equation 6.8 are given in the following three equations to aid readability (6.9, 6.10, 6.11).

$$C(b, PIA) = \exp[0.23b(PIA)] - 1 \tag{6.9}$$

$$I(r_0, r_2) = 0.46b \int_{r_0}^{r_2} [Z_h(s)]^b ds \tag{6.10}$$

$$I(r_1, r_2) = 0.46b \int_{r_1}^{r_2} [Z_h(s)]^b ds \text{ for } r_0 < r_1 < r_2 \tag{6.11}$$

In the above equations r_0 is the starting range of the segment being profiled, r_2 is the end of the segment, and r_1 is each range gate within the segment. b is the scaling exponent from Equation 6.7 which has been shown to be effectively constant for a given radar frequency (Bringi and Chandrasekar, 2001) and PIA is the path integrated attenuation, which can be obtained using Equation 6.12 as per the principles covered in the previous section on linear correction,

$$\begin{aligned} PIA &= 2\alpha \int_{r_0}^{r_2} K_{DP}(s) ds \\ &= \alpha[\Phi_{DP}(r_2) - \Phi_{DP}(r_0)] \end{aligned} \tag{6.12}$$

The above equation uses a fixed value for α for the segment, ignoring any variation due to temperature change and is used throughout this analysis. Recent studies have shown that the variation of α with temperature is insignificant compared to variability due to the DSD and the effects of temperature variation have also been shown to cancel out when using specific attenuation for rainfall estimation and radar calibration (Diederich et al., 2015a; Wang et al., 2014). The other potential unknown required to implement the ZPHI algorithm is the exponent b. Research by Park et al. (2005) indicates b is equal to 0.780 on average with a standard deviation of 0.019 across their scattering simulations for an X-band radar with frequency 9.375 GHz, while Diederich et al. (2015a) use a value of 0.78 at 10 °C, with an increase (decrease) of 0.04 for every 10 °C increase (decrease) in temperature. For the remainder of this study a fixed value of 0.78 will be applied, which is consistent with these other studies given the summer climate in Cornwall.

6.2.2.2 Implementation of automated calculations using ZPHI

While the manual implementation of the ZPHI algorithm on a single radial is trivial one of the main challenges of the method for operational implementation is the automation of the process to successfully identify segment start and end points to allow the calculations required in Equations 6.12, 6.10 and 6.11. The COPE dataset, while not as extensive as operational datasets is sufficiently large to require automated processing of ZPHI. The following methodology has been used to generate the radial segment locations required for the algorithms. The start of each radial segment has been identified as the first 10 continuous range gates which contain rain as identified by the fuzzy logic QC process provided that the window starts at a range beyond 4.5 km (to avoid near radar clutter effects) and no further than 75 km from the radar. r_0 is then defined as the first range gate of the window, with $\Phi_{DP}(r_0)$ defined as the median Φ_{DP} of the first three gates of the window. The smoothed phase shift described in section 6.1 is used for this process. Similarly the end of each segment (r_2) is defined as the last range gate of the last 10 gates of continuous rainfall, provided that the last gate is no closer to the radar than 7.5 km, no further from the radar than 105 km and at am altitude no greater than 2000 m, which is a conservative approximation of the base of the melting layer (in contrast, Diederich et al. (2015a) require a temperature no less than 6 °C at the end of a segment). As for $\Phi_{DP}(r_0)$, $\Phi_{DP}(r_2)$ is taken to be the median Φ_{DP} of the last 3 gates of the window. To

further constrain the calculations, the segment defined by r_2 and r_0 must be at least 10 gates long and the phase shift difference across the segment must be positive.

Figure 6.5 shows an example from 17 August 2013, during a widespread frontal rainfall event. The algorithm identifies the starting differential phase shift, avoiding the region of decreasing phase shift possibly associated with ground clutter interference at the start of the radial and also identifies the end of the segment along with a suitable value for the differential phase shift at the end of the segment. The results are comparable to what would be observed manually and allow the calculation of specific attenuation for this radial. Several implementations of this methodology omit the identification of a starting range and phase shift, instead using the beginning of the radial and a predefined system differential phase shift offset for the calculations, however several examples during COPE indicate decreasing differential phase shift within the first 5 km as a result of beam interaction with ground clutter targets and the above methodology more accurately derives the total path integrated attenuation in these cases.

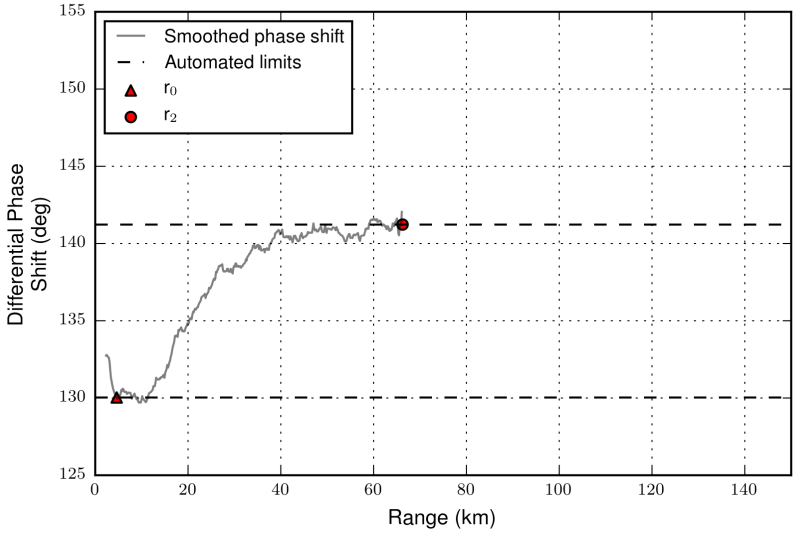

FIGURE 6.5: Automation of ZPHI limit identification using the smoothed profile of Ψ_{DP}. The radial shown is taken from the 2013-08-17 12:16UTC radar volume at an azimuth of 150° and elevation of 0.5° . The smoothed phase shift is shown by the solid grey line, with the red triangle indicating the range defined as r_0 by the automated procedure and the red circle showing r_2. The dashed lines indicate the corresponding differential phase shift values used to calculate the total segment differential phase shift.

Figure 6.6 provides an example of the automated procedure using the same radial previously shown in Figure 6.3. This particular example shows the difficulty of defining these automation parameters, with the placement of r_2 coinciding with a drop in phase shift which introduces a one degree underestimation into the total path integrated attenuation for this radial. Throughout the radial there are several small drops in differential phase shift that could introduce a similar error, if different parameters were used for defining the end of the segment and the current set of parameters have been chosen to produce robust results within 75 km of the radar, where the radar beam is closer to the ground. Several examples from the field campaign show decreasing differential phase shift within the last 20-30 km of the radial, possibly related to non-uniform beam filling at these longer ranges where the radar beam is broader, and it is these examples that have led to limiting the maximum range of the segment to 105 km from the radar, despite this specific example.

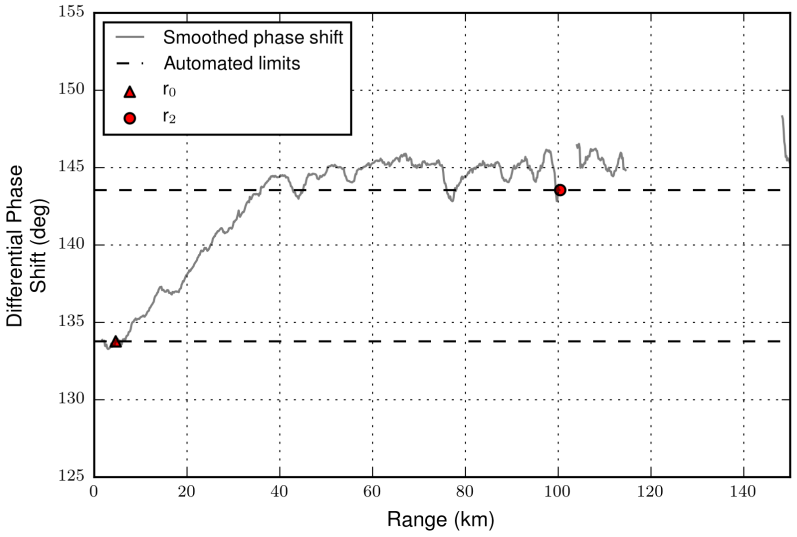

FIGURE 6.6: Automation of ZPHI limit identification using the smoothed profile of Ψ_{DP}. The radial shown is taken from the 2013-08-17 12:16UTC radar volume at an azimuth of 72° and elevation of 0.5° . The smoothed phase shift is shown by the solid grey line, with the red triangle indicating the range defined as r_0 by the automated procedure and the red circle showing r_2. The dashed lines indicate the corresponding differential phase shift values used to calculate the total segment differential phase shift.

This automated procedure allows the COPE dataset to be processed using the ZPHI method, with a single segment per radial and the same α values as used in section 6.2.1.

6.2.3 ZPHI results

The following section presents examples of attenuation correction using ZPHI compared to the earlier implementation of the linear method, focusing on the uncertainty in corrected horizontal reflectivity along with estimates of specific attenuation and differential reflectivity. The first example presented is from the stratiform event on 17 August 2013, with the PPIs shown in Figure 6.7 observed at 12:16UTC. The original quality controlled horizontal reflectivity is shown in the top left panel, with each of the remaining panels showing the horizontal reflectivity corrected for attenuation with the ZPHI method, with a different value of α used in each to represent the bounds (0.14 to 0.35 dB/deg) of the likely atmospheric α values at X-band and the expected value (0.27 dB/deg).

Through comparison of the PPIs it is difficult to identify changes in reflectivity either between uncorrected and corrected data, or between the different corrected fields. Across the lowest elevation scan beyond the range at which ZPHI processing begins (4.5 km) the average difference between the reflectivity corrected with the expected α of 0.27 dB/deg and the uncorrected reflectivity is 1.2 dBZ, while the average difference between the upper and lower α bounds is 0.9 dBZ. Figure 6.8 shows the correction along a single radial, previously shown in Figure 6.3, with the magnitude of the reflectivity correction (2 dBZ) at this range falling within the lower end of the uncertainty bounds of the previously implemented linear method and the uncertainty range for the ZPHI method being approximately half the range of the linear method. The difference between the two bounds can be attributed to a combination of factors, firstly the estimated system phase shift used in the linear correction is based on the whole radar volume rather than attributing an independent value to each azimuth, secondly the ZPHI method for this radial underestimates the segment end phase shift by 2° as shown in Figure 6.6 and finally that the distribution of attenuation along a radial is a function of reflectivity in the ZPHI method rather than following the differential phase shift profile exactly as in the linear methodology. Conversely the radial shown in Figure 6.5 where the automated ZPHI limits closely match those identified by eye has only a slight reduction in uncertainty bounds for the ZPHI method when compared to those from the linear methodology.

The lower panel in Figure 6.8 shows the specific attenuation derived by the ZPHI methodology as a function of the α value used, which shows firstly that specific attenuation in

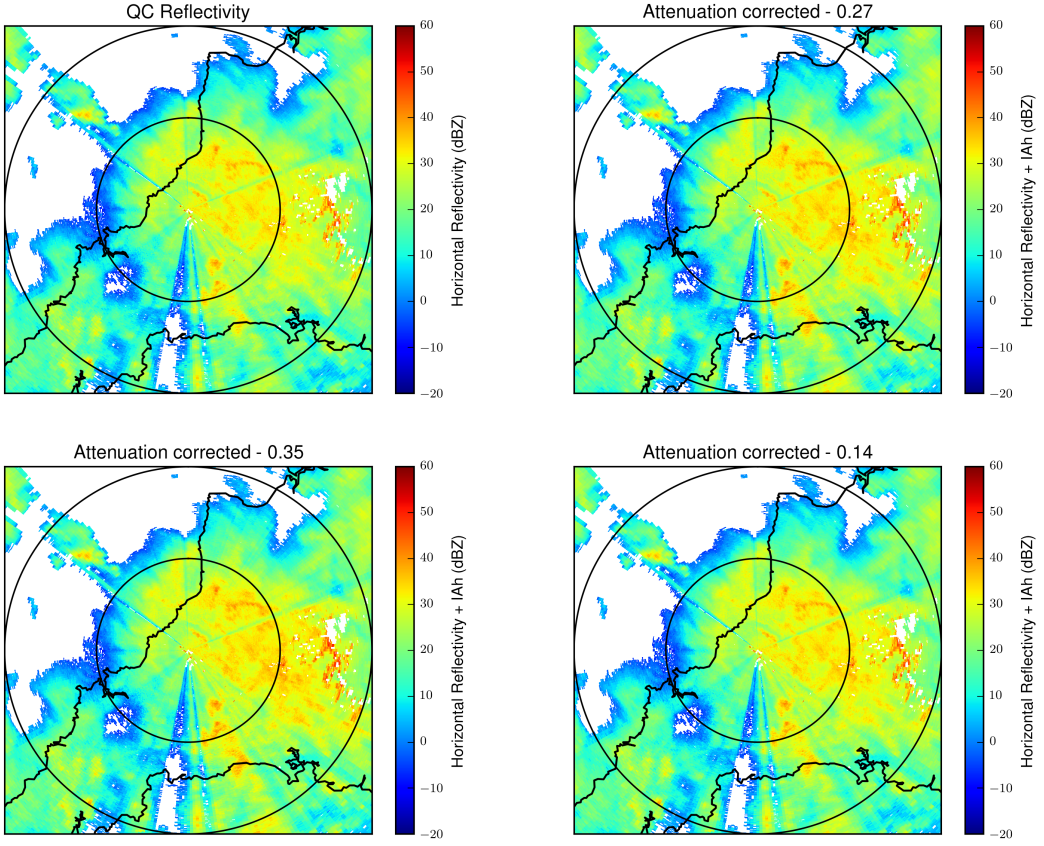

FIGURE 6.7: Horizontal reflectivity PPIs from the 2013-08-17 12:16UTC radar volume at an elevation of 0.5°. The top left PPI shows quality controlled but uncorrected reflectivity and the other three PPIs show attenuation corrected reflectivity through application of the ZPHI technique, with α varying through the PPIs. The top right plot uses the expected α value of 0.27 dB/deg, the bottom left shows the α value which leads to the highest corrected reflectivity values (0.35 dB/deg) and the bottom right shows the lowest corrected reflectivity values ($\alpha = 0.14$ dB/deg). Range rings are shown at 25 km and 50 km.

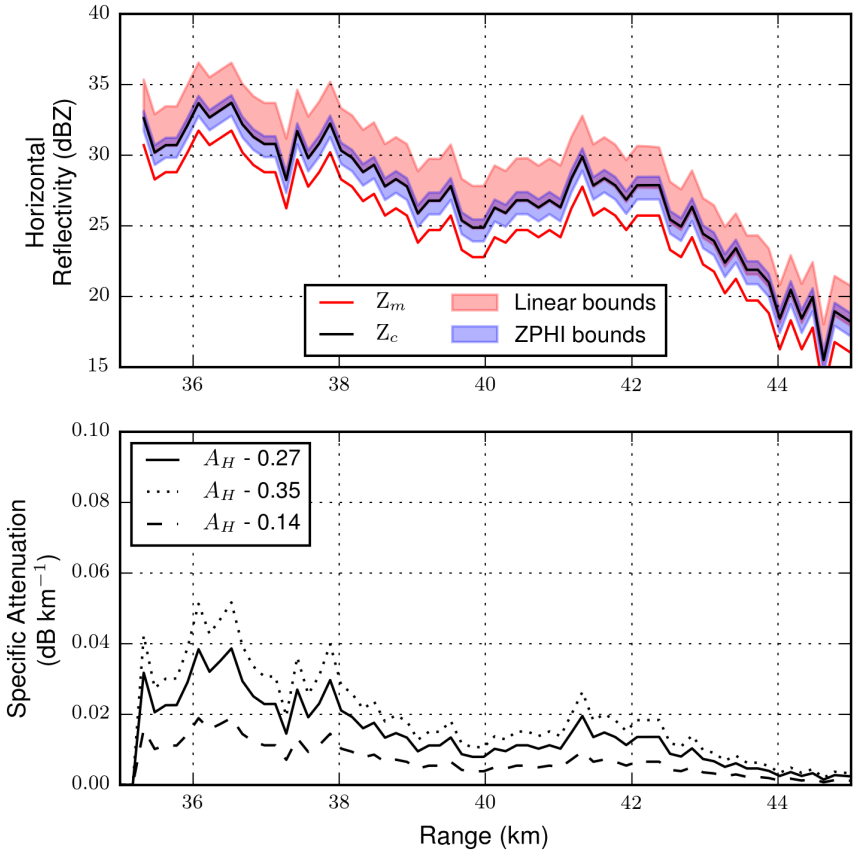

FIGURE 6.8: Radial profiles of reflectivity taken from the PPIs shown in Figure 6.7 (top panel) and specific attenuation (bottom panel). The radial shown is from the 2013-08-17 12:16UTC radar volume at an azimuth of 72° and elevation of 0.5° . The top panel shows the uncorrected horizontal reflectivity (red line), the reflectivity corrected for attenuation using ZPHI and an α of 0.27 dB/deg (solid black line) and the uncertainty ranges due to *alpha* variation for the ZPHI method (blue fill) and the linear method (red fill).

low intensity stratiform rainfall is low, and that the variation as a result of changing α is up to a factor of two, which could be significant for rainfall estimation based on specific attenuation (see Chapter 7).

Figure 6.9 recreates Figure 6.8 using the previously seen convective example from 2 August 2013 (17:51 UTC, 86° azimuth and 0.5° elevation) where peak corrected reflectivity is 59.5 dBZ. Prior to the peak corrected reflectivity the uncertainty resulting from α variation is significantly smaller for the ZPHI methodology than for the linear method. Beyond the peak reflectivity the ZPHI uncertainty quickly expands to match the uncertainty in the linear method, as the majority of the path integrated attenuation is distributed in this region. The automation of limit detection is successful for this case,

with the final difference in differential phase shift being 94.8° when using the automated procedure and 96° when implementing the linear method with a fixed system phase offset (an error of only 1.25%).

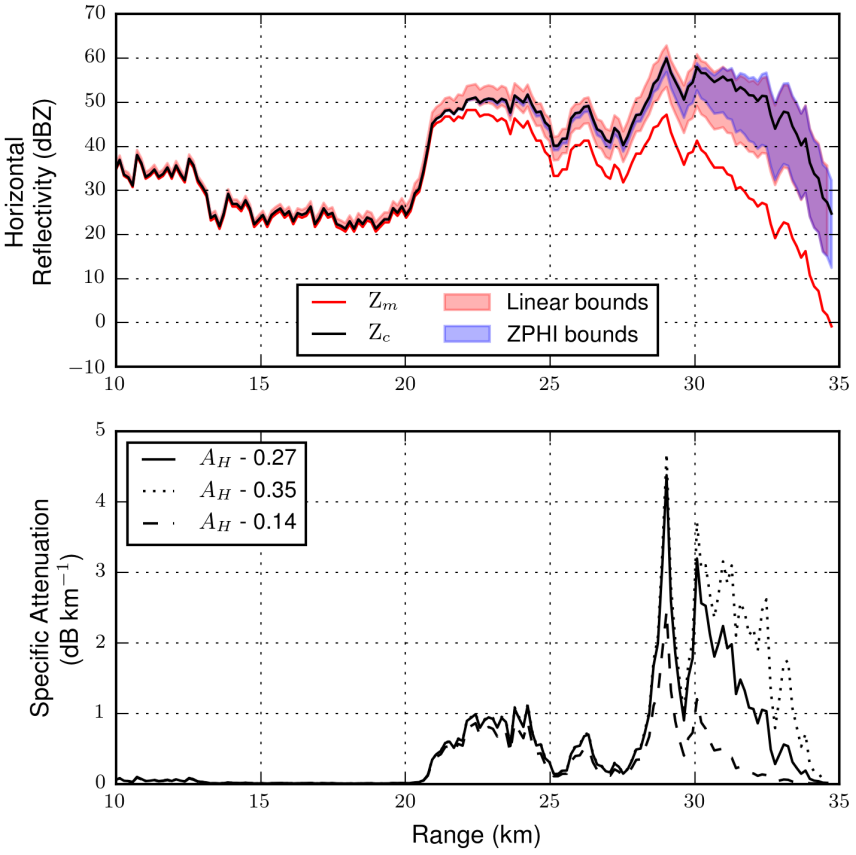

FIGURE 6.9: Radial profiles of reflectivity (top panel) and specific attenuation (bottom panel) from the 2013-08-02 17:51UTC radar volume at an azimuth of 86° and elevation of 0.5°. The top panel shows the uncorrected horizontal reflectivity (red line), the reflectivity corrected for attenuation using ZPHI and an α of 0.27 dB/deg (solid black line) and the uncertainty ranges due to *alpha* variation for the ZPHI method (blue fill) and the linear method (red fill).

Unlike beam blockage and persistent clutter echoes the effects of attenuation are difficult to validate with long duration integrations and statistics, due to the localised, transient nature of the effect. For example, attenuation correction will have no impact on echo occurrence statistics, as an echo is always required to be present for attenuation correction to be possible. The rainfall statistics in Chapter 7 provide a method of validation for the attenuation correction, but are constrained by the location of rain gauge observations and the number of events within the COPE database.

6.3 Correcting for partial beam blockage using dual polarisation

Traditional partial beam blockage correction techniques rely on theoretical beam propagation models combined with digital terrain models, as detailed in section 2.2. Given the additional data requirements and uncertainties resulting from these techniques, utilising the consistency of multiple dual polarisation parameters has been proposed as a new solution to correcting reflectivity for partial beam blockage (see section 2.4.2).

The following section uses the specific attenuation values calculated in the previous section to calculate the reflectivity bias for each azimuth. The technique utilises a theoretical transformation from specific attenuation to reflectivity given their proportionality to the atmospheric DSD. As reflectivity has been corrected for attenuation then the difference between the theoretically calculated reflectivity ($Z(A_h)$) and the corrected reflectivity is a result of miscalibration and beam blockage. As measurement errors can strongly influence this comparison on a single gate or radial basis, a longer duration summation is used to produce a more stable result.

6.3.1 Reflectivity bias estimates from specific attenuation - methodology

The method presented here was first used by Diederich et al. (2015a) to calculate reflectivity biases for X-band radars in Germany. Firstly specific attenuation must be calculated, as has been done in the previous section which can then be converted to theoretical reflectivity using Equation 6.13 with a_1 and b_1 set based on temperature (and radar wavelength).

$$Z(A_h) = a_1 A_h^{b_1} \tag{6.13}$$

To maintain consistency with the previous section invariant values for a_1 and b_1 have been used here taking the values equivalent to a fixed temperature of 10 °C ($a_1 = 1.15 \times 10^{-4}$ and $b_1 = 0.78$). A direct bias correction can then be obtained for any range gate for which it was possible to calculate specific attenuation, as simply the difference between

the theoretical reflectivity from specific attenuation and the corrected reflectivity in logarithmic units, which is identical to the logarithm of the linear ratio of the theoretical reflectivity from specific attenuation and the attenuation corrected horizontal reflectivity (Equation 6.14).

$$\begin{aligned} B_A(r) &= Z(A_h)(r) - Z_c(r) \\ &= 10 \times \log 10 \frac{10^{0.1Z(A_h)(r)}}{10^{0.1Z_c(r)}} \end{aligned} \tag{6.14}$$

By summing or averaging over a larger spatial or temporal window a more accurate estimate of the bias can be obtained which mitigates DSD variability, temperature fluctuations and measurement noise to give a bias correction for that window (Equation 6.15).

$$B_A = 10 \times \log 10 \frac{\sum 10^{0.1Z(A_h)}}{\sum 10^{0.1Z_c}} \tag{6.15}$$

The bias of the COPE dataset has been analysed for each of the α values used in the previous section, with the averaging domain firstly extended on a gate by gate basis to a whole day, then to each individual azimuth (beyond 15 km) for a single day and then finally to each azimuth for the entire field campaign. The azimuthal analysis has been done beyond 15 km to identify the end of beam bias correction, which may be a result of more than one blockage within that first 15 km.

6.3.2 Reflectivity bias estimates from specific attenuation - results

Firstly the results for a single α (0.27 dB/deg) are presented for the 17 August 2013 using both individual gate summations and azimuthal summations. Figure 6.10 shows that while the results are broadly comparable for the two summations the gate by gate method fluctuates within an individual azimuth, suggesting the time domain is not sufficient to remove the effects of DSD variation, temperature variation and measurement uncertainty. This is unsurprising as the average number of observations included within each gate summation is only 18, with a maximum of 43 observations, this contrasts to the azimuthal

method, where each azimuth contains on average 11000 observations, with the maximum in any single azimuth being 20681. However the gate by gate analysis does provide some localised insight, with evidence that Dartmoor is strongly influencing the results despite the radar QC process, with measured reflectivity up to 5 dB lower than expected over Dartmoor and lower than expected beyond the high ground. These results are not reflected in the azimuthal segments which begin at 15 km, suggesting this region might need multiple segments to account for the additional blockage experienced in the range gates beyond Dartmoor. Segmenting the azimuths between 75° and 110° into two summations, one between 15 km and 45 km range and the second beyond 60 km range indicates that the region beyond Dartmoor is blocked by up to an additional 2.3 dBZ compared to the region closer to the radar, which will need to be accounted for in the beam blockage corrections.

The strongest regions of blockage are to the south of the radar, which correspond to Brown Willy and Rough Tor, two hills in excess of 350 m elevation located within 6 km of the radar (Figure 4.4) and to the north west, which corresponds to the location of the old airfield control tower which was within 500 m of the radar. In both these locations the dual polarisation calculations indicate the radar beam is blocked by over 90% when scanning at 0.5° elevation. There is also another prominent, narrow blockage (>5 dBZ) to the east north east of the radar, which corresponds to the location of the radar operating container and wider blockages to the south west and south east which can be attributed to forested areas and higher topography.

Repeating the above analysis using α values of 0.14 and 0.35 dB/deg provides a measure of the uncertainty in the beam blockage calculations that can be attributed to α. In absolute terms an increase (decrease) in α increases (decreases) the bias correction required (Figure 6.11, left panel) for the entire radar scan, however if the lowest bias correction is taken to represent the radar miscalibration (in relation to α) and the azimuthal results are zeroed using this value to represent the bias resulting from beam blockage then there is almost no change in the bias that can be attributed to beam blockage (Figure 6.11, right panel). This indicates that using the relative change in bias between the unblocked and blocked regions of the radar scan gives an estimate of partial beam blockage that is independent of the α value used in the calculations. Utilising this result beam blockage for the entire

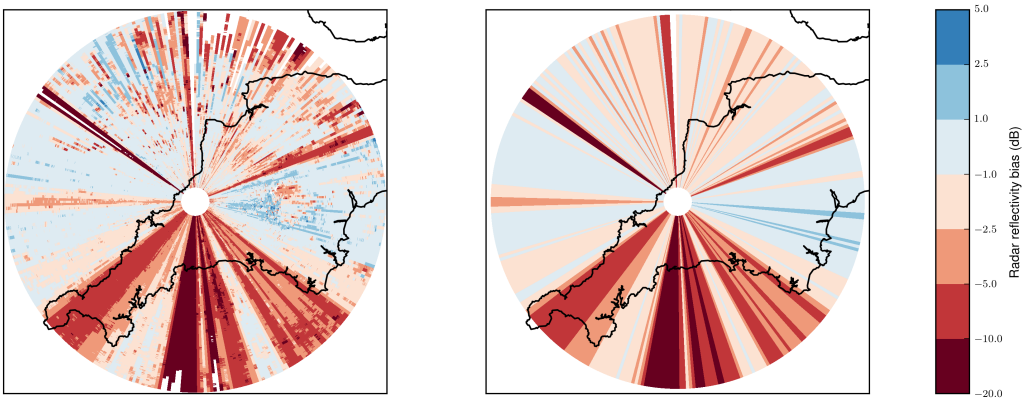

FIGURE 6.10: Measured reflectivity bias at 0.5° elevation computed on an individual gate basis (left panel) and along each azimuth starting at 15 km (right panel). Both panels use all available data from 17 August 2013, a day of widespread stratiform rainfall particularly suitable for this methodology. Panels are 200 km squares centred on the radar.

COPE dataset can be calculated using a single value of α (taken to be 0.27 dB/deg as this agrees well with the radar calibration in unblocked sectors).

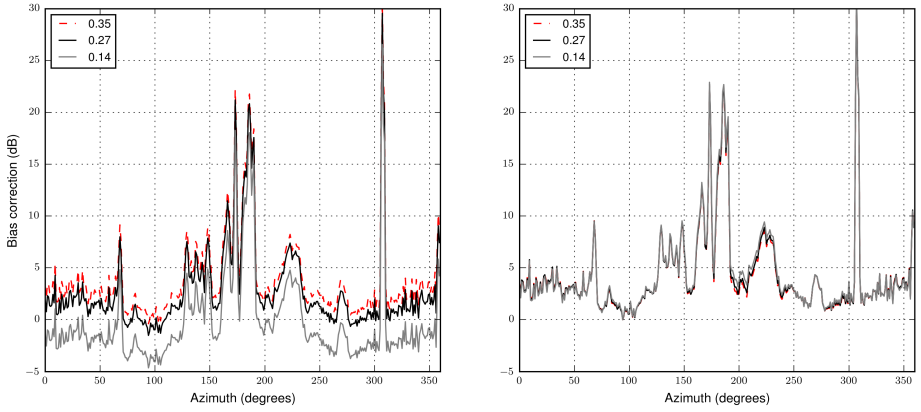

FIGURE 6.11: Dual polarisation estimates of bias correction for 2013-08-17. The left panel shows the absolute radar bias corrections calculated using three different values for α, 0.35 dB/deg (red line), 0.27 dB/deg (black line) and 0.14 dB/deg (grey line). The right panel shows the results normalised to start at a bias of zero, with each line plotted as per the left panel.

Expanding the beam blockage analysis from a single day (2013-08-17) to include all matching files from the COPE dataset increased the number of usable files by 963 to 1074 files in total. This increased the average number of observations per azimuthal segment

from 11000 to 24500, with no single range gate containing more than 105 usable observations for the comparison. This comparatively small increase compared to the number of files added is a result of the distributed convective rainfall that occurred during the majority of the project as opposed to the widespread stratiform rainfall that occurred on the 17 August. The result of extending the analysis is shown in Figure 6.12, with the most prominent beam blockages maintained from the single day analysis, but with increases in the estimated blockage throughout the region between 200° and 280° azimuth. Again the region beyond Dartmoor has been analysed as a separate segment with Dartmoor again causing an additional 1 dB to 2.5 dB of blockage.

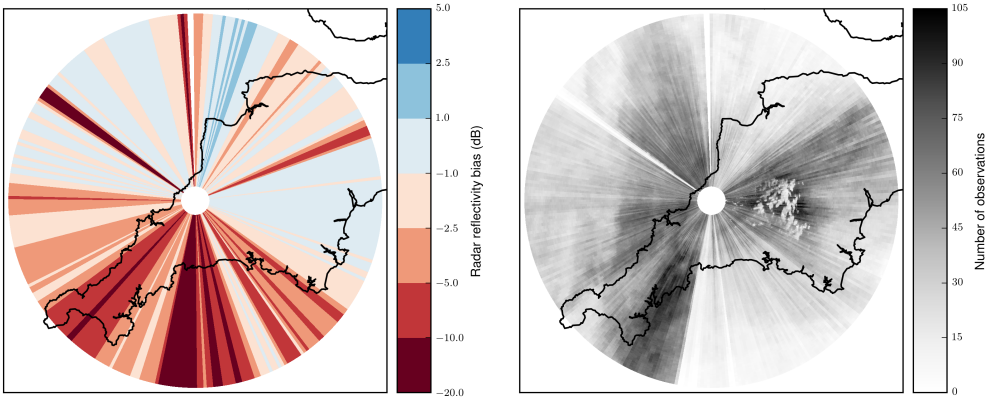

FIGURE 6.12: Measured reflectivity bias at 0.5° elevation computed along each azimuth starting at 15 km (left panel) and the number of valid observations in each range gate during the COPE field campaign (right panel). Both panels use all available data from the field campaign and are 200 km squares centred on the radar.

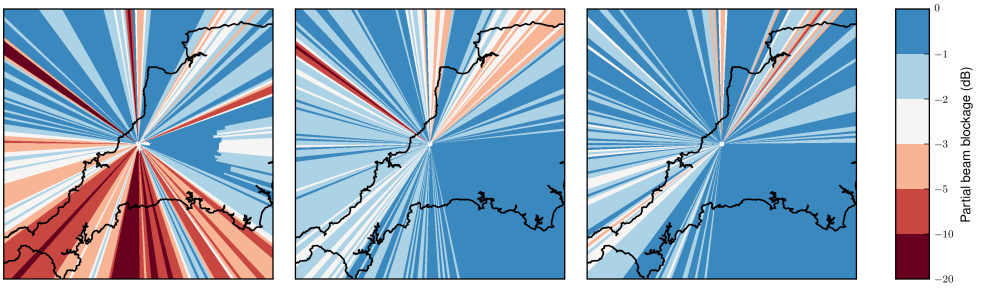

FIGURE 6.13: Partial beam blockage correction maps generated using the specific attenuation consistency with attenuation corrected reflectivity for the entire COPE field campaign. The left panel is the correction for 0.5° elevation, the middle panel is for 1.5° and the right panel is for 2.5° . All panels are 150 km squares centred on the radar.

A correction map has then been generated for each of the elevations up to 2.5° with the location of the last prominent blockage in each azimuth (within the first 15 km) taken as the starting point for each segment. The final correction maps for 0.5° and 1.5° are shown in Figure 6.13. At the higher elevations, particularly 2.5° there are fewer valid observations leading to unexpected results, the most obvious example of which is the apparent increase in blockage with increasing elevation angle between 30° and 50° seen in Figure 6.13. Similarly the region between 25° and 40° at 2.5° elevation has a calculated blockage of between 1.5 dB and 5 dB despite the analysis in section 4.3 showing the influence of beam blockage at 2.5° is minimal, as does inspection of individual scans, which all suggests that the results should be viewed with caution. This region has only 1500 observations per radial segment on average which is clearly insufficient for reliable results. Diederich et al. (2015a) found that the method produced stable absolute calibration results when accumulated over 19 rainy days (±1 dB), but with variation of up to 10 dB for bias calculated on a daily basis.

The typical suitability of the corrections are shown in Figure 6.14 which contains two examples of reflectivity corrected with the PBB maps. The first of these examples is taken from the 17 August 2013 (previously seen in Figure 6.7) and the second of which is from 18 July 2013 (previously seen in Figure 5.19). On the 17 August example, the blocked azimuth at 67° is well corrected as are the beam blockages to the south east and the south west, however the blockage caused by the control tower at 305° is severely over corrected, and this section should be ignored in favour of using higher elevation scans which are not blocked as the severity of the blockage (estimated at 30 dB, which equates to a beam blocked fraction of 0.999) and instances of reflection from the control tower surface lead to unreliable results. The region due south of the radar is potentially under corrected in the first example, which contrasts to the second example from the 18 July 2013 where the correction appears to be at least 5 dB too large when compared to higher elevations and adjacent azimuths. Given over 50% of the valid data used in calculating the corrections comes from the 17 August it is unsurprising that the correction is more applicable to that day than an earlier time, where changes in atmospheric and ground conditions may have been responsible for a different level of beam blockage occurring.

These examples highlight two major uncertainties with the method applied, one is how much data is required for the results to be quantitatively accurate representations of

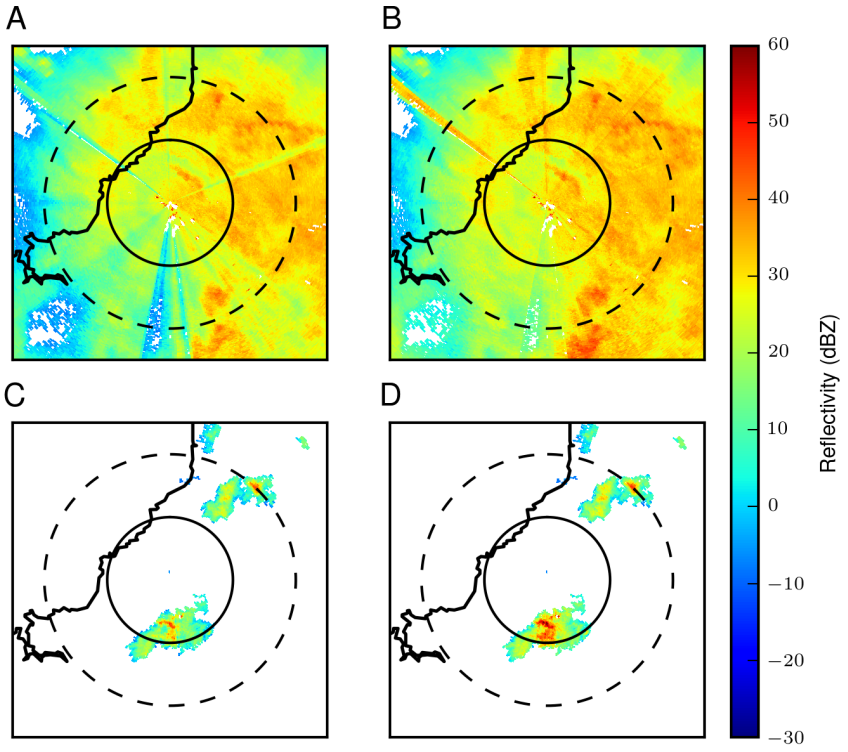

FIGURE 6.14: Examples of partial beam blockage correction from COPE. Panel A shows the uncorrected reflectivity from 17-08-2013 12:16UTC at 0.5° elevation and panel B shows that reflectivity corrected for partial beam blockage. Panel C shows the uncorrected reflectivity from 18-07-2013 14:38UTC at 0.5° elevation while D shows that reflectivity corrected for beam blockage. All four panels are 50 km squares centred on the radar with range rings at 10 km (solid line) and 20 km (dashed line).

the beam blockage and the other being whether the average quantity over this duration ever truly represents a single scan, given the natural variations in refractivity, vegetation, surface wetness etc. which can all affect the amount of beam blockage occurring at any one time. Due to the relatively small amount of available data from the COPE field campaign it is not possible to do full sensitivity studies on the variation of calculated correction with changing number of observations. The impact of these uncertainties, particularly daily variability, on rainfall estimates and the total rainfall accumulations for COPE are shown in Chapter 7.

6.4 Dual polarisation correction - conclusions

The results presented in this chapter show that dual polarisation has been successfully utilised to correct the COPE dataset for attenuation and beam blockage, however the methods used are susceptible to high levels of uncertainty due to measurement errors and atmospheric variability. Clearly the accuracy of the phase shift measurements of the radar are crucial to these corrections as phase shift is the key parameter in all of the methods presented here, and Section 6.1 presents a new method of smoothing phase shift measurements which successfully obtains the forward propagation atmospheric phase shift signal from the measurement noise and the included backscatter component. The method is capable of retaining negative regions of phase shift as it does not assume monotonic increase along the radial path, and while the data supports this approach it is not clear whether these regions are due to atmospheric effects or the impact of geometric effects as the beam broadens. Future research with the NCAS mobile radar would benefit from considering the effects of scan speed and PRF on the accuracy of phase shift measurements as phase shift underpins all elements of dual polarisation correction (miscalibration, attenuation and beam blockage).

The greatest uncertainties in the attenuation correction methods presented are the parameters α and β, with corrected reflectivity varying by up to 20 dBZ in the most extreme cases, which is a significant range when generating instantaneous rainfall rates. Of the two methods the ZPHI approach has less uncertainty throughout the radial than the linear method in these extreme cases, and should be the preferred method of correction where possible as it is also less influenced by phase shift measurement errors along the radial. It should also be noted that both methods are only suitable for correcting for attenuation which occurs below the melting layer, while this is not a problem for the COPE field campaign, as the summer melting level in this region is suitably high to allow rainfall estimates to be taken from below the melting layer, it could be a factor in corrections of future field campaigns.

This research has shown that using dual polarisation to correct for partial beam blockage is viable despite the uncertainty in α which hinders attenuation correction, however stable results require more data than is available from the COPE campaign, particularly at higher elevation angles (1.5° and 2.5°).

The implications of these uncertainties when considering accurate QPE are explored in the following Chapter which utilises these corrections along with rain gauge observations and uncorrected data to address uncertainty within the radar processing chain.

Chapter 7

Multi-parameter quantitative precipitation estimation

The derivation of accurate quantitative precipitation estimates from radar has been an area of ongoing research since radar's introduction for weather observation in the 1950s (Atlas and Banks, 1951; Villarini and Krajewski, 2010a). As the previous chapters have shown there are numerous uncertainties and errors in the measurement of radar moments used in these calculations, which dual polarisation can be used to offset, while dual polarisation also offers an increased number of radar moments to use for QPE. The following chapter firstly explores the benefits of dual polarisation for radar QPE when used to correct and constrain reflectivity measurements before going on to investigate the use of differential reflectivity, specific differential phase shift and specific attenuation as rainfall estimators in conjunction with reflectivity or as an alternative. All of these rainfall estimates are compared with rain gauge observations of rainfall from the EA network (Chapter 3) to assess their accuracy and provide guidance on the suitability of the estimators along with their uncertainty. Finally two methods of combining these estimates into a single, optimum rainfall estimate are considered, a decision tree and a weighted average which both aim to reduce the uncertainty in the final rainfall estimate, particularly during high intensity rainfall.

7.1 Accumulation methodology

Before comparing rainfall estimates from radar to ground observations it is necessary to outline the methodology used to allow this comparison. Radars provide an instantaneous measure of the atmosphere at a fixed moment in time, which in the case of QPE is a rainfall intensity in millimetres per hour, averaged over a radar range gate (which can vary between 200 m^2 and 0.4 km^2 in area depending on range) while rain gauges provide a measure of accumulation over a period of time at a fixed point in space (generally over an area of 200 cm^2). Clearly the difference in temporal and spatial scale does not allow a direct comparison to be made and for this work any comparisons will be based on integrating the radar rainfall intensities into 15 minute accumulations to match the temporal sampling of the rain gauge data obtained from the EA. These 15 minute accumulations can then be summed to create rainfall accumulations at any greater time period, which will remove some of the random variability of the comparisons to provide a clearer picture of any systematic differences between the ground observations and the radar.

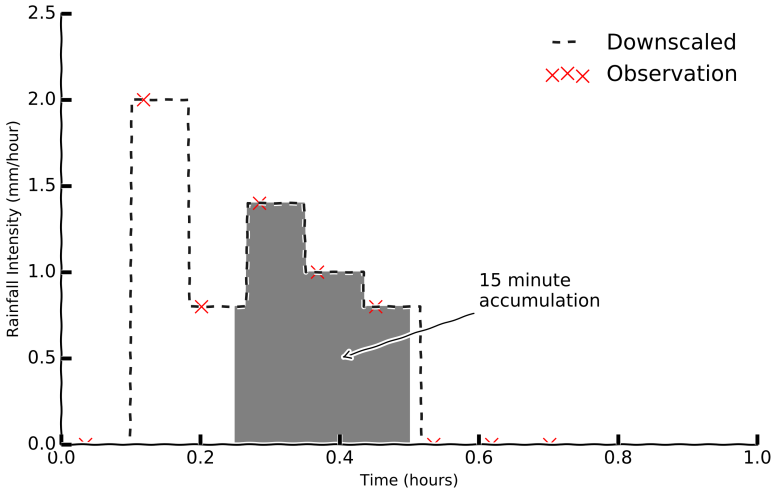

FIGURE 7.1: Derivation of rainfall accumulations through simple projection onto a regularly spaced time grid. Red crosses represent the instantaneous measurements obtained by the radar, the dashed line is the downscaled projection of these measurements in time, using forward projection. The grey shaded area represents an accumulation in millimetres as a time-intensity integral.

This temporal integration has been achieved by projecting the instantaneous radar measurements onto a regular time grid (30s spacing), with the intensities then being converted

into millimetres per time interval and summed into 15 minute accumulations. This approach (sketched in Figure 7.1) manages the semi-regular spacing of the radar scans during the COPE project, which were collected at approximately 4.5 minute intervals with some larger gaps. The projection of intensities in time is limited to a maximum of 5 minutes, therefore missing radar scans are treated as zero accumulation within a 15 minute window, rather than older scans being projected over the missing time interval, therefore missing data gaps can only contribute to an underestimation of total accumulation in any 15 minute interval. Although there are more sophisticated techniques available for integrating radar data in time which incorporate the motion of the rainfall between radar scans including the generation of two dimensional advection fields or the implementation of optical flow techniques (Tabary, 2007; Bowler et al., 2004) the implementation of these techniques for COPE introduces further smoothing and adjustment that will mask the underlying impact of radar uncertainty with regards to rainfall accumulation.

Comparison between rain gauges and radar QPE in this chapter is based only on those times when the radar was operational, limited to 15 minute intervals where at least some data was recorded or projected. It is also limited to radar scans which contained azimuth data spaced at one degree intervals with 1000 range gates at 0.15 km spacing. As a result of the volume scan patterns employed during COPE the number of scans which meet these criteria vary between elevation angles and therefore final accumulations may not be directly comparable between elevations, which will be noted in the analysis where relevant.

7.2 Horizontally polarised reflectivity as a rainfall estimator

The following section uses horizontally polarised reflectivity as the sole estimator for rainfall estimation, analogous to a single polarisation radar system. In doing so it shows the benefits of using dual polarisation for radar quality control and correction as outlined in the previous two chapters. Rainfall estimates have been calculated using the decibel

reflectivity to rainfall conversion shown in Equation 7.1, where Z_e is the equivalent reflectivity factor. This relationship is the inverse of the relationship detailed in Section 2.1, where $a = 200$ and $b = 1.6$.

$$R = \left(\frac{10^{0.1Z_e}}{200} \right)^{0.625} \tag{7.1}$$

To establish a baseline for comparison the measured reflectivity (Z_m) has been converted to rainfall in addition to the reflectivity after QC (Z_{QC}), the attenuation corrected reflectivity (Z_A) and the fully corrected reflectivity (Z_C) which accounts for beam blockage. The attenuation corrected reflectivity in this instance refers to correction using the ZPHI method and a fixed α value of 0.27 dB/deg, the impact of different attenuation corrections will be shown later in this section.

7.2.1 Total rainfall accumulation during COPE

The total rainfall accumulation for all valid COPE scans are shown in Figure 7.2 at the full range of the radar and Figure 7.3 for the area within 50 km of the radar. Progressing from Panel A to Panel B in both these figures shows the reduction in accumulation over the Dartmoor area in particular, with peak rainfall accumulation from the raw reflectivity measured at 27426.8 mm and from the filtered reflectivity at 333.3 mm which is a far more reasonable estimate but still high enough to suggest contamination from ground clutter. As this maximum accumulation is within 3 km of the radar to the north west it strongly suggests the cause of such a large accumulation is ground clutter contamination of the rainfall intensities in this area. The improvement between Z_m and Z_{QC} is also shown by the rainfall accumulations over the St Clether rain gauge (83° azimuth, 5.7 km range), where accumulations from Z_m are 143.1 mm compared to 6.6 mm when using Z_{QC} which compare to a rain gauge total accumulation of 19.0 mm. The raw reflectivity measurements produce significant over estimates in rainfall accumulation as a result of ground clutter in this area due to a combination of topography and wind turbines. The post QC data largely removes this erroneous accumulation but at the expense of valid rainfall during the field campaign contributing to an underestimation of 65% for this gauge site.

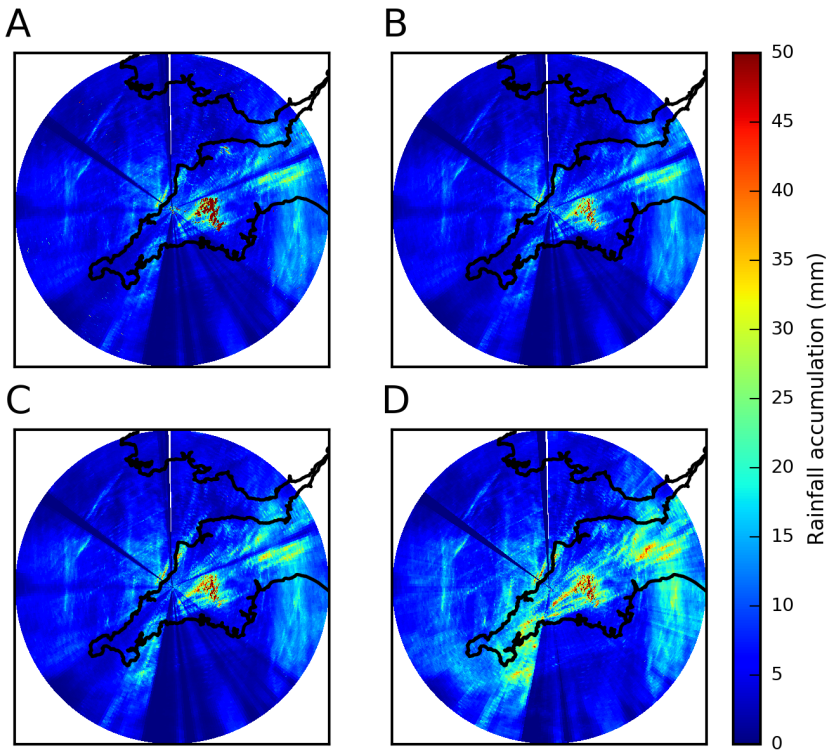

FIGURE 7.2: Total rainfall accumulation for the COPE field campaign as measured by the NCAS mobile weather radar at an elevation of 0.5° . Panel A shows the rainfall as derived from Z_m, B the accumulation from Z_{QC}, C the accumulation from Z_A and D the accumulation from Z_C. Each panel is a 300 km square centred on the radar and contains the accumulation from 1131 valid scans across the field campaign.

Between Panels B and C there is an increase in the rainfall accumulations in the lines of rainfall to the north of the radar and to the south east of the radar as a result of attenuation correction. This is most noticeable in the accumulations on the west facing north Cornwall coast around Bude where rainfall accumulations increase from 25 mm to over 40 mm. This region is most noticeable because the convective line which generated this rainfall aligned with the direction of the radar beams causing high attenuation along this direction as the beam travelled through the majority of the convective line. The change from Panel C to Panel D is greatest in overall intensity and the blocked sectors to the south west, south east and north-north-east are well corrected in the near field region however the blocked region to the south east is still visible at longer ranges. This occurs as only the rainfall measured by the radar can be corrected for beam blockage

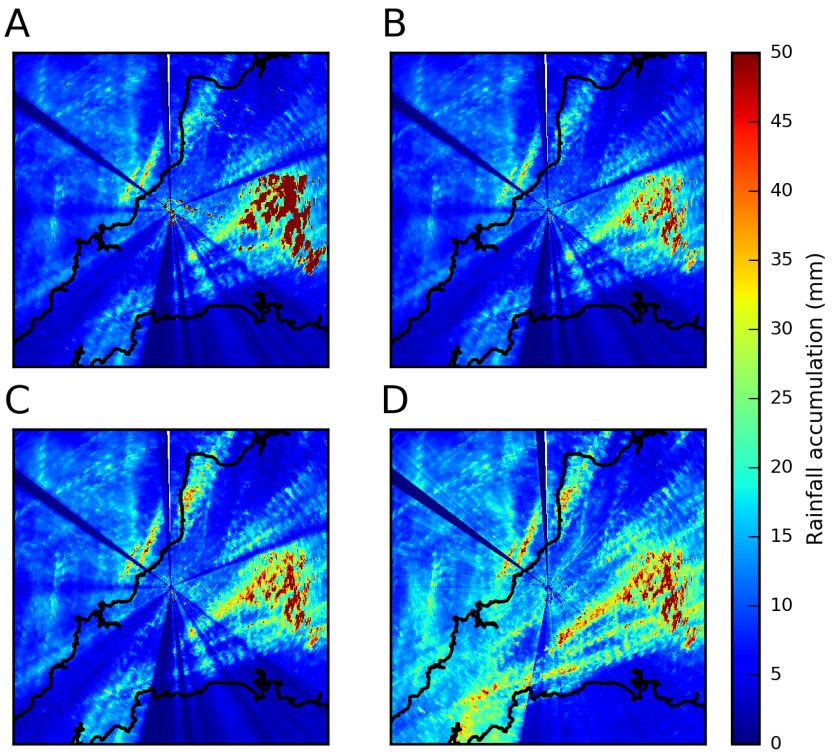

FIGURE 7.3: Total rainfall accumulation for the COPE field campaign as measured by the NCAS mobile weather radar at an elevation of 0.5° . Panel A shows the rainfall as derived from Z_m, B the accumulation from Z_{QC}, C the accumulation from Z_A and D the accumulation from Z_C. Each panel is a 100 km square centred on the radar and contains the accumulation from 1131 valid scans across the field campaign.

and if the rainfall is at a lower intensity and/or affected by attenuation as is the case here then it is not recoverable by beam blockage correction techniques. This has a greater impact at longer range as the radar's minimum detectable reflectivity increases with range, further decreasing the signals available for correction. For this reason the blockages to the south of the radar are still clearly visible at most ranges as the beam blockage is in excess of 20 dBZ although the rainfall accumulations in this region (average of 5 mm beyond 15 km) are still significantly higher than in the original rainfall estimates from Z_m (average of 0.5 mm beyond 15 km). The sector between 305° and 310° blocked by the radar control tower has been removed from the accumulations due to extreme overcorrection and reflection effects. Figure 7.4 compares the total accumulations at each of the EA rain gauges across the peninsula with rainfall accumulations from each

of the four reflectivity estimates. For each of the estimates it is clear that the radar underestimates total accumulation when using reflectivity as the rainfall estimator, with the fully corrected reflectivity showing a significant improvement when compared to the other stages of the processing chain. Linear regression shows the measured reflectivity has no correlation with the rain gauge data ($R^2 = 0.05$) and R^2 increases through each of the processing steps, with the final corrected reflectivity having an R^2 of 0.36, a gradient of 0.58 and an offset of 3.23 mm. Clearly the offset between gauge and radar should be zero and a linear regression with fixed offset instead shows an improvement in R^2 from -0.01 to 0.34 with a gradient change from 0.45 to 0.72 through the processing (Z_M to Z_C). This improvement is also shown in the mean absolute percentage differences (MAPD) for the gauges, which decreases from 86% to 31% throughout the processing, with a final mean percentage difference (MPD) of 26% indicating the systematic under measurement by the radar when compared to the rain gauges.

Often the rainfall calculated from higher elevations is used in preference to the lowest elevation to avoid beam blockage and ground clutter, with many radar processing chains incorporating the idea of a lowest usable elevation angle for each location (Harrison et al., 2012; Tabary, 2007). Generating rainfall accumulations with data from an elevation angle of 1.5° for the COPE campaign shows the increased elevation increases the gradient of the relationship between radar and rain gauge data in all but the fully corrected case and R^2 increases from 0.0 to 0.26 for Z_{QC} and from 0.05 to 0.39 for Z_A. However for Z_C the correlation decreases from 0.34 to 0.15 when comparing the two elevations. The reduction in R^2 from Z_A to Z_C at 1.5° elevation is indicative of the uncertainty within the PBB correction at this elevation. The beam blockage correction calculations for 1.5° contain fewer valid data points than the equivalent calculations for 0.5° , leading to greater variability in the results. Despite the decrease in correlation between the observations the PBB correction does improve the MAPD from 36% (Z_A) to 28% (Z_C) suggesting the PBB correction improves the rainfall estimates on average, despite greater variability between locations. This is a marginal improvement on the MAPD obtained when using fully corrected 0.5° elevation reflectivity (31%) which could be attributed to the different number of comparisons in each dataset (1.5° scans did not feature in several of the COPE scan strategies, see Section 3.2), or could be a result of St Clether being much better represented by the higher elevation data due to the reduction in ground clutter returns and mixed signal echoes for this gauge site.

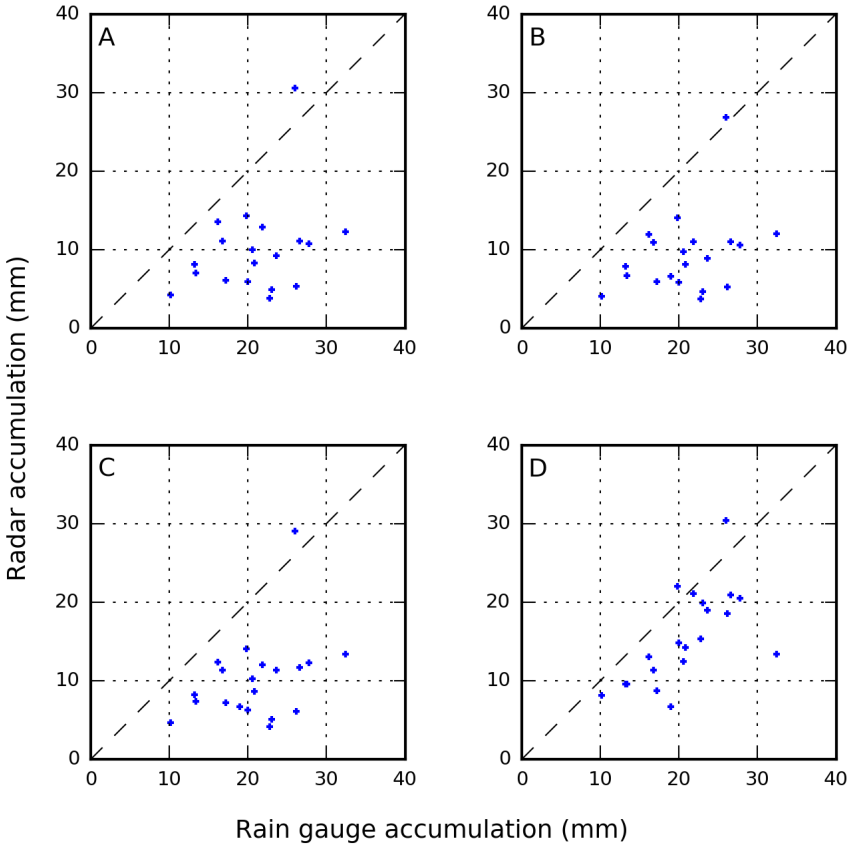

FIGURE 7.4: Comparison of rain gauge total rainfall accumulation for the COPE field campaign with rainfall as measured by the NCAS mobile weather radar at an elevation of 0.5° . The y-axis of panel A shows the rainfall accumulation from Z_m, B the accumulation from Z_{QC}, C the accumulation from Z_A and D the accumulation from Z_C. Each blue cross represents the total for each of the EA rain gauge sites. Panel A contains one less data point than the other panels as the St Clether gauge has been omitted due to its extreme raw rainfall total. The dashed line in each panel is the one to one line.

Figure 7.5 shows the total rainfall accumulations from the 1.5° elevation scans across a 100 km square centred on the radar, which is spatially similar to Figure 7.3 but with some notable differences. The rainfall accumulations over Dartmoor are much lower, and spatially continuous which suggests they are better representations of the true rainfall in this area, while the accumulations to the north are much lower (20 mm compared to 40 mm at 0.5°). It is much harder to validate this region, the closest rain gauge is Tamar Lakes which is located at a radar azimuth of 28° and a range of 29.1 km however this lies on the edge of the intense region of rainfall as seen at 0.5° . The radar accumulation at this location was 9.6 mm at 0.5° and 8.22 mm at 1.5° compared to 13.40 mm for the gauge, which suggests the lower elevation is more representative but this result can't be reliably

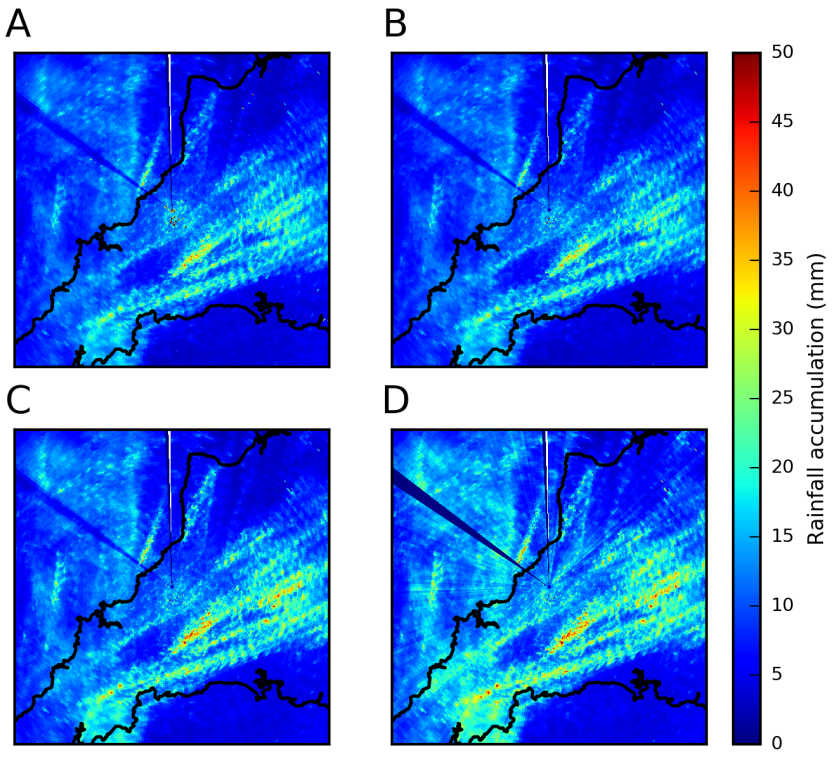

FIGURE 7.5: Total rainfall accumulation for the COPE field campaign as measured by the NCAS mobile weather radar at an elevation of 1.5°. Panel A shows the rainfall as derived from Z_m, B the accumulation from Z_{QC}, C the accumulation from Z_A and D the accumulation from Z_C. Each panel is a 100 km square centred on the radar and contains the accumulation from 1131 valid scans across the field campaign.

extrapolated to the north west to cover the higher accumulations observed in this area highlighting the difficulty of validating radar rainfall estimates even in a location that is covered by a widely distributed rain gauge network.

Overall the total rainfall accumulations suggest that unless correction for partial beam blockage is possible it is better to use data from a higher elevation than use blocked low elevation data, but once correction is possible the reduced height of the beam at the low elevation generates more representative rainfall estimates. They also indicate regions of persistent ground clutter still present problems for the radar's QPE despite the QC processing and more work needs to be done to handle these regions to obtain accurate QPE. Rainfall accumulations from the next available elevation indicates this could be

achieved by merging in data from a height above the ground clutter, subject to a lack of representatively due to increasing while another solution could be to selectively merge in the velocity filtered reflectivity data from the radar while avoiding the inherent issues previously observed in this field. These options will be explored more in the future and are touched on briefly in Chapter 8.

7.2.2 Widespread stratiform rainfall of low intensity - an example of uncertainty in reflectivity rainfall estimates

The following example highlights an interesting case which explores the uncertainty in radar QPE. The case highlights the benefits of the processing system outlined in this thesis, while also demonstrating a situation that is difficult to account for when using radar QPE. On the 17 August 2013 a warm front passed across the Cornish peninsula causing widespread rainfall of 1 to 2 mm/hr intensity with rainfall accumulations of 5.4 mm to 10.4 mm recorded in the EA rain gauges. Radar data from the event has previously been shown in Figures 5.12, 6.7 and 6.14 while Figure 7.6 shows a further example of the fully corrected reflectivity along with the location of the three rain gauges used to illustrate this case study.

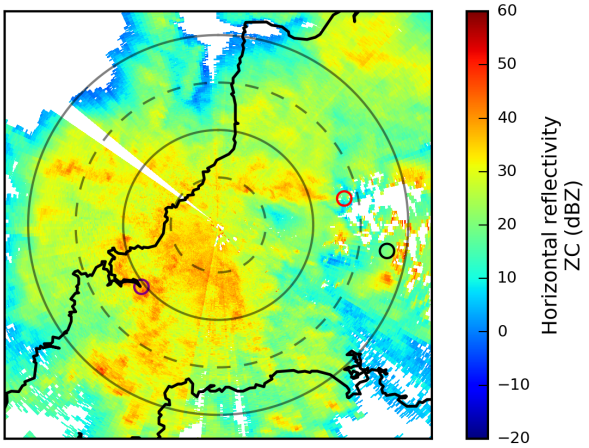

FIGURE 7.6: Corrected horizontal reflectivity PPI at 0.5° elevation, 2013-08-17 11:57 UTC. Range rings are spaced at 10 km intervals, and the panel is 90 km square centred on the radar. Each of the open circles shows the location of a rain gauge used in this section, the purple circle to the west is Wadebridge, the red circle to the east is Roadford and the black circle to the east is Mary Tavy.

The first rain gauge of interest is located at Wadebridge, at a radar azimuth of 233° and a range of 20.7 km (purple circle, Figure 7.6), where 8.2 mm of rainfall was recorded by the gauge during the radar operating period on this day. This location is within a sector of the 0.5° elevation scan blocked by Davidstow woods which requires a correction of 6 dBZ and the benefit of this correction can clearly be seen in Figure 7.7 which shows the cumulative rainfall accumulation from this gauge as measured by the gauge and the radar.

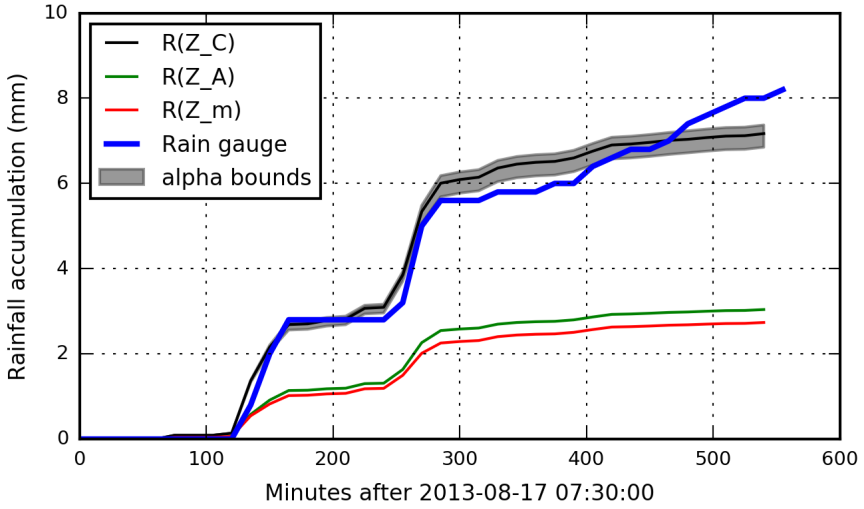

FIGURE 7.7: Rainfall accumulations at Wadebridge. The thick solid blue line is the accumulation as measured by the tipping bucket rain gauge, while each of the remaining lines is the accumulation of the radar pixel containing the rain gauge. The solid red line is from the measured reflectivity (Z_m), the solid green line is the accumulation from attenuation corrected reflectivity (Z_A, with $\alpha = 0.27$ dB/deg) and the solid black line is the fully corrected reflectivity (Z_C). The grey region represents the variation of the fully corrected accumulation when changing α from 0.14 to 0.35 dB/deg during attenuation correction.

In the Figure, the rainfall from corrected reflectivity (Z_C) after 5 hours is within 0.5 mm of the rain gauge accumulation and could be considered to agree within the measurement uncertainty of both instruments (considering attenuation correction and gauge evaporation). This contrasts greatly to the rainfall record generated from the original measured reflectivity (Z_m) which is 3.5 mm less than that recorded by the rain gauge at this time, indicating the magnitude of the correction is reasonable during this time period. However during the four hour period from 12:30 to 16:30 the rain gauge measures an additional 2.4 mm of rainfall compared to 1.1 mm estimated by the radar a swing in percentage

error from 9% to -54% which is a considerable difference. The first hypothesis to explain this change is that the beam blockage is causing under measurement of rainfall during periods of lower intensity rainfall. Observations shows there is no total blockage of the rainfall signal during this period which would be required to create a low intensity under measurement by the radar and the success of the correction within the first five hours of the data record suggests the magnitude of the correction is robust in these conditions. Investigation of additional rain gauge records (Figure 7.8) indicate a similar shift in measurement accuracy occurs across the peninsula which suggests that the change is more fundamental, either to the radar hardware or to the atmospheric conditions.

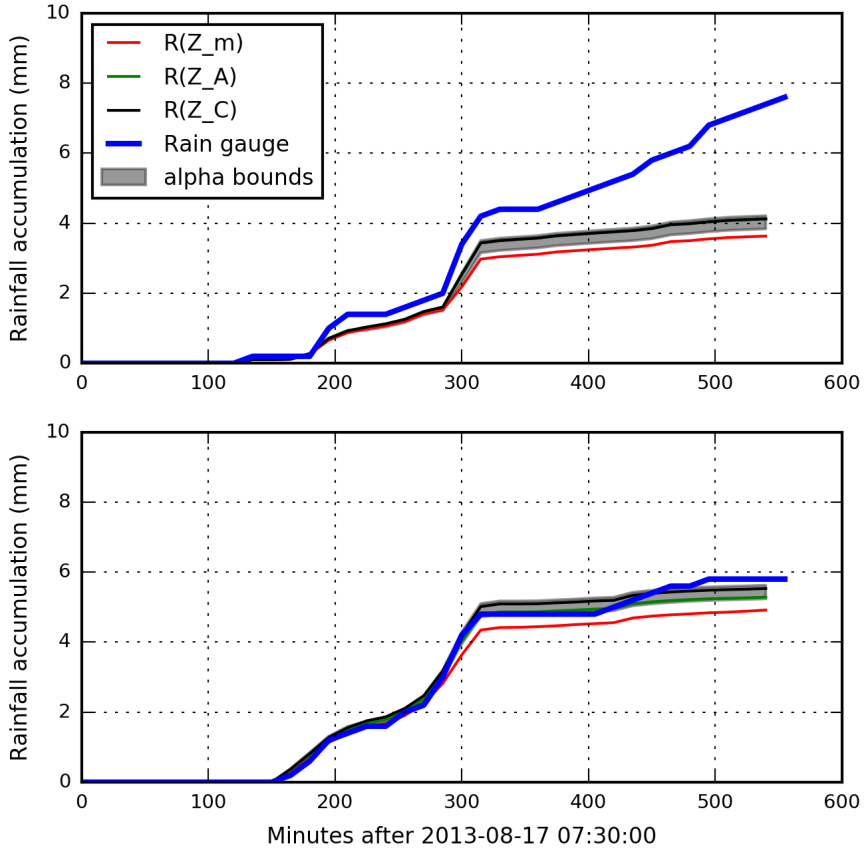

FIGURE 7.8: Rainfall accumulations at Mary Tavy (top panel) and Roadford (bottom panel). The thick solid blue lines are the accumulation as measured by the tipping bucket rain gauges, while each of the remaining lines is the accumulation of the radar pixels containing each of the rain gauges. Each of the lines is as per Figure 7.7, with the attenuation corrected green line in the top panel being directly overlain by the fully corrected reflectivity as the PBB correction at this location is 0 dBZ.

Figure 7.8 shows the rainfall records for Mary Tavy, which is located at an azimuth

of 101° and a range of 36 km (black open circle, Figure 7.6) and Roadford, which is located at an azimuth of 80° and a range of 27.2 km. The change in rainfall intensity observed at Wadebridge is also visible in the rain gauge records at these sites, with the change occurring later as the sites progress eastwards, and the radar rainfall estimates in each location maintain a near constant intensity after 12:30 in each location. The radar underestimates the rainfall accumulation at Mary Tavy by 80% in the late afternoon period compared to a 20% underestimation up to 12:30 while the radar underestimates Roadford by 58% after 14:00 compared to an overestimate of 6% up to 12:30.

These locations suggest the hardware is unlikely to be at fault as indicators would be a shift in the radar rainfall accumulations that match the timing of the rain gauge accumulations but not the intensity or a concurrent change in the radar accumulations across all locations, the absence of which suggests the atmospheric conditions are the most likely cause of the significant underestimation of accumulation during this period.

To investigate the cause of the underestimation additional data from the vertically pointing micro rain radar (MRR) installed as part of the COPE project was investigated. Figure 7.9 shows the time height profile of rainfall intensity estimated by the MRR during this time period, with the two periods of moderate rainfall seen in the rain gauge records observed as full depth rainfall intensities of greater than 4 mm/hour occurring at 09:30 and 12:00, while the rainfall observed after 13:00 is concentrated within 400 m of the surface and at a much lower intensity.

The time-height data suggests low level rainfall generation following the passage of the surface warm front at this time, which could explain the underestimation of the radar in this situation as the beam overshoots the region of increasing rainfall intensity. A quasi-vertical profile of reflectivity generated using data from the 8.5° elevation scans allows further investigation of the vertical structure of the rainfall in this case (Figure 7.10) and indicates a strong increase in the observed reflectivity close to the surface during the period between 13:30 and 16:00, particularly after 15:00.

The average vertical reflectivity gradient observed in the period between 15:00 and 16:30 is $-5\,\mathrm{dBZkm}^{-1}$ in the first 200 m of the profile (between 400 m and 600 m above sea level) increasing to $-20\,\mathrm{dBZkm}^{-1}$ once the profile is 800 m above ground, which could indicate the corrected reflectivity above the rain gauges is as much as 2.5 dBZ lower

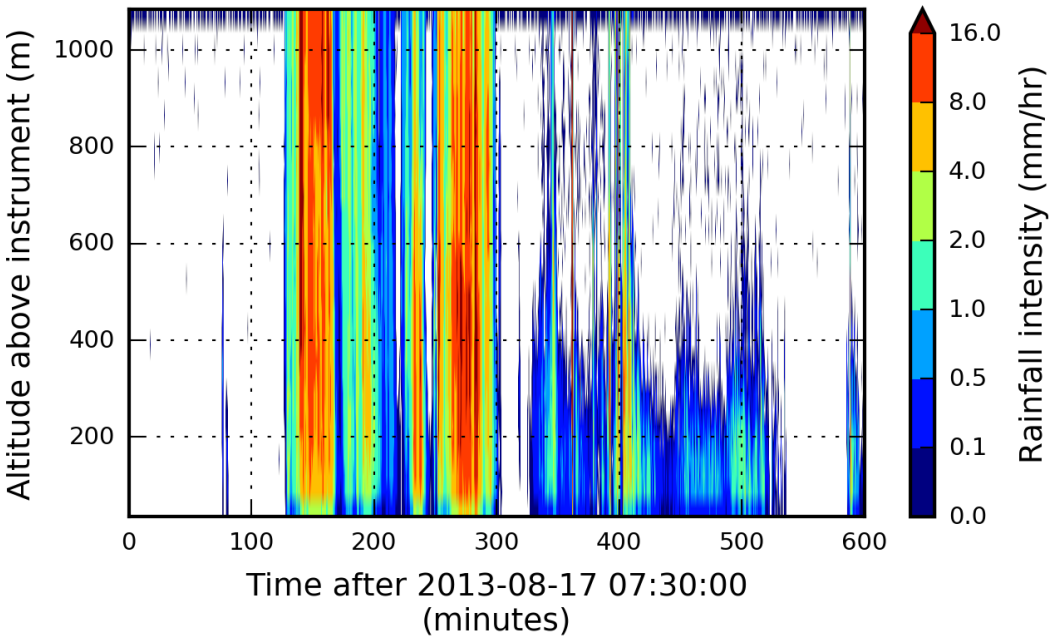

FIGURE 7.9: Time-height profile of micro rain radar data obtained during the COPE field campaign on 2013-08-17. Data contains 31 vertical levels at 35 m spacing, with 30 s sampling intervals.

than the true surface reflectivity during this time period (Wadebridge is located at 2 m above sea level while the radar beam centre is at 505 m at this range). To correct for this apparent vertical intensification of rainfall requires the following assumptions, firstly that the vertical gradient of horizontal reflectivity as measured within 5 km of the radar represents a homogeneous stratiform layer which extends over the rain gauges, and secondly that the vertical gradient can be extended to the surface with further increases in reflectivity below the observation sites (both the X-band radar and the MRR are located at approximately 300 m above sea level), both of which would be difficult to justify without the support of the rain gauge observations. However this case provides an opportunity to test the correction against external data, the results of which are shown in Figure 7.11 for Wadebridge.

The first correction (VPRa) is simply a linear VPR with a gradient of -5 dBZ/km, as given by the average reflectivity gradient during the period from 15:00 to 16:30 in the QVP which is effectively an addition of 2.5 dBZ for Wadebridge. This correction is applied to Z_C for all times after 14:45 UTC, which is the time the QVP of reflectivity

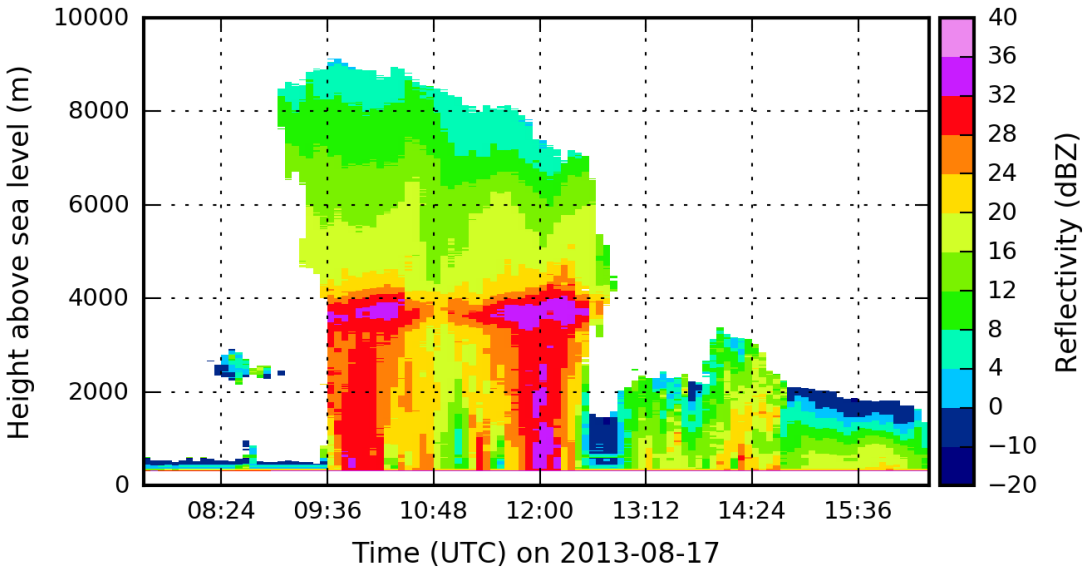

FIGURE 7.10: Quasi-vertical profile of reflectivity generated from measured reflectivity using the 8.5° elevation scans on 2013-08-17. Each vertical data point must contain at least 270 azimuths to be included within the vertical profile. Vertical data separation at 8.5° varies from 22.5 m at ground level to 23.5 m at 10 km altitude due to earth curvature with range.

begins to show a homogeneous vertical gradient of reflectivity around the radar. During this period the correction only adds an additional 0.1 mm to the rainfall at Wadebridge and clearly doesn't account for the difference between the rain gauge and the radar, with both the magnitude and timing of the correction seen to be wrong. The second correction (VPRb) is a more bespoke correction for this site, with 5 dBZ added to each scan after 13:50, representing a doubling of the reflectivity gradient to −10 dBZ/km. This is more representative of the atmospheric conditions slightly higher in the atmosphere as observed during the QVP rather than the profile very close to surface. The second profile adequately models the vertical changes in reflectivity with the radar rainfall accumulation closely matching the rain gauge accumulation until 15:15, after this time the radar begins to underestimate the rainfall accumulation indicating a further intensification of the vertical gradient of reflectivity which would require further site specific tuning to correct.

This case study indicates the potential importance of vertical profile of reflectivity correction even in cases where the radar beam is well below the melting layer. The first 5

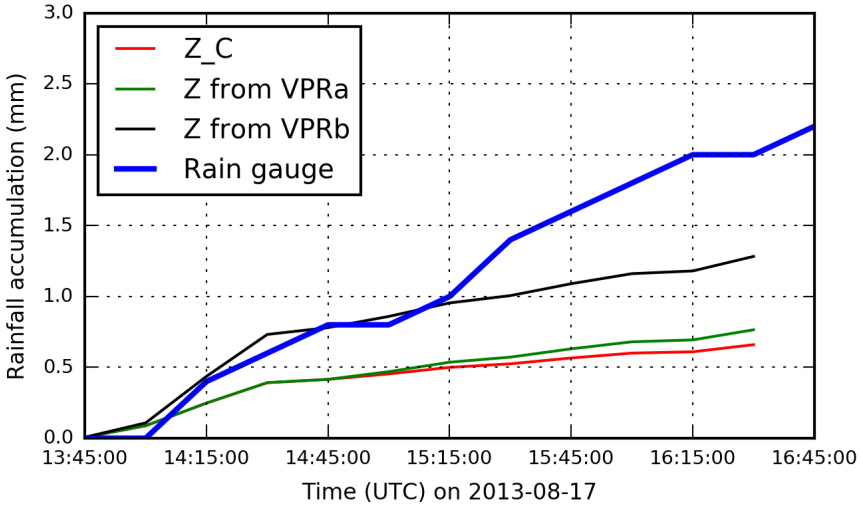

FIGURE 7.11: Rainfall accumulations at Wadebridge corrected using a vertical profile of reflectivity. The thick solid blue line is the accumulation as measured by the tipping bucket rain gauge, while each of the remaining lines is the accumulation of the radar pixel containing the rain gauge. The solid red line is from the corrected reflectivity (Z_C), the solid green line is the accumulation from reflectivity corrected with a 2.5 dBZ offset applied from 14:45 onwards (VPRa) and the solid black line is the accumulation from reflectivity corrected with a 5 dBZ offset applied from 13:50 onwards (VPRb).

hours of the day suggest that the corrected reflectivity values obtained using dual polarisation corrections produce much better QPEs than the original measured reflectivity data and that the uncertainty introduced by attenuation correction is not significant in the case of moderate intensity stratiform rainfall of this type. The case study also suggests quasi-vertical profiles (QVPs) of reflectivity may be used for vertical profile of reflectivity correction below the melting layer and this is something that should be explored in future research, particularly when more stratiform rainfall data is available. This idea is explored briefly in Chapter 8.

7.3 Dual polarisation moments as direct rainfall estimators

In addition to the use of dual polarisation moments for the correction of the measured reflectivity several studies have used these moments to directly estimate rainfall, either in conjunction with the horizontal reflectivity or as an independent estimate. The following section details the use of Z_{DR}, K_{DP} and specific attenuation as rain rate estimators, again

comparing these estimates to the rain gauge observations available for COPE along with rainfall estimates from the corrected horizontal reflectivity.

7.3.1 Differential reflectivity as a rainfall estimator

Differential reflectivity is used in conjunction with horizontal reflectivity to estimate rainfall rate. As Z_{DR} indicates the equivolume drop diameter for the distribution it is indicative of the size distribution of drops contributing to the horizontal reflectivity, which is proportional to D^6 and the number concentration of the drops. Therefore the higher the Z_{DR} the lower the number of drops required to generate the same horizontal reflectivity and the lower the rainfall rate compared to a distribution containing a larger number of smaller drops. Equation 7.2 indicates the typical relationship used at X-band to estimate rainfall using reflectivity and differential reflectivity (Bringi and Chandrasekar, 2001), where both Z_e and Z_{DR} are in logarithmic units. This equation is represented visually in Figure 7.12 which also shows the equivalent representations of the reflectivity only rainfall relationships first shown in Figure 2.1 which represent drizzle, convection and the UKMO standard reflectivity-rain relationship. The phase space indicates that convective conditions are generally associated with larger drop sizes (higher Z_{DR}) than drizzle (low Z_{DR}) and that the same horizontal reflectivity can produce vastly different rain rates depending on the bulk drop size.

$$R = 3.9 \times 10^{-3}(10^{0.107Z_e})(10^{-0.597Z_{DR}}) \tag{7.2}$$

The phase space can also be used to indicate some of the advantages and weaknesses of using both reflectivity and differential reflectivity, particularly in attenuating rainfall events. Taking a simple case where the measured horizontal reflectivity is 40 dBZ and the measured Z_{DR} is 1 dB, then the estimated rainfall rate would be 9.45 mm/hour. If the path phase shift to this point is 20° then the total horizontal attenuation would be 5.4 dBZ and the total differential attenuation would be 0.9 dB giving actual values of 45.4 dBZ and 1.9 dB respectively. These would estimate a rain rate of 10.38 mm/hour which indicates that the original measured rainfall rate is only a slight underestimate of the actual if attenuation correction is not possible and atmospheric conditions are as expected with regards to α and β. This contrasts to the results obtained using only measured reflectivity

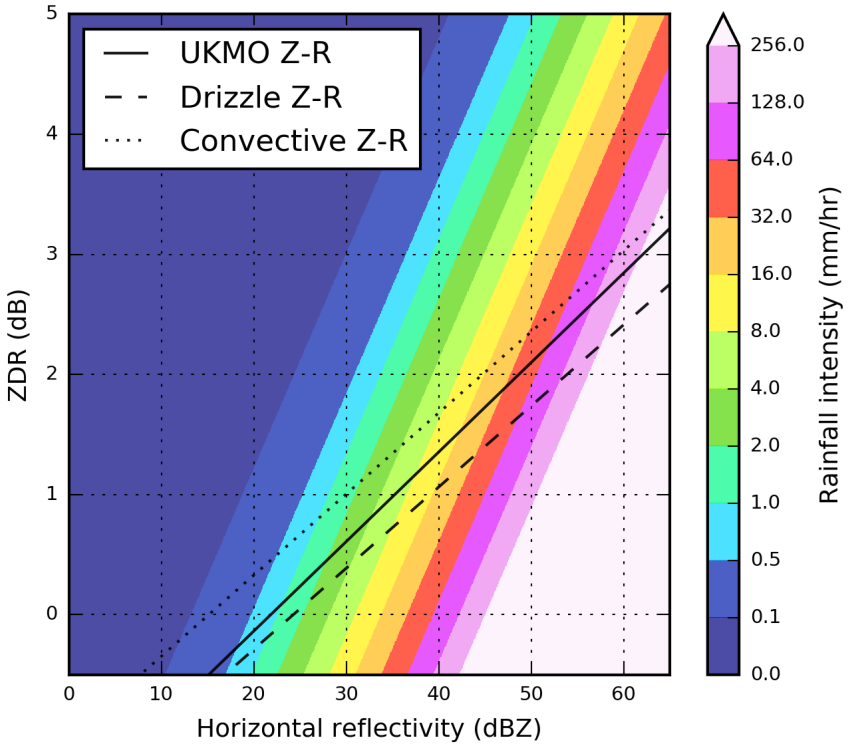

FIGURE 7.12: Two dimensional representation of the R(Z_h,Z_{DR}) relation for X-band radars. The colormap represents the rainfall intensity from the two radar moments. The plotted lines represent the one dimensional rainfall equations which only use reflectivity to estimate rainfall intensity, the solid line is the UKMO relationship ($a = 200$, $b = 1.6$), the dashed line is the assumed Z-R relationship for drizzle ($a = 140$, $b = 1.5$) and the dotted line is the assumed Z-R relationship for convective rainfall ($a = 500$, $b = 1.5$).

where the measured rain rate is 11.5 mm/hour compared to an attenuation corrected rain rate of 25 mm/hour. This is visible within the 2D phase space, where attenuation and differential attenuation move values towards the bottom left, almost parallel to the lines of equivalent rainfall intensity within the plot. However in situations where horizontal attenuation is much lower than differential attenuation (say β is doubled as a result of a strong convective updraught) this no longer holds true and the rainfall estimated from the measured values would be an overestimate of rainfall rate, which is maintained if both reflectivity and Z_{DR} are both not accurately corrected (if the average atmospheric β is used for example). This is noticeable if we return to the example in Section 6.2.1, Figure 6.4 and convert the corrected Z_h and Z_{DR} into rainfall intensity using equation 7.2 which leads to significant estimates of rainfall intensity which are clearly incorrect when the Z_{DR} is under corrected relative to the horizontal reflectivity. Figure 7.13 illustrates this, with

the uncertainty bounds indicating the two most extreme scenarios. Firstly the case where differential reflectivity is over corrected with respect to the reflectivity ($\alpha = 0.14\,\mathrm{dBZ/deg}$ and $\beta = 0.06\,\mathrm{dB/deg}$ being the extreme of this) leads to very low rainfall intensities and secondly when differential reflectivity is significantly under corrected compared to the reflectivity ($\alpha = 0.33\,\mathrm{dBZ/deg}$ and $\beta = 0.03\,\mathrm{dB/deg}$) which leads to extremely high rainfall estimates. The bounds illustrate the extreme cases which are unlikely to occur in reality, but the average case in this example is exhibiting signs of under correction of Z_{DR} which leads to rainfall intensity estimates of over 400 mm/hour between 30 km and 35 km range in comparison to those generated with just reflectivity which are no more than 100 mm/hour at the same range. In this case this results from the corrected differential reflectivity still being below zero, which is clearly inconsistent with observations of rainfall and suggests that β should be higher for some of this radial, most likely in the region of high reflectivity at 28 km which is probably a "hot-spot". Doviak and Zrnić (1984) noted that R(Z,Z_{DR}) performs best when the random errors in differential reflectivity are small, which is clearly not the case when differential attenuation of this magnitude is introduced, nor is it the case when rainfall rates are very low as measurement noise has a greater effect at low intensities both of which suggest that differential reflectivity may produce less accurate rainfall accumulations than the single moment approach, which has been tested through the generation of multiple rainfall accumulations using R(Z,Z_{DR}).

The most straightforward rainfall estimate using R(Z,Z_{DR}) is to take the moments as measured filtered using fuzzy logic to include only rainfall echoes, with the expectation that in most cases any attenuation will be counteracted by differential attenuation as discussed above. Secondly reflectivity can be corrected for partial beam blockage, which should generate better estimates, then both fields can be corrected for attenuation using ZPHI. To correct differential reflectivity for attenuation the specific horizontal attenuation can be converted to specific differential attenuation using a fixed ratio as described by Park et al. (2005) and set here to 0.14 as per the average value found for X-band in that paper. Given the errors noted by Doviak and Zrnić (1984) and the problems in attenuating situations a final accumulation is proposed which uses R(Z,Z_{DR}) when reflectivity is greater than 10 dBZ and Z_{DR} is greater than 0.2 dB but R(Z) otherwise. This avoids the situations where Z_{DR} is attenuated to below zero and not adequately corrected, and also the light rainfall situations where measurement of Z_{DR} is most uncertain (10 dBZ is a less conservative threshold for this than the one proposed by Doviak and Zrnić (1984) who

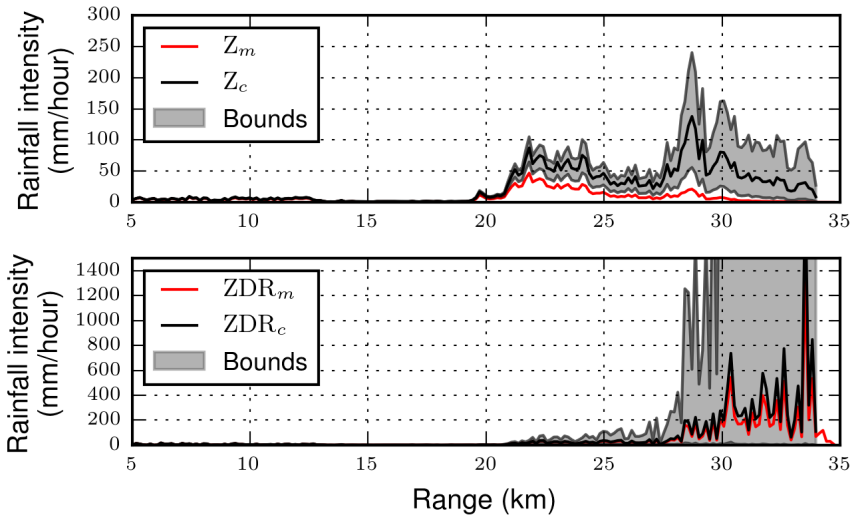

FIGURE 7.13: Rainfall estimates following correction of horizontal reflectivity and differential reflectivity using a linear transformation of Ψ_{DP}. Data shown is taken from the 2013-08-02 17:51UTC radar volume at an azimuth of 86° and elevation of 0.5° . Rainfall estimates from measured radar variables are shown by solid red lines, with the top panel showing rainfall from the UKMO Z-R relationship using horizontal reflectivity corrected with an α of 0.27 dBZ/deg (solid black line) and bounded with α of 0.14 and 0.35 dBZ/deg. The lower panel shows rainfall estimated using Equation 7.2 where the solid red line is the measured values of horizontal reflectivity and Z_{DR} and the solid black line is the reflectivity corrected using an α of 0.27 dB/deg and the Z_{DR} corrected with a β of 0.045 dB/deg. The bounds on the lower plot are equivalent to an α of 0.14 dBZ/deg paired with a β of 0.06 dB/deg for the lower extreme and an α of 0.35 dBZ/deg paired with a β of 0.03 dB/deg for the upper extreme.

propose a rainfall intensity of 20 mm/hour as the threshold, equivalent to a reflectivity of 43.8 dBZ if using the UKMO R-Z relationship). The total rainfall accumulations for each of these methods is shown in Figure 7.14 and is significantly different to the totals obtained using just reflectivity as seen in Figure 7.2. Firstly the filtered results from each method (Panel A of Figure 7.14 and Panel B of Figure 7.2) show that the differential reflectivity method is far more susceptible to ground clutter contamination which passes through the filter, with a much greater area of Dartmoor exceeding 50 mm of accumulation. In addition the rainfall accumulations at the furthest ranges, particularly to the east, are noticeably greater (>30 mm compared to <20 mm) when using differential reflectivity which could be indicative of a DSD containing more small drops leading to higher rainfall estimates or it could be a result of sampling wet snow above the bright band (which typically has a Z_{DR} of 0.1 to 0.2 dB) with moderate reflectivity which leads to higher rainfall estimates than the Z-R method. Comparison between Panels C and

D (Figure 7.14) indicates that the echoes contributing to the majority of this rainfall accumulation must have a Z_{DR} of below 0.2 dB as the combined estimate in Panel D is much lower in this region than the pure R(Z,Z_{DR}) method.

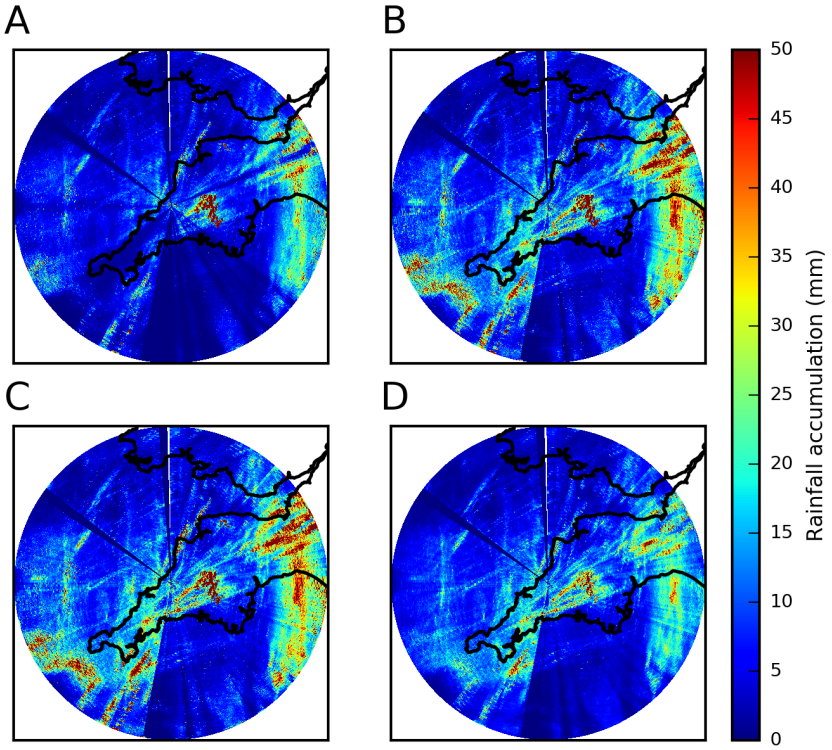

FIGURE 7.14: Total rainfall accumulation for the COPE field campaign as measured by the NCAS mobile weather radar at an elevation of 0.5° when using R(Z,Z_{DR}) as the rainfall estimator. Panel A shows the rainfall as derived from Z_{QC} and Z_{DR}, B the accumulation when Z_{QC} is corrected for beam blockage and C the rainfall accumulation using Z_C with attenuation corrected Z_{DR} (ratio of A_h to A_{DR} set to 0.14) and D shows the accumulation from a combination of R(Z,Z_{DR}) and R(Z). Each panel is a 300 km square centred on the radar and contains the accumulation from 1131 valid scans across the field campaign.

With the exception of Dartmoor it is not clear whether the pure R(Z,Z_{DR}) method is bettered by the combination of R(Z,Z_{DR}) and R(Z), although the accumulations appear smoother. Close to the radar the two method produce largely equivalent results, with slightly more rainfall when using the pure method which indicates accumulations that are driven more by warm rain and smaller drops. The pure method also has much greater localised variation in the estimates at far range which is a likely indicator of measurement

variation strongly influencing the results. Comparison to rain gauges shows that the pure method has the lowest mean percentage difference of all the methods analysed so far (2% compared to 26% for R(Z_C)) but it's MAPD is 40% compared to 31% for fully corrected reflectivity. These results indicate that the rainfall totals are less biased than the reflectivity estimates but have a much greater spread across the sample, with large over and under estimates compared to the rain gauges.

Figure 7.15 shows scatter plot comparisons of radar and rain gauge for each of the four R(Z,Z_{DR}) methods. Linear regression with zero offset indicates little difference in the R^2 of the pure method (0.28) and the combined method (0.32) which are both lower than the R^2 of R(Z_C) (0.34). The gradients of these regressions are 1.05 and 0.78 respectively.

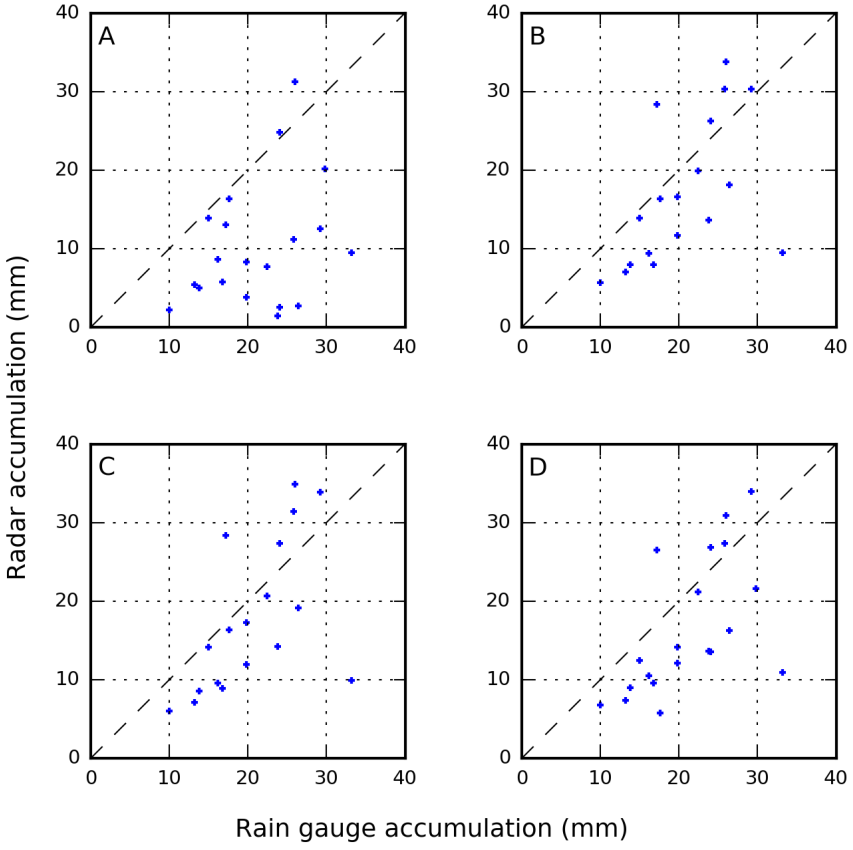

FIGURE 7.15: Comparison of rain gauge total rainfall accumulation for the COPE field campaign with rainfall as estimated by the NCAS mobile weather radar at an elevation of 0.5° using R(Z,Z_{DR}). Each of the panels y-axes shows the rainfall accumulations as taken from the panels of Figure 7.14, A is QC filtered, B is corrected for beam blockage, C includes attenuation correction of Z_h and Z_{DR} and D merges R(Z) and R(Z,Z_{DR}). Each blue cross represents the total for each of the EA rain gauge sites. The dashed line in each panel is the one to one line.

Removing Mary Tavy, which the radar systematically underestimates in all methods (rain gauge total of 33.2 mm), and St Clether, which is influenced heavily by ground clutter, increases the gradient of both methods to 1.15 and 0.86 respectively and also the R^2 to 0.42 and 0.51 respectively. Although a limited set of points for regression analysis the comparison to rain gauges provides an indication that rainfall estimation using R(Z,Z_{DR}) is less biased than using reflectivity alone, but that measurement and correction uncertainty lead to greater variability in the estimates, decreasing the correlation between the radar results and the rain gauge totals. Combining the two methods as in Panel D of Figures 7.14 and 7.15 decreases the variability caused by erroneous Z_{DR} measurements while providing rainfall estimates that are slightly biased towards under measurement by the radar relative to the rain gauges, but less biased than those estimates using reflectivity alone. Clearly the combination of the two methods could be improved to more accurately identify situations where one is more appropriate than the other, using additional radar variables and information from the fuzzy classifier along with case studies but this will be explored in conjunction with combining rainfall estimates from the other dual polarisation moments available (K_{DP} and A_h) in Section 7.4.

7.3.2 Specific differential phase shift as a rainfall estimator

As shown in Section 2.4.3 specific differential phase is an often used estimator for rainfall intensity due to its reduced sensitivity to the DSD when compared to reflectivity. It is also insensitive to hail and graupel (as they have a circular effective cross section) and is used to measure the liquid rainfall content of echoes which contain a mixture of ice and liquid rainfall. The signal processor of the mobile radar generates K_{DP} using Fourier transformation of the measured phase shift, which can be used to assess the performance of K_{DP} in the first instance, given there are several alternative methodologies for the calculation of K_{DP} (Schneebeli and Berne, 2012; Wang and Chandrasekar, 2009; Ryzhkov and Zrnic, 1996, for example). One feature of all proposed methodologies is the difficultly of accurately calculating low values of K_{DP} due to measurement noise in the phase shift, which leads to K_{DP} being utilised more at higher rainfall rates. To examine this uncertainty two rainfall accumulations have been generated here, one which uses R(K_{DP}) whenever possible, only utilising R(Z_C) when K_{DP} is not estimated and a second which selectively uses R(K_{DP}). This second method uses R(Z_C) when the measured K_{DP} is

below 0.5 deg/km and/or when R(Z_C) is below 5 mm/hr, it uses R(K_{DP}) when R(Z_C) is greater than 10 mm/hr and the weighted average of R(Z_C) and R(K_{DP}) when the rainfall rate is between 5 and 10 mm/hr where the weighting for R(K_{DP}) varies linearly from 0 at 5 mm/hr to 1 at 10 mm/hr. Through the process the X-band R(K_{DP}) relationship from Ryzhkov et al. (2014) is used, where the rainfall coefficient is 16.9 and the exponent is 0.801.

Figure 7.16 shows the total rainfall accumulations out to 150 km range for each of these methods, with the large difference being a result of overestimation of rainfall by R(K_{DP}) at low rainfall rates where the estimation uncertainty has the greatest effect on rainfall rates. Taking a true rainfall rate of 2 mm/hr, the equivalent K_{DP} would be 0.07 deg/km, which when the measurement accuracy is no better than 0.2 deg/km is not accurately recordable, with rainfall estimates in the range 0 to 6 mm/hr being probable at these intensities. When the rainfall rate is more intense the measurement uncertainty no longer dominates the estimates, and with thresholding the performance of R(K_{DP}) is much more reliable as seen in Panel B.

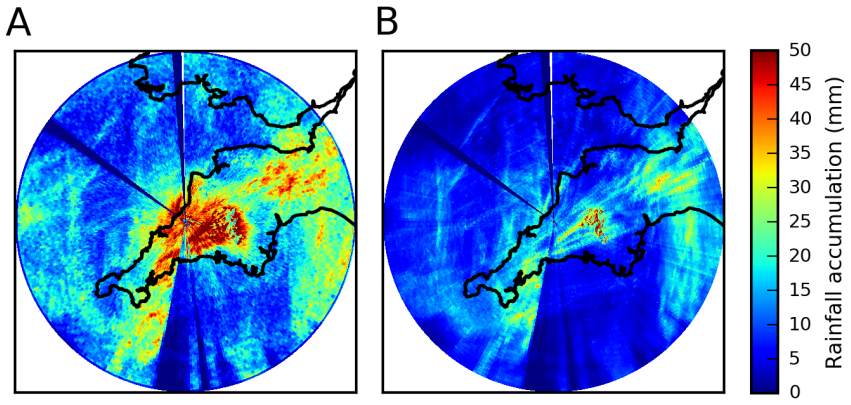

FIGURE 7.16: Total rainfall accumulation for the COPE field campaign as measured by the NCAS mobile weather radar at an elevation of 0.5° when using R(K_{DP}) as the rainfall estimator. Panel A shows the accumulation when using R(K_{DP}) whenever possible while B shows the accumulation when selectively using R(K_{DP}) at only moderate to heavy rainfall intensities. Each panel is a 300 km square centred on the radar and contains the accumulation from 1131 valid scans across the field campaign.

This improvement is observed in the correlations between radar accumulations and the rain gauges, with R^2 increasing from -0.04 to 0.26 and the gradient reducing from 1.68 to 0.70. The results for the second method are within the same range as the other approaches explored so far, showing no benefit to using K_{DP} over the other methods. However previous research has indicated $R(K_{DP})$ to be beneficial during periods of intense rainfall, and a closer look at its performance in this situation is required.

7.3.2.1 Performance in intense rainfall

The following example shows the benefit of using $R(K_{DP})$ during periods of intense rainfall by focusing on a period of convective rainfall on 2 August 2013, where a line of convective cells developed along a convergence line running along the peninsula. This example has previously been seen in Figure 7.13 where the problem of attenuation correction for both reflectivity and differential reflectivity was examined and Figure 7.17 repeats the rainfall estimates from corrected reflectivity alongside the rainfall estimate obtained solely from using $R(K_{DP})$ for this radial. During the first 15 km of the shown radial there is generally good agreement between the two estimates but the previous observations about estimation errors in lighter rainfall are shown between 10.5 and 13 km where $R(K_{DP})$ estimates zero rainfall despite the reflectivity signature and between 13 and 19 km where $R(K_{DP})$ is estimating 6 mm/hr compared to reflectivity estimates of under 2 mm/hr. During the most intense period of rainfall, between 27 and 35 km the general trend of the two estimates is similar, but the $R(K_{DP})$ has a much smoother profile and a lower peak rainfall intensity. One reason for this is the contamination of the reflectivity estimates with ice phase hydrometeors which lead to higher reflectivity being observed than would be generated solely from the liquid water content of the precipitation while another reason is the smoothing required to generate acceptable estimates of K_{DP} from the noisy data, as smoothing always leads to a reduction in peak intensity. The $R(K_{DP})$ lies within the uncertainty bounds of the reflectivity estimates due to the significant amount of attenuation occurring in this example, and given $R(K_{DP})$ provides a rainfall measurement which is not affected by attenuation it can be used to examine the value of α used in this study in these cases, with good agreement seen between the $R(K_{DP})$ and the $R(Z_C)$ when α=0.27 dBZ/degree in the region beyond the rainfall maximum.

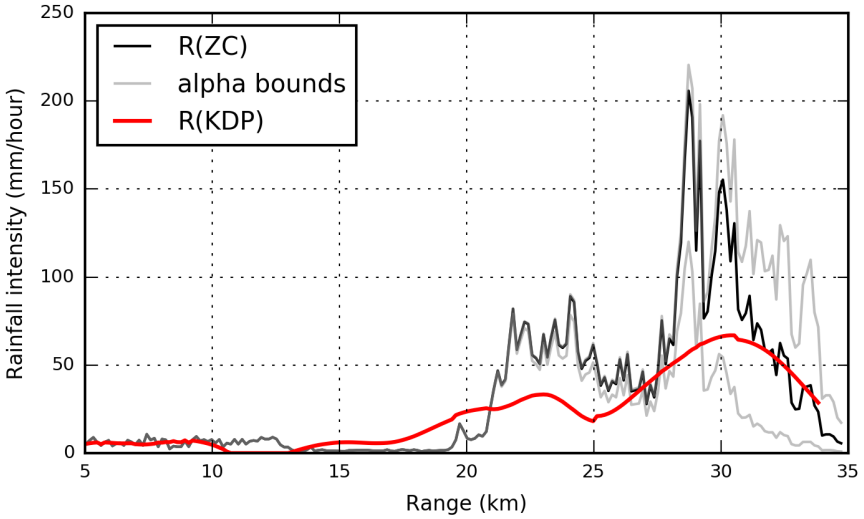

FIGURE 7.17: Rainfall estimates using R(K_{DP}) compared to R(Z_C). Data shown is taken from the 2013-08-02 17:51UTC radar volume at an azimuth of 86° and elevation of 0.5° . Rainfall estimates from the radar calculated K_{DP} is shown by the solid red line, with the solid black line showing rainfall from the horizontal reflectivity corrected with an α of 0.27 dBZ/deg (solid black line). The gray lines show the rainfall when correcting using an α of 0.14 and 0.35 dBZ/deg (bottom and top respectively)

This example, and others from the field campaign, indicate that R(K_{DP}) adds useful information to rainfall estimates in these higher intensity cases but the overly smooth profile of K_{DP}, particularly in convective cells and the difficulty in obtaining reliable estimates of low values of K_{DP} indicates an alternative estimation of K_{DP} will be required to obtain more accurate rainfall accumulations in the future. Alternative estimation techniques exist which adapt the length of the filtering window applied to the data depending on the reflectivity observed at that point, which gives higher spatial resolution within the region of peak rainfall intensity leading to higher maximum intensities in convective cells (Wang and Chandrasekar, 2009; Matrosov et al., 2006; Brandes et al., 2001). Given this is likely to provide more accurate rainfall estimates in these regions a more sophisticated estimation should be explored for the mobile X-band radar in the future.

7.3.3 Specific horizontal attenuation as a rainfall estimator

Generating rainfall estimates using specific horizontal attenuation is a recent development in radar QPE and simply involves a theoretical transformation from attenuation to rainfall

intensity using Equation 7.3 where a and b are temperature and frequency dependant (Ryzhkov et al., 2014; Wang et al., 2014; Diederich et al., 2015a,b).

$$R = a(A_h)^b \tag{7.3}$$

As in the work on beam blockage correction, the temperature dependant values for a and b have been set to those for an atmospheric temperature of 10 °C ($a = 45.5$ and $b = 0.83$) and rain rates have been generated using A_h derived during the ZPHI attenuation processing. Rainfall rates have been generated using just A_h, using A_h in-filled with R(Z_C) when missing, and using a tighter definition of A_h which requires at least 4° of phase shift along the radial segment again in-filled with R(Z_C) when R(A) is not available. The first of these methods leads to rainfall underestimation as conditions are not always suitable for the ZPHI method to generate A_h (Figure 7.18, Panel A). The second method boosts these regions while also in-filling the region beyond 105 km range and within 4.5 km where the constraints imposed during ZPHI calculation prevent A_h estimation (Panel B, Figure 7.18). The third method, as proposed by Diederich et al. (2015b) provides more stable estimates of A_h by enforcing the condition of minimum phase shift along the radial and ensures complete coverage by in-filling with R(Z_C). A fourth estimate has also been generated which utilises the theoretical reflectivity estimated from specific attenuation as in Section 6.3, but then applies the standard UKMO Marshall-Palmer rain rate conversion for reflectivity. In theory this estimate should be less accurate than the specific attenuation estimates as the coefficient and exponent for R(A) are DSD invariant, while the Marshall-Palmer relationship assumes a DSD to fit the rainfall estimate, however as the theoretical reflectivity is immune to beam blockage any changes in beam blockage should be accounted for leading to a more reliable estimate than a pure R(Z_C) estimate.

Total rainfall accumulations for each of these four rainfall estimation techniques are shown in Figure 7.18 to the full range of the radar. In Panel A the absence of rainfall estimation beyond 105 km and within 4.5 km is visible as zero accumulation in these areas. Rainfall estimation over Dartmoor is reduced compared to any previous method of rainfall estimation, suggesting R(A_h) could provide the most reliable rainfall estimates in regions of ground clutter while rainfall accumulations are elevated close to the radar, particularly

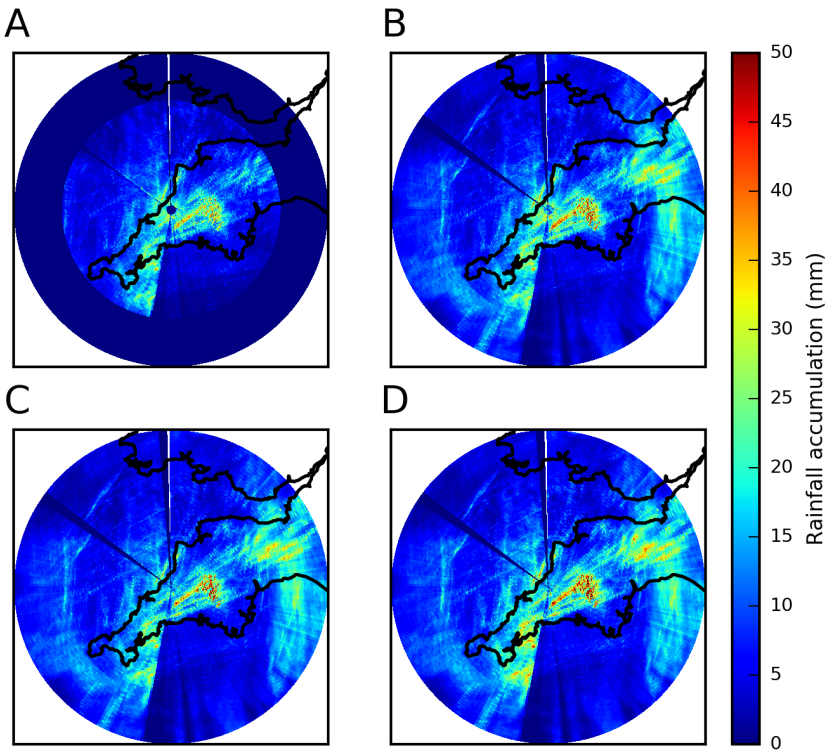

FIGURE 7.18: Total rainfall accumulation for the COPE field campaign as measured by the NCAS mobile weather radar at an elevation of 0.5° when using $R(A_h)$ as the rainfall estimator. Panel A shows the rainfall as derived from $R(A_h)$ only, B the accumulation when $R(A_h)$ is in filled with $R(Z_C)$ when not available, C the accumulation when $R(A_h)$ is used only if the path phase shift is greater than 4° otherwise use $R(Z_C)$ and D shows the accumulation from $R(Z(A_h))$ when path phase shift is greater than 4° otherwise use $R(Z_C)$. Each panel is a 300 km square centred on the radar and contains the accumulation from 1131 valid scans across the field campaign.

to the west, compared to previous estimates, which is a function of specific attenuation estimation in low total phase shift radials, as the effect is seen to disappear when applying a threshold of 4° as in Panel C. Introducing $R(Z_C)$ estimates when A_h is not calculated leads to increased accumulations (as expected) and the rainfall accumulation along the convective line region to the south east of the radar increases from the mid thirties to over 40 mm (Panel B). All four methods show resilience to beam blockage, with the blocked segments to the south west and north east not noticeable in any of the panels. However the methods all still suffer from the sensitivity drop to the south and south east of the radar, and this region is unrecoverable in all cases, suggesting higher elevation

data will always be needed for accurate rainfall estimates in this region. Panel C which shows the R(A_h) parametrisation of rainfall and Panel D which uses the theoretical reflectivity combined with the UKMO Z-R parametrisation are spatially similar but the UKMO parametrisation generates uniformly higher rainfall totals, particularly noticeable between 190° and 200° azimuth off the south coast of the Cornish peninsula.

This difference is noticeable in the comparisons with rain gauge rainfall totals seen in Figure 7.19 where only 3 sites have a higher radar accumulation than rain gauge accumulation in Panel C which uses R(A_h) while 6 sites have a higher rainfall accumulation in Panel D which uses the theoretical transformation approach. Linear regression gradients are 0.72 and 0.81 for each of the methods respectively with R^2 equal to 0.27 and 0.32 respectively, suggesting using a single rainfall parametrisation provides the most correlated results and that rainfall estimates using the theoretical reflectivity more closely match rain gauge observations than the R(A_h) parametrisation. The mean absolute percentage differences for each method are 29% and 24% respectively, both of which are lower than the difference when using corrected reflectivity alone or when using any of the methods which utilise differential reflectivity for rainfall estimation. Removing St Clether and Mary Tavy as in the previous two sections increases both the gradient and R^2 for each method, to 0.78 and 0.47 for R(A_h) and to 0.88 and 0.53 for R(Z(A_h)) and reduces the mean absolute percentage differences to 25% (R(A_h)) and 21% (R(Z(A_h))).

Contrary to the expectation that R(A_h) would outperform R(Z(A_h)) these results suggest that the derived reflectivity technique is more representative of the conditions during the field campaign. Analysis of the temperature variation of the parameters in Equation 7.3 and in the theoretical derivation of Z from A_h shows this result to be temperature invariant, and that the closest agreement between rain gauges and radar is obtained for both methods when using the parameters for 20 °C although the average increase in accumulation between 10 °C and 20 °C is only 0.5 mm for the R(A_h) technique and 0.3 mm for the R(Z(A_h)) method. These small changes in accumulations suggest that the influence of temperature variation is negligible for this method of rainfall estimation as has also been theorised by Wang et al. (2014), while Diederich et al. (2015b) noticed only a slight variation when using a fixed temperature compared to a variable temperature for each scan.

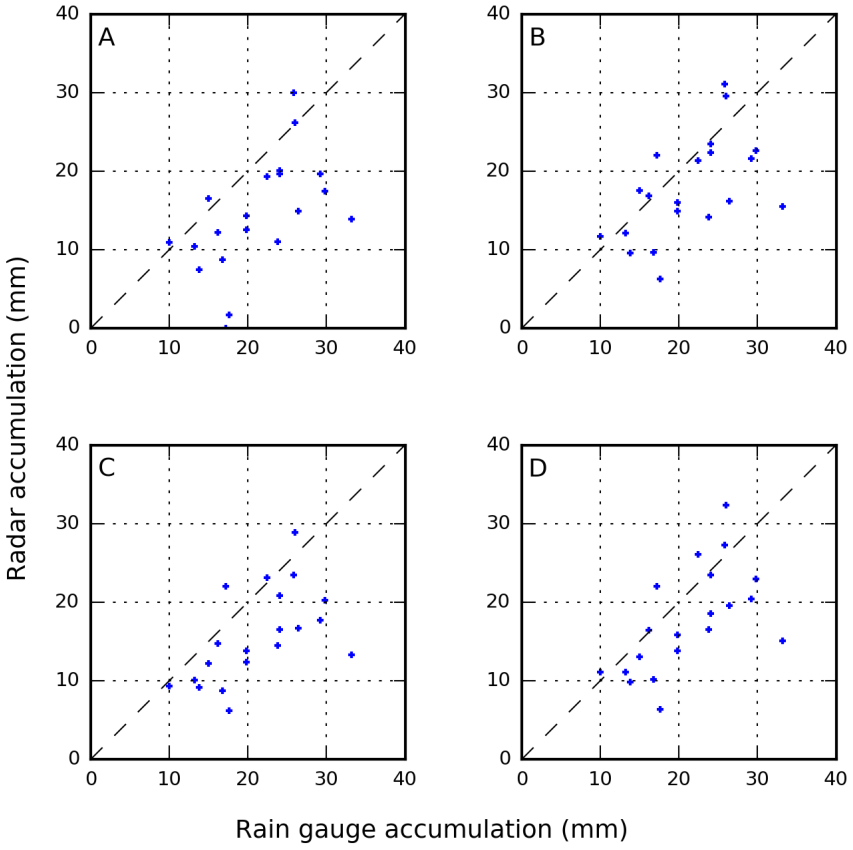

FIGURE 7.19: Comparison of rain gauge total rainfall accumulation for the COPE field campaign with rainfall as estimated by the NCAS mobile weather radar at an elevation of 0.5° using R(A_h). Each of the panels y-axes shows the rainfall accumulations as taken from the panels of Figure 7.18, A is R(A_h), B is R(A_h) with R(Z_C), C is as B but with R(A_h) only when path phase shift is greater than 4° and D is as C but with R($Z(A_h)$) instead of R(A_h). Each blue cross represents the total for each of the EA rain gauge sites. The dashed line in each panel is the one to one line.

Of the rainfall estimation methods explored in this Chapter the R(Z(A_h)) method provides the closest comparison to rain gauge observations provided missing data is in filled with an alternative rainfall estimate (in this case R(Z_C)). The R(A_h), R(Z_C) and thresholded R(Z_C,Z_{DR}) methods are the next most reliable, depending on how they are judged with R(A_h) having the lowest mean absolute percentage difference, R($Z_C Z_{DR}$) the gradient closest to 1 and R(Z_C) the highest correlation. Each of the methods explored appears to have an advantage in certain situations, R(Z(A_h)) provides good results when it is possible to estimate A_h well, R(K_{DP}) is beneficial during intense rainfall and when attenuation has introduced greater uncertainty into R(Z(A_h)) and R(Z_C) while R(Z, Z_{DR}) is more resilient to attenuation in light to moderate rainfall events provided Z_{DR} is reliable.

Given the corrections applied to reflectivity, R(Z_C) is producing good rainfall estimates and is always required in light rainfall and those situations where it is not possible to use the other methods, all of which leads to the expectation that merging each of these fields depending on the observed conditions should provide a more reliable rainfall estimate than the use of any one method. Dixon et al. (2015) and Cifelli et al. (2011) provide two examples of this approach which combine estimators through the use of a decision tree or through a weighting based on hydrometeor type certainty from a classification scheme. The following section explores variations on these techniques which combine the rainfall estimates using the accuracy of each method rather than the inferred rainfall type as used in previous studies.

7.4 Combining rainfall estimates

The combination of multiple dual polarisation rainfall estimates should lead to a more accurate rainfall product than using any one single approach and new techniques are emerging which have shown this to be possible (Dixon et al., 2015; Cifelli et al., 2011). None of these techniques have as yet made use of rainfall estimates from specific attenuation, and given R(A_h) and R(Z(A_h)) were two of the best performing rainfall estimators when compared to the rain gauges in COPE the following section explores two techniques for incorporating these estimates into combined estimators that also use R(Z_C), R(Z_C,Z_{DR}) and R(K_{DP}).

7.4.1 Methods of combining radar rainfall estimates

The first technique uses a simple decision tree to select the rainfall estimate which is likely to have the best rainfall estimate with the lowest uncertainty, the process for which is shown in Figure 7.20. The decision tree uses specific differential phase shift where the path maximum phase shift is high, where possible, or when the predicted rainfall rate from the other estimators exceeds 120 mm/hour, it then prefers specific attenuation based rainfall estimates where they are available to the other methods and finally uses differential reflectivity in moderate rainfall where it is valid otherwise reverting to corrected reflectivity. So for each range gate only one method is used, which is likely

to be the most accurate estimate for that particular range gate. A second method is to combine the estimates using a weighted average, where the weight for each rainfall product is a function of factors which determine its accuracy and uncertainty.

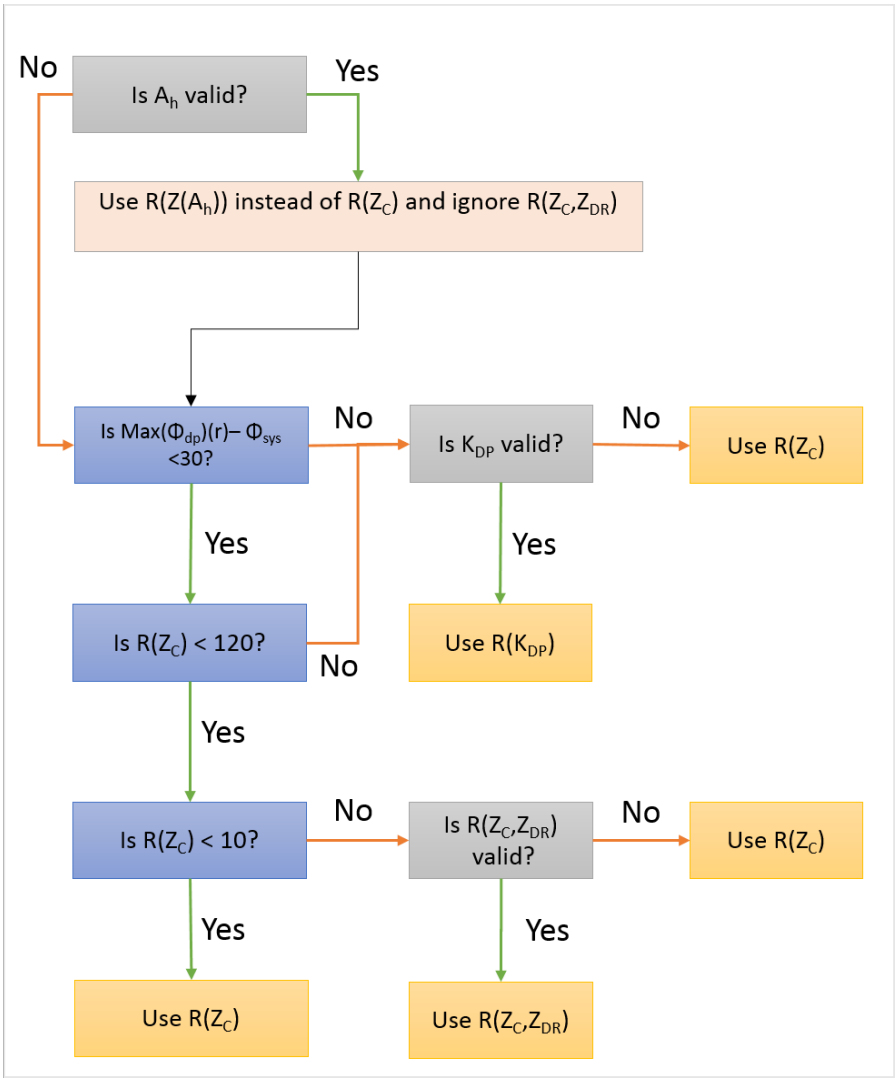

FIGURE 7.20: Flowchart describing the decision tree required to select the most appropriate rainfall estimator from the four methods available. Green arrows represent answering yes to each decision (grey box) and orange arrows represent answering no. The selected rainfall options are shown in the orange boxes. For this method a valid R(Z_C,Z_{DR}) is obtained in any case where the corrected differential reflectivity is greater than 0.5 dB, while valid K_{DP} requires the radar to have calculated K_{DP} and it to have a value greater than 0.5 (deg/km). The maximum Φ_{DP} at a range gate represents the highest smoothed phase shift up to that point along the radial.

The weighting for each of the dual polarisation rainfall estimates is based on the maximum phase shift along the radial up to that point and the corrected reflectivity, the weighting for R(Z_C) is also based on the partial beam blockage correction, while R(Z_C,Z_{DR}) also

uses the corrected differential reflectivity. In the case of R(Z(A_h)) the theoretical reflectivity is used in preference to the corrected reflectivity. Figure 7.21 shows the weights for each of these four variables, with the total weight for each variable at every range gate being the multiplication of each weight calculated at that range gate, and the rainfall being the weighted average of the four rainfall estimates. For example the weighting for R(Z_C) for an echo with a reflectivity of 50 dBZ, a radial maximum phase shift of 40 degrees and a differential reflectivity of 0.4 dB in an unblocked region of the scan (PBB = 0 dBZ) would be 0.325 ($1 \times 0.325 \times 1$), while for R(Z_C,Z_{DR}) it would be 0 ($1 \times 0 \times 0$), for R(K_{DP}) it would be 0.75 (1×0.75) and for R($Z(A_h)$) it would be 0.5 (0.5×1).

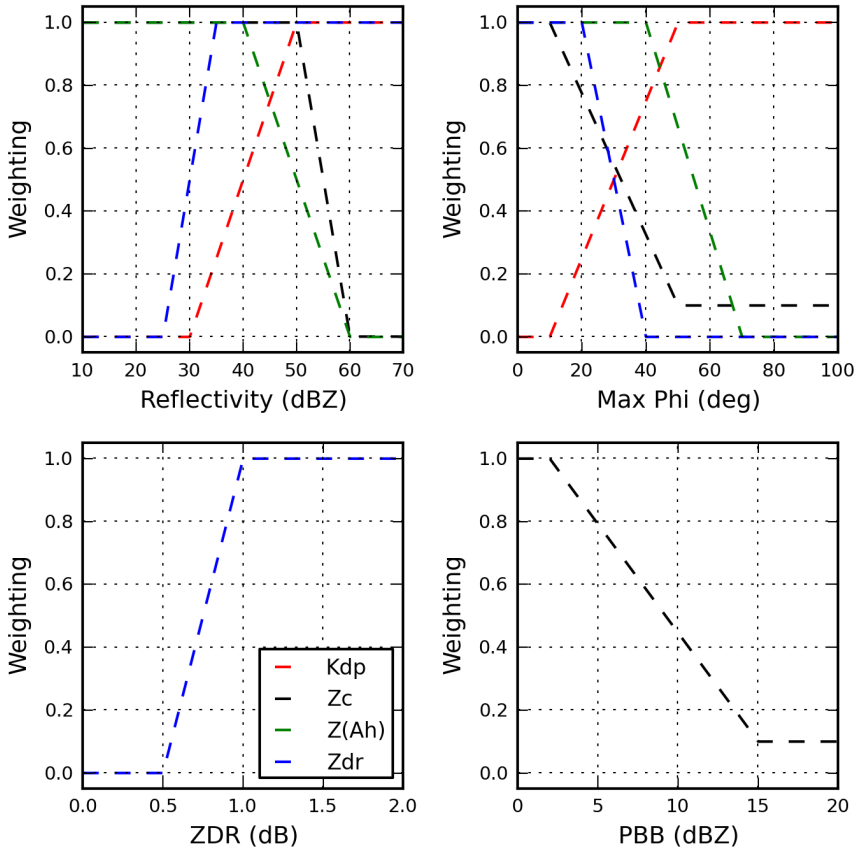

FIGURE 7.21: Weighting functions to calculate the weighted average rainfall from dual polarisation at each range gate. Each of the dashed lines represents a rainfall estimation method, red is R(K_{DP}), blue is R(Z_C,Z_{DR}), black is R(Z_C) and green is R(Z(A_h). Each panel represents a different weighting factor for the rainfall, the top left is corrected reflectivity (Z(A_h) for R(Z(A_h)), the top right is the maximum phase shift along the radial so far, the bottom left is differential reflectivity and the bottom right is the partial beam blockage correction applied to reflectivity. Total weightings for each rainfall estimate are the product of the weightings shown here.

7.4.2 Results of combining rainfall estimates

Both of the described methods of combining multiple dual polarisation rainfall estimates have been applied to the COPE radar data, with total rainfall accumulations for each at 0.5° elevation shown in Figure 7.22 with the decision tree method yielding much higher rainfall accumulations than the weighted average method. In the accumulation resulting from the convective line which spans the peninsula to the south of the radar, both methods yield lower rainfall estimates than all of the previous estimates with the exception of selective R(K_{DP}), showing the influence of R(K_{DP}) in these areas of the combined estimates. Unfortunately, given the location of the rain gauges this effect is not visible within the verification results.

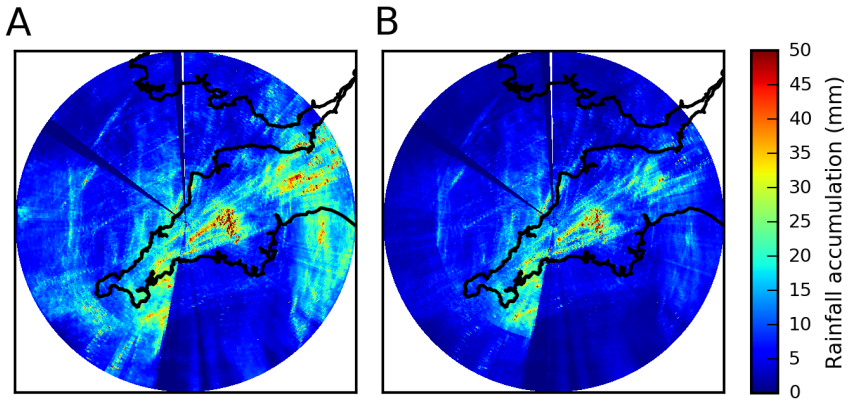

FIGURE 7.22: Total rainfall accumulation for the COPE field campaign as measured by the NCAS mobile weather radar at an elevation of 0.5° when using a combination of rainfall estimators. Panel A shows the accumulation when using rainfall produced with the decision tree method while B shows the accumulation when rainfall is estimated using a weighted average of the available rainfall estimates. Each panel is a 300 km square centred on the radar and contains the accumulation from 1131 valid scans across the field campaign.

Comparison to rain gauges shows the combined method to have a gradient of 0.82 and a correlation coefficient of 0.31, which is similar to each of the individual methods, and its mean absolute percentage difference is 25% which is bettered only by the theoretical R(Z(A_h)) approach. The weighted method has a much shallower gradient of 0.69 and a correlation coefficient of 0.44, the highest correlation of any method used to estimate

rainfall. The shallower gradient suggests the weightings are biased towards rainfall estimates which produce lower rainfall intensities and there is future potential to study how changing the combination weightings influences the rainfall estimates provided, but the high correlation between gauges suggests the method is producing consistent rainfall estimates. Removing St Clether and Mary Tavy from the regression analysis improves both estimates, with the decision tree having a gradient of 0.88, a correlation of 0.48 and a MAPD of 21% while the weighted method has a gradient of 0.76, a correlation of 0.65 and a MAPD of 28%.

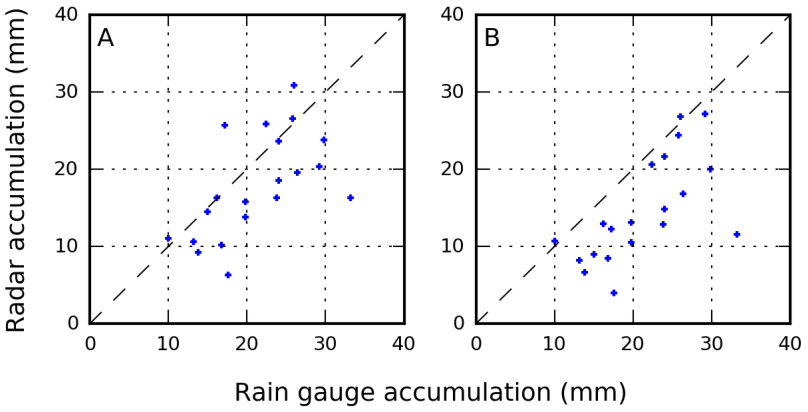

FIGURE 7.23: Comparison of rain gauge total rainfall accumulation for the COPE field campaign with rainfall as estimated by the NCAS mobile weather radar at an elevation of 0.5° using combined rainfall estimates. Each of the panels y-axes shows the rainfall accumulations as taken from the panels of Figure 7.22, A is using the decision tree and B is using the weighted average. Each blue cross represents the total for each of the EA rain gauge sites. The dashed line in each panel is the one to one line.

While these results indicate combining radar estimates to form a single merged product is viable, they do not suggest they provide more accurate rainfall representations than just using the best single variable rainfall estimate available ($\mathrm{R}(\mathrm{Z}(A_h))$, at least for the rain gauge locations. The previous schemes all combined ice phase estimates in addition to liquid rainfall estimates, which is unnecessary for COPE given the location of the rain gauges and the height of the melting layer during the project and it is in these conditions, along with the high intensity convective events hinted at in the widespread total accumulations that combined estimates are likely to have the greatest value. The estimates provided here could potentially be improved through adjustment of the weighting

factors, or values used in the decision tree and objectively doing so is an further item for exploration in future work.

7.5 Rainfall estimation conclusions

This chapter has covered the estimation of rainfall using a number of dual polarisation estimators and also the more traditional use of horizontal reflectivity. Rainfall estimation using horizontal reflectivity (Section 7.2) showed the following:

- The introduction of quality control and data correction through dual polarisation methods significantly improves rainfall estimates from horizontal reflectivity
- The single biggest improvement to the accuracy of rainfall estimates from 0.5° elevation scan is gained through the correction of partial beam blockage
- In the absence of PBB correction, it is better to use rainfall estimates from the 1.5° elevation scan, rather than the lower elevation
- Rainfall estimation in regions of ground clutter is inadequate, due to mixed echo signals generating extreme rainfall intensities, and an alternative estimate should be used in regions of persistent ground clutter

The introduction of a case study demonstrated the accuracy of R(Z_C) in typical moderate rainfall conditions, but introduced another source of error previously neglected in this thesis, the vertical profile of reflectivity. Most vertical profile of reflectivity corrections focus on correcting for the effects of the melting layer and differences between reflectivity above and below it in stratiform and convective situations. Given the melting level height during the field campaign was in excess of 2500 m and the rain gauges were all located within 50 km of the radar vertical reflectivity gradients were not considered as all the rainfall estimates have been taken from the warm region below the melting layer in which a zero gradient is usually prescribed. The example detailed however shows a strong vertical profile of reflectivity below the melting layer, with a gradient of up to -20 dBZ/km with very localised timing of initiation and development which makes correction very difficult. Further research into both the atmospheric conditions observed

and the development of a localised VPR correction for this case could lead to further accuracy improvements and should be considered in the future.

Section 7.3 covered the use of dual polarisation estimators and showed the following:

- The most accurate method of rainfall estimation for the COPE field campaign is to use specific attenuation transformed to reflectivity in conjunction with the UKMO R-Z relationship where the total path phase shift is greater than 4° and R(Z_C) otherwise, which yields a mean absolute percentage difference compared to the rain gauges of 24% for total rainfall accumulation during the field campaign.
- Rainfall estimated with specific differential phase is most reliable in intense rainfall situations. This is advantageous as these situations are also those with the greatest uncertainty for the other methods of rainfall estimation.
- The radars calculated K_{DP} has a low spatial resolution, even in high intensity rainfall situations, which leads to reductions in the peak rainfall estimated and an alternative method of calculation could yield further improvements in R(K_{DP}) estimates.
- Use of R(Z,Z_{DR}) estimates of rainfall is highly dependent on the accuracy of the differential reflectivity measurements in light rainfall and the robustness of attenuation correction in heavy rainfall. This can lead to significant errors in the rainfall estimates for both light and heavy rainfall.
- Rainfall estimation using differential reflectivity has most value when attenuation correction has not been possible in moderate rainfall events with low phase shift, as the complementary nature of the horizontal attenuation and differential attenuation lead to smaller errors in these estimates than when using uncorrected reflectivity alone.

The above conclusions lend themselves to merging the rainfall estimates from each of the dual polarisation parameters to reduce the uncertainty in the final rainfall estimate. Section 7.4 covers two techniques for merging the estimates, one which selects the single most appropriate estimate using a decision tree and one which combines the rainfall estimates using a weighted average where the weighting for each estimate is a function

of their perceived accuracy at that range gate. Total rainfall accumulations from these methods suggest the following:

- Combining with a decision tree produces rainfall estimates which more closely match the rain gauge totals, with accuracy very similar to using the single best dual polarisation rainfall estimate.
- Looking beyond the rain gauge locations the decision tree method produces lower, more realistic rainfall accumulations in the areas affected most by convective rainfall during the campaign due to the inclusion of K_{DP} estimates in these regions
- The weighted combination has the highest correlation with the rain gauge totals, but underestimates more than any of the individual corrected methods

It is not clear whether the combination of rainfall estimates leads to more representative rainfall totals than using a consistent single rainfall estimate given the rainfall data available. The increased correlation observed for the weighted average combination could be indicative of a reduction in uncertainty as a result of merging more than one estimate however more optimal weights may lead to a closer fit between the radar estimates and the rain gauges. One possibility is to use the fractional classification from a fuzzy classifier to weight the different estimates as proposed by Dixon et al. (2015) and this should be explored in the future in conjunction with a hydrometeor classification scheme for the radar.

The decision tree based combined rainfall estimate is recommended as the most suitable method of rainfall estimation for the COPE field campaign, given its performance in relation to the rain gauges and during high intensity rainfall events. Future work is likely to improve rainfall estimates by improving rainfall estimates in regions of persistent ground clutter, by introducing vertical profile corrections within the sub melting layer region and by improving the weighted combination of rainfall estimates. There are two other notable areas of further work which will improve rainfall estimates, one is to improve the spatial resolution of K_{DP} in intense rainfall and the other is to explore the impact of more advanced accumulation methodologies on the correlation between radar and rain gauge observations.

Chapter 8

Synthesis

This thesis presents the processing chain for the NCAS mobile X-band weather radar, the first of its kind in the UK with a view to continued implementation and improvement of the processing chain on future field campaigns. The processing chain leverages the dual polarisation radar moments available from the radar to undertake quality control, data correction and rainfall estimation methods which are not possible with a single polarisation radar.

The schematic in Figure 8.1 summarises the steps within the processing chain, indicating where within this thesis each stage of the process lies. The process outlined includes a two stage quality control process to remove second trip and non meteorological echoes, which requires the generation of several new radar fields. After quality control the radar reflectivity data is corrected for the effects of attenuation and partial beam blockage using a simplification of the ZPHI methodology of Testud et al. (2000). Finally rainfall estimates are generated using each of the available dual polarisation parameters and a final rainfall product is derived which combines those estimates.

Throughout the development of this scheme several areas of uncertainty have been assessed which impact on the final QPE obtained from the radar and the following chapter summarises these findings, the main advantages of the processing chain and provides details of future research which will further improve the processing chain and make wider use of the dual polarisation observations and QPE obtained from the radar during both COPE and more recent field campaigns.

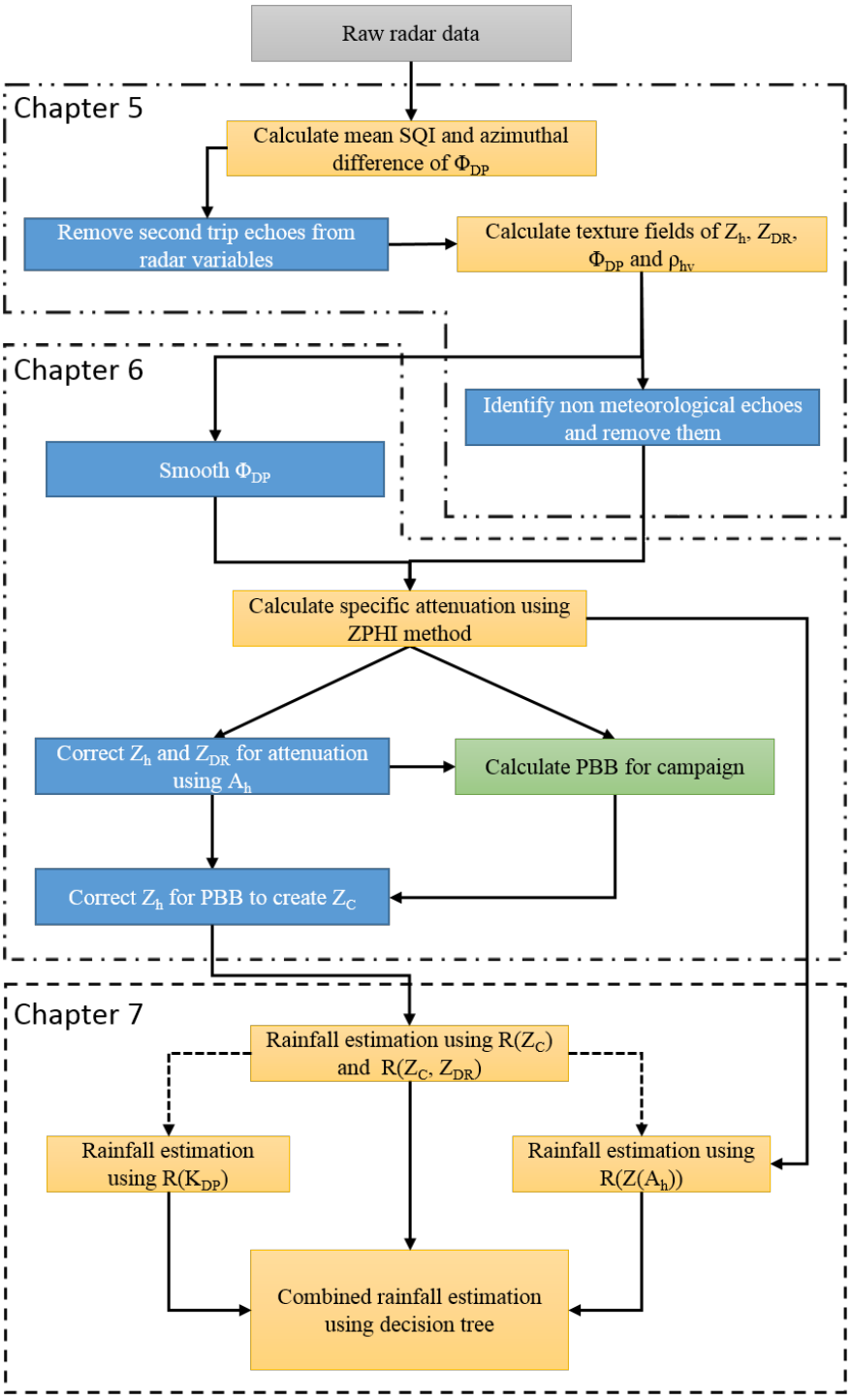

FIGURE 8.1: Schematic overview of the radar processing chain developed in this these. Yellow boxes represent new radar fields derived during the processing, while blue boxes represent adjustment of existing radar fields. The flow applies to each individual file within a dataset, with the exception of partial beam blockage calculations, which require multiple files to obtain a correction (green box). Where each stage fits within the thesis is indicated by the dashed and dot dashed boxes.

8.1 Conclusions

Analysis of the radar data - requirements for the processing chain

In Chapter 4 the raw reflectivity data from the COPE field campaign is analysed using long term statistics and the following systematic errors are identified:

- Persistent regions of ground clutter within the lowest elevation PPI indicated by echo occurrence percentages in excess of 90% with average reflectivity greater than 40 dBZ
- Areas of significant beam blockage where azimuthal variation in echo occurrence showed clear drops in the 0.5° elevation scan compared to higher elevation scans
- An abundance of low intensity echoes within 30 km of the radar which had a reflectivity of below -1.4 dBZ

Each of these errors sources has required attention within the processing chain and has driven its development, with ground clutter and low intensity echoes filtered in Chapter 5 and partial beam blockage corrected for in Chapter 6.

Chapter 4 also analyses long term statistics for the filtered reflectivity field available from the signal processor, which was found to reduce but not remove the majority of ground clutter signals due to it underestimating the intensity of clutter signals in dry conditions. An individual example from Burn airfield also highlighted its tendency to reduce the intensity of rainfall echoes along the zero velocity isodop. Both of these errors made it beneficial to find an alternative method of clutter removal.

Quality control - successful removal of spurious radar echoes

Chapter 5 details the successful development of two quality control procedures for the radar, the first of which removes second trip echoes using a combination of normalised coherent power measurements from the radar and the median azimuthal difference in phase shift, which is a new parameter derived for the filtering which takes advantage of the staggered PRF operating during COPE. Removal of second trip echoes benefited the

phase shift smoothing required in Chapter 6, leading to more accurate corrections of the radar data for the effects of attenuation.

Chapter 5 also demonstrates the successful implementation of a fuzzy logic non meteorological echo identification scheme with the following key features.

- Radial texture fields of reflectivity, differential reflectivity, phase shift and correlation coefficient were calculated to aid identification of spurious echoes
- The radial implementation improved computation time and a novel parametric correction was applied to these fields to account for the increasing natural variation in Φ_{DP}, Z_{DR} and ρ_{hv} with range
- Membership functions were derived using limited training data, allowing future expansion of the method to include other spurious echo types
- Testing at Burn airfield showed the method to be transferable to new locations

Despite the success of the scheme there are examples of erroneous data removal, typically in convective cells and within and above the melting level which indicate expansion of the fuzzy logic scheme is required. The introduction of additional meteorological classes in the future should resolve these issues as they relate to meteorological echoes with dual polarisation signatures that do not fit within the existing classes or more closely resemble ground clutter rather than precipitation.

Reflectivity correction - the greatest source of uncertainty

Chapter 6 covers the correction of the radar reflectivity and differential reflectivity fields for two beam propagation effects, attenuation and partial beam blockage using both the linear approach and a modified implementation of the ZPHI approach.

Both corrections utilise differential phase shift and the radar's signal processor output of this data is extremely noisy in its raw form and effected by second trip echoes in its smoothed form requiring a new filtering methodology to be developed. The filtering methodology builds on the iterative approach of Hubbert and Bringi (1995) but introduces two new approaches, the first being to use ρ_{hv} as a weighting parameter in the moving

average and the second being to use two iterations with variable filter length, the first to identify and remove backscatter differential phase and the second to smooth the remaining data at a finer spatial resolution.

The implementation of corrections for attenuation and beam blockage has led to the following conclusions:

- The ratio parameters α and β, which define the ratio of specific differential phase shift to attenuation (horizontal and differential) are the biggest source of uncertainty in the correction calculations
- Using the ZPHI methodology for attenuation correction reduces the uncertainty caused by α along the majority of the radar beam when compared to using the linear method of attenuation correction
- The specific attenuation generated by the ZPHI method can be utilised to correct for beam blockage with stable results requiring a large number of observations
- The beam blockage correction calculated is immune to the uncertainty in α provided the data sample is large and the radar has been calibrated by alternative means

Chapter 6 shows that using dual polarisation to correct for attenuation and beam blockage is possible despite the uncertainties inherent within the corrections and Chapter 7 confirms that these corrections have a beneficial impact on rainfall estimates despite these uncertainties.

Rainfall estimation - uncertainty reduction through dual polarisation

The rainfall estimates derived in Chapter 7 provide the following conclusions:

- The radar processing chain greatly improves performance of rainfall estimates generated from horizontal reflectivity, with the mean absolute percentage difference to rain gauge accumulations reducing from 86% for raw data to 31% for the fully corrected reflectivity
- Without full correction for PBB and attenuation it is better to use higher elevation reflectivity data than the 0.5° data

- Rainfall estimated using a theoretical conversion of specific attenuation to reflectivity provides the most accurate rainfall estimates of any of the dual polarisation variables, with a MAPD of 24%
- Specific differential phase (K_{DP}) produces the rainfall estimates with the least uncertainty in areas of high intensity rainfall, but has large uncertainty at low rainfall rates due to estimation errors
- Combining multiple rainfall estimates improves performance in high intensity rainfall due to the inclusion of K_{DP} while maintaining performance in lower rainfall intensities by using specific attenuation and reflectivity (MAPD of 25%)

During Chapter 7 several improvements and extensions to the processing chain are noted, including the requirement to improve rainfall estimation in regions of persistent ground clutter, the benefit of hydrometeor classification for the merging of rainfall estimates, improving the radars estimates of K_{DP} and the potential application of quasi-vertical profiles of radar moments for vertical gradient correction. The following section expands on these areas further, introducing the concepts to stimulate future research into these areas with the mobile X-band radar.

8.2 Future work

The following section introduces opportunities for future work which develop from this thesis, the first three of which are aimed more towards further improving the processing chain of the radar, while the remaining two have a more outward focus on other aspects of radar hydrometeorology. In practice each method can be beneficially applied to both radar processing and atmospheric science providing improvements in both QPE and process understanding.

8.2.1 Merging QC reflectivity with radar filtered reflectivity

A potential improvement to the radar processing chain would be the inclusion of data from the radar filtered reflectivity product where appropriate. Chapter 4 showed the radar filtered reflectivity had two issues, the first being an under removal of ground

clutter returns in dry conditions and the second being removal of rainfall along the zero velocity isodop. As ground clutter signals have been identified using the fuzzy classifier one potential approach would be to derive a fixed clutter map based on the reflectivity data, the reflectivity signal for which would be set to invalid where the classifier identifies ground clutter but to the radar filtered reflectivity where a rainfall echo is identified. This approach would improve the reflectivity measurements in mixed echo type conditions where both a ground clutter and rainfall echo are combined. A further extension of this could then be using the radar filtered reflectivity in conditions where the fuzzy classifier has identified a ground clutter echo outside of the clutter map, which could improve performance when meteorological echoes have a similar signature to ground clutter echoes, such as in narrow convective cores with high reflectivity and rapid spatial variability.

8.2.2 Expansion of the fuzzy logic scheme

The expansion of the fuzzy logic classification scheme to include different hydrometeor types including graupel, wet snow, hail and ice will lead to improvements in false classification during quality control and has the potential to improve rainfall estimates through selective combination of the moments used depending on the main echo signatures identified within a range gate. Existing classification schemes at X-band exist in the USA based on the theoretical simulation of dual polarisation moments using T-matrix scattering simulations (Schneider et al., 2013; Dolan and Rutledge, 2009). Modification of the membership functions in these schemes to fit the fuzzy logic framework defined here is one possible route to an expanded classification scheme while another option is to empirically define new functions based on the observations obtained during COPE and the additional field campaigns listed in Appendix B. Given many hydrometeor classification schemes require a temperature profile to determine the difference between liquid and solid phase precipitation there may be the need to incorporate external data into the processing chain. Alternatively melting layer identification techniques could be applied to the radar data, particularly to the QVP analysis noted later in this Chapter, to define the 0 °C height which is required by these schemes. The introduction of hydrometeor

classification to the fuzzy logic scheme also has the potential to improve atmospheric process studies through the comparison of radar derived hydrometeor type with modelled hydrometeors and aircraft observations.

8.2.3 Estimating K_{DP} with increased spatial resolution

The current radar estimates of specific differential phase shift have low spatial resolution as a result of the smoothing undertaken in their production. This low resolution leads to the underestimation of peak rainfall when using K_{DP} and offsets between regions when merging multiple rainfall estimates together. Alternative schemes exist for the calculation of K_{DP} which advocate a variable length window for calculation of the gradient of Φ_{DP} which decreases (increases) in length when reflectivity is high (low) and these could be tested as a first alternative for K_{DP} estimation with the mobile radar (Brandes et al., 2001). Increasing the spatial resolution of K_{DP} will improve rainfall estimates and allow better process studies in convective cells where the gradients currently calculated are unrepresentative of the rates of change occurring across a small distance. Another option to explore is the modification of the new smoothing methodology for Φ_{DP} developed in this thesis, which currently uses two window lengths. Dynamic adjustment of these filter lengths based on reflectivity values could lead to improved K_{DP} estimates in light rainfall through an extension of the filtering window in these regions which will reduce the uncertainty in low values of K_{DP}.

8.2.4 QVP

Quasi vertical profiles (QVP) of radar variables are an emerging method of visualising dual polarisation radar data which use azimuthal averaging to reduce the measurement uncertainty of dual polarisation moments and create a representation of the vertical structure of stratiform storms (Kumjian et al., 2016; Ryzhkov et al., 2016; Schrom and Kumjian, 2016). During Chapter 7 QVP of reflectivity were used to successfully identify the cause of radar underestimation of ground rainfall during a period of low intensity post frontal precipitation, though not to correct explicitly for the error due to local variations. The application of QVP to case studies to improve our understanding of cloud microphysics has great potential as a future application of the mobile radar, while QVP will

also be useful for numerical weather model evaluation. Figure 8.2 provides an example of QVP showing the changing height profile of three dual polarisation moments (horizontal reflectivity, differential reflectivity and the co-polar correlation coefficient) along with a true vertical profile of Doppler velocity from the recent radar deployment during RAINS (see Appendix B). Though none of the radar parameters have been corrected there are some clear signals in the height profiles beyond the obvious delineation of the melting layer including the change in differential reflectivity above the melting layer, which appears to be linked to echo top height and also decreases of the correlation coefficient within the melting layer and broadening of its structure linked to the highest sub melting level reflectivity. The investigation of these observations and others from COPE, RAINS and other radar field campaigns will be a fascinating future application of the radar data processing described in this study and will link strongly to the hydrometeor classification work described earlier in this chapter.

8.2.5 Hydrological modelling and uncertainty

An original intention of this thesis was to incorporate dual polarisation radar estimates of rainfall into hydrological models to develop an understanding of the uncertainty in flow simulations driven by radar input. To undertake this research data from the Bealsmill river gauge (Section A.3) was obtained for the COPE field campaign, along with river level and UKMO network radar data from the preceding summers to allow calibration of a rainfall-runoff model. Unfortunately the nature of the mobile radar deployment site in Cornwall prevented continuous operation of the radar, making river runoff modelling impossible without splicing together data records and the summer was particularly dry, leading to only a single example of elevated river levels at the gauging site over the course of the field campaign. Preliminary research presented at international conferences suggested that the parametric uncertainty within hydrological models is as significant as the uncertainty in radar rainfall estimates and that further connected studies combining the two sources of uncertainty would be beneficial (Dufton et al., 2014; Dufton and Collier, 2013). Although these studies are not possible using the data from the COPE field campaign, the data obtained during the RAINS campaign (Appendix B) in 2016 will provide an excellent opportunity to revisit this research in the future.

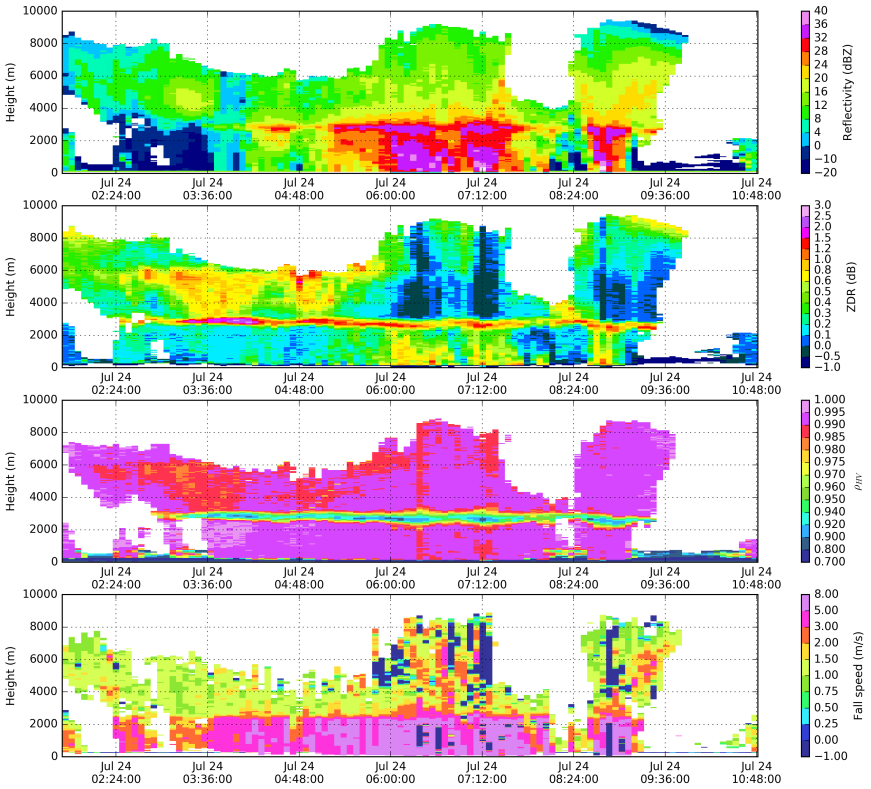

FIGURE 8.2: Quasi vertical profiles of reflectivity (top panel), differential reflectivity (second panel), correlation coefficient (third panel) and true vertical profile of radial velocity (bottom panel) from 24 July 2016 during the RAINS field campaign. Data from a 20° elevation PPI scan has been averaged azimuthally and projected onto a vertical plane to represent the vertical structure of the precipitation system. Vertical data is an average of a bird bath 90° scan obtained immediately after each PPI volume.

8.3 Final synthesis

This thesis develops the NCAS X-band dual polarisation mobile weather radar's processing chain to allow generation of accurate quantitative precipitation estimates for the COPE field campaign. The processing chain leverages dual polarisation radar moments to quality control the radar data using a fuzzy logic classifier, correct the data using a modified version of the ZPHI method and to generate multiple rainfall estimates. The final rainfall estimate derived for the field campaign combines the dual polarisation rainfall estimates to reduce uncertainty in both light and heavy rainfall using a logical decision

tree. Several areas of improvement for the processing chain have been identified and presented as potential areas of future work, along with two new areas of research this thesis can complement (QVPs and hydrological model uncertainty).

Appendix A

Appendix A: The COPE field campaign

The information in this appendix relates to the COPE field campaign and details the scan strategies used by the mobile radar, the location of EA rain gauges in relation to the radar deployment site and the location of the EA river level gauge at Bealsmill.

A.1 Radar scan strategy during COPE

During COPE a number of different scan strategies were employed. The following section describes the operations on each day, with scans not covered in Section 3.2 explained in detail. Also noted are periods when the COPE scans were operating but with a slight adjustment in settings due to human error.

2013-06-20 and 2013-06-27

One the first two days of the campaign scans with very similar characteristics to COPE10 were operating, with the filtering settings on the radar being adjusted to identify and optimum approach. 76 scans were collected in total, 70 on the 20 June and 6 on the 27 June.

2013-07-01

16 scans were collected all using a testing volume which contained 5 elevations (0.5, 1, 2, 3, 5°), with 300 m gate spacing, 164 gates per radial, a PRF of 500 Hz and a pulse width of two microseconds. These scans were testing an option for clear air scanning with the radar.

2013-07-02 and 2013-07-03

84 scans were collected on 2 July and 47 on 3 July all testing COPE10,

2013-07-04

Between 09:47 and 12:45 37 scans were collected testing COPE10, after which 25 clear air scans were collected containing 4 elevations (0.5, 1, 2 and 3°), with 332 gates at 300m spacing with a PRF of 500 HZ and a pulse length of two microseconds. At 15:11 these scans were changed to a pulse length of one microsecond and 664 gates per radial at 150 m spacing and 10 of these scans were collected.

2013-07-05

More clear air testing was done, with 55 scans collected. Throughout the day the pulse length of the radar changed between one and two microseconds with the gate spacing varying accordingly (150 m and 300 m), the remaining scan parameters were as per the clear air scan described in Section 3.2.

20130716 and 2013-07-17

COPE clear air operated on both these days, with 46 scans collected on 16 July and 48 scans collected on 17 July.

2013-07-18

COPE clear air was operated for the first 14 scans of the day, starting at 08:48 before switching to COPE10 (first scan at 10:22). Four COPE10 scans were collected before a change was made such that COPE10 was running but with only 993 gates per radial at 150 m spacing (10:38), a change which persisted throughout the day in all COPE variant scans collected. At 11:11 COPE30 was activated, with 4 scans collected before switching back to COPE10 for another 13 scans. At 12:20 the scans were switched to COPE20, before increasing the maximum elevation again at 12:41 (COPE30) and again at 12:49 (COPE40). At 13:09 a new scan (X1) was introduced containing 15 elevations with a maximum elevation angle of 45.5° as convective cells were observed closer to the radar and a single scan was collected. A further adjustment was made (X2) to have more consistent elevation spacing with a maximum at 42.5° . After 2 of these scans were collected the radar was switched back to COPE10 (993 range gates) for 6 scans, then to COPE20 for 1 scan and back to X2 for a further 4 scans before a final switch back to COPE10 for the last 13 scans of the day.

2013-07-23 to 2013-07-31

After the repeated changes on 18 July the radar operated only in COPE10 mode for the next 6 active days in July (23, 25, 27, 28, 29 and 31) but was returned to having 1000 range gates per radial at a spacing of 150 m. 388 scans were collected over these 6 days.

2013-08-02

The radar collected 41 scans using COPE10 between 09:55 and 13:34 before changing to COPE30 for two scans. After these two scans an azimuth spacing error was introduced to the COPE30 scans with 401 azimuths collected per sweep at 0.9° spacing (compared to 361 at 1° spacing). The radar collected 8 scans using COPE30 with the azimuth error before switching to COPE10 at 14:25 with no errors. 15 scans were collected with COPE10 before COPE30 (with error) was resumed for 2 scans, then 10 scans at COPE20 (normal) and a final 22 scans were then collected at COPE30 with azimuth error.

2013-08-03

71 scans were collected on 03 August starting with 27 COPE10 scans. Then a single scan with only 9 elevations, before a single COPE10 scan and then a COPE10 scan with an azimuth error (3434 radials for 10 elevations). Normal COPE10 then resumed for 26 scans before a switch to COPE20 at 14:36 after which 14 scans were collected.

2013-08-05

The radar scanned using COPE10 for the first 11 scans of the day, then collected 18 scans at COPE20 (12:13 to 13:38) before switching back to COPE10 for 13 scans (13:43 to 14:42), then back to COPE20 for 5 scans (14:47 to 15:05) and back to COPE10 for the last 4 scans of the day.

2013-08-06

The first 8 scans of the day were using the COPE clear air strategy before switching to COPE10 for the remainder of the day (69 scans).

2013-08-14 and 2013-08-15

The radar operated only in COPE10 in these two days, collecting 56 scans and 72 scans respectively.

2013-08-17

This was the final day of data collection for the COPE field campaign and the radar started the day scanning using COPE10 at 07:31 before switching to COPE20 at 08:56 after 17 scans had been collected. 9 scans were then collected using COPE20 before the radar was switched back to COPE10 for the remainder of the day collecting 86 more scans.

A.2 Location of rain gauges relative to the mobile radar

The following table provides the name and location (relative to the radar) of each of the 20 Environment Agency rain gauges for which data was obtained for the duration of the COPE field campaign.

TABLE A.1: Location of the Environment Agency rain gauges relative to the position of the radar. Both references are given to provide the location of the nearside corner of the range gate in which the rain gauge is located, for example 1° azimuth means the rain gauge is located between 1° and 2° in azimuth and 12.3 km means the rain gauge lies between a range of 12.3 km and 12.45 km.

Rain gauge	Azimuth	Range (km)
Bastreet	134°	12.3
Bodmin	202°	20.4
Crowford	44°	19.35
De Lank	195°	8.85
Lanreath	175°	28.5
Lee Moor	119°	47.7
Luxulyan	202°	29.1
Mary Tavy	101°	36.0
Newquay	232°	42.6
Otterham	1°	4.35
Roadford	80°	27.15
St Cleer	151°	20.25
St Clether	84°	5.7
St Columb	229°	32.55
Stoke Climsland	118°	22.8
Tamar Lakes	28°	29.1
Trebrown Blackadon	151°	28.05
Trefrida	24°	11.55
Wadebridge	233°	20.7
Werrington	84°	17.85

A.3 River level stations

The EA in England also maintains a wide network of river level and flow monitoring sites. To allow future assessment of the impact of radar rainfall estimates on hydrological simulations data for the River Inny at Bealsmill were obtained from the EA to cover the period of the COPE campaign. The Inny catchment upstream of Bealsmill lies to the south east of Davidstow with the radar deployment site in the headwaters of the catchment. The catchment lies wholly within 25 km of the radar and covers 105 km^2

(Fig. A.1). The monitoring station is a broad crested weir, with the rating curve most recently recalibrated in December 2009.

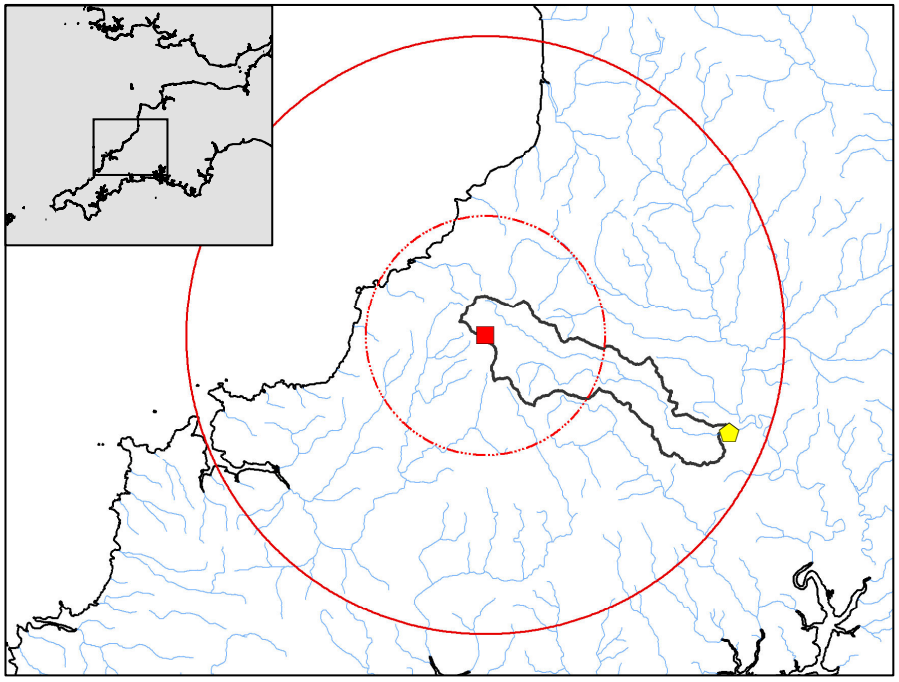

FIGURE A.1: Location of the Bealsmill river gauge (yellow pentagon) in relation to the Davidstow radar deployment site. Range rings are at 10 km and 25 km.

Appendix B

Appendix B: Other radar deployments

Since the completion of the COPE field campaign the radar has been deployed on several additional field campaigns, all of which have provided data that will be beneficial in further testing and improving the processing chain developed during this thesis. These campaigns include ICE-D in Cape Verde, SESAR in Germany and RAINS in Scotland, all of which are shown on the map in Figure B.1 and described in turn in the sections below.

B.1 ICE-D

The Ice in Clouds Experiment - Dust (ICE-D) field campaign took place in August 2015, sited on the island of Praia, Cape Verde. The primary aim of the project was to examine the influence of Saharan dust on cloud microphysics and precipitation development, in both convective and stratiform clouds. To this aim the BAe-146 research aircraft flew from Praia collecting in-situ measurements of dust and cloud hydrometeors, while the mobile X-band radar was deployed on Praia, along with ground based aerosol instrumentation. The mobile radar operated a near continuous scan cycle, collecting volume scans at five minute intervals between 3 August and 25 August 2015. Some testing data was also collected in the week preceding 3 August. During the campaign the radar generally operated a default volume scan containing a low elevation (1°) surveillance scan to

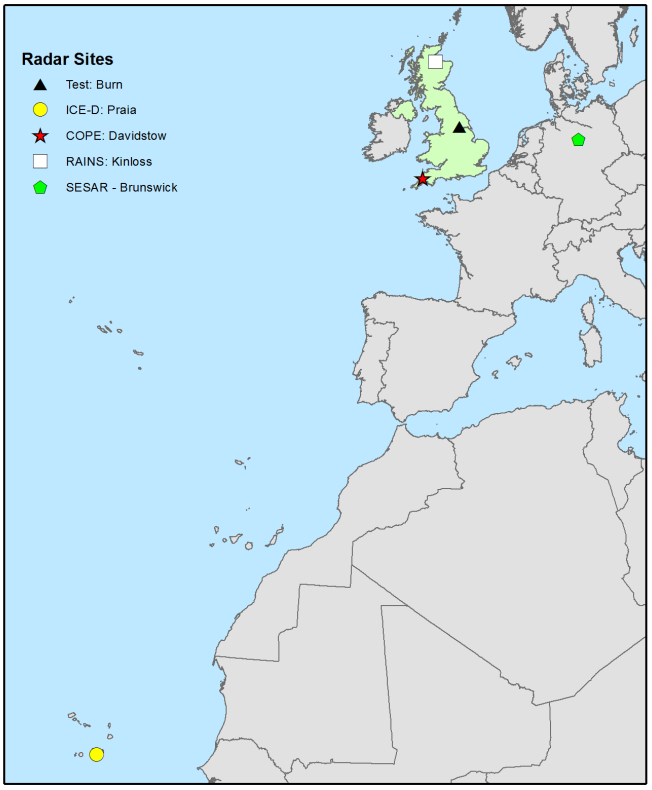

FIGURE B.1: Location of NCAS mobile weather radar deployments since 2013. COPE is shown by the red star, Burn by the black triangle, ICE-D by the yellow circle, SESAR by the green pentagon and RAINS by the white square.

300 km range and 12 scans to 150 km range (1° to 10° in 1° intervals and then a 12° and 15° scan). Data from the campaign will be used in the future to validate and improve the attenuation correction procedures applied in Section 6.2.2 and to investigate the use of quasi-vertical profiles of dual polarimetric variables for visualising changes in cloud microphysics through time (Section 8.2.4).

B.2 SESAR

SESAR (Single European Sky ATM Research) is the technical pillar of the Single European Sky project initiated in 2004 by the European Commission. As part of that project the mobile radar was deployed by Selex ES GmbH (on loan from NCAS) in collaboration with the German Aerospace Centre (DLR) at Braunschweig airport in northern Germany, contributing to a unique set of meteorological sensors being piloted for use in air traffic management. During the project the radar operated a continuous scan strategy from

27 January 2015 to 18 May 2015, using a volume scan containing 10 sweeps at varied elevations up to 90° (1°, 2°, 3°, 5°, 7°, 12°, 20°, 30°, 60° and 90°), with rapid antenna rotation speeds of up to $36\,^{\circ}\,s^{-1}$. Data from the high elevation sweeps will be used for the analysis of quasi-vertical profiles of dual polarimetric variables (Section 8.2.4).

B.3 RAINS

The Radar Applications in Northern Scotland (RAINS) project is an ongoing collaboration between NCAS and the Scottish Environmental Protection Agency (SEPA) to improve rainfall observations in northern Scotland where UKMO national radar coverage is sparse. As part of the project the NCAS mobile radar was deployed at Kinloss from January 2016 to August 2016 operating on a continuous basis. Volume scans were collected at sub 5 minute intervals and includes 12 elevation angles from 0.5° to 30° (0.5° , 1° , 1.5° , 2° , 3° , 4° , 5° , 6° , 7° , 10° , 20° and 30°) while also including a 90° birdbath scan. The data collected (>50000 volume scans) will provide valuable dual polarisation data for both radar QPE analysis and microphysical studies of precipitation above the melting layer.

References

Al-Sakka, H., Boumahmoud, A.-A., Fradon, B., Frasier, S. J., and Tabary, P.: A new fuzzy logic hydrometeor classification scheme applied to the French X-, C-, and S-band polarimetric radars, Journal of Applied Meteorology and Climatology, 52, 2328–2344, 2013.

Alfieri, L., Salamon, P., Pappenberger, F., Wetterhall, F., and Thielen, J.: Operational early warning systems for water-related hazards in Europe, Environmental Science & Policy, 21, 35–49, 2012.

Anagnostou, E. N.: A convective/stratiform precipitation classification algorithm for volume scanning weather radar observations, Meteorological Applications, 11, 291–300, 2004.

Atencia, A., Mediero, L., Llasat, M., and Garrote, L.: Effect of radar rainfall time resolution on the predictive capability of a distributed hydrologic model, Hydrology and Earth System Sciences, 15, 3809–3827, 2011.

Atlas, D.: Radar calibration: Some simple approaches, Bulletin of the American Meteorological Society, 83, 1313–1316, 2002.

Atlas, D. and Banks, H. C.: The interpretation of microwave reflections from rainfall, Journal of Meteorology, 8, 271–282, 1951.

Atlas, D., Ulbrich, C. W., Marks, F. D., Amitai, E., and Williams, C. R.: Systematic variation of drop size and radar-rainfall relations, Journal of Geophysical Research: Atmospheres, 104, 6155–6169, 1999.

Austin, P. M. and Bemis, A. C.: A quantitative study of the "bright band" in radar precipitation echoes, Journal of Meteorology, 7, 145–151, 1950.

Bachmann, S. and Zrnić, D. S.: Spectral density of polarimetric variables separating biological scatterers in the VAD display, Journal of Atmospheric and Oceanic Technology, 24, 1186–1198, 2007.

Baeck, M. L. and Smith, J. A.: Rainfall estimation by the WSR-88D for heavy rainfall events, Weather and Forecasting, 13, 416–436, 1998.

Balakrishnan, N. and Zrnić, D. S.: Use of polarization to characterize precipitation and discriminate large hail, Journal of the Atmospheric Sciences, 47, 1525–1540, 1990.

Battan, L. J.: Radar observation of the atmosphere, University of Chicago Press, 1973.

Bech, J., Codina, B., Lorente, J., and Bebbington, D.: The sensitivity of single polarization weather radar beam blockage correction to variability in the vertical refractivity gradient, Journal of Atmospheric and Oceanic Technology, 20, 845–855, 2003.

Bechini, R., Chandrasekar, V., Cremonini, R., and Lim, S.: Radome attenuation at X-band radar operations, in: Proc. Sixth European Conf. on Radar in Meteorology and Hydrology, 2010.

Bell, M. M., Lee, W.-C., Wolff, C. A., and Cai, H.: A Solo-based automated quality control algorithm for airborne tail Doppler radar data, Journal of Applied Meteorology and Climatology, 52, 2509–2528, 2013.

Berenguer, M., Sempere-Torres, D., Corral, C., and Sánchez-Diezma, R.: A fuzzy logic technique for identifying nonprecipitating echoes in radar scans, Journal of Atmospheric and Oceanic Technology, 23, 1157–1180, 2006.

Berne, A. and Krajewski, W. F.: Radar for hydrology: Unfulfilled promise or unrecognized potential?, Advances in Water Resources, 51, 357–366, 2013.

Beven, K. J.: Rainfall-runoff modelling: the primer, Wiley, 2011.

Biggs, E. M. and Atkinson, P. M.: A comparison of gauge and radar precipitation data for simulating an extreme hydrological event in the Severn Uplands, UK, Hydrological Processes, 25, 795–810, 2011.

Blyth, A. M., Bennett, L. J., and Collier, C. G.: High-resolution observations of precipitation from cumulonimbus clouds, Meteorological Applications, 22, 75–89, 2015.

Bowler, N. E., Pierce, C. E., and Seed, A.: Development of a precipitation nowcasting algorithm based upon optical flow techniques, Journal of Hydrology, 288, 74–91, 2004.

Bowler, N. E., Pierce, C. E., and Seed, A. W.: STEPS: A probabilistic precipitation forecasting scheme which merges an extrapolation nowcast with downscaled NWP, Quarterly Journal of the Royal Meteorological Society, 132, 2127–2156, 2006.

Brandes, E. A. and Ikeda, K.: Freezing-level estimation with polarimetric radar, Journal of Applied Meteorology, 43, 1541–1553, 2004.

Brandes, E. A., Ryzhkov, A. V., and Zrnic, D. S.: An evaluation of radar rainfall estimates from specific differential phase, Journal of Atmospheric and Oceanic Technology, 18, 363–375, 2001.

Bringi, V. and Chandrasekar, V.: Polarimetric Doppler weather radar: principles and applications, Cambridge University Press, 2001.

Bringi, V., Vivekanandan, J., and Tuttle, J.: Multiparameter radar measurements in Colorado convective storms. Part II: Hail detection studies, Journal of the Atmospheric Sciences, 43, 2564–2577, 1986.

Bringi, V., Chandrasekar, V., Meischner, P., Hubbert, J., and Golestani, Y.: Polarimetric radar signatures of precipitation at S and C-bands, in: IEE Proceedings F (Radar and Signal Processing), vol. 138, pp. 109–119, IET, 1991.

Broxton, P., Troch, P. A., Schaffner, M., Unkrich, C., and Goodrich, D.: An all-season flash flood forecasting system for real-time operations, Bulletin of the American Meteorological Society, 95, 399–407, 2014.

Carlson, P. E.: Measurement of snowfall by radar, Tech. rep., DTIC Document, 1968.

Chandrasekar, V., Keränen, R., Lim, S., and Moisseev, D.: Recent advances in classification of observations from dual polarization weather radars, Atmospheric Research, 119, 97–111, 2013.

Chilson, P. B., Frick, W. F., Kelly, J. F., Howard, K. W., Larkin, R. P., Diehl, R. H., Westbrook, J. K., Kelly, T. A., and Kunz, T. H.: Partly cloudy with a chance of migration: weather, radars, and aeroecology, Bulletin of the American Meteorological Society, 93, 669–686, 2012.

Cho, Y.-H., Lee, G. W., Kim, K.-E., and Zawadzki, I.: Identification and removal of ground echoes and anomalous propagation using the characteristics of radar echoes, Journal of Atmospheric and Oceanic Technology, 23, 1206–1222, 2006.

Ciach, G. J.: Local random errors in tipping-bucket rain gauge measurements, Journal of Atmospheric and Oceanic Technology, 20, 752–759, 2003.

Ciach, G. J., Krajewski, W. F., and Villarini, G.: Product-error-driven uncertainty model for probabilistic quantitative precipitation estimation with NEXRAD data, Journal of Hydrometeorology, 8, 1325–1347, 2007.

Cifelli, R., Chandrasekar, V., Lim, S., Kennedy, P., Wang, Y., and Rutledge, S.: A new dual-polarization radar rainfall algorithm: Application in Colorado precipitation events, Journal of Atmospheric and Oceanic Technology, 28, 352–364, 2011.

Cole, S. J. and Moore, R. J.: Hydrological modelling using raingauge-and radar-based estimators of areal rainfall, Journal of Hydrology, 358, 159–181, 2008.

Collier, C.: Accuracy of rainfall estimates by radar, Part I: Calibration by telemetering raingauges, Journal of Hydrology, 83, 207–223, 1986.

Collier, C.: Applications of weather radar systems: a guide to uses of radar data in meteorology and hydrology, vol. 1, John Wiley & Sons Inc, 1996.

Collier, C.: Flash flood forecasting: What are the limits of predictability?, Quarterly Journal of the Royal Meteorological Society, 133, 3–23, 2007.

Collis, S., Heistermann, M., Helmus, J., Michelson, D., and Pfaff, T.: 8th European Conference on Radar in Meteorology and Hydrology short course, 2014.

Conway, D., van Garderen, E. A., Deryng, D., Dorling, S., Krueger, T., Landman, W., Lankford, B., Lebek, K., Osborn, T., Ringler, C., Thurlow, J., Zhu, T., and Dalin, C.: Climate and southern Africa's water-energy-food nexus, Nature Climate Change, 5, 837–846, 2015.

Da Silveira, R. B. and Holt, A. R.: An automatic identification of clutter and anomalous propagation in polarization-diversity weather radar data using neural networks, Geoscience and Remote Sensing, IEEE Transactions on, 39, 1777–1788, 2001.

Delrieu, G., Creutin, J., and Saint-Andre, I.: Mean KR relationships: Practical results for typical weather radar wavelengths, Journal of Atmospheric and Oceanic Technology, 8, 467–476, 1991.

Delrieu, G., Caoudal, S., and Creutin, J.: Feasibility of using mountain return for the correction of ground-based X-band weather radar data, Journal of Atmospheric and Oceanic Technology, 14, 368–385, 1997.

Delrieu, G., Serrar, S., Guardo, E., and Creutin, J. D.: Rain measurement in hilly terrain with X-band weather radar systems: Accuracy of path-integrated attenuation estimates derived from mountain returns, Journal of Atmospheric and Oceanic Technology, 16, 405–416, 1999.

Diederich, M., Ryzhkov, A., Simmer, C., Zhang, P., and Trömel, S.: Use of specific attenuation for rainfall measurement at X-band radar wavelengths. Part I: Radar calibration and partial beam blockage estimation, Journal of Hydrometeorology, 16, 487–502, 2015a.

Diederich, M., Ryzhkov, A., Simmer, C., Zhang, P., and Trömel, S.: Use of specific attenuation for rainfall measurement at X-band radar wavelengths. Part II: Rainfall estimates and comparison with rain gauges, Journal of Hydrometeorology, 16, 503–516, 2015b.

Dillencourt, M. B., Samet, H., and Tamminen, M.: A general approach to connected-component labeling for arbitrary image representations, Journal of the ACM (JACM), 39, 253–280, 1992.

Dixon, M. J. and Hubbert, J.: The seperation of noise and signal components in Doppler radar returns, in: Extended Abstracts, Seventh European Conf. on Radar in Meteorology and Hydrology, 2012.

Dixon, M. J., Wilson, J., Weckwerth, T., Albo, D., and Thompson, E.: A dual-polarization QPE method based on the NCAR Particle ID algorithm Description and preliminary results, in: AMS 37th Conference on Radar Meteorology, 2015.

Dolan, B. and Rutledge, S. A.: A theory-based hydrometeor identification algorithm for X-band polarimetric radars, Journal of Atmospheric and Oceanic Technology, 26, 2071–2088, 2009.

Doviak, R., Bringi, V., Ryzhkov, A. V., Zahrai, A., and Zrnić, D. S.: Considerations for polarimetric upgrades to operational WSR-88D radars, Journal of Atmospheric and Oceanic Technology, 17, 257–278, 2000.

Doviak, R. J. and Zrnić, D. S.: Doppler Radar & Weather Observations, Academic press, 1984.

Duchon, C. E. and Essenberg, G. R.: Comparative rainfall observations from pit and aboveground rain gauges with and without wind shields, Water Resources Research, 37, 3253–3263, 2001.

Dufton, D. and Collier, C.: Using ensembles to represent uncertainty in UK radar rainfall estimates: some initial findings, in: Proceedings of the International Conference on Flood Resilience: Experiences in Asia and Europe, Exeter, 2013.

Dufton, D. and Collier, C.: Fuzzy logic filtering of radar reflectivity to remove non-meteorological echoes using dual polarization radar moments, Atmospheric Measurement Techniques, 8, 3985–4000, 2015.

Dufton, D., Bennett, L. J., and Collier, C.: Using dual polarization radar data to analyse ensemble uncertainty in hydrological flow simulations, in: Proceedings of the International Symposium on Weather Radar and Hydrology, Washington DC, 2014.

Environment Agency and DEFRA: Understanding the risks, empowering communities, building resilience. Summary strategy, Tech. rep., EA Technical Publication, 2011.

Figueras i Ventura, J., Boumahmoud, A.-A., Fradon, B., Dupuy, P., and Tabary, P.: Long-term monitoring of French polarimetric radar data quality and evaluation of several polarimetric quantitative precipitation estimators in ideal conditions for operational implementation at C-band, Quarterly Journal of the Royal Meteorological Society, 138, 2212–2228, 2012.

Friedrich, K., Hagen, M., and Einfalt, T.: A quality control concept for radar reflectivity, polarimetric parameters, and Doppler velocity, Journal of Atmospheric and Oceanic Technology, 23, 865–887, 2006.

Fujiwara, M.: Raindrop size distribution in warm rain as measured in Hawaii, Tellus, 19, 392–402, 1967.

Fulton, R. A., Breidenbach, J. P., Seo, D.-J., Miller, D. A., and O'Bannon, T.: The WSR-88D rainfall algorithm, Weather and Forecasting, 13, 377–395, 1998.

Gabella, M. and Perona, G.: Simulation of the orographic influence on weather radar using a geometric-optics approach, Journal of Atmospheric and Oceanic Technology, 15, 1485–1494, 1998.

Galletti, M. and Zrnić, D. S.: Degree of polarization at simultaneous transmit: Theoretical aspects, Geoscience and Remote Sensing Letters, IEEE, 9, 383–387, 2012.

Gematronik Weather Radar Systems: Instruction manual, Rainbow 5: Products and Algorithms, 2012.

Germann, U., Berenguer, M., Sempere-Torres, D., and Salvadè, G.: Ensemble radar precipitation estimation–a new topic on the radar horizon, in: Proceedings of the 4th European Conference on Radar in Meteorology and Hydrology ERAD, Barcelona, pp. 18–22, 2006a.

Germann, U., Galli, G., Boscacci, M., and Bolliger, M.: Radar precipitation measurement in a mountainous region, Quarterly Journal of the Royal Meteorological Society, 132, 1669–1692, 2006b.

Germann, U., Berenguer, M., Sempere-Torres, D., and Zappa, M.: REAL – Ensemble radar precipitation estimation for hydrology in a mountainous region, Quarterly Journal of the Royal Meteorological Society, 135, 445–456, 2009.

Giangrande, S. E. and Ryzhkov, A. V.: Calibration of dual-polarization radar in the presence of partial beam blockage, Journal of Atmospheric and Oceanic Technology, 22, 1156–1166, 2005.

Giangrande, S. E., McGraw, R., and Lei, L.: An application of linear programming to polarimetric radar differential phase processing, Journal of Atmospheric and Oceanic Technology, 30, 1716–1729, 2013.

Giuli, D., Gherardelli, M., Freni, A., Seliga, T., and Aydin, K.: Rainfall and clutter discrimination by means of dual-linear polarization radar measurements, Journal of Atmospheric and Oceanic Technology, 8, 777–789, 1991.

Golding, B.: Nimrod: A system for generating automated very short range forecasts, Meteorological Applications, 5, 1–16, 1998.

Golding, B.: Long lead time flood warnings: reality or fantasy?, Meteorological Applications, 16, 3–12, 2009.

Goudenhoofdt, E. and Delobbe, L.: Evaluation of radar-gauge merging methods for quantitative precipitation estimates, Hydrology and Earth System Sciences, 13, 195–203, 2009.

Gourley, J. J. and Calvert, C. M.: Automated detection of the bright band using WSR-88D data, Weather and Forecasting, 18, 585–599, 2003.

Gourley, J. J., Tabary, P., and Parent du Chatelet, J.: A fuzzy logic algorithm for the separation of precipitating from nonprecipitating echoes using polarimetric radar observations, Journal of Atmospheric and Oceanic Technology, 24, 1439–1451, 2007.

Gourley, J. J., Illingworth, A. J., and Tabary, P.: Absolute calibration of radar reflectivity using redundancy of the polarization observations and implied constraints on drop shapes, Journal of Atmospheric and Oceanic Technology, 26, 689–703, 2009.

Grazioli, J., Tuia, D., and Berne, A.: Hydrometeor classification from polarimetric radar measurements: a clustering approach, Atmospheric Measurement Techniques, 8, 149–170, 2015.

Gu, J.-Y., Ryzhkov, A., Zhang, P., Neilley, P., Knight, M., Wolf, B., and Lee, D.-I.: Polarimetric attenuation correction in heavy rain at C band, Journal of Applied Meteorology and Climatology, 50, 39–58, 2011.

Gunn, K. and Marshall, J.: The distribution with size of aggregate snowflakes, Journal of Meteorology, 15, 452–461, 1958.

Gunn, K. L. S. and East, T. W. R.: The microwave properties of precipitation particles, Quarterly Journal of the Royal Meteorological Society, 80, 522–545, 1954.

Habib, E., Krajewski, W. F., and Kruger, A.: Sampling errors of tipping-bucket rain gauge measurements, Journal of Hydrologic Engineering, 6, 159–166, 2001.

Hall, M. P., Goddard, J. W. F., and Cherry, S. M.: Identification of hydrometeors and other targets by dual-polarization radar, Radio Science, 19, 132–140, 1984.

Hapuarachchi, H., Wang, Q., and Pagano, T.: A review of advances in flash flood forecasting, Hydrological Processes, 25, 2771–2784, 2011.

Hardaker, P., Holt, A., and Collier, C.: A melting-layer model and its use in correcting for the bright band in single-polarization radar echoes, Quarterly Journal of the Royal Meteorological Society, 121, 495–525, 1995.

Harper, W. G.: Detection of bird migration by centimetric radar- a cause of radar 'angels', Proceedings of the Royal Society of London. Series B-Biological Sciences, 149, 484–502, 1958.

Harrison, D. L., Driscoll, S. J., and Kitchen, M.: Improving precipitation estimates from weather radar using quality control and correction techniques, Meteorological Applications, 7, 135–144, 2000.

Harrison, D. L., Scovell, R. W., and Kitchen, M.: High-resolution precipitation estimates for hydrological uses, Proceedings of the Institution of Civil Engineers-Water Management, 162, 125, 2009.

Harrison, D. L., Norman, K., Pierce, C., and Gaussiat, N.: Radar products for hydrological applications in the UK, Proceedings of the Institution of Civil Engineers-Water Management, 165, 89–103, 2012.

Harrison, D. L., Georgiou, S., Gaussiat, N., and Curtis, A.: Long-term diagnostics of precipitation estimates and the development of radar hardware monitoring within a radar product data quality management system, Hydrological Sciences Journal, 59, 1277–1292, 2014.

Hildebrand, P. H.: Iterative correction for attenuation of 5 cm radar in rain, Journal of Applied Meteorology, 17, 508–514, 1978.

Hitschfeld, W. and Bordan, J.: Errors inherent in the radar measurement of rainfall at attenuating wavelengths, Journal of Meteorology, 11, 58–67, 1954.

Hooper, J. and Kippax, A.: The bright band - a phenomenon associated with radar echoes from falling rain, Quarterly Journal of the Royal Meteorological Society, 76, 125–132, 1950.

Hubbert, J. and Bringi, V.: An iterative filtering technique for the analysis of copolar differential phase and dual-frequency radar measurements, Journal of Atmospheric and Oceanic Technology, 12, 643–648, 1995.

Hubbert, J. C., Dixon, M., Ellis, S. M., and Meymaris, G.: Weather radar ground clutter. Part I: Identification, modeling, and simulation, Journal of Atmospheric and Oceanic Technology, 26, 1165–1180, 2009.

Huggel, A., Schmid, W., and Waldvogel, A.: Raindrop size distributions and the radar bright band, Journal of Applied Meteorology, 35, 1688–1701, 1996.

Humphrey, M., Istok, J., Lee, J., Hevesi, J., and Flint, A.: A new method for automated dynamic calibration of tipping-bucket rain gauges, Journal of Atmospheric and Oceanic Technology, 14, 1513–1519, 1997.

Illingworth, A. J. and Caylor, I. J.: Cross polar observations of the bright band, in: 24th Conference on Radar Meteorology, Tallahassee, FL, pp. 323–327, 1989.

Jameson, A.: Microphysical interpretation of multiparameter radar measurements in rain. Part III: Interpretation and measurement of propagation differential phase shift between orthogonal linear polarizations, Journal of the Atmospheric Sciences, 42, 607–614, 1985.

Jameson, A.: The effect of temperature on attenuation-correction schemes in rain using polarization propagation differential phase shift, Journal of Applied Meteorology, 31, 1106–1118, 1992.

Jewell, S. A. and Gaussiat, N.: An assessment of kriging-based rain-gauge–radar merging techniques, Quarterly Journal of the Royal Meteorological Society, 141, 2300–2313, 2015.

Jiang, S., Ren, L., Hong, Y., Yong, B., Yang, X., Yuan, F., and Ma, M.: Comprehensive evaluation of multi-satellite precipitation products with a dense rain gauge network and optimally merging their simulated hydrological flows using the Bayesian model averaging method, Journal of Hydrology, 452, 213–225, 2012.

Jordan, P., Seed, A., and Austin, G.: Sampling errors in radar estimates of rainfall, Journal of Geophysical Research: Atmospheres, 105, 2247–2257, 2000.

Joss, J. and Germann, U.: Solutions and problems when applying qualitative and quantitative information from weather radar, Physics and Chemistry of the Earth, Part B: Hydrology, Oceans and Atmosphere, 25, 837–841, 2000.

Joss, J. and Lee, R.: The application of radar–gauge comparisons to operational precipitation profile corrections, Journal of Applied Meteorology, 34, 2612–2630, 1995.

Joss, J., Schram, K., Thams, J., and Waldvogel, A.: On the Quantitative Determination of Precipitation by a Radar., Tech. rep., DTIC Document, 1970.

Kitchen, M., Brown, R., and Davies, A.: Real-time correction of weather radar data for the effects of bright band, range and orographic growth in widespread precipitation, Quarterly Journal of the Royal Meteorological Society, 120, 1231–1254, 1994.

Klaassen, W.: Radar observations and simulation of the melting layer of precipitation, Journal of the Atmospheric Sciences, 45, 3741–3753, 1988.

Kollat, J. B., Kasprzyk, J. R., Thomas Jr, W. O., Miller, A. C., and Divoky, D.: Estimating the impacts of climate change and population growth on flood discharges in the United States, Journal of Water Resources Planning and Management, 138, 442–452, 2012.

Kumjian, M. R.: Principles and applications of dual-polarization weather radar. Part I: Description of the polarimetric radar variables, Journal of Operational Meteorology, 1, 226–242, 2013.

Kumjian, M. R., Mishra, S., Giangrande, S. E., Toto, T., Ryzhkov, A. V., and Bansemer, A.: Polarimetric radar and aircraft observations of saggy bright bands during MC3E, Journal of Geophysical Research: Atmospheres, 121, 3584–3607, 2016.

Kurri, M. and Huuskonen, A.: Measurements of the transmission loss of a radome at different rain intensities, Journal of Atmospheric and Oceanic Technology, 25, 1590–1599, 2008.

Lakshmanan, V., Fritz, A., Smith, T., Hondl, K., and Stumpf, G.: An automated technique to quality control radar reflectivity data, Journal of Applied Meteorology and Climatology, 46, 288–305, 2007.

Lakshmanan, V., Karstens, C., Krause, J., and Tang, L.: Quality control of weather radar data using polarimetric variables, Journal of Atmospheric and Oceanic Technology, 31, 1234–1249, 2014.

Lane, J.: Radar echoes from clear air in relation to refractive-index variations in the troposphere, Electrical Engineers, Proceedings of the Institution of, 116, 1656–1660, 1969.

Lang, T. J., Nesbitt, S. W., and Carey, L. D.: On the correction of partial beam blockage in polarimetric radar data, Journal of Atmospheric and Oceanic Technology, 26, 943–957, 2009.

Lanza, L. G. and Vuerich, E.: The WMO field intercomparison of rain intensity gauges, Atmospheric Research, 94, 534–543, 2009.

Leon, D. C., French, J. R., Lasher-Trapp, S., Blyth, A. M., Abel, S. J., Ballard, S., Barrett, A., Bennett, L. J., Bower, K., Brooks, B., Brown, P., Charlton-Perez, C., Choularton, T., Clark, P., Collier, C., Crosier, J., Cui, Z., Dey, S., Dufton, D., Eagle, C., Flynn, M. J., Gallagher, M., Halliwell, C., Hanley, K., Hawkness-Smith, L., Huang, Y., Kelly, G., Kitchen, M., Korolev, A., Lean, H., Liu, Z., Marsham, J., Moser, D., Nicol, J., Norton, E. G., Plummer, D., Price, J., Ricketts, H., Roberts, N., Rosenberg, P. D., Simonin, D., Taylor, J. W., Warren, R., Williams, P. I., and Young, G.: The COnvective Precipitation Experiment (COPE): Investigating the origins of heavy precipitation in the southwestern UK, Bulletin of the American Meteorological Society, 97, 1003–1020, 2016.

Liechti, K., Zappa, M., Fundel, F., and Germann, U.: Probabilistic evaluation of ensemble discharge nowcasts in two nested Alpine basins prone to flash floods, Hydrological Processes, 27, 5–17, 2013.

Lim, S., Cifelli, R., Chandrasekar, V., and Matrosov, S.: Precipitation classification and quantification using X-band dual-polarization weather radar: Application in the hydrometeorology testbed, Journal of Atmospheric and Oceanic Technology, 30, 2108–2120, 2013.

Liu, C. and Krajewski, W. F.: A comparison of methods for calculation of radar - rainfall hourly accumulations, JAWRA Journal of the American Water Resources Association, 32, 305–315, 1996.

Llort, X., Velasco-Forero, C., Roca-Sancho, J., and Sempere-Torres, D.: Characterization of uncertainty in radar-based precipitation estimates and ensemble generation, in: Fifth European Conference on Radar in Meteorology and Hydrology, vol. 12, 2008.

Manz, A., Smith, A., and Hardaker, P.: Comparison of different methods of end to end calibration of the UK weather radar network, Physics and Chemistry of the Earth, Part B: Hydrology, Oceans and Atmosphere, 25, 1157–1162, 2000.

Marshall, J., Langille, R., and Palmer, W. M. K.: Measurement of rainfall by radar, Journal of Meteorology, 4, 186–192, 1947.

Marshall, J., Hitschfeld, W., and Gunn, K.: Advances in radar weather, Advances in geophysics, 2, 1–56, 1955.

Marshall, J. S. and Hitschfeld, W.: Interpretation of the fluctuating echo from randomly distributed scatterers. Part I, Canadian Journal of Physics, 31, 962–994, 1953.

Marzano, F. S., Scaranari, D., Montopoli, M., and Vulpiani, G.: Supervised classification and estimation of hydrometeors from C-band dual-polarized radars: A Bayesian approach, Geoscience and Remote Sensing, IEEE Transactions on, 46, 85–98, 2008.

Matrosov, S. Y.: Evaluating polarimetric X-band radar rainfall estimators during HMT, Journal of Atmospheric and Oceanic Technology, 27, 122–134, 2010.

Matrosov, S. Y., Kropfli, R. A., Reinking, R. F., and Martner, B. E.: Prospects for measuring rainfall using propagation differential phase in X-and Ka-radar bands, Journal of Applied Meteorology, 38, 766–776, 1999.

Matrosov, S. Y., Clark, K. A., Martner, B. E., and Tokay, A.: X-band polarimetric radar measurements of rainfall, Journal of Applied Meteorology, 41, 941–952, 2002.

Matrosov, S. Y., Cifelli, R., Kennedy, P. C., Nesbitt, S. W., Rutledge, S. A., Bringi, V., and Martner, B. E.: A comparative study of rainfall retrievals based on specific differential phase shifts at X-and S-band radar frequencies, Journal of Atmospheric and Oceanic Technology, 23, 952–963, 2006.

Matrosov, S. Y., Cifelli, R., and Gochis, D.: Measurements of heavy convective rainfall in the presence of hail in flood-prone areas using an X-band polarimetric radar, Journal of Applied Meteorology and Climatology, 52, 395–407, 2013.

Maynard, R. H.: Radar and weather, Journal of Meteorology, 2, 214–226, 1945.

Meischner, P., Bringi, V., Heimann, D., and Höller, H.: A squall line in southern Germany: Kinematics and precipitation formation as deduced by advanced polarimetric and Doppler radar measurements, Monthly weather review, 119, 678–701, 1991.

Meischner, P., Collier, C., Illingworth, A., Joss, J., and Randeu, W.: Advanced weather radar systems in Europe: The COST 75 action, Bulletin of the American Meteorological Society, 78, 1411–1430, 1997.

Melnikov, V. M., Istok, M. J., and Westbrook, J. K.: Asymmetric radar echo patterns from insects, Journal of Atmospheric and Oceanic Technology, 32, 659–674, 2015.

Moore, R., Cole, S., Bell, V., and Jones, D.: Issues in flood forecasting: ungauged basins, extreme floods and uncertainty., pp. 103–122, 2006.

Morris, J., Penning-Rowsell, E., and Chatterton, J.: The costs of the summer 2007 floods in England, Tech. rep., Joint Defra/Environment Agency Flood and Coastal Erosion Risk Management Research and Development Programme, 2010.

Mueller, E. A. and Larkin, R. P.: Insects observed using dual-polarization radar, Journal of Atmospheric and Oceanic Technology, 2, 49–54, 1985.

Neale, W.: Summary of Findings and Conclusions from survey distributed by the Inter-Agency Committee on the Hydrological Use of Weather Radar, Tech. rep., Thames Water Utilities Ltd, 2012.

Nguyen, C. M., Moisseev, D. N., and Chandrasekar, V.: A parametric time domain method for spectral moment estimation and clutter mitigation for weather radars, Journal of Atmospheric and Oceanic Technology, 25, 83–92, 2008.

Nicol, J. and Austin, G.: Attenuation correction constraint for single-polarisation weather radar, Meteorological Applications, 10, 345–354, 2003.

Pamment, J. and Conway, B.: Objective identification of echoes due to anomalous propagation in weather radar data, Journal of Atmospheric and Oceanic Technology, 15, 98–113, 1998.

Park, H. S., Ryzhkov, A. V., Zrnić, D. S., and Kim, K.-E.: The hydrometeor classification algorithm for the polarimetric WSR-88D: Description and application to an MCS, Weather and Forecasting, 24, 730–748, 2009.

Park, S., Bringi, V., Chandrasekar, V., Maki, M., and Iwanami, K.: Correction of radar reflectivity and differential reflectivity for rain attenuation at X band. Part I: Theoretical and empirical basis, Journal of Atmospheric and Oceanic Technology, 22, 1621–1632, 2005.

Plank, V. G.: A meteorological study of radar angels, Tech. rep., DTIC Document, 1956.

Price, D., Hudson, K., Boyce, G., Schellekens, J., Moore, R. J., Clark, P., Harrison, T., Connolly, E., and Pilling, C.: Operational use of a grid-based model for flood forecasting, Proceedings of the Institution of Civil Engineers-Water Management, 165, 65–77, 2012.

Qi, Y., Zhang, J., and Zhang, P.: A real-time automated convective and stratiform precipitation segregation algorithm in native radar coordinates, Quarterly Journal of the Royal Meteorological Society, 139, 2233–2240, 2013.

Quintero, F., Sempere-Torres, D., Berenguer, M., and Baltas, E.: A scenario-incorporating analysis of the propagation of uncertainty to flash flood simulations, Journal of Hydrology, 460–461, 90–102, 2012.

Rico-Ramirez, M. and Cluckie, I.: Bright-band detection from radar vertical reflectivity profiles, International Journal of Remote Sensing, 28, 4013–4025, 2007.

Rico-Ramirez, M. A. and Cluckie, I. D.: Classification of ground clutter and anomalous propagation using dual-polarization weather radar, Geoscience and Remote Sensing, IEEE Transactions on, 46, 1892–1904, 2008.

Rosenfeld, D., Amitai, E., and Wolff, D. B.: Classification of rain regimes by the three-dimensional properties of reflectivity fields, Journal of Applied Meteorology, 34, 198–211, 1995.

Ryzhkov, A. and Zrnic, D.: Assessment of rainfall measurement that uses specific differential phase, Journal of Applied Meteorology, 35, 2080–2090, 1996.

Ryzhkov, A., Ganson, S., Kumjian, M., and Kaltenboeck, R.: Polarimetric characteristics of dry and melting hail at different radar wavelengths, in: Extended Abstracts, Seventh European Conf. on Radar in Meteorology and Hydrology, 2012.

Ryzhkov, A., Zhang, P., Reeves, H., Kumjian, M., Tschallener, T., Trömel, S., and Simmer, C.: Quasi-vertical profiles - A new way to look at polarimetric radar data, Journal of Atmospheric and Oceanic Technology, 33, 551–562, 2016.

Ryzhkov, A. V. and Zrnić, D. S.: Precipitation and attenuation measurements at a 10-cm wavelength, Journal of Applied Meteorology, 34, 2121–2134, 1995.

Ryzhkov, A. V. and Zrnić, D. S.: Radar polarimetry at S, C, and X bands: Comparative analysis and operational implications, in: 32nd AMS International Conference on Radar Meteorology, Alberquerque, 2005.

Ryzhkov, A. V. and Zrnic, D. S.: Depolarization in ice crystals and its effect on radar polarimetric measurements, Journal of Atmospheric and Oceanic Technology, 24, 1256–1267, 2007.

Ryzhkov, A. V., Giangrande, S. E., Melnikov, V. M., and Schuur, T. J.: Calibration issues of dual-polarization radar measurements, Journal of Atmospheric and Oceanic Technology, 22, 1138–1155, 2005a.

Ryzhkov, A. V., Schuur, T. J., Burgess, D. W., Heinselman, P. L., Giangrande, S. E., and Zrnić, D. S.: The joint polarization experiment, Bulletin of the American Meteorological Society, 86, 809–824, 2005b.

Ryzhkov, A. V., Kumjian, M. R., Ganson, S. M., and Zhang, P.: Polarimetric radar characteristics of melting hail. Part II: Practical implications, Journal of Applied Meteorology and Climatology, 52, 2871–2886, 2013.

Ryzhkov, A. V., Diederich, M., Zhang, P., and Simmer, C.: Potential utilization of specific attenuation for rainfall estimation, mitigation of partial beam blockage, and radar networking, Journal of Atmospheric and Oceanic Technology, 31, 599–619, 2014.

Sachidananda, M. and Zrnic, D.: Differential propagation phase shift and rainfall rate estimation, Radio Science, 21, 235–247, 1986.

Sánchez-Diezma, R., Zawadzki, I., and Sempere-Torres, D.: Identification of the bright band through the analysis of volumetric radar data, Journal of Geophysical Research: Atmospheres (1984–2012), 105, 2225–2236, 2000.

Scarchilli, G., Gorgucci, E., Chandrasekar, V., and Dobaie, A.: Self-consistency of polarization diversity measurement of rainfall, Geoscience and Remote Sensing, IEEE Transactions on, 34, 22–26, 1996.

Schneebeli, M. and Berne, A.: An extended Kalman filter framework for polarimetric X-band weather radar data processing, Journal of Atmospheric and Oceanic Technology, 29, 711–730, 2012.

Schneider, C., Laizé, C., Acreman, M., and Florke, M.: How will climate change modify river flow regimes in Europe?, Hydrology and Earth System Sciences, 17, 325–339, 2013.

Schrom, R. S. and Kumjian, M. R.: Connecting microphysical processes in Colorado winter storms with vertical profiles of radar observations, Journal of Applied Meteorology and Climatology, 2016.

Schröter, K., Llort, X., Velasco-Forero, C., Ostrowski, M., and Sempere-Torres, D.: Implications of radar rainfall estimates uncertainty on distributed hydrological model predictions, Atmospheric Research, 100, 237–245, 2011.

Sekhon, R. and Srivastava, R.: Snow size spectra and radar reflectivity, Journal of the Atmospheric Sciences, 27, 299–307, 1970.

Seliga, T. and Bringi, V.: Potential use of radar differential reflectivity measurements at orthogonal polarizations for measuring precipitation, Journal of Applied Meteorology and Climatology, 15, 69–76, 1976.

Seliga, T. and Bringi, V.: Differential reflectivity and differential phase shift: Applications in radar meteorology, Radio Science, 13, 271–275, 1978.

Serafin, R. J. and Wilson, J. W.: Operational weather radar in the United States: Progress and opportunity, Bulletin of the American Meteorological Society, 81, 501–518, 2000.

Serrar, S., Delrieu, G., Creutin, J.-D., and Uijlenhoet, R.: Mountain reference technique: Use of mountain returns to calibrate weather radars operating at attenuating wavelengths, Journal of Geophysical Research: Atmospheres (1984–2012), 105, 2281–2290, 2000.

Sevruk, B.: Methods of correction for systematic error in point precipitation measurement for operational use. Operational hydrology report no. 21, Tech. rep., 1982.

Sevruk, B., Ondrás, M., and Chvíla, B.: The WMO precipitation measurement intercomparisons, Atmospheric Research, 92, 376–380, 2009.

Sieck, L. C., Burges, S. J., and Steiner, M.: Challenges in obtaining reliable measurements of point rainfall, Water Resources Research, 43, 2007.

Smith, C. J.: The reduction of errors caused by bright bands in quantitative rainfall measurements made using radar, Journal of Atmospheric and Oceanic Technology, 3, 129–141, 1986.

Smyth, T. and Illingworth, A.: Correction for attenuation of radar reflectivity using polarization data, Quarterly Journal of the Royal Meteorological Society, 124, 2393–2415, 1998a.

Smyth, T. and Illingworth, A.: Radar estimates of rainfall rates at the ground in bright band and non-bright band events, Quarterly Journal of the Royal Meteorological Society, 124, 2417–2434, 1998b.

Steiner, M. and Smith, J. A.: Use of three-dimensional reflectivity structure for automated detection and removal of nonprecipitating echoes in radar data, Journal of Atmospheric and Oceanic Technology, 19, 673–686, 2002.

Steiner, M., Houze Jr, R. A., and Yuter, S. E.: Climatological characterization of three-dimensional storm structure from operational radar and rain gauge data, Journal of Applied Meteorology, 34, 1978–2007, 1995.

Tabary, P.: The new French operational radar rainfall product. Part I: Methodology, Weather and Forecasting, 22, 393–408, 2007.

Tabary, P., Vulpiani, G., Gourley, J. J., Illingworth, A. J., Thompson, R. J., and Bousquet, O.: Unusually high differential attenuation at C band: Results from a two-year

analysis of the French Trappes polarimetric radar data, Journal of Applied Meteorology and Climatology, 48, 2037–2053, 2009.

Testud, J., Le Bouar, E., Obligis, E., and Ali-Mehenni, M.: The rain profiling algorithm applied to polarimetric weather radar, Journal of Atmospheric and Oceanic Technology, 17, 332–356, 2000.

Torres, S. M. and Zrnić, D. S.: Ground clutter canceling with a regression filter, Journal of Atmospheric and Oceanic Technology, 16, 1364–1372, 1999.

Trömel, S., Kumjian, M. R., Ryzhkov, A. V., Simmer, C., and Diederich, M.: Backscatter differential phase - Estimation and variability, Journal of Applied Meteorology and Climatology, 52, 2529–2548, 2013.

Tyynelä, J., Leinonen, J., Moisseev, D., Nousiainen, T., and von Lerber, A.: Modeling radar backscattering from melting snowflakes using spheroids with nonuniform distribution of water, Journal of Quantitative Spectroscopy and Radiative Transfer, 133, 504–519, 2014.

Uijlenhoet, R., Steiner, M., and Smith, J. A.: Variability of raindrop size distributions in a squall line and implications for radar rainfall estimation, Journal of Hydrometeorology, 4, 43–61, 2003.

Veldkamp, T. I., Wada, Y., de Moel, H., Kummu, M., Eisner, S., Aerts, J. C., and Ward, P. J.: Changing mechanism of global water scarcity events: Impacts of socioeconomic changes and inter-annual hydro-climatic variability, Global Environmental Change, 32, 18–29, 2015.

Villarini, G. and Krajewski, W. F.: Empirically-based modeling of spatial sampling uncertainties associated with rainfall measurements by rain gauges, Advances in Water Resources, 31, 1015–1023, 2008.

Villarini, G. and Krajewski, W. F.: Review of the different sources of uncertainty in single polarization radar-based estimates of rainfall, Surveys in Geophysics, 31, 107–129, 2010a.

Villarini, G. and Krajewski, W. F.: Sensitivity studies of the models of radar-rainfall uncertainties, Journal of Applied Meteorology and Climatology, 49, 288–309, 2010b.

Villarini, G., Mandapaka, P. V., Krajewski, W. F., and Moore, R. J.: Rainfall and sampling uncertainties: A rain gauge perspective, Journal of Geophysical Research: Atmospheres (1984–2012), 113, 2008.

Vivekanandan, J., Bringi, V., Hagen, M., and Meischner, P.: Polarimetric radar studies of atmospheric ice particles, Geoscience and Remote Sensing, IEEE Transactions on, 32, 1–10, 1994.

Vivekanandan, J., Yates, D. N., and Brandes, E. A.: The influence of terrain on rainfall estimates from radar reflectivity and specific propagation phase observations, Journal of Atmospheric and Oceanic Technology, 16, 837–845, 1999.

Vivekanandan, J., Zhang, G., Ellis, S. M., Rajopadhyaya, D., and Avery, S. K.: Radar reflectivity calibration using differential propagation phase measurement, Radio Science, 38, 2003.

Wang, Y. and Chandrasekar, V.: Polarization isolation requirements for linear dual-polarization weather radar in simultaneous transmission mode of operation, Geoscience and Remote Sensing, IEEE Transactions on, 44, 2019–2028, 2006.

Wang, Y. and Chandrasekar, V.: Algorithm for estimation of the specific differential phase, Journal of Atmospheric and Oceanic Technology, 26, 2565–2578, 2009.

Wang, Y., Zhang, P., Ryzhkov, A. V., Zhang, J., and Chang, P.-L.: Utilization of specific attenuation for tropical rainfall estimation in complex terrain, Journal of Hydrometeorology, 15, 2250–2266, 2014.

Watson-Watt, R.: Radar in war and in peace, Nature, 156, 319–324, 1945.

Wexler, R. and Atlas, D.: Radar Reflectivity and Attenuation of Rain, Journal of Applied Meteorology, 2, 276–280, 1963.

Wilson, J. W. and Brandes, E. A.: Radar measurement of rainfall - a summary, Bulletin of the American Meteorological Society, 60, 1048–1058, 1979.

Wilson, J. W., Weckwerth, T. M., Vivekanandan, J., Wakimoto, R. M., and Russell, R. W.: Boundary layer clear-air radar echoes: Origin of echoes and accuracy of derived winds, Journal of Atmospheric and Oceanic Technology, 11, 1184–1206, 1994.

Wu, S.-J., Lien, H.-C., Hsu, C.-T., Chang, C.-H., and Shen, J.-C.: Modeling probabilistic radar rainfall estimation at ungauged locations based on spatiotemporal errors which correspond to gauged data, Hydrology Research, 46, 39–59, 2015.

Zadeh, L. A.: A computational approach to fuzzy quantifiers in natural languages, Computers & Mathematics with applications, 9, 149–184, 1983.

Zappa, M., Jaun, S., Germann, U., Walser, A., and Fundel, F.: Superposition of three sources of uncertainties in operational flood forecasting chains, Atmospheric Research, 100, 246–262, 2011.

Zhang, P., Zrnić, D. S., and Ryzhkov, A. V.: Partial beam blockage correction using polarimetric radar measurements, Journal of Atmospheric and Oceanic Technology, 30, 861–872, 2013.

Zhu, D. and Cluckie, I.: A preliminary appraisal of Thurnham dual polarisation radar in the context of hydrological modelling structure, Hydrology Research, 43, 736–752, 2012.

Zrnić, D. S. and Ryzhkov, A. V.: Advantages of rain measurements using specific differential phase, Journal of Atmospheric and Oceanic Technology, 13, 454–464, 1996.

Zrnić, D. S. and Ryzhkov, A. V.: Observations of insects and birds with a polarimetric radar, Geoscience and Remote Sensing, IEEE Transactions on, 36, 661–668, 1998.

Zrnić, D. S. and Ryzhkov, A. V.: Polarimetry for weather surveillance radars, Bulletin of the American Meteorological Society, 80, 389–406, 1999.

Zrnić, D. S., Melnikov, V. M., and Ryzhkov, A. V.: Correlation coefficients between horizontally and vertically polarized returns from ground clutter, Journal of Atmospheric and Oceanic Technology, 23, 381–394, 2006.